Computational Methods and Measurements for Direct and Inverse Scattering of Microwaves

Wingren, Niklas

2024

Document Version:
Publisher's PDF, also known as Version of record

Computational Methods and Measurements for Direct and Inverse Scattering of Microwaves

Niklas Wingren

Doctoral Dissertation

Lund University
Lund, Sweden
2024

Department of Electrical and Information Technology
Division of Electromagnetics and Nanoelectronics
Lund University
Box 118, 221 00 Lund, Sweden

Series of licentiate and doctoral theses
ISSN: 1654-790X; No. 170
ISBN: 978-91-7895-994-5 (print)
ISBN: 978-91-7895-995-2 (digital)

Typeset in Computer Modern 10 pt using LaTeX and BibTeX.
Printed in Sweden by *Tryckeriet i E-huset*, Lund University, Lund.
March, 2024

DON’T PANIC

Abstract

Electromagnetic waves are widely used in society today for a multitude of applications. Design of electromagnetic devices and applications requires accurate methods for evaluating performance, which often means modern computational methods. While these methods have seen tremendous development in recent decades, it is still very important to perform measurements to validate the performance of devices and software. This dissertation contains work on the computational side as well as validating measurements.

The dissertation consists of two parts. Part I is an introduction to the subject, and Part II consists of five scientific papers. The introduction gives an overview of the topics which are important for understanding the scientific papers of Part II and puts the research in a wider context. Of the scientific papers in Part II, two are published in peer-reviewed international journals, one is accepted for publication, and two are under review.

The problem of electromagnetic scattering has long been important in radar, where it is the mechanism for detection. This is often called the direct scattering problem, where a known object is illuminated by an incident wave and the scattered wave is computed. In Paper I, a computational code implementing the finite element-boundary integral method is presented. The code, which is publicly available at https://www.github.com/nwingren/fe2ms, was developed using open-source software to accelerate the development process. While this code is verified in Paper I, there were no comparisons to measurements. In Paper II, a complete design process was performed using the code from Paper I, with manufacturing using 3D printing and measurements of the performance to validate the computations. This acted both as a demonstration of using the code practically, and as a validation. One advantage of the finite element-boundary integral method used in the code is that problems with highly complex media can be solved. This was utilized in Paper III where characteristic modes were computed for a an inhomogeneous, bianisotropic, and nonreciprocal object.

A different problem is that of inverse scattering, for which the scattered wave is known but the object or incident wave is unknown. This is a more complicated problem which requires the modern computational methods available today, and can be used to discern properties of an object, for example for nondestructive testing. In Paper IV, a method for nondestructive testing of singly curved composite panels using millimeter waves is presented together with measurements of real panels. The method is based on computational electromagnetics and was designed specifically for detection of sparsely distributed flaws in such panels. Microwaves and millimeter waves are relatively new in nondestructive testing compared to other methods like ultrasound. One possible development would be to combine the new and the old by utilizing interaction between acoustic and electromagnetic waves. As a way to demonstrate that this might be possible, microwaves scattered by ultrasound were measured in Paper V in air, where the interaction would be much weaker than in nondestructive testing settings.

Populärvetenskaplig sammanfattning

Elektromagnetiska vågor och deras tillämpningar utgör en viktig del av våra liv även om många av oss kanske inte tänker på det. Våra mobiltelefoner innehåller ett stort antal antenner för att kunna koppla upp sig mot internet, hitta vår position via GPS eller spela upp musik via Bluetooth. Vi använder en antenn inuti vårt bankkort när vi ska betala trådlöst, och våra bilar håller ständig uppsikt för hinder med inbyggda radarsensorer. En viktig förutsättning för denna utveckling är de verktyg för elektromagnetiska beräkningar som är tillgängliga för dagens ingenjörer.

En huvuddel av avhandlingen täcker just elektromagnetiska beräkningar. Utvecklingen av nya tillämpningar inom elektromagnetismen ställer höga krav på en motsvarande utveckling av verktyg som används vid beräkningar för nya system. Ingenjörer som designar nya system använder sig främst av kommersiella datorprogram, men dessa bygger i sin tur på nya metoder från akademisk forskning. Metoden för elektromagnetiska beräkningar jag använt mig av lämpar sig vid problem med komplicerade materialstrukturer. Mitt arbete har fokuserat på öppen källkod, vilket innebär att datorprogram görs fritt tillgängliga för andra att använda och modifiera. Då jag använt andras program som byggblock har utvecklingen av mitt program kunnat accelereras, och jag hoppas att andra kan få liknande hjälp av mitt arbete. Utöver att jag har utvecklat ett öppet tillgängligt beräkningsprogram har jag även visat hur det kan användas för olika typer av beräkningsproblem. I ett av dessa har jag kunnat använda mitt beräkningsprogram för att designa en ny typ av elektromagnetisk struktur där en prototyp senare uppmättes med god överenstämmelse. Programmet har även kunnat användas för en ny typ av teoretisk beräkning som kommersiella datorprogram inte klarar av.

En annan del av avhandlingen handlar om tillämpningar inom avbildning för industriell produktion. Utvecklingen av exempelvis trådlös kommunikation har gjort att tekniken som används blivit billigare och mer kraftfull. Detta är något som öppnar möjligheter att använda tekniken inom områden som inte tidigare varit praktiska. Ett exempel är att vi idag effektivt kan använda mikrovågor för att avbilda föremål på sätt som inte vanligt ljus kan göra. Detta sker på stor skala i säkerhetskontroller på flygplatser, men stora möjligheter finns även inom bland annat industriell kvalitetskontroll och medicinsk avbildning. Som del av den här avhandlingen har jag arbetat med avbildning med mikrovågor för att kunna utföra oförstörande provning av kompositmaterial som används i flygplan. Oförstörande provning är ett samlingsnamn för olika metoder som används för att hitta defekter i en produkt utan att påverka dess funktion. Detta är viktigt inom många olika industrier, men särskilt inom flygindustrin är oförstörande provning en nödvändighet för alla strukturella delar. Ofta används ultraljud för detta, men mikrovågor är känsliga för andra typer av defekter och kan därför vara av intresse. Tidigare metoder utvecklade i samma forskargrupp fokuserade på plana paneler, men jag utvecklade metoden till att även kunna användas på

krökta paneler. I flygplan är många ytor krökta för att få till rätt aerodynamik och därför är detta ett viktigt steg.

Då ultraljud används ofta inom oförstörande provning är det nära till hands att försöka kombinera ultraljud med mikrovågor och dra nytta av båda metodernas fördelar. Växelverkan mellan elektromagnetiska vågor och akustiska vågor har undersökts tidigare, men inte för de våglängder som är aktuella inom oförstörande provning. För att undersöka hur väl det skulle fungera testade jag att mäta detta, men i luft i stället för typiska material för flygplan. Detta gjorde det möjligt för mig att mäta växelverkan i vår labbmiljö med befintlig utrustning. Växelverkan i luft är väldigt svag, men jag lyckades trots det detektera växelverkan mellan de två typerna av vågor. Detta bådar gott för mätningar i andra material än luft där effekten väntas vara starkare.

Preface

This dissertation summarizes the research I have carried out at the Department of Electrical and Information Technology, Lund University, Sweden. The dissertation starts with a research overview followed by the scientific papers as listed below. The papers are not ordered chronologically, but rather according to their general topics.

List of Included Papers

I. N. Wingren and D. Sjöberg, "Using Open Source to Accelerate Development of a Finite Element-Boundary Integral Code," *IEEE Open Journal of Antennas and Propagation*, vol. 5, no. 3, pp. 587–600, 2024.

Contributions of the author: I developed the computational software, performed the numerical tests and wrote the paper.

II. N. Wingren and D. Sjöberg, "Demonstrating Reconfigurability in Water-based Electromagnetic Devices using a 3D-printed Siphon," *Microwave and Optical Technology Letters*, Vol. 66, No. 7, 2024.

Contributions of the author: I designed and manufactured the device, performed the numerical simulations and measurements, processed the data and wrote the paper.

III. N. Wingren, D. Sjöberg, M. Gustafsson, J. Lundgren, M. Capec, L. Jelinek, and K. Schab, "Characteristic Modes of Nonreciprocal Systems," *IEEE Antennas and Wireless Propagation Letters*, vol. 23, no. 12, pp. 4483–4487, 2024.

Contributions of the author: I performed the numerical simulations of the third example, analyzed the corresponding data and wrote parts of the paper.

IV. N. Wingren and D. Sjöberg, "Nondestructive Testing Using mm-Wave Sparse Imaging Verified for Singly Curved Composite Panels," *IEEE Transactions on Antennas and Propagation*, Vol. 71, No. 1, pp. 1185–1189, 2022.

Contributions of the author: I extended the algorithm to singly curved structures, performed the measurements, post-processed the data and wrote the paper.

V. N. Wingren and D. Sjöberg, "Measurements of microwave scattering by ultrasound in air at oblique incidence," *Europhysics Letters*, Vol. 131, No. 5, 2020.

Contributions of the author: I designed the experimental setup, performed the measurements and wrote the paper.

Other Scientific Work by the Author

The author of this dissertation is also the author or co-author of the following publications and scientific work which are related to but not considered part of the dissertation:

VI. N. Wingren and D. Sjöberg "Simulating Magnetized Plasma using an Accelerated Finite Element-Boundary Integral Code" *XXXVth URSI General Assembly and Scientific Symposium (URSI GASS),* Sapporo, Japan, 2023.

VII. N. Wingren and D. Sjöberg "An Accelerated Finite Element-Boundary Integral Code Developed using Open Source Software" *Swedish Microwave Days,* Stockholm, Sweden, 2023.

VIII. N. Wingren and D. Sjöberg "Investigating Low-Rank Approximations for the Finite Element-Boundary Integral Method" *17th European Conference on Antennas and Propagation (EuCAP),* Florence, Italy, 2023.

IX. N. Wingren and D. Sjöberg "Finite Element-Boundary Integral Simulation of Icing Effects on a Marine Radar Reflector" *3rd URSI Atlantic and Asia Pacific Radio Science Meeting (AT-AP-RASC),* Gran Canaria, Spain, 2022.

X. N. Wingren, D. Sjöberg, and M. Gustafsson "Conformal Sparse Image Reconstruction on Singly Curved Surfaces" *15th European Conference on Antennas and Propagation (EuCAP),* Düsseldorf, Germany, 2021.

XI. N. Wingren and D. Sjöberg, "Analytical Modeling and Multiphysics Simulation of Acousto-Electromagnetic Interaction" *14th European Conference on Antennas and Propagation (EuCAP),* Copenhagen, Denmark, 2020.

Acknowledgments

First, I would like to thank my main supervisor Daniel Sjöberg for guiding me throughout my PhD studies. When I started my master's thesis you were a great supervisor, and this played an important role in my decisions as we started discussing possible PhD studies. Even during the initial time when you were head of department, you would always find time for discussion regardless of how many meetings were in your calendar. I would also like to thank my assistant supervisor Mats Gustafsson. There are many times I have walked into your office with a problem and left with a new perspective and a clear path forward. To have two supervisors who make themselves available for discussions and who are as supporting as you are has been invaluable as a PhD student.

As the projects I have worked in during my studies have been collaborations with industrial partners, there are people who have helped me from the industrial side of things. Tomas Lundin, Torleif Martin, Christer Larsson, and Erik Söderström have all been involved in my two main projects and have helped me understand questions and problems from the industrial perspective.

My work could, of course, never have been done without funding. A large majority has been funded through the National Aeronautics Research Program (NFFP), which I would like to thank together with its partners in the Swedish Governmental Agency for Innovation Systems (VINNOVA), the Swedish Armed Forces, and the Swedish Defence Materiel Administration (FMV). I would also like to thank the LM Ericsson Research Foundation and the International Union of Radio Science for additional support in attending conferences.

I would like to thank my predecessor in the EKAS 2 project, Jakob Helander, for handing over your code to me and helping me understand it in the beginning of my studies. I would also like to thank Johan Lundgren for introducing me to mm-wave near-field scanning, and for being my co-assistant in teaching many courses. This includes the ever exciting task of grading lab reports, which I also thank Ben Nel for sharing with me. Another thank you goes to Zhongyunshen Zhu who, together with Mats, Ben, and me, shared the confusing experience of figuring out remote teaching in March 2020. There are also many people who I may not have worked much with, but who still have made the office a nice place to be. So thank you Casimir, Alexandros, Anton, Abinaya, Heera, Saketh, Navya, Gautham, Patrik, Robin, Marcus, Hannes, Philipp, Anette, Louise, André, Duc, Karthik, Paula, Lars-Erik, Lars, Erik, Mattias, and Johannes.

I want to thank my friends who have made the time as a PhD student easier by giving me time *not* to be a PhD student. I hope that the progress I have made in the research field of "building airplanes" is clear in this dissertation! Finally, I would like to thank my family who have always supported me and who have made this journey possible.

Lund, March 2024
Niklas Wingren

Acronyms and Abbreviations

2G	second generation of cellular networks
5G	fifth generation of cellular networks
6G	sixth generation of cellular networks
ACA	adaptive cross approximaiton
AIM	adaptive integral method
API	application programming interface
BI	boundary integral
BSD	Berkeley software distribution
CAD	computer-aided design
CEM	computational electromagnetics
CFIE	combined field integral equation
COCOMO	constructive cost model
DUT	device under test
DFT	discrete Fourier transform
EDUT	example device under test
EFIE	electric field integral equation
EM	electromagnetic
EPS	expanded polystyrene
FDTD	finite-difference time-domain
FE	finite element
FEM	finite element method
FFCx	FEniCSx form compiler
FFT	fast Fourier transform
GPL	general purpose license
HEM	hybrid electromagnetic
IF	intermediate frequency
JIT	just-in-time

MFIE	magnetic field integral equation
MLFMA	multilevel fast multipole algorithm
mm-wave	millimeter wave
MoM	method of moments
NDT	nondestructive testing
NEC	numerical electromagnetic code
PDE	partial differential equation
PEC	perfect electric conductor
PET	polyethylene terephthalate
PETG	polyethylene terephthalate glycol
PMC	perfect magnetic conductor
PML	perfectly matched layer
RCS	radar cross section
RWG	Rao-Wilton-Glisson
RASS	radio acoustic sounding system
Rx	receive
SAR	synthetic aperture radar
SLOC	source lines of code
SNR	signal-to-noise ratio
SVD	singular value decomposition
STL	stereolithography
TE	transverse electric
TM	transverse magnetic
Tx	transmit
UFL	unified form language

Contents

Part I: Introduction and Research Overview

1 Background and Motivation

Electromagnetic waves are widely used in all areas of modern society. Broadcasting like radio, terrestrial television and satellite television have been part of society for a long time, with radio broadcasting being widely available in many parts of the world a century ago [153]. In recent decades, however, other types of wireless communications have changed our world profoundly. While various analog forms of mobile communication technologies had been available earlier, the release of the digital second generation of cellular networks (2G) in 1991 [6] made wireless communications widely available and adopted by the public. Development since then has been rapid with the latest release being 5G in 2019 [164], and 6G currently under development [164]. During the same time, other wireless communication technologies like WiFi and Bluetooth have been developed as well, and today we find all these technologies neatly packaged in small cell phones together with other wireless technologies like satellite navigation and near-field communication. All these require antennas, and the design of these hidden away in a small package is not an easy task. One major reason why it is even possible to design a smartphone with all its electromagnetic capability is the use of modern electromagnetic computations [153].

Another application of electromagnetic waves is radar and remote sensing. Radar is originally an acronym for radio detection and ranging, and this essentially describes the technology which uses electromagnetic waves to determine position, velocity and possibly other properties of objects remotely. The first large-scale development of radar was for military applications before and during World War II [78, 153]. For much of the time since then, radar has been widely applied in various military systems as well as in aviation, meteorological, and marine applications [115]. However, with the rise of wireless communication since the 1990s, radio-frequency hardware has seen much technical development and as a consequence it became cheaper and more energy efficient. As radar uses similar hardware, the civilian applications of radar have become much more numerous with radar today being used widely in automotive applications [155], civilian surveillance [9], and low-cost, low-power sensors [1, 67, 140]. An example of a low-cost, low-power radar sensor is the Acconeer A121 sensor shown in Figure 1. Radar is widely used in the field of remote sensing to determine properties of an environment and produce large scale images of certain properties. This includes monitoring of various environmental properties of our planet using satellite-based radar system, which is an application that has become very important in Earth and climate science [12, 114]. Such a satellite-based radar system is seen in Figure 1. It has a very different size compared to the small Acconeer sensor, showing how radar systems can be useful at different scales. In most radar applications, it is important to understand how different targets react to illumination by electromagnetic waves from the radar transmitter. This is a complex task as this response can only be analytically computed for a few special geometries. It is possible to use various approximations, but for high-fidelity re-

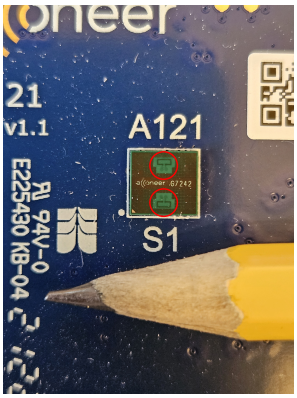

Figure 1: Two examples of radar systems. Left: Acconeer A121 radar sensor mounted on a circuit board with transmitting and receiving antennas encircled in red. Right: Sentinel-1A radar imaging satellite seen with its large radar antenna facing the camera (Photo: ©ESA–S. Corvaja, 2014).

sults it is necessary to use electromagnetic computations. Much of the efforts in electromagnetic computations have been in search of lowering the response of an object to radar in, for example, stealth aircraft [71, 78, 153]. These applications can set very high demands on the capability of the computational methods used, and many advances in such methods and software can be related back to uses in military applications. For example, an early computational code called the numerical electromagnetic code (NEC) was developed primarily to solve problems for the US air force and navy, but also laid much of the groundwork for development of methods and software which is widely used today in all electromagnetic applications [24, 25].

Electromagnetic computations have now been mentioned as an important enabling tool for our modern use of electromagnetic waves, and there is an interest in its continued development to support the general development in electromagnetics. In all fields of engineering, it is crucial to be able to compute and predict the capabilities of a designed object before manufacturing it. In some cases, this can be done analytically and that was the way most engineering was done before modern computers. For electromagnetics, there are generally few problems that can be solved analytically, and this limited engineering designs for much of the time since the first applications of electromagnetic waves in the early 1900s [153]. With the advent of computers, however, new types of methods using numerical computations became possible. This is a development seen in most areas of engineering, and many of the methods which are used in electromagnetics have their origin in methods used in other areas of physics. This is understandable since the methods themselves solve mathematical equations, and these equations are not necessarily tied to any particular branch of physics. The most accurate numerical methods used in electromagnetics are typically based on reformulating the basic equations of Maxwell's equations to other equations which are suit-

able for numerical solution, often categorized as differential equations or integral equations [35]. These two types of equations lead to different characteristics of the numerical methods, and in this dissertation methods from both types of equations are used. While the improved performance of computers was a large part of why numerical methods became popular, improvements of the numerical methods themselves have certainly played a role. The way that the numerical cost of popular methods scale with larger problem sizes means that increased computational power might not give much improvement in actual performance of a method. With development of algorithms to reduce this scaling of numerical cost, often referred to as acceleration or compression methods, the usefulness of computational methods in electromagnetics has been improved [35, 71].

With this great applicability of electromagnetic computations, it is important to consider the way methods are implemented. In most user settings, commercial software packages for computations are used. This is not strange, as such software is typically easy to use, well-tested, and optimized in its performance [35]. For academic research into the methods themselves, on the other hand, the use of such software is not ideal since it is generally not possible to modify. Instead, researchers develop the software themselves to be able to access all of the constituent parts. This is not without its drawbacks though, as development can be very time-consuming and much work might be necessary to implement basic methods from which to build upon. One way to reduce these issues is by using an open-source approach, *i.e.*, developing software which is freely distributed for others to use. It is not always easy to have a unified approach though, as there are different programming languages used, different conventions for implementing methods, and the fact that not everyone will want to distribute their software freely. Nevertheless, it is possible to accelerate the development of computational software by using freely available open-source packages, as was the case for computational software developed for work in this dissertation.

The development of various computational methods were often originally prompted by a need to solve a direct scattering problem, *i.e.*, finding the scattered electromagnetic wave for a known object illuminated by a known incident wave. This can also be applied to antenna problems, where the antenna feed can be formulated as the incident wave. Another important, but typically much more difficult, problem is the inverse scattering problem. Here, the scattered wave is known, but either the scattering object or the incident wave is unknown [56]. To make matters worse, in practical settings the scattered wave is measured and will include noise and other measurement errors. To be able to solve the inverse problem, methods used in the direct problem are typically applied, but with additions to ensure that the inverse solution is accurate. This often comes in the form of optimization formulations where the direct problem, or problems similar to it, may need to be solved many times for different source distributions [56, 98]. Solutions of inverse problems, for this reason, often require efficient direct solvers. With the development of faster methods in computational electromagnetics (CEM), as well as improved performance on the computer hardware side, the solution of inverse problems have become increasingly attainable in recent decades. One

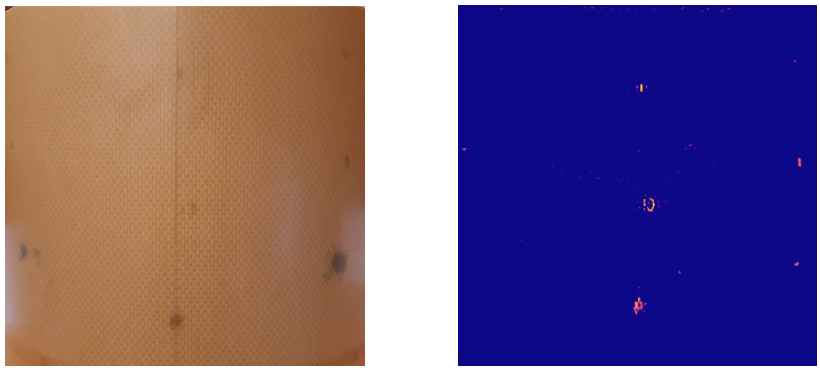

Figure 2: Example of an industrially manufactured composite panel (left) and an image indicating flaws (right).

use of inverse scattering is for nondestructive testing (NDT) in industrial settings. This is an area in which other physical phenomena like ultrasound and x-rays have been used for many decades, while the use of microwaves is relatively new [131, 168]. The typical use case is to detect flaws in a manufactured product without affecting it negatively [131]. In many cases, it can also be interesting to do this by generating an image, showing the possible locations of flaws as seen in Figure 2. For microwaves, such imaging has been performed with a wide range of methods which are not related to inverse scattering [2, 98]. Often, these methods are computationally cheaper than the alternatives based on inverse scattering, but with less information regarding the physical characteristics of the sample. Furthermore, methods in inverse scattering can use prior knowledge of the sample to improve images in ways not possible using traditional methods [98].

For NDT, as in similar areas like medical imaging, an interesting idea is the simultaneous use of multiple physical phenomena [42]. In particular, the wide use of ultrasound makes for an interesting possible combination with the newer microwave methods, especially since there are well-known interaction mechanisms for the interaction between acoustic and electromagnetic waves. This interaction has been known for over a century [22], but has found most of its use in the optical frequency range of electromagnetic waves. This field of acousto-optics has led to the development of many devices in photonics [79, 123], but there are also some applications where radar systems have been enhanced with acoustic transmitters for detection of atmospheric phenomena otherwise undetectable [88, 89]. In acousto-optics, the two waves essentially travel perpendicular to each other, while in the radar setting they travel in parallel. For a possible NDT application, it might be interesting to have an oblique incidence to limit the region in which possible flaws could interact with the waves. Study of this type of interaction based on possible use in NDT is included in this dissertation.

1.1 Structure

The structure of this introduction is as follows. Section 2 gives a brief overview of the electromagnetic theory necessary for the work in this dissertation, and particularly for the other sections of this introduction. Section 3 describes the computational methods used in this dissertation, methods of accelerating computations, and issues related to implementing computational methods in software. Section 4 introduces the topic of imaging using electromagnetic waves, and describes two different methods of doing so. Section 5 describes some techniques for measuring electromagnetic waves, issues that arise and how to solve them, and how these techniques were used in the included papers. Section 6 describes the contributions of different parts of this dissertation and how they fit together, and finally section 7 concludes this introduction and provides an outlook on possible future work.

1.2 Notation

In this introduction, the notation is as follows

- Scalars are written in italic as A.
- Vectors are written in bold italic as $\boldsymbol{A}$.
- Matrices are written in bold upright as $\mathbf{A}$.
- The entry on row m, column n of a matrix $\mathbf{A}$ is written as A_{mn}.
- Tensors are written with double overlines as $\overline{\overline{A}}$.

Matrix notation is generally used for numerical matrices in a fixed basis. Tensor notation, however, is used for physical properties where there may not be a reference to a particular basis. Vector notation is the same for both numerical vectors and physical vectors though. This is consistent within the introduction, but not in the included papers.

2 Basic Electromagnetic Theory

Maxwell's equations are a set of coupled partial differential equations (PDE) which are the basis of all classical electromagnetics. A general, time-dependent form of Maxwell's equations is [68, 80]

$$\nabla \times \boldsymbol{\mathcal{E}}(\boldsymbol{r},t) = -\frac{\partial \boldsymbol{\mathcal{B}}(\boldsymbol{r},t)}{\partial t} \tag{2.1}$$

$$\nabla \times \boldsymbol{\mathcal{H}}(\boldsymbol{r},t) = \boldsymbol{\mathcal{J}}(\boldsymbol{r},t) + \frac{\partial \boldsymbol{\mathcal{D}}(\boldsymbol{r},t)}{\partial t} \tag{2.2}$$

$$\nabla \cdot \boldsymbol{\mathcal{D}}(\boldsymbol{r},t) = \rho_{\mathrm{e}}(\boldsymbol{r},t) \tag{2.3}$$

$$\nabla \cdot \boldsymbol{\mathcal{B}}(\boldsymbol{r},t) = 0 \tag{2.4}$$

where $\boldsymbol{\mathcal{E}}$ is the electric field (unit V/m), $\boldsymbol{\mathcal{H}}$ is the magnetic field (unit A/m), $\boldsymbol{\mathcal{D}}$ is the electric flux density (unit $\mathrm{As/m^2}$), $\boldsymbol{\mathcal{B}}$ is the magnetic flux density (unit $\mathrm{Vs/m^2}$), $\boldsymbol{\mathcal{J}}$ is the electric current density (unit $\mathrm{A/m^2}$) and ρ_{e} is the electric charge (unit As). In free space, the fields are also connected as $\boldsymbol{\mathcal{D}} = \varepsilon_0 \boldsymbol{\mathcal{E}}$ and $\boldsymbol{\mathcal{B}} = \mu_0 \boldsymbol{\mathcal{H}}$ where ε_0 and μ_0 are the permittivity and permeability of free space, respectively (other cases are discussed in section 2.2). These constants have numerical values [143]

$$\varepsilon_0 \approx 8.854 \cdot 10^{-12}\,\mathrm{F/m} \tag{2.5}$$

$$\mu_0 \approx 1.257 \cdot 10^{-6}\,\mathrm{H/m}. \tag{2.6}$$

It is noticeable that Maxwell's equations are not fully symmetric in the sense that there are only electric currents and charges. A more symmetric version would be [68, 71]

$$\nabla \times \boldsymbol{\mathcal{E}}(\boldsymbol{r},t) = -\boldsymbol{\mathcal{M}}(\boldsymbol{r},t) - \frac{\partial \boldsymbol{\mathcal{B}}(\boldsymbol{r},t)}{\partial t} \tag{2.7}$$

$$\nabla \times \boldsymbol{\mathcal{H}}(\boldsymbol{r},t) = \boldsymbol{\mathcal{J}}(\boldsymbol{r},t) + \frac{\partial \boldsymbol{\mathcal{D}}(\boldsymbol{r},t)}{\partial t} \tag{2.8}$$

$$\nabla \cdot \boldsymbol{\mathcal{D}}(\boldsymbol{r},t) = \rho_{\mathrm{e}}(\boldsymbol{r},t) \tag{2.9}$$

$$\nabla \cdot \boldsymbol{\mathcal{B}}(\boldsymbol{r},t) = \rho_{\mathrm{m}}(\boldsymbol{r},t). \tag{2.10}$$

where the magnetic current density $\boldsymbol{\mathcal{M}}$ and charge ρ_{m} have been introduced. These new quantities have never been observed in nature, but they can be useful as theoretical sources in certain applications. They will, for example, make an appearance in this dissertation with the discussion of the surface equivalence theorem, which in turn is a crucial building block for many of the computational methods presented later.

An alternative to the time-domain formulation above is to express the equations in the frequency domain, by utilizing the Fourier transform. The electric field in frequency and time domain respectively are connected to each other

as [71, 80]

$$\boldsymbol{E}(\boldsymbol{r},\omega) = \int_{-\infty}^{\infty} \boldsymbol{\mathcal{E}}(\boldsymbol{r},t)\mathrm{e}^{-\mathrm{j}\omega t}\,\mathrm{d}t \tag{2.11}$$

$$\boldsymbol{\mathcal{E}}(\boldsymbol{r},t) = \frac{1}{2\pi}\int_{-\infty}^{\infty} \boldsymbol{E}(\boldsymbol{r},\omega)\mathrm{e}^{\mathrm{j}\omega t}\,\mathrm{d}\omega \tag{2.12}$$

and similarly for all other quantities. The quantity $\boldsymbol{E}(\boldsymbol{r},\omega)$ is a complex quantity for the electric field in the frequency domain. For many applications, it is practical to assume a time-harmonic behavior of the electromagnetic fields, i.e.

$$\boldsymbol{\mathcal{E}}(\boldsymbol{r},t) = \boldsymbol{E}_0(\boldsymbol{r})\cos(\omega t + \phi) \tag{2.13}$$

where ϕ is a phase factor contained within $\boldsymbol{E}(\boldsymbol{r},\omega)$ in the frequency domain. The relation between time and frequency domain quantities then simplifies to

$$\boldsymbol{\mathcal{E}}(\boldsymbol{r},t) = \mathrm{Re}\{\boldsymbol{E}(\boldsymbol{r},\omega)\mathrm{e}^{\mathrm{j}\omega t}\}, \tag{2.14}$$

again exemplified by the electric field. Maxwell's equations are often used in a form given by time-harmonic fields, i.e. [71]

$$\nabla \times \boldsymbol{E}(\boldsymbol{r},\omega) = -\boldsymbol{M}(\boldsymbol{r},\omega) - \mathrm{j}\omega\boldsymbol{B}(\boldsymbol{r},\omega) \tag{2.15}$$

$$\nabla \times \boldsymbol{H}(\boldsymbol{r},\omega) = \boldsymbol{J}(\boldsymbol{r},\omega) + \mathrm{j}\omega\boldsymbol{D}(\boldsymbol{r},\omega) \tag{2.16}$$

$$\nabla \cdot \boldsymbol{D}(\boldsymbol{r},\omega) = \rho_\mathrm{e}(\boldsymbol{r},\omega) \tag{2.17}$$

$$\nabla \cdot \boldsymbol{B}(\boldsymbol{r},\omega) = \rho_\mathrm{m}(\boldsymbol{r},\omega) \tag{2.18}$$

where magnetic current density and charge were again included. The ω is typically not written explicitly further in this introduction, unless there is some dependence on frequency or other reason to specify it. It should be noted that fields in the frequency domain can be defined in different ways. In this thesis, the definition follows (2.14), but it is common in the literature to define it using the exponential $\mathrm{e}^{-\mathrm{i}\omega t}$ instead. For the time-harmonic fields, and other complex quantities, this time convention can be changed by substituting the imaginary unit j for $-\mathrm{i}$ anywhere it appears [80].

2.1 Electromagnetic Waves

For time-varying electromagnetic fields, the concept of electromagnetic waves arises. Here, this is exemplified using the time-harmonic formulation, but it holds for any time variation as this can be transformed to the frequency domain (as seen in (2.11)). In the simplest case, we consider electromagnetic fields in free space with purely electric currents $\boldsymbol{J}$ acting as sources. If the curl is applied to (2.15), one obtains

$$\nabla \times \nabla \times \boldsymbol{E}(\boldsymbol{r}) = -\mathrm{j}\omega\mu_0\nabla \times \boldsymbol{H}(\boldsymbol{r}) = \omega^2\mu_0\varepsilon_0\boldsymbol{E}(\boldsymbol{r}) - \mathrm{j}\omega\mu_0\boldsymbol{J}(\boldsymbol{r}) \tag{2.19}$$

where $\nabla \times \boldsymbol{H}$ was identified with the left-hand side of (2.16). Cleaning this up gives

$$\nabla \times \nabla \times \boldsymbol{E}(\boldsymbol{r}) - k_0^2 \boldsymbol{E} = -\mathrm{j} k_0 \eta_0 \boldsymbol{J}(\boldsymbol{r}) \tag{2.20}$$

which is often called the curl-curl equation or the vector wave equation. In the equation, the wave number k_0 was introduced as $k_0 = \omega / c_0$ where c_0 is the propagation speed of the wave as

$$c_0 = \frac{1}{\sqrt{\varepsilon_0 \mu_0}} = 299\,792\,458\,\mathrm{m/s} \tag{2.21}$$

otherwise known as the speed of light in vacuum. The wave impedance of free space $\eta_0 = \sqrt{\mu_0 / \varepsilon_0}$ was also introduced. Solutions to (2.20) are electromagnetic waves with frequency f and wavelength λ given by

$$f = \frac{\omega}{2\pi} \tag{2.22}$$

$$\lambda = \frac{c_0}{f}. \tag{2.23}$$

The exact solution to (2.20) of course depends on the problem, but there are some canonical wave solutions that are particularly important. Two of them are illustrated here: plane waves and spherical waves. For simplicity, only the scalar complex amplitudes $A = |\boldsymbol{E}|$ are considered at first. Plane waves can be expressed as [80]

$$A(\boldsymbol{r}) = A_0 \mathrm{e}^{-\mathrm{j} k_0 \hat{\boldsymbol{k}} \cdot \boldsymbol{r}} \tag{2.24}$$

where A_0 is a complex amplitude of the wave and $\hat{\boldsymbol{k}}$ is a unit vector in the direction of propagation. The plane wave is what many might think of when they hear the word wave, as flat wavefronts propagating in a single direction. Plane waves are simple to analyze, and they can act as good approximations in many applications such as scattering. Spherical waves, on the other hand, can be expressed as [80]

$$A(r) = F_0 \frac{\mathrm{e}^{-\mathrm{j} k_0 r}}{r} \tag{2.25}$$

where r is the radial coordinate from an origin and F_0 is an amplitude (unit V). The appearance of the spherical wave is shown to the left in Figure 3. In contrast to the plane wave, the spherical wave has a clear source at $r = 0$ and a diminishing amplitude as it propagates further from its source, which in terms of power scales as $1/r^2$. This is the well-known inverse square law. As indicated in Figure 3, spherical waves can be approximated as plane waves if the distance from the source becomes large enough, and within a small enough angular region.

While plane wave approximations is a useful concept for observations far from a radiator, a more general one is that of near fields and far fields. This is related to how an electromagnetic wave radiated by a source evolves with increasing range. Far enough away from the source, the electric field can be expressed on the particular form [80]

$$\boldsymbol{E}(\boldsymbol{r}) = \frac{\mathrm{e}^{-\mathrm{j} k_0 r}}{r} \boldsymbol{F}(\hat{\boldsymbol{r}}) \tag{2.26}$$

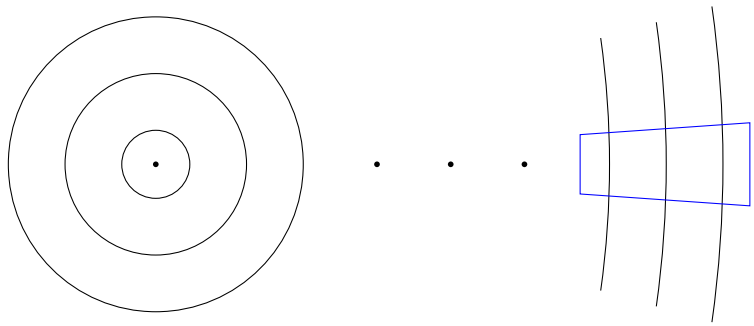

Figure 3: Spherical wave propagating from a source. Within a small angular region far from the source (marked in blue) it is approximately a plane wave.

where $\boldsymbol{F}(\hat{\boldsymbol{r}})$ is called the far-field amplitude and only depends on the direction $\hat{\boldsymbol{r}}$, and not the distance r from the source. By comparing (2.26) to (2.25), it is clear that electromagnetic waves in the far field behave as spherical waves, but with an amplitude that depends on the direction. The far-field amplitude is always perpendicular to the propagation direction $\hat{\boldsymbol{k}}$ (transverse), and the fields in this region behave as $\boldsymbol{E} = \eta_0 \boldsymbol{H} \times \hat{\boldsymbol{k}}$. The polarization of ideal spherical waves in (2.25) and plane waves in (2.24) follow this. Closer to the source, *i.e.*, in the near field, the electric field can have more complicated forms. It is not clear, however, from (2.26) where the cutoff between near and far fields occurs. There is no exact, universally agreed upon definition of this, but a common rule for the cutoff range between near and far fields is the Fraunhofer distance given by [11, 147]

$$r > \frac{2D^2}{\lambda} \tag{2.27}$$

where D is introduced as the largest dimension of the radiating source, though it is often also added that $r \gg \lambda$ and $r \gg D$ [80].

2.2 Constitutive Relations of Different Media

While Maxwell's equations as presented in (2.1)–(2.4) hold for any medium, they do not provide any information on how charges and currents in the medium behave. This is described by the constitutive relations of a medium, which connect the fields $\boldsymbol{\mathcal{E}}$ and $\boldsymbol{\mathcal{H}}$ to $\boldsymbol{\mathcal{D}}$ and $\boldsymbol{\mathcal{B}}$. The work presented in this dissertation is limited to linear media, which limits the types of relations which are possible. In the time domain, general linear constitutive relations can be expressed using convolutions

on the form [80]

$$\boldsymbol{\mathcal{D}}(t) = \varepsilon_0 \left(\overline{\overline{\varepsilon}} \cdot \boldsymbol{\mathcal{E}}(t) + \int_{-\infty}^{t} \overline{\overline{\chi}}_{\mathrm{ee}}(t-t') \cdot \boldsymbol{\mathcal{E}}(t') \, \mathrm{d}t' + \eta_0 \int_{-\infty}^{t} \overline{\overline{\chi}}_{\mathrm{em}}(t-t') \cdot \boldsymbol{\mathcal{H}}(t') \, \mathrm{d}t' \right) \tag{2.28}$$

$$\boldsymbol{\mathcal{B}}(t) = \mu_0 \left(\frac{1}{\eta_0} \int_{-\infty}^{t} \overline{\overline{\chi}}_{\mathrm{me}}(t-t') \cdot \boldsymbol{\mathcal{E}}(t') \, \mathrm{d}t' + \overline{\overline{\mu}} \cdot \boldsymbol{\mathcal{H}}(t) + \int_{-\infty}^{t} \overline{\overline{\chi}}_{\mathrm{mm}}(t-t') \cdot \boldsymbol{\mathcal{H}}(t') \, \mathrm{d}t' \right) \tag{2.29}$$

where $\overline{\overline{\varepsilon}}$, $\overline{\overline{\mu}}$ describe the so-called optical response of the medium, which is the response to the fields $\boldsymbol{\mathcal{E}}$ and $\boldsymbol{\mathcal{H}}$ on a shorter time frame than the other terms. The four different $\overline{\overline{\chi}}_{\mathrm{xy}}$ are susceptibilities describing the response of the medium to electric and magnetic fields. The subscript xy indicates that the susceptibility describes response on field x due to field y, where they can be e (electric) and m (magnetic). The double overline indicates that the quantity is a tensor (specifically a dyadic tensor). This type of constitutive relation containing nonzero $\overline{\overline{\chi}}_{\mathrm{em}}$ and $\overline{\overline{\chi}}_{\mathrm{me}}$ is often called magnetoelectric.

Commonly, however, constitutive relations are expressed in the frequency domain. As the Fourier transform of a convolution is a regular product, the relations become mathematically simpler in this case. The general linear constitutive relations can then be expressed as [80]

$$\boldsymbol{D}(\omega) = \varepsilon_0 \left(\overline{\overline{\varepsilon_{\mathrm{r}}}}(\omega) \cdot \boldsymbol{E}(\omega) + \eta_0 \overline{\overline{\xi}}(\omega) \cdot \boldsymbol{H}(\omega) \right) \tag{2.30}$$

$$\boldsymbol{B}(\omega) = \mu_0 \left(\frac{1}{\eta_0} \overline{\overline{\zeta}}(\omega) \cdot \boldsymbol{E}(\omega) + \overline{\overline{\mu_{\mathrm{r}}}}(\omega) \cdot \boldsymbol{H}(\omega) \right). \tag{2.31}$$

In this, new quantities for the constitutive relations have been introduced from Fourier transformation of the previous ones. $\overline{\overline{\varepsilon_{\mathrm{r}}}}$ is called the relative permittivity and $\overline{\overline{\mu_{\mathrm{r}}}}$ is called the relative permeability. The quantities for the magnetoelectric coupling from $\boldsymbol{H}$ to $\boldsymbol{D}$ and $\boldsymbol{E}$ to $\boldsymbol{B}$ do not have similar universal names. This type of magnetoelectric relation is often called bianisotropic since both electric and magnetic fields are connected (bi) by tensors (anisotropic). However, most applications do not require these kinds of constitutive relations and there are simpler ones that are often seen. Media without magnetoelectric interaction is described using only relative permittivity and relative permeability as

$$\boldsymbol{D}(\omega) = \varepsilon_0 \overline{\overline{\varepsilon_{\mathrm{r}}}}(\omega) \cdot \boldsymbol{E}(\omega) \tag{2.32}$$

$$\boldsymbol{B}(\omega) = \mu_0 \overline{\overline{\mu_{\mathrm{r}}}}(\omega) \cdot \boldsymbol{H}(\omega). \tag{2.33}$$

Commonly, there are no magnetic effects ($\mu_0 \overline{\overline{\mu_{\mathrm{r}}}}(\omega) = \mu_0$) in which case the medium is called dielectric. As expressed above, it is still an anisotropic medium since the relative permittivity is a tensor, but an even simpler variety is the isotropic dielectric where it also holds that $\overline{\overline{\varepsilon_{\mathrm{r}}}}(\omega) = \varepsilon_{\mathrm{r}}(\omega) \overline{\overline{I}}$ where $\overline{\overline{I}}$ is the identity

tensor. In the constitutive relations presented above, a frequency dependence has been implied. This is generally the case, and such media are called dispersive [80]. Often in this dissertation, problems are considered only at a single frequency which means that dispersion does not play a role in the results. This often holds for small changes in frequency as well, where the dispersion is relatively small.

In general, medium parameters in the frequency domain constitutive relations are allowed to be complex-valued, and the properties determine the nature of losses in the medium. A medium can be lossless, meaning that waves propagating there do not lose or gain power, for which it holds that [80]

$$\overline{\overline{\varepsilon_\mathrm{r}}} = \overline{\overline{\varepsilon_\mathrm{r}}}^\mathrm{H} \tag{2.34}$$

$$\overline{\overline{\mu_\mathrm{r}}} = \overline{\overline{\mu_\mathrm{r}}}^\mathrm{H} \tag{2.35}$$

$$\overline{\overline{\xi}} = \overline{\overline{\zeta}}^\mathrm{H} \tag{2.36}$$

with $^\mathrm{H}$ indicating a Hermitian transpose. For a medium which is not lossless, waves propagating there can either lose or gain power, and they are called passive and active, respectively. For a passive medium (including the lossless case) it holds that [80]

$$\omega \operatorname{Im} \overline{\overline{\varepsilon_\mathrm{r}}} \leq 0 \tag{2.37}$$

$$\omega \operatorname{Im} \overline{\overline{\mu_\mathrm{r}}} \leq 0 \tag{2.38}$$

$$\omega \left\{ 4 \operatorname{Im} \overline{\overline{\mu_\mathrm{r}}} - \left(\overline{\overline{\xi}} - \overline{\overline{\zeta}}^\mathrm{H} \right)^\mathrm{H} \cdot \left(\operatorname{Im} \overline{\overline{\varepsilon_\mathrm{r}}} \right)^{-1} \cdot \left(\overline{\overline{\xi}} - \overline{\overline{\zeta}}^\mathrm{H} \right) \right\} \leq 0. \tag{2.39}$$

These inequalities should be interpreted to be valid for all Hermitian quadratic forms over the matrices in the left-hand side. Furthermore, the imaginary parts of dyadic tenors are interpreted as $\operatorname{Im} \overline{\overline{A}} = (\overline{\overline{A}} - \overline{\overline{A}}^\mathrm{H})/2\mathrm{j}$. If the conditions for a passive medium are simplified for the commonly used isotropic media, they become

$$\omega \operatorname{Im} \varepsilon_\mathrm{r} \leq 0 \tag{2.40}$$

$$\omega \operatorname{Im} \mu_\mathrm{r} \leq 0. \tag{2.41}$$

For isotropic dielectric media fulfilling Ohm's law $\boldsymbol{J} = \sigma \boldsymbol{E}$ with a real-valued permittivity ε_r' and electric conductivity σ, a direct relation between conductivity and losses is found by rewriting (2.16) as

$$\nabla \times \boldsymbol{H} = \boldsymbol{J} + \mathrm{j}\omega \boldsymbol{D} = \sigma \boldsymbol{E} + \mathrm{j}\omega \varepsilon_0 \varepsilon_\mathrm{r}' \boldsymbol{E} = \mathrm{j}\omega \varepsilon_0 \varepsilon_\mathrm{r} \boldsymbol{E} \tag{2.42}$$

with

$$\varepsilon_\mathrm{r} = \varepsilon_\mathrm{r}' - \mathrm{j} \frac{\sigma}{\omega \varepsilon_0}. \tag{2.43}$$

Another property that can be seen in the constitutive relations is reciprocity. Reciprocity is easier to understand if a one-dimensional network model is considered, as shown in Figure 4. This model contains an object (network) which

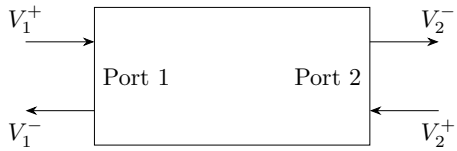

Figure 4: One-dimensional waves in a two-port network.

has two ports from which waves can enter and leave. Such a network can be described using the scattering parameters defined as the scattering matrix [110]

$$\begin{pmatrix} V_1^- \\ V_2^- \end{pmatrix} = \begin{bmatrix} S_{11} & S_{12} \\ S_{21} & S_{22} \end{bmatrix} \begin{pmatrix} V_1^+ \\ V_2^+ \end{pmatrix} \tag{2.44}$$

with in-going waves V^+ and out-going waves V^- as indicated in Figure 4. In a reciprocal network, the scattering matrix is symmetrical, which holds for a network with any number of ports [110]. What this means in our two-port network is that if we have in-going waves $V_1^+ = V_a$, $V_2^+ = 0$ and an out-going wave $V_2^- = V_b$, the situation can be reversed as $V_1^+ = 0$, $V_2^+ = V_a$ and $V_1^- = V_b$. Note that the reflected waves (V_1^- in the first case, V_2^- in the second) do not need to be the same. The property of reciprocity can also be defined more generally for media with constitutive relations instead of S-parameters and electromagnetic fields instead of voltages. For a medium to be reciprocal, its constitutive relations must be such that [80]

$$\overline{\overline{\varepsilon_\mathrm{r}}} = \overline{\overline{\varepsilon_\mathrm{r}}}^\mathrm{T} \tag{2.45}$$

$$\overline{\overline{\mu_\mathrm{r}}} = \overline{\overline{\mu_\mathrm{r}}}^\mathrm{T} \tag{2.46}$$

$$\overline{\overline{\xi}} = -\overline{\overline{\zeta}}^\mathrm{T}. \tag{2.47}$$

While these relations make consequences more complex to define than in the two-port network example, the same general property holds in that sources (currents) and effects (fields) in two points can be interchanged for the same result in a reciprocal medium. There are many examples of nonreciprocal media and situations that have important effects.

A nonreciprocal medium used in practical applications is the magnetized ferrite, which is used in many microwave devices such as the circulator which is a multi-port device in which signals can only propagate in one direction (*e.g.*, $1 \to 2 \to 3 \to 1$ for three ports) [110]. Another important nonreciprocal medium is magnetized plasma, which is found naturally in the ionosphere and causes polarization rotation of electromagnetic waves in different directions depending on the direction of travel [71, 147]. Finally, nonreciprocal artificial materials have been popular recently, with examples as nonreciprocal metamaterials obtaining nonreciprocity in new ways like modulation of the surface in space and time [27, 137].

2.3 Boundary Conditions

Maxwell's equations together with suitable constitutive relations describe the physics of classical electromagnetism within a certain medium. However, they do not describe what happens at the boundary between different media. For this reason, additional conditions are required at each such instance. These are commonly described as boundary conditions, although the fact that they appear at interfaces within problem domain means that they might not be so in a strict mathematical sense. The conditions are defined at any surface with a normal vector $\hat{\boldsymbol{n}}$ pointing from region 2 to region 1 are given by [71]

$$\hat{\boldsymbol{n}} \times (\boldsymbol{E}_1 - \boldsymbol{E}_2) = -\boldsymbol{M}_\mathrm{s} \tag{2.48}$$

$$\hat{\boldsymbol{n}} \cdot (\boldsymbol{D}_1 - \boldsymbol{D}_2) = \rho_\mathrm{e,s} \tag{2.49}$$

$$\hat{\boldsymbol{n}} \times (\boldsymbol{H}_1 - \boldsymbol{H}_2) = \boldsymbol{J}_\mathrm{s} \tag{2.50}$$

$$\hat{\boldsymbol{n}} \cdot (\boldsymbol{B}_1 - \boldsymbol{B}_2) = \rho_\mathrm{m,s}. \tag{2.51}$$

$\boldsymbol{J}_\mathrm{s}$ and $\boldsymbol{M}_\mathrm{s}$ are electric and magnetic surface currents and $\rho_\mathrm{e,s}$ and $\rho_\mathrm{m,s}$ are electric and magnetic surface charges. As previously stated, magnetic charges and currents are not physically shown to exist, but can be useful as fictitious quantities.

A commonly used boundary condition is for the boundary of a perfect electric conductor (PEC) object. PEC is an idealized model of an electric conductor in that it has an unlimited supply of electric charge which can perfectly oppose any fields on its interior, which can be seen as an electric conductivity $\sigma \to \infty$ [80]. Furthermore, as it is a model for a physical medium only electric currents and charges are supported on its boundary. The PEC boundary conditions can thus be expressed as [80]

$$\hat{\boldsymbol{n}} \times \boldsymbol{E} = \boldsymbol{0} \tag{2.52}$$

$$\hat{\boldsymbol{n}} \cdot \boldsymbol{D} = \rho_\mathrm{e,s} \tag{2.53}$$

$$\hat{\boldsymbol{n}} \times \boldsymbol{H} = \boldsymbol{J}_\mathrm{s} \tag{2.54}$$

$$\hat{\boldsymbol{n}} \cdot \boldsymbol{B} = 0. \tag{2.55}$$

While electric conductors typically are lossy due to a finite conductivity, the PEC model works well for many metals in the microwave frequency range. However, as the frequency reaches the optical range, metals no longer behave as classical conductors and the PEC model is not accurate [147]. In computations, the model is very beneficial since bulk conductors can be replaced by a boundary condition, reducing the number of unknowns in the problem. Analogously to PEC, a perfect magnetic conductor (PMC) can be defined to only support magnetic currents and

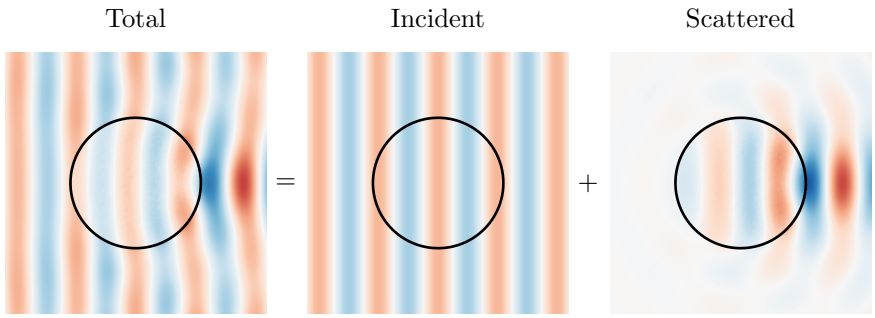

Figure 5: Scattering of an electromagnetic wave by a dielectric cylinder, shown for the component of $\boldsymbol{E}$ perpendicular to paper. The total electric field is considered a sum of the incident field and the scattered field.

charges on its boundary [71]. This PMC boundary condition can be expressed as

$$\hat{\boldsymbol{n}} \times \boldsymbol{E} = -\boldsymbol{M}_{\mathrm{s}} \tag{2.56}$$
$$\hat{\boldsymbol{n}} \cdot \boldsymbol{D} = 0 \tag{2.57}$$
$$\hat{\boldsymbol{n}} \times \boldsymbol{H} = \boldsymbol{0} \tag{2.58}$$
$$\hat{\boldsymbol{n}} \cdot \boldsymbol{B} = \rho_{\mathrm{m,s}}. \tag{2.59}$$

While the PMC does not resemble any physical medium as the PEC, it is possible to create artificial materials which act as PMC within certain limited conditions on, for example, frequency or propagation direction of a wave. This includes well-known structures like the mushroom high-impedance surface [132] and gaps in strip-based artificial soft/hard surfaces [76]. PEC and PMC boundary conditions can also be used in computations for problems with symmetries such that the fields are known *a priori* to act as if such surfaces were present, which reduces the number of unknowns.

2.4 Scattering

When electromagnetic waves encounter obstacles, typically in the form of a medium with different properties, interaction with the object causes scattering of the wave. An overview of how this problem is normally set up is shown in Figure 5 where the electric field of the wave is considered. The total electric field $\boldsymbol{E}$ is shown as a sum of the incident field $\boldsymbol{E}^{\mathrm{inc}}$ and the scattered field $\boldsymbol{E}^{\mathrm{sc}}$. The incident field is the field that would have been present without the obstacle, a plane wave in this case. The scattered field can be considered to be generated by sources on and in the obstacle to give the total field.

To compute the scattering of a general obstacle, it is almost always necessary to use numerical methods. In certain cases there are analytical solutions, with one of the most commonly known being the sphere. In the case of spherical symmetry, scattering problems are solved by the well-known Mie series solution [80, 94].

The simplest one is for a PEC sphere, but solutions are also possible for many other objects with spherical symmetry, including homogeneous dielectric, PEC coated by dielectric and multilayered spheres [41, 80]. The Mie series solution is particularly interesting for use in verification of numerical codes as it is well known and exact.

A quantity that is commonly used to quantify electromagnetic scattering by an obstacle is the radar cross section (RCS), which considers how an obstacle scatters an incident plane wave. This is typically specified to be monostatic or bistatic, where the former only considers the reverse of the incident wave direction while the latter considers scattering in all directions. The bistatic RCS σ is defined by an IEEE standard [141], but here it is introduced based on incident and scattered electric fields as [71, 115]

$$\sigma(\theta, \phi, \theta^{\mathrm{inc}}, \phi^{\mathrm{inc}}) = \lim_{r\to\infty} 4\pi r^2 \frac{|\boldsymbol{E}^{\mathrm{sc}}(r, \theta, \phi)|^2}{|\boldsymbol{E}^{\mathrm{inc}}(\theta^{\mathrm{inc}}, \phi^{\mathrm{inc}})|^2} \tag{2.60}$$

where $\boldsymbol{E}^{\mathrm{inc}}(\theta^{\mathrm{inc}}, \phi^{\mathrm{inc}})$ is the electric field of a plane wave incident in the direction $(\theta^{\mathrm{inc}}, \phi^{\mathrm{inc}})$ and $\boldsymbol{E}^{\mathrm{sc}}(r, \theta, \phi)$ is the scattered electric field in the point (r, θ, ϕ). The scattered electric field can be replaced by the far-field amplitude from (2.26) as

$$\sigma(\theta, \phi, \theta^{\mathrm{inc}}, \phi^{\mathrm{inc}}) = \lim_{r\to\infty} 4\pi r^2 \frac{|\mathrm{e}^{-\mathrm{j}k_0 r} \boldsymbol{F}^{\mathrm{sc}}(\theta, \phi)/r|^2}{|\boldsymbol{E}^{\mathrm{inc}}(\theta^{\mathrm{inc}}, \phi^{\mathrm{inc}})|^2} = 4\pi \frac{|\boldsymbol{F}^{\mathrm{sc}}(\theta, \phi)|^2}{|\boldsymbol{E}^{\mathrm{inc}}(\theta^{\mathrm{inc}}, \phi^{\mathrm{inc}})|^2}. \tag{2.61}$$

It is seen that this expression has the advantage that dependence on r and the limit are eliminated from the expression, and the RCS on this form is fairly simple to compute.

While not necessarily exact, many scattering problems can be solved approximately if the object is very large or small compared to the wavelength. For very small objects, Rayleigh scattering dominates and this can be solved analytically, though it is an approximation [80]. For very large objects, the classical laws of ray optics become useful and the RCS of PEC objects approach the geometrical cross section [80, 115]. It is generally in the region between where the scattering problem can be the most difficult to solve, and this is where full numerical solutions can be necessary. An indication of this can be seen by looking at the monostatic RCS of a PEC sphere computed from the Mie series for increasing sphere radius. This is shown in Figure 6, where three different scattering regimes can be seen. For very small radii the RCS increases monotonically, which is followed by significant variation, and finally at very large radii the RCS approaches a constant value. These are called the Rayleigh, resonance and optical scattering regimes, respectively [115].

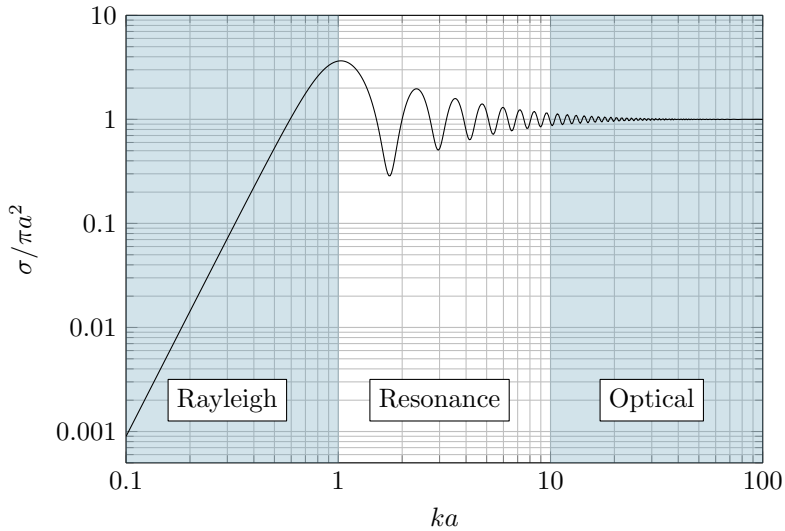

Figure 6: Monostatic RCS normalized to geometric cross-section for a PEC sphere of increasing radius. Rough ka ranges of different scattering regimes are indicated.

2.5 Mechanical Perturbations of the Medium

In many cases, a medium can change its electromagnetic properties due to other physical phenomena. In this dissertation there are two examples that deserve special focus: acoustic waves, which is relevant in Paper V, and rotating media, which is relevant in Paper III. Both of these phenomena are based on mechanical perturbations which are time-harmonic in their nature, and this time-harmonic nature affects how electromagnetic waves interact with them. Recently, there has been a large interest in phenomena similar to these, where properties of a system are time-modulated to introduce new interesting effects, as already mentioned with respect to nonreciprocal effects at the end of section 2.2.

2.5.1 Acoustic Waves

The possibility for interaction between acoustic and electromagnetic waves has been known since at least 1922 [22], and the theory of acousto-optics developed in the following decades [79]. Following the invention of the laser, acousto-optics has been applied to photonic devices used to modify properties of laser beams like modulators and filters [79, 123]. While most development has been in acousto-optics, interaction between acoustic and electromagnetic waves is not limited to optical frequencies. An application at other electromagnetic frequencies is radio-acoustic sounding which uses collocated radar and acoustic transmitters to measure atmospheric properties like temperature profiles [88, 89], but with other

possible uses including forest fire detection [122] or aircraft wake vortices [119].

In its most basic form, interaction between electromagnetic and acoustic waves can be understood as the acoustic wave modulating the density of a medium, which in turn affects its dielectric properties and causes the electromagnetic wave to scatter [79, 123]. In fluids, this is a fairly correct picture as acoustic waves directly correspond to changes in density in this case. In solids, the picture becomes more difficult since more modes of acoustic, or rather elastic, waves are possible. For example, acoustic waves based on pressure are still supported as so called p-waves, but so are s-waves which are waves based on shear strain in the solid [118].

Photoelasticity provides the theory for how elastic phenomena affect electromagnetic properties of a medium. In solids, it is generally the case that both elastic and electromagnetic properties are tensors, which makes for somewhat complicated relations between them [79]. A relation for small perturbations in a mechanically and electromagnetically isotropic medium is [157]

$$\varepsilon = \varepsilon_0(\varepsilon_\mathrm{r} + \varepsilon_1) \tag{2.62}$$

$$\varepsilon_1 = \frac{\varepsilon_\mathrm{r}\mathfrak{p}}{K}p \tag{2.63}$$

where $\mathfrak{p}$ is a scalar photoelastic constant, K is the bulk modulus and p is the acoustic pressure. For fluids, an expression for the scalar photoelastic constant can be found using the Lorentz-Lorenz relations as [79, 157]

$$\mathfrak{p} = \frac{(\varepsilon_\mathrm{r} - 1)(\varepsilon_\mathrm{r} + 2)}{3\varepsilon_\mathrm{r}^2}. \tag{2.64}$$

From this, it can be understood that interaction in air, or other media with ε_r close to 1, is very weak.

Depending on the wavelengths of the acoustic and electromagnetic waves, and the overlap of the waves, strong scattering is due to different mechanisms. This can be quantified by the Klein-Cook parameter defined as [77, 79]

$$Q = \frac{2\pi\lambda L}{\Lambda^2} \tag{2.65}$$

where λ is the electromagnetic wavelength, Λ is the acoustic wavelength and L is the length of the overlap between the waves. The main scattering mechanism is Raman-Nath diffraction if $Q \ll 1$, and Bragg diffraction if $Q \gg 1$ [77]. The typical case where Raman-Nath diffraction is important is in acousto-optics for thin beams where $\lambda \ll \Lambda$ and waves have perpendicular incidence [123]. In cases where $\lambda \sim \Lambda$ it is not immediately clear which mechanism is most relevant, but L only needs to be a small number of wavelengths for Bragg diffraction to dominate [77]. For the work presented in Paper V of this dissertation, Bragg diffraction dominates, and as such this will be the focus here.

Bragg diffraction as a general concept has its base in X-ray crystallography where the X-ray wavelength is phase matched to the separation between planes

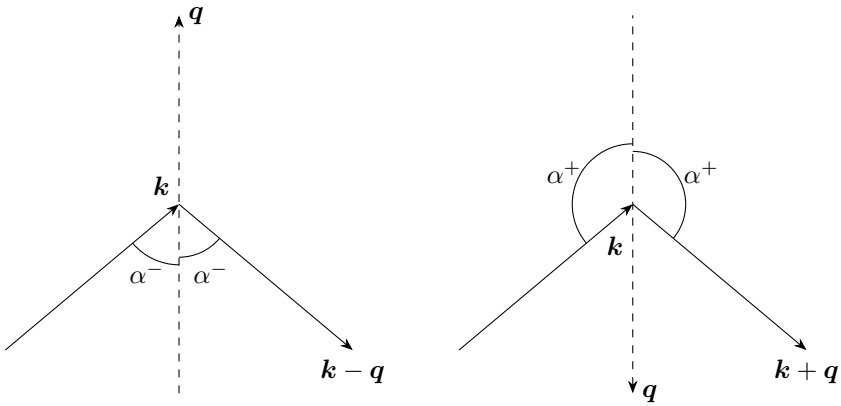

Figure 7: Incident acoustic ($\boldsymbol{q}$) and electromagnetic ($\boldsymbol{k}$) wave vectors, as well as scattered electromagnetic wave vector with the angle α shown. Both (-) and (+) cases of (2.66) are shown.

of atoms in a crystal lattice [20]. In interaction between acoustic and electromagnetic waves, the mechanism is similar but the planes of atoms are replaced by the acoustic wavefront which is moving, as opposed to the crystal lattice. The condition given by Bragg's law for strong scattering due to phase matching is essentially the same though, with crystal parameters exchanged for acoustic ones. It is usually expressed using the angle of incidence of the electromagnetic wave on the acoustic wave [79, 123], but here is expressed using the angle between the electromagnetic and acoustic propagation directions α as [157]

$$\cos\alpha = \mp\frac{\lambda}{2\Lambda}. \tag{2.66}$$

The angle α for the two cases shown in Figure 7 for the acoustic wave vector $\boldsymbol{q}$, the electromagnetic wave vector $\boldsymbol{k}$ for the incident wave, and the electromagnetic wave vector $\boldsymbol{k} \pm \boldsymbol{q}$ for the scattered wave [123]. While the condition for strong scattering is the same in X-ray crystallography and acousto-electromagnetic interaction, the moving acoustic wave introduces some differences. Most prominently, the scattered electromagnetic wave exhibits a positive or negative frequency shift by the acoustic frequency, which can be understood by looking at the wave vectors for the scattered electromagnetic wave. As seen in Figure 7, sign of the frequency shift is the same as the sign in (2.66), and as such coupled to the angle α. This frequency shift can be crucial in measurements involving the interaction as it clearly indicates that a measured electromagnetic wave was scattered by the acoustic wave and not some other mechanism. In Paper V, for example, measurements would not have been possible without the existence of this frequency shift as the power scattered by the acoustic wave was significantly lower than even the leakage between transmitting and receiving antennas.

2.5.2 Rotating Media

Rapidly rotating dielectric media exhibit interesting electromagnetic properties. In the general case, it needs to be considered under the framework of the micro-Doppler effect, which considers objects under motion like rotation and vibration [31]. In the case of a rotating circular cylinder, the radial velocities which typically cause effects such as the micro-Doppler effect vanish. For sufficiently rapid rotations though, typically near 1 % of the speed of light, other effects become apparent, and it can be found that the object acts as if it were fully bianisotropic to a first order approximation [145]. While the problem is fairly exotic, it is interesting to study as it is bianisotropic, nonreciprocal and inhomogeneous by no other cause than mechanical rotation. The derivation of effective constitutive relations for moving media starts with the relations for a linear isotropic medium at rest, but are transformed to the laboratory frame. For non-relativistic speeds and to a first order approximation, the constitutive relations become [145, 147]

$$\boldsymbol{D} = \varepsilon_0 \varepsilon_\mathrm{r} \boldsymbol{E} + \frac{n^2 - 1}{c_0^2} \boldsymbol{v} \times \boldsymbol{H} \tag{2.67}$$

$$\boldsymbol{B} = \mu_0 \mu_\mathrm{r} \boldsymbol{H} - \frac{n^2 - 1}{c_0^2} \boldsymbol{v} \times \boldsymbol{E} \tag{2.68}$$

where $n = \sqrt{\varepsilon_\mathrm{r} \mu_\mathrm{r}}$ is the refractive index and $\boldsymbol{v}$ is the velocity vector at a particular point. For a circular cylinder rotating with angular frequency Ω around z, the velocity vector is

$$\boldsymbol{v} = \Omega \hat{\boldsymbol{z}} \times \boldsymbol{r} = \Omega (x \hat{\boldsymbol{y}} - y \hat{\boldsymbol{x}}) \tag{2.69}$$

in a Cartesian coordinate system. If this velocity is inserted in (2.67), the constitutive relations can be written using the bianisotropic parameters defined in (2.30)–(2.31) as

$$\overline{\overline{\varepsilon_\mathrm{r}}} = \varepsilon_\mathrm{r} \overline{\overline{I}} \tag{2.70}$$

$$\overline{\overline{\mu_\mathrm{r}}} = \mu_\mathrm{r} \overline{\overline{I}} \tag{2.71}$$

$$\overline{\overline{\xi}} = \Omega \frac{n^2 - 1}{c_0} \begin{bmatrix} 0 & 0 & x \\ 0 & 0 & y \\ -x & -y & 0 \end{bmatrix} \tag{2.72}$$

$$\overline{\overline{\zeta}} = -\overline{\overline{\xi}} \tag{2.73}$$

from which the inhomogeneous, bianisotropic, and nonreciprocal nature of the model is clear.

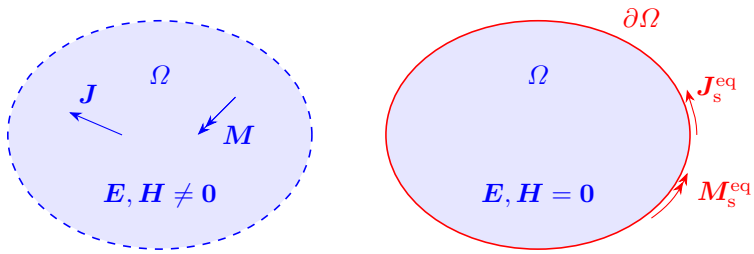

Figure 8: Illustration of the surface equivalence theorem with sources in Ω (left) replaced by equivalent surface currents on $\partial\Omega$ (right).

2.6 The Surface Equivalence Theorem

A powerful result from electromagnetic theory is the surface equivalence theorem, or surface equivalence principle. This states that sources within a volume Ω can be replaced by equivalent currents on the boundary $\partial\Omega$ and still give the same solution in the region outside Ω [58]. This is illustrated in Figure 8. While the solution outside Ω is the same after replacing the sources by equivalent currents, this is not the case for the solution inside of Ω. In fact, there is an infinite number of valid equivalent currents, and they result in different solutions inside Ω. There are some common choices though, with the most common one being the zero field, or Love condition. This sets the fields inside Ω to zero, which means that the equivalent currents can be found from the boundary conditions (2.48) and (2.50) to be

$$\boldsymbol{J}_{\mathrm{s}}^{\mathrm{eq}} = \hat{\boldsymbol{n}} \times \boldsymbol{H} \tag{2.74}$$

$$\boldsymbol{M}_{\mathrm{s}}^{\mathrm{eq}} = \boldsymbol{E} \times \hat{\boldsymbol{n}}. \tag{2.75}$$

This direct relationship between currents and fields can be very practical, as is seen in section 3.3 of this introduction.

One issue that can arise in numerical applications of the equivalence theorem is the use of both electric and magnetic currents. In such applications, currents represent unknowns, and having both types would double the number of unknowns for a problem as compared with only one type of current. There are some ways of using either electric or magnetic currents in the equivalence theorem. One way of doing this is to consider the volume Ω filled with PMC, and electric currents on the surface $\partial\Omega$. This gives the same equivalent currents as in (2.74), and a dual method uses PEC and magnetic currents to give (2.75) instead [58]. However, this can be troublesome in numerical applications as the use of PMC or PEC require other methods than in the standard zero field case [111]. One exception is if the region Ω is a half space, meaning that $\partial\Omega$ is an infinite plane. In that case, the method of images can be used to eliminate the PMC/PEC and instead give equivalent currents as twice those in (2.74) and (2.75) [58]. Other methods for using only one of the electric and magnetic

currents exist, with some able to use the same methods as for free space. Typically they do not give the same simple relationships between currents and fields as in (2.74) and (2.75) though [111].

2.7 Integral Equations

Integral equations are important in many different electromagnetic problems. In particular, there are many numerical methods based on integral equations, some of which are described in more detail later in this dissertation.

The integral equations of interest in this work are based on the equivalence theorem. This enables the replacement of all electromagnetic phenomena within a closed object by equivalent surface currents on its boundary.

An important concept for integral equations is that of Green's functions, which is a general concept in mathematics with great applicability in electromagnetics. It can be likened to the impulse response in dynamical systems theory, but applied to differential operators. Generally, a Green's function is similar to the fundamental solution E which is [66]

$$LE = \delta \tag{2.76}$$

for a differential operator L and the Dirac delta distribution δ. As for impulse responses in dynamical systems theory, other problems involving L and a source term f can be solved by a convolution $E * f$ [66]. The Green's function is similar, but also take boundary conditions into account [134]. In electromagnetics, a Green's function can be obtained for the magnetic vector potential $\boldsymbol{A}$ (in the Lorenz gauge) in free space as the solution to [80]

$$\nabla^2 G_0(\boldsymbol{r}, \boldsymbol{r}') + k_0^2 G_0(\boldsymbol{r}, \boldsymbol{r}') = -\delta(\boldsymbol{r} - \boldsymbol{r}') \tag{2.77}$$

which is

$$G_0(\boldsymbol{r}, \boldsymbol{r}') = \frac{\mathrm{e}^{-\mathrm{j}k_0|\boldsymbol{r}-\boldsymbol{r}'|}}{4\pi|\boldsymbol{r} - \boldsymbol{r}'|}. \tag{2.78}$$

This Green's function can then be used to find vector potentials due to current sources, and this can in turn be used to find the electric and magnetic fields. Such a relation for the electric field can be written as [71]

$$\boldsymbol{E}(\boldsymbol{r}) = -\mathrm{j}k_0\eta_0 \int_\Omega \left[\boldsymbol{J}(\boldsymbol{r}')G_0(\boldsymbol{r}, \boldsymbol{r}') + \frac{1}{k_0^2}\boldsymbol{J}(\boldsymbol{r}') \cdot \nabla\nabla G_0(\boldsymbol{r}, \boldsymbol{r}') \right] \mathrm{d}V' + \int_\Omega \boldsymbol{M}(\boldsymbol{r}') \times \nabla G_0(\boldsymbol{r}, \boldsymbol{r}') \, \mathrm{d}V' \tag{2.79}$$

where both electric and magnetic currents inside a volume Ω are included.

To simplify notation of different integral equations, it is useful to introduce the integral operators [71]

$$\mathscr{L}(\boldsymbol{X})(\boldsymbol{r}) = \mathrm{j}k_0 \oint_{\partial\Omega} \left[\boldsymbol{X}(\boldsymbol{r}')G_0(\boldsymbol{r},\boldsymbol{r}') + \frac{1}{k_0^2}\nabla' \cdot \boldsymbol{X}(\boldsymbol{r}')\nabla G_0(\boldsymbol{r},\boldsymbol{r}') \right] \mathrm{d}S' \tag{2.80}$$

$$\mathscr{K}(\boldsymbol{X})(\boldsymbol{r}) = \oint_{\partial\Omega} \boldsymbol{X}(\boldsymbol{r}') \times \nabla G_0(\boldsymbol{r},\boldsymbol{r}') \,\mathrm{d}S' \tag{2.81}$$

defined for the closed surface $\partial\Omega$. The magnetic field and electric current are also scaled as $\bar{\boldsymbol{H}} = \eta_0 \boldsymbol{H}$, $\bar{\boldsymbol{J}} = \eta_0 \boldsymbol{J}$ for compactness. The integral equations considered here appear from a scattering problem where a volume Ω is illuminated by incident fields $\boldsymbol{E}^{\mathrm{inc}}$, $\bar{\boldsymbol{H}}^{\mathrm{inc}}$. To obtain the scattered field, the surface equivalence theorem can be applied using the zero field condition inside Ω, giving [32, 71]

$$\boldsymbol{E}^{\mathrm{inc}}(\boldsymbol{r}) - \mathscr{L}(\bar{\boldsymbol{J}}_{\mathrm{s}})(\boldsymbol{r}) + \mathscr{K}(\boldsymbol{M}_{\mathrm{s}})(\boldsymbol{r}) = \begin{cases} \boldsymbol{E}(\boldsymbol{r}) & \boldsymbol{r} \notin \Omega \\ \boldsymbol{0} & \boldsymbol{r} \in \Omega \end{cases} \tag{2.82}$$

$$\bar{\boldsymbol{H}}^{\mathrm{inc}}(\boldsymbol{r}) - \mathscr{L}(\boldsymbol{M}_{\mathrm{s}})(\boldsymbol{r}) - \mathscr{K}(\bar{\boldsymbol{J}}_{\mathrm{s}})(\boldsymbol{r}) = \begin{cases} \bar{\boldsymbol{H}}(\boldsymbol{r}) & \boldsymbol{r} \notin \Omega \\ \boldsymbol{0} & \boldsymbol{r} \in \Omega \end{cases}. \tag{2.83}$$

Classic integral equations are obtained in the limit of $\boldsymbol{r} \to \partial\Omega$, and by taking a cross product by $\hat{\boldsymbol{n}}$ as [71]

$$-\hat{\boldsymbol{n}} \times \mathscr{L}(\bar{\boldsymbol{J}}_{\mathrm{s}})(\boldsymbol{r}) + \hat{\boldsymbol{n}} \times \mathscr{K}(\boldsymbol{M}_{\mathrm{s}})(\boldsymbol{r}) = -\hat{\boldsymbol{n}} \times \boldsymbol{E}^{\mathrm{inc}}(\boldsymbol{r}) \tag{2.84}$$

$$\hat{\boldsymbol{n}} \times \mathscr{L}(\boldsymbol{M}_{\mathrm{s}})(\boldsymbol{r}) + \hat{\boldsymbol{n}} \times \mathscr{K}(\bar{\boldsymbol{J}}_{\mathrm{s}})(\boldsymbol{r}) = \hat{\boldsymbol{n}} \times \bar{\boldsymbol{H}}^{\mathrm{inc}}(\boldsymbol{r}) \tag{2.85}$$

where the first is the electric field integral equation (EFIE) and the second is the magnetic field integral equation (MFIE).

The equations written on this form are not fully usable as the integral operators contain a singularity which needs to be extracted, which can be done analytically as shown in many reference books [71, 80, 146, 152]. This treatment only affects the $\mathscr{K}$ operator as the extracted term vanishes for $\mathscr{L}$. For the $\mathscr{K}$ operator then, the extracted term depends on if the operator acts on the inside or outside of the volume enclosed by $\partial\Omega$. This is due to the extraction technique which depends on deformation of $\partial\Omega$ by a small region such that the singular point is excluded from the region of interest. The operator as modified by this extraction, $\tilde{\mathscr{K}}$, is given by [71]

$$\hat{\boldsymbol{n}} \times \mathscr{K}(\boldsymbol{X})(\boldsymbol{r}) = \hat{\boldsymbol{n}} \times \tilde{\mathscr{K}}(\boldsymbol{X})(\boldsymbol{r}) \pm \frac{1}{2}\boldsymbol{X}(\boldsymbol{r}) \tag{2.86}$$

if the surface $\partial\Omega$ is smooth. Here $+$ corresponds to evaluation on the outside of Ω and $-$ to evaluation on the inside. The integral equations in (2.84) and (2.85) are now written as

$$\frac{1}{2}\boldsymbol{M}_{\mathrm{s}}(\boldsymbol{r}) - \hat{\boldsymbol{n}} \times \mathscr{L}(\bar{\boldsymbol{J}}_{\mathrm{s}})(\boldsymbol{r}) + \hat{\boldsymbol{n}} \times \tilde{\mathscr{K}}(\boldsymbol{M}_{\mathrm{s}})(\boldsymbol{r}) = -\hat{\boldsymbol{n}} \times \boldsymbol{E}^{\mathrm{inc}}(\boldsymbol{r}) \tag{2.87}$$

$$\frac{1}{2}\bar{\boldsymbol{J}}_{\mathrm{s}}(\boldsymbol{r}) + \hat{\boldsymbol{n}} \times \mathscr{L}(\boldsymbol{M}_{\mathrm{s}})(\boldsymbol{r}) + \hat{\boldsymbol{n}} \times \tilde{\mathscr{K}}(\bar{\boldsymbol{J}}_{\mathrm{s}})(\boldsymbol{r}) = \hat{\boldsymbol{n}} \times \bar{\boldsymbol{H}}^{\mathrm{inc}}(\boldsymbol{r}) \tag{2.88}$$

with evaluation on the outside of Ω.

2.8 Characteristic Modes

Characteristic modes are an example of a set of orthogonal solutions to a scattering problem which can be useful in many design problems [53, 82]. Here, the characteristic modes are introduced from the perspective of a pure PEC object, which is a commonly used formulation [57]. For a PEC medium, the boundary supports electric but not magnetic currents. This makes the EFIE in (2.84) take on the form

$$\hat{\boldsymbol{n}} \times \mathscr{L}(\bar{\boldsymbol{J}})(\boldsymbol{r}) = \hat{\boldsymbol{n}} \times \boldsymbol{E}^{\text{inc}}(\boldsymbol{r}). \tag{2.89}$$

This can be written in a different form as

$$\mathcal{Z}(\boldsymbol{I}) = \boldsymbol{V} \tag{2.90}$$

where $\mathcal{Z}$ corresponds to the $\mathscr{L}$-operator acting on current densities represented as $\boldsymbol{I}$ for an incident field represented as $\boldsymbol{V}$. The notation is chosen to resemble concepts from circuit theory, and consequently $\mathcal{Z}$ is called the impedance operator, $\boldsymbol{I}$ the current vector, and $\boldsymbol{V}$ the voltage vector. This notation is commonly used in the method of moments (MoM) computational method which is based on integral equations, and which is further discussed in section 3.2. In that case, discretization of the problem means that $\mathcal{Z}$, $\boldsymbol{I}$, and $\boldsymbol{V}$ are represented by matrices and vectors, but here the problem is considered from a pure operator point of view. Looking at the $\mathscr{L}$-operator defined in (2.80), it is clear that it is complex and as such the impedance operator is rewritten as

$$\mathcal{Z} = \mathcal{R} + \mathrm{j}\mathcal{X} \tag{2.91}$$

with $\mathcal{R}$ and $\mathcal{X}$ called resistance and reactance, respectively, following the theme from circuit theory. These new operators can in turn be used to define a generalized eigenvalue problem as

$$\mathcal{X}(\boldsymbol{I}_n) = \lambda_n \mathcal{R}(\boldsymbol{I}_n) \tag{2.92}$$

where the solutions are called characteristic modes with eigenvectors $\boldsymbol{I}_n$ and eigenvalues λ_n [57].

Characteristic modes have been known for a significant time [44, 95], but were not widely used until more recently with the emergence of many applications in antenna design [26, 82]. The recent work has mostly been based on the eigenvalue decomposition (2.92) described in [57], which limits applications to solvers and formulations based on an impedance operator. Recent work has shown how a formulation based on scattering problems, as originally proposed in [44], can be used more generally [28, 53, 54]. This formulation is in many ways more versatile than (2.92) in that the characteristic modes can be computed by solving a scattering problem independent of the underlying operator. Characteristic modes can then be computed using arbitrary solvers for electromagnetic scattering problems [28, 85].

3 Computational Methods

Much of the success of modern electromagnetic applications can be attributed to the development of increasingly capable computational methods together with the growth in available computational power in recent decades. While the theory based on Maxwell's equations is highly descriptive of electromagnetic phenomena, there are few problems which can be computed analytically. For this reason, computational methods are indispensable to the modern electromagnetic designer. Computational methods in electromagnetics can be organized in many different ways. One common way to group them is by their theoretical accuracy, which results in the grouping into full wave solvers and asymptotic solvers. Full wave solvers attempt to solve electromagnetic problems without any approximations to Maxwell's equations themselves. This should not be confused with exact solutions as approximations do appear in later stages. Asymptotic solvers, on the other hand, approximate the equations to be solved as the first step and, as a result, they can become computationally more efficient compared to full wave solvers. However, they can only be used if the original assumptions behind the approximations hold.

While asymptotic solvers have very clear cases where the original assumptions break down, it is important to remember that all computational methods have limitations. With full wave solvers it can be easy to think that the solution should be accurate regardless of what electromagnetic problem it is applied to. As will be seen in this section, there are still many approximations that are done in full wave solvers. An example of this is the very step of generating a mesh for a problem geometry, which is an important step in many computational methods. This can be seen as an approximation of the original geometry, but in a way it is rather a replacement of one geometry by another. A typical idea in numerical methods is that increasingly small mesh elements should result in a numerical solution converging to the actual solution. This, however, is not always the case. Many of the most useful computational methods in electromagnetics suffer from the so-called low-frequency breakdown if the mesh size becomes too small. If, in the original problem, Maxwell's equations were considered at a high frequency for the problem size, the selected method may seem very suitable. After meshing, however, Maxwell's equations should be considered for each mesh element, which is essentially a different problem. For very small mesh elements, Maxwell's equations behave in a very different way, closer to electro- and magnetostatics, and this is the basic issue which causes the low-frequency breakdown [32]. Of course, there are remedies to this problem, but its existence is a good reminder that even full wave solvers are not universally applicable without considering the basic assumptions.

When implementing a computational method, another element of uncertainty enters in the form of errors and bugs in the implementation. To ensure that solutions are accurate, verification is crucial. This can take on many different forms, from verification of individual subroutines to comparison of full solutions

to benchmark solutions. Ideally, verification should take place at every level of the computational code, but at the end it is the comparison of full solutions that is most often used to convince others that the code is accurate. The most common example for this is likely the solution of scattering by a sphere, where a comparison can be made to the analytical Mie solution. However, this is not without its drawbacks, as there can be errors in a code which are not visible for that particular problem. Confidence in the accuracy of a particular code should increase with the number of correctly computed benchmark solutions, and a single sphere should not be sufficient for generalizing that a code is correct for all problems. The benchmark which is offered by the Mie solution should not be ignored though, as it provides an excellent first benchmark which is easy to obtain.

In this dissertation, the focus of computational methods is on full wave solvers, with the finite element method (FEM), the method of moments (MoM) and the finite element-boundary integral (FE-BI) method which is a hybrid combining the two. The FE-BI method is implemented in the FE2MS computational code described in Paper I and used in Papers II and III, and the theoretical background to that code is given in this section. The code uses not only FE-BI, but also the adaptive cross approximation (ACA) which is introduced here. Furthermore, Paper IV presents an imaging method with similarities to MoM, and an acceleration method for matrix-vector products which is introduced in this section. The topic of computational methods is, of course, very large and this section focuses only on the methods important to the rest of this dissertation. For a more general overview, the reader is directed to some of the many textbooks on the topic [35, 71, 120].

3.1 The Finite Element Method

The finite element method (FEM) is a versatile computational method which has seen use in a wide range of applications for different branches of physics. It is a method which solves PDEs with suitable boundary conditions using the idea of a subdivision of the computational domain into finite elements: small, regularly shaped subdomains where the solution can be approximated to be on a simple form, typically based on polynomial functions [21, 38]. The subdivided geometry is called a mesh, with individual subdomains called mesh elements, and the functions for approximating the solution called basis functions. The mathematical foundation of FEM rests on calculus of variations and the problem of minimizing functionals, which in physical terms corresponds to minimizing the energy of a particular solution [38]. The variational formulation which is central to this requires the PDE to be reformulated on a weak form which takes into account both the function corresponding to the unknown, and a test function [21]. An alternative, but equivalent, way to motivate a FEM formulation is using the weighted residual method. Typically, this introduces the expansion in basis functions at an earlier stage, and the derivations are generally more direct than using calculus

of variations [35, 71]. For a PDE, the typical procedure for obtaining its weak form is multiplication of the equation by a test function, integration over the full domain, and integration by parts [38].

In electromagnetics, FEM is typically used to solve a PDE similar to (2.20) (possibly with other constitutive relations) for either the electric field $\boldsymbol{E}$ or the magnetic field $\boldsymbol{H}$. The way the weak form is discretized, material parameters are local to the finite elements, which makes FEM particularly suitable to problems that are highly inhomogeneous. As shown in the following parts of this section, it is also possible to use very general constitutive relations in FEM, although the weak forms do change. If there is no magnetoelectric coupling, the corresponding parameters in the constitutive relations (2.30)–(2.31) are $\overline{\overline{\xi}} = \overline{\overline{\zeta}} = \overline{\overline{0}}$. If these relations are inserted in Maxwell's equations (2.15)–(2.16), we obtain

$$\nabla \times \boldsymbol{E} = -\mathrm{j}\omega\mu_0 \overline{\overline{\mu_\mathrm{r}}} \cdot \boldsymbol{H} \tag{3.1}$$

$$\nabla \times \boldsymbol{H} = \boldsymbol{J} + \mathrm{j}\omega\varepsilon_0 \overline{\overline{\varepsilon_\mathrm{r}}} \cdot \boldsymbol{E}. \tag{3.2}$$

By taking the curl of the first equation, they can be combined into a vector wave equation on the form

$$\nabla \times \left(\overline{\overline{\mu_\mathrm{r}}}^{-1} \cdot \nabla \times \boldsymbol{E} \right) - k_0^2 \overline{\overline{\varepsilon_\mathrm{r}}} \cdot \boldsymbol{E} = -\mathrm{j}k_0\eta_0 \boldsymbol{J}. \tag{3.3}$$

A weak form based on this equation can be written as (see A.1 for details)

$$\begin{aligned} \int_\Omega \left[(\nabla \times \boldsymbol{W}_m) \cdot \left(\overline{\overline{\mu_\mathrm{r}}}^{-1} \cdot \nabla \times \boldsymbol{E} \right) - k_0^2 \boldsymbol{W}_m \cdot \overline{\overline{\varepsilon_\mathrm{r}}} \cdot \boldsymbol{E} \right] \mathrm{d}V \\ + \oint_{\partial\Omega} \boldsymbol{W}_m \cdot \left[\hat{\boldsymbol{n}} \times \left(\overline{\overline{\mu_\mathrm{r}}}^{-1} \cdot \nabla \times \boldsymbol{E} \right) \right] \mathrm{d}S = -\mathrm{j}k_0\eta_0 \int_\Omega \boldsymbol{W}_m \cdot \boldsymbol{J} \, \mathrm{d}V. \end{aligned} \tag{3.4}$$

In the case where full magnetoelectric coupling is considered, the situation is more complicated. Inserting the full constitutive relations (2.30)–(2.31) in Maxwell's equations (2.15)–(2.16) gives

$$\nabla \times \boldsymbol{E} = -\mathrm{j}\omega\mu_0 \left(\frac{1}{\eta_0} \overline{\overline{\zeta}} \cdot \boldsymbol{E} + \overline{\overline{\mu_\mathrm{r}}} \cdot \boldsymbol{H} \right) \tag{3.5}$$

$$\nabla \times \boldsymbol{H} = \boldsymbol{J} + \mathrm{j}\omega\varepsilon_0 \left(\overline{\overline{\varepsilon_\mathrm{r}}} \cdot \boldsymbol{E} + \eta_0 \overline{\overline{\xi}} \cdot \boldsymbol{H} \right). \tag{3.6}$$

These can be combined into one equation (see A.2 for details)

$$\begin{aligned} \nabla \times \left(\overline{\overline{\mu_\mathrm{r}}}^{-1} \cdot \nabla \times \boldsymbol{E} \right) - k_0^2 \left(\overline{\overline{\varepsilon_\mathrm{r}}} - \overline{\overline{\xi}} \cdot \overline{\overline{\mu_\mathrm{r}}}^{-1} \cdot \overline{\overline{\zeta}} \right) \cdot \boldsymbol{E} \\ + \mathrm{j}k_0 \left[\nabla \times \left(\overline{\overline{\mu_\mathrm{r}}}^{-1} \cdot \overline{\overline{\zeta}} \cdot \boldsymbol{E} \right) - \overline{\overline{\xi}} \cdot \overline{\overline{\mu_\mathrm{r}}}^{-1} \cdot \nabla \times \boldsymbol{E} \right] = -\mathrm{j}k_0\eta_0 \boldsymbol{J} \end{aligned} \tag{3.7}$$

and a corresponding weak form

$$\int_\Omega (\nabla \times \boldsymbol{W}_m) \cdot \left(\overline{\overline{\mu_\mathrm{r}}}^{-1} \cdot \nabla \times \boldsymbol{E}\right) \mathrm{d}V - k_0^2 \int_\Omega \boldsymbol{W}_m \cdot \left(\overline{\overline{\varepsilon_\mathrm{r}}} - \overline{\overline{\xi}} \cdot \overline{\overline{\mu_\mathrm{r}}}^{-1} \cdot \overline{\overline{\zeta}}\right) \cdot \boldsymbol{E} \, \mathrm{d}V$$
$$+ \mathrm{j}k_0 \int_\Omega (\nabla \times \boldsymbol{W}_m) \cdot \overline{\overline{\mu_\mathrm{r}}}^{-1} \cdot \overline{\overline{\zeta}} \cdot \boldsymbol{E} \, \mathrm{d}V - \mathrm{j}k_0 \int_\Omega \boldsymbol{W}_m \cdot \left(\overline{\overline{\xi}} \cdot \overline{\overline{\mu_\mathrm{r}}}^{-1} \cdot \nabla \times \boldsymbol{E}\right) \mathrm{d}V$$
$$+ \oint_{\partial\Omega} \boldsymbol{W}_m \cdot \left[\hat{\boldsymbol{n}} \times \left(\overline{\overline{\mu_\mathrm{r}}}^{-1} \cdot \nabla \times \boldsymbol{E}\right)\right] \mathrm{d}S - \mathrm{j}k_0 \oint_{\partial\Omega} \hat{\boldsymbol{n}} \cdot \left[\boldsymbol{W}_m \times \left(\overline{\overline{\mu_\mathrm{r}}}^{-1} \cdot \overline{\overline{\zeta}} \cdot \boldsymbol{E}\right)\right] \mathrm{d}S$$
$$= -\mathrm{j}k_0 \eta_0 \int_\Omega \boldsymbol{W}_m \cdot \boldsymbol{J} \, \mathrm{d}V. \quad (3.8)$$

In general, the PDE that FEM is solving needs suitable boundary conditions to be well posed. In the previous sections these have not been considered and as such, the weak forms in (3.4) and (3.8) cannot be expected to be used as they are. Modification of the weak forms would be necessary, and this depends on the type of boundary condition used. Additionally, there could be different boundary conditions on different parts of the boundary $\partial\Omega$ which further affects the weak forms. The PEC boundary condition defined in (2.52)–(2.55) is one of the most useful boundary conditions in practical applications due to the ubiquity of conducting materials. In the electric field FEM formulation used here, it is simple to define using only (2.52) which sets the tangential electric field to zero on the PEC boundary. With some of the most common FEM basis functions this is simple to implement as it only corresponds to setting certain unknowns to zero [72].

Another type of boundary condition which is important is the class of absorbing boundary conditions. As FEM requires the full computational domain to be discretized, simulations with open boundaries, as in typical scattering, pose a problem. Absorbing boundary conditions aim to solve this by, ideally, being formulated such that all waves approaching such a boundary are absorbed perfectly. This emulates an open boundary where the wave propagates to infinity without further interactions. Many absorbing boundary conditions are based on enforcing a radiation condition at the boundary such that waves are absorbed at normal incidence, but reflected at oblique angles. To avoid reflections it can be necessary to place the boundary at a large distance from the simulated object, increasing the number of unknowns [71]. Another type of absorbing boundary condition is the perfectly matched layer (PML), which is technically not a boundary condition but rather an anisotropic medium specially designed to absorb waves that enter [71, 147]. This medium is placed as a layer surrounding the computational domain sufficiently thick to absorb all waves before they reach the outer boundary, at which a PEC boundary condition is often used [71]. One important consideration for all absorbing boundary conditions is the shape of the object to be simulated. Since all waves are absorbed at such a boundary it is critical that it is not placed in a way that interferes with the object. One example of this is shown in Figure 9 where an object exhibiting multiple reflections is shown with absorbing boundary conditions placed differently. To ensure that all characteristics of an object are captured, absorbing boundary conditions can often not be placed conformal to the object. In some cases, like for highly concave objects,

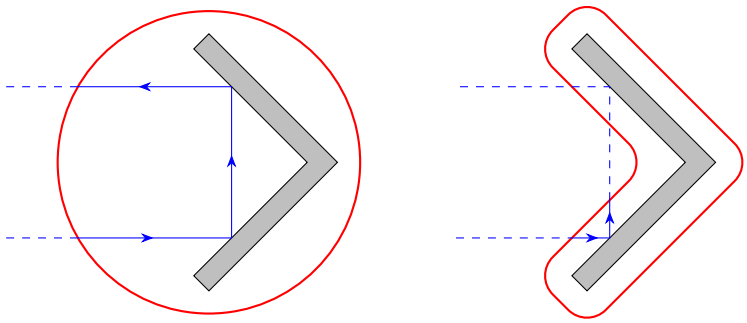

Figure 9: Object exhibiting multiple reflection with absorbing boundary condition (red) placed such that an incident wave (blue) is reflected correctly (left) or is absorbed prematurely (right).

this can lead to a large number of additional unknowns in the FEM problem. This is one of the reasons why other methods like the FE-BI method can be of interest, as will be discussed in section 3.3.

3.2 The Method of Moments

The method of moments (MoM), or boundary element method as it is commonly known outside of electromagnetics, is a computational method based on integral equations. For electromagnetics, this often means either of, or a combination of, the EFIE (2.84) and the MFIE (2.85). It has similarities to FEM, but where FEM is based on a PDE, the integral equations which MoM is based on lead to different characteristics. In FEM, the field solution is directly given by the unknown of the problem, for example $\boldsymbol{E}$ in the PDE (3.3), and is intrinsically linked to the discretization. To determine the solution in a larger region, that region needs to be discretized. In MoM, on the other hand, the solution to the integral equation is typically electric and magnetic currents, and $\boldsymbol{E}$ can be computed from these in arbitrary points of space using (2.79).

One of the most common uses of MoM is for problems involving PEC objects using the EFIE. As discussed in section 2.3, PEC objects only support electric currents and charges. The EFIE in (2.84) is then simplified to

$$\hat{\boldsymbol{n}} \times \mathscr{L}(\bar{\boldsymbol{J}}_\mathrm{s})(\boldsymbol{r}) = \hat{\boldsymbol{n}} \times \boldsymbol{E}^\mathrm{inc}(\boldsymbol{r}) \tag{3.9}$$

for $\boldsymbol{r}$ on a closed PEC surface $\partial\Omega$. In fact, this equation is valid even for open surfaces despite the fact that the EFIE is typically derived only for closed surfaces [32], and for this reason the surface is denoted S in the following. To solve this problem, the unknown current $\bar{\boldsymbol{J}}_\mathrm{s}$ is expanded in a finite set of N basis functions, which could be global or local functions on the surface S. This gives a

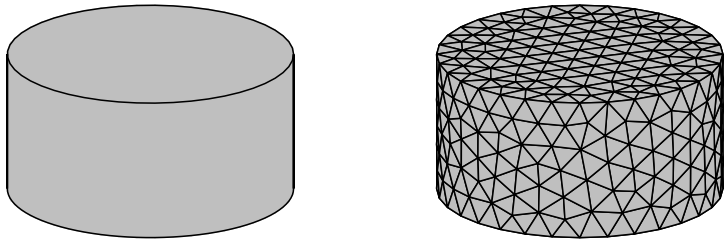

Figure 10: A surface and its triangular mesh representation.

representation

$$\bar{\boldsymbol{J}}_\mathrm{s} = \sum_{n=0}^{N-1} \boldsymbol{\Lambda}_n(\boldsymbol{r}) I_n \tag{3.10}$$

where $\boldsymbol{\Lambda}_n$ are basis functions and I_n unknown coefficients. Most commonly, local basis functions are used on a triangular mesh which approximates the surface as shown in Figure 10. The most commonly used basis functions are the linear Rao-Wilton-Glisson (RWG) basis functions [112] which are defined on pairs of triangles sharing an edge in triangular meshes. Expansion in basis functions is not sufficient for a unique solution though, as there will be N unknown coefficients and only one equation.

Furthermore, the discretization introduces an error (residual) due to the finite number of basis functions. The weighted residual method is used to produce a linear system while minimizing the errors introduced by the discretization. The way this is done is by introducing a set of test functions $\boldsymbol{T}_m$ and taking the inner product of these and the discretized equation of interest, in this case (3.9) with the expansion of unknowns in (3.10). The test functions can then be selected to minimize the error after inner product by the discretized equation. If the test functions are selected to be orthogonal to the residual, this error will be eliminated. This is the goal of the Galerkin method [21], typically leading to test functions being the same as the basis functions [32]. In this case it means $\boldsymbol{T}_m = \boldsymbol{\Lambda}_m$ which gives a linear system on the form [32]

$$\mathbf{Z}\boldsymbol{I} = \boldsymbol{V} \tag{3.11}$$

with

$$\begin{aligned} Z_{mn} &= \int_S \boldsymbol{\Lambda}_m(\boldsymbol{r}) \cdot \mathscr{L}(\boldsymbol{\Lambda}_n)(\boldsymbol{r}) \,\mathrm{d}S \\ &= \mathrm{j}k_0 \int_S \boldsymbol{\Lambda}_m(\boldsymbol{r}) \cdot \int_S \left[\boldsymbol{\Lambda}_n(\boldsymbol{r}') G_0(\boldsymbol{r}, \boldsymbol{r}') + \frac{1}{k_0^2} \nabla' \cdot \boldsymbol{\Lambda}_n(\boldsymbol{r}') \nabla G_0(\boldsymbol{r}, \boldsymbol{r}') \right] \mathrm{d}S' \,\mathrm{d}S \end{aligned} \tag{3.12}$$

and

$$V_m = \int_S \boldsymbol{\Lambda}_m(\boldsymbol{r}) \cdot \boldsymbol{E}^\mathrm{inc}(\boldsymbol{r}) \,\mathrm{d}S \tag{3.13}$$

where the $\hat{\boldsymbol{n}}\times$ operations originally in (3.9) were removed by noting that it is sufficient that the left- and right-hand sides of (3.9) are tangential to the PEC surface. After scalar products of this equation by tangential test functions, the resulting Z_{mn} and V_m are the same regardless of whether the terms in (3.9) are tangential or not.

The integrals making up the entries of $\mathbf{Z}$ are generally not possible to compute analytically (as opposed to many FEM integrals), and some numerical quadrature is typically performed to obtain the matrix entries [35, 71]. One issue stemming from the Galerkin testing is that some entries of $\mathbf{Z}$ become singular. This comes from the fact that if both $\boldsymbol{\Lambda}_m$ and $\boldsymbol{\Lambda}_n$ are nonzero on a mesh triangle, the inner integral will cover $\boldsymbol{r} = \boldsymbol{r}'$ where the Green's function is singular. One aspect of this singularity was handled in section 2.7, but that was only for the inner operator before Galerkin testing was introduced. It is possible to alter the testing and quadrature procedure such that $\boldsymbol{r} = \boldsymbol{r}'$ never occurs [35, 86], but other methods are typically more accurate [35]. Such methods include singularity subtraction which subtracts a singular part of the integrand that can be solved analytically [8, 40, 48], and singularity cancellation which introduces a coordinate transformation where the singularity is canceled out [39, 75]. For better accuracy, it is also necessary to consider the outer (test) integral when the basis and testing mesh elements are the same or adjacent [106, 108, 109, 150].

While the EFIE and MFIE are widely used in MoM, theory predicts a number of issues with them, with one of the more well known being the issue of interior resonances [32]. The effect of this issue is that the solution to the aforementioned integral equations become inaccurate at certain frequencies. To explain this, it is useful to look at the equivalence theorem while exchanging the volumes being the interior and exterior. If we let the fields be zero for $\boldsymbol{r} \notin \Omega$ in the right-hand sides of (2.82) and (2.83), the problem becomes that of a resonance cavity shaped as Ω with PEC at $\partial\Omega$. At precisely the resonance frequencies of this cavity, the problem of interior resonances will occur for the integral equations as the cavity solution is a valid solution to the equation. Mathematically, this means that there is a null-space of the EFIE/MFIE operator at these frequencies, which causes both issues with inaccurate solutions and an ill-conditioned problem [32]. The latter occurs for other frequencies near the resonance which is an issue for iterative solutions of the problem (this is further discussed in sections 3.3 and 3.4). A common way to remove the issue of interior resonances is by combining the EFIE and MFIE into the combined field integral equation (CFIE) [32].

3.3 The Finite Element–Boundary Integral Method

As hinted toward at the end of section 3.1, the hybridization of FEM and MoM could potentially be advantageous in certain situations, and a commonly used name for such a hybrid method is the finite element-boundary integral (FE-BI) method. The discussions on FEM and MoM by themselves have revealed some

ways the methods complement each other. While FEM is well-suited toward computations involving highly inhomogeneous or even complex media, this is much more difficult and computationally expensive in MoM where it typically requires a volumetric formulation instead of surface formulations similar to that in section 3.2. On the other hand, FEM has several difficulties when it comes to problems involving free space where absorbing boundary conditions need to be used and concave geometries can lead to a large number of unknowns, while the integral equations in MoM inherently handle free space outside the discretized region. These differences and the ways in which the methods complement each other were understood early in the development of FEM and MoM, and hybrid methods have a long history. Very early work on such hybrid methods was done for other types of problems than the electromagnetic wave problems of this dissertation, like scalar potential problems [90, 133]. For the electromagnetic wave problems considered here, the FE-BI method was first introduced as a way to implement free-space boundaries in FEM since modern absorbing boundary conditions like PML were not yet developed. Early methods for doing this included coupling FEM with spherical meshes to spherical harmonics at the free-space boundary [92, 96]. One of the earliest papers mentioning the term "finite element-boundary integral" for electromagnetic wave problems is actually related to a method based on spherical vector harmonics in the boundary integral part, and differs significantly from later methods which use the term [97]. Hybrid methods similar to the one described in this dissertation were later developed for wave propagation in tissue for medical applications [102], and for scattering more generally [70, 165, 166]. As new and faster methods for solving integral equations have been developed, they have typically also been employed for the BI part of the FE-BI method [49, 130, 154, 156]. As will be discussed later in this dissertation, the BI part of the hybrid method dominates in memory use, and as such it is the most important part to make more efficient. While much of the work in FE-BI methods was conducted in the 1990s, there are still developments up to this day. An important topic to handle is the ill-conditioned nature of the FE-BI system matrix. Work related to this includes developing better preconditioners [87, 160], ans alternative solution strategies using domain decomposition [10, 50, 161, 162] or $\mathcal{H}$-matrices [156].

In this section, the formulation of the FE-BI method used in the FE2MS computational code (discussed in Paper I) is introduced. The description roughly follows that in [71, 72], but with some differences and emphasis added to parts where it is important for understanding the work in this thesis. The FE-BI method as discussed in this dissertation uses FEM inside of a volume Ω with a weak form suitable for the media inside. A sketch of this geometry is seen in Figure 11 where it is seen that Ω can contain bianisotropic media, PEC, and current sources. Outside of Ω the medium is free space, though that could be changed to another isotropic medium, and there can be an incident wave. On the boundary $\partial\Omega$, an integral equation is used, for example the EFIE in (2.84). This means that the boundary condition on $\partial\Omega$ is not explicitly known, and instead a boundary condition enforcing Maxwell's equations, or more specifically, Faraday's

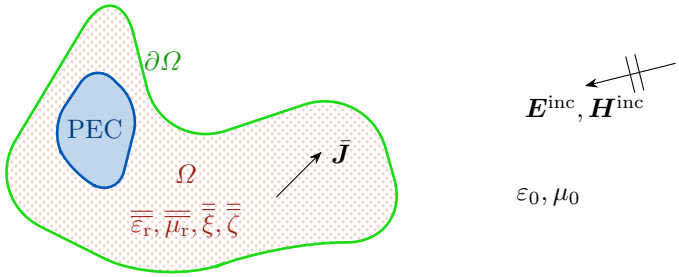

Figure 11: Problem geometry for the FE-BI method.

law is used. That is, a boundary condition equivalent to (2.15) written as

$$\hat{\boldsymbol{n}} \times \left(\bar{\bar{\mu}}_\mathrm{r}^{-1} \cdot \nabla \times \boldsymbol{E}\right) = -\mathrm{j}k_0 \hat{\boldsymbol{n}} \times \bar{\boldsymbol{H}}, \ \boldsymbol{r} \in \partial\Omega \tag{3.14}$$

where the scaling of the magnetic field $\bar{\boldsymbol{H}} = \eta_0 \boldsymbol{H}$ and the electric current $\bar{\boldsymbol{J}} = \eta_0 \boldsymbol{J}$ that was used when introducing MoM is now extended to FEM parts. This condition is inserted in the weak forms, giving

$$\int_\Omega \left[(\nabla \times \boldsymbol{W}_m) \cdot \left(\bar{\bar{\mu}}_\mathrm{r}^{-1} \cdot \nabla \times \boldsymbol{E}\right) - k_0^2 \boldsymbol{W}_m \cdot \bar{\bar{\varepsilon}}_\mathrm{r} \cdot \boldsymbol{E}\right] \mathrm{d}V + \mathrm{j}k_0 \oint_{\partial\Omega} \hat{\boldsymbol{n}} \cdot \left(\boldsymbol{W}_m \times \bar{\boldsymbol{H}}\right) \mathrm{d}S = -\mathrm{j}k_0 \int_\Omega \boldsymbol{W}_m \cdot \bar{\boldsymbol{J}} \, \mathrm{d}V \tag{3.15}$$

for media without magnetoelectric coupling and

$$\begin{aligned} &\int_\Omega (\nabla \times \boldsymbol{W}_m) \cdot \left(\bar{\bar{\mu}}_\mathrm{r}^{-1} \cdot \nabla \times \boldsymbol{E}\right) \mathrm{d}V - k_0^2 \int_\Omega \boldsymbol{W}_m \cdot \left(\bar{\bar{\varepsilon}}_\mathrm{r} - \bar{\bar{\xi}} \cdot \bar{\bar{\mu}}_\mathrm{r}^{-1} \cdot \bar{\bar{\zeta}}\right) \boldsymbol{E} \, \mathrm{d}V \\ &+ \mathrm{j}k_0 \int_\Omega (\nabla \times \boldsymbol{W}_m) \cdot \bar{\bar{\mu}}_\mathrm{r}^{-1} \cdot \bar{\bar{\zeta}} \cdot \boldsymbol{E} \, \mathrm{d}V - \mathrm{j}k_0 \int_\Omega \boldsymbol{W}_m \cdot \left(\bar{\bar{\xi}} \cdot \bar{\bar{\mu}}_\mathrm{r}^{-1} \cdot \nabla \times \boldsymbol{E}\right) \mathrm{d}V \\ &+ \mathrm{j}k_0 \oint_{\partial\Omega} \hat{\boldsymbol{n}} \cdot \left(\boldsymbol{W}_m \times \bar{\boldsymbol{H}}\right) \mathrm{d}S = -\mathrm{j}k_0 \int_\Omega \boldsymbol{W}_m \cdot \bar{\boldsymbol{J}} \, \mathrm{d}V \end{aligned} \tag{3.16}$$

for media with magnetoelectric coupling (see A.1–A.2 for details). These weak forms contain two unknown fields $\boldsymbol{E}$ and $\bar{\boldsymbol{H}}$ on $\partial\Omega$ which are connected using an integral equation. When this connection is to be made, the unknowns need to be related to each other. In the FE part, the unknowns are the fields $\boldsymbol{E}$ and $\bar{\boldsymbol{H}}$ while in BI part they are the currents $\bar{\boldsymbol{J}}$ and $\boldsymbol{M}$. Using the surface equivalence theorem with the zero field condition in (2.74) and (2.75), these are related as $\bar{\boldsymbol{J}}_\mathrm{s} = \hat{\boldsymbol{n}} \times \bar{\boldsymbol{H}}$ and $\boldsymbol{M}_\mathrm{s} = \boldsymbol{E} \times \hat{\boldsymbol{n}}$. The use of the zero field equivalence theorem means that standard free space integral equations can be used to give the true solution without special regard to the medium inside Ω.

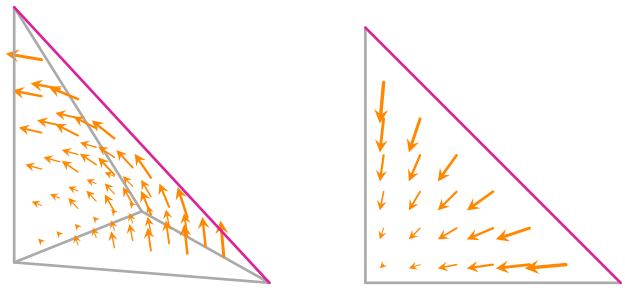

Figure 12: Basis functions used in the FE (left) and BI (right) parts. The triangle to the right is the same as the front face of the tetrahedron to the left. Adapted from [128] (CC-BY-4.0).

3.3.1 Basis Functions

Next, the solution in both FEM and MoM rests upon expanding the unknowns into a discrete set of basis functions, which means that they also need to be connected. In the FE part, the expansion uses curl-conforming basis functions $\boldsymbol{N}$, meaning that the functions are defined such that $\nabla \times \boldsymbol{N}$ is square integrable [46]. In the BI part, the expansion uses divergence-conforming basis functions $\boldsymbol{\Lambda}$, which instead are such that $\nabla \cdot \boldsymbol{\Lambda}$ is square integrable [46]. Essentially, the curl or divergence of such basis functions will not contain Dirac delta functions, making them suitable in expressions with curl or divergence (like the FE or BI expressions). Figure 12 shows an example of a lowest order Nédélec curl-conforming basis function on a tetrahedron and a lowest order Raviart-Thomas divergence-conforming basis function on a triangle (equivalent to RWG functions but often defined with a different normalization). As these are linear functions, the curl- or divergence-conforming property means that $\nabla \times \boldsymbol{N}$ or $\nabla \cdot \boldsymbol{\Lambda}$ is constant. Both types of basis functions are so called edge based, meaning that they are linked to edges in the mesh, as can be seen for the basis functions in Figure 12 which are linked to the highlighted edges. If the FE unknowns $\boldsymbol{E}$ and $\bar{\boldsymbol{H}}$ are expanded using curl-conforming basis functions, they can be written as

$$\boldsymbol{E}(\boldsymbol{r}) = \sum_{n=0}^{N_\mathrm{I}-1} \boldsymbol{N}_n^\mathrm{I}(\boldsymbol{r}) E_n^\mathrm{I} + \sum_{n=0}^{N_\mathrm{S}-1} \boldsymbol{N}_n^\mathrm{S}(\boldsymbol{r}) E_n^\mathrm{S} \tag{3.17}$$

$$\bar{\boldsymbol{H}}(\boldsymbol{r}) = \sum_{n=0}^{N_\mathrm{S}-1} \boldsymbol{N}_n^\mathrm{S}(\boldsymbol{r}) \bar{H}_n^\mathrm{S} \tag{3.18}$$

where N_I is the number of mesh edges on the interior of Ω and N_S is the number of mesh edges on the external boundary $\partial\Omega$. The superscripts I and S similarly indicate whether a basis function and its corresponding degree of freedom are based on an interior or boundary edge, respectively. If the BI unknowns $\bar{\boldsymbol{J}}_\mathrm{s}$ and $\boldsymbol{M}_\mathrm{s}$ are to be expanded in basis functions, it is important that they can be connected to the FE expansions. This is quite naturally done though, as a curl-

conforming basis function transforms into a divergence-conforming one under the rotation around a surface normal. This means that a suitable expansion is obtained for $\boldsymbol{r} \in \partial\Omega$ as

$$\bar{\boldsymbol{J}}_{\mathrm{s}}(\boldsymbol{r}) = \hat{\boldsymbol{n}} \times \bar{\boldsymbol{H}}(\boldsymbol{r}) = \sum_{n=0}^{N_{\mathrm{S}}-1} \left(\hat{\boldsymbol{n}} \times \boldsymbol{N}_n^{\mathrm{S}}(\boldsymbol{r})\right) \bar{H}_n^{\mathrm{S}} = \sum_{n=0}^{N_{\mathrm{S}}-1} \boldsymbol{\Lambda}_n(\boldsymbol{r}) \bar{H}_n^{\mathrm{S}} \tag{3.19}$$

$$\boldsymbol{M}_{\mathrm{s}}(\boldsymbol{r}) = \boldsymbol{E}(\boldsymbol{r}) \times \hat{\boldsymbol{n}} = -\sum_{n=0}^{N_{\mathrm{S}}-1} \left(\hat{\boldsymbol{n}} \times \boldsymbol{N}_n^{\mathrm{S}}(\boldsymbol{r})\right) E_n^{\mathrm{S}} = -\sum_{n=0}^{N_{\mathrm{S}}-1} \boldsymbol{\Lambda}_n(\boldsymbol{r}) E_n^{\mathrm{S}} \tag{3.20}$$

with the derived divergence-conforming basis functions $\boldsymbol{\Lambda}_n$. If $\boldsymbol{N}_n$ is a lowest order Nédélec basis function on a tetrahedron, the derived $\boldsymbol{\Lambda}_n$ is a lowest order Raviart-Thomas basis function on a triangle. By careful inspection of figure 12, it can be seen that the Raviart-Thomas function is obtained by rotating the Nédélec function 90° around the facet normal.

3.3.2 Finite Element Matrix Blocks

The finite element formulations can be separated into integrals involving $\boldsymbol{E}$ and integrals involving $\bar{\boldsymbol{H}}$. The expansions in (3.17) and (3.18) are used, and the test functions $\boldsymbol{W}_m$ in the weak forms are set to be equal to the basis functions. For media without magnetoelectric coupling, using the $\boldsymbol{E}$ integrals of the weak form in (3.15) results in a matrix $\mathbf{K}$ with entries

$$K_{mn}^{\mathrm{XY}} = \int_\Omega \left[(\nabla \times \boldsymbol{N}_m^{\mathrm{X}}) \cdot \left(\overline{\overline{\mu_{\mathrm{r}}}}^{-1} \cdot \nabla \times \boldsymbol{N}_m^{\mathrm{Y}} \right) - k_0^2 \boldsymbol{N}_m^{\mathrm{X}} \cdot \overline{\overline{\varepsilon_{\mathrm{r}}}} \cdot \boldsymbol{N}_m^{\mathrm{Y}} \right] \mathrm{d}V \tag{3.21}$$

where $\mathrm{X}, \mathrm{Y} \in \{\mathrm{I}, \mathrm{S}\}$ indicate if corresponding unknowns are on the interior of Ω or on the external boundary $\partial\Omega$. For media with magnetoelectric coupling as the weak form in (3.16), the matrix entries instead become

$$\begin{aligned} K_{mn}^{\mathrm{XY}} = & \\ & \int_\Omega (\nabla \times \boldsymbol{N}_m^{\mathrm{X}}) \cdot \left(\overline{\overline{\mu_{\mathrm{r}}}}^{-1} \cdot \nabla \times \boldsymbol{N}_m^{\mathrm{Y}} \right) \mathrm{d}V - k_0^2 \int_\Omega \boldsymbol{N}_m^{\mathrm{X}} \cdot \left(\overline{\overline{\varepsilon_{\mathrm{r}}}} - \overline{\overline{\xi}} \cdot \overline{\overline{\mu_{\mathrm{r}}}}^{-1} \cdot \overline{\overline{\zeta}} \right) \cdot \boldsymbol{N}_m^{\mathrm{Y}} \mathrm{d}V \\ & + \mathrm{j}k_0 \int_\Omega (\nabla \times \boldsymbol{N}_m^{\mathrm{X}}) \cdot \overline{\overline{\mu_{\mathrm{r}}}}^{-1} \cdot \overline{\overline{\zeta}} \cdot \boldsymbol{N}_m^{\mathrm{Y}} \mathrm{d}V - \mathrm{j}k_0 \int_\Omega \boldsymbol{N}_m^{\mathrm{X}} \cdot \left(\overline{\overline{\xi}} \cdot \overline{\overline{\mu_{\mathrm{r}}}}^{-1} \cdot \nabla \times \boldsymbol{N}_m^{\mathrm{Y}} \right) \mathrm{d}V. \end{aligned} \tag{3.22}$$

The integrals involving $\bar{\boldsymbol{H}}$ are the same for both types of media, resulting in a matrix $\mathbf{B}$ with entries

$$B_{mn} = \mathrm{j}k_0 \oint_{\partial\Omega} \hat{\boldsymbol{n}} \cdot (\boldsymbol{N}_m^{\mathrm{S}} \times \boldsymbol{N}_n^{\mathrm{S}}) \mathrm{d}S. \tag{3.23}$$

Since this only contains basis functions evaluated on the boundary $\partial\Omega$, it can also be rewritten using divergence-conforming basis functions as

$$B_{mn} = \mathrm{j}k_0 \oint_{\partial\Omega} \hat{\boldsymbol{n}} \cdot ([-\hat{\boldsymbol{n}} \times \boldsymbol{\Lambda}_m] \times [-\hat{\boldsymbol{n}} \times \boldsymbol{\Lambda}_n]) \,\mathrm{d}S = \mathrm{j}k_0 \oint_{\partial\Omega} \hat{\boldsymbol{n}} \cdot (\boldsymbol{\Lambda}_m \times \boldsymbol{\Lambda}_n) \,\mathrm{d}S. \tag{3.24}$$

The linear system built up by the matrices $\mathbf{K}^{\mathrm{XY}}$ and $\mathbf{B}$ can be expressed as

$$\begin{bmatrix} \mathbf{K}^{\mathrm{II}} & \mathbf{K}^{\mathrm{IS}} & \mathbf{0} \\ \mathbf{K}^{\mathrm{SI}} & \mathbf{K}^{\mathrm{SS}} & \mathbf{B} \end{bmatrix} \begin{pmatrix} \boldsymbol{E}^{\mathrm{I}} \\ \boldsymbol{E}^{\mathrm{S}} \\ \bar{\boldsymbol{H}}^{\mathrm{S}} \end{pmatrix} = \begin{pmatrix} \boldsymbol{b}^{\mathrm{I}} \\ \boldsymbol{b}^{\mathrm{S}} \end{pmatrix}. \tag{3.25}$$

This is underdetermined as the BI part has not yet been accounted for. The entries in the right-hand side are obtained as

$$b_m^{\mathrm{Y}} = -\mathrm{j}k_0 \int_{\Omega} \boldsymbol{N}_m^{\mathrm{Y}} \cdot \bar{\boldsymbol{J}} \,\mathrm{d}V \tag{3.26}$$

from the right-hand sides of (3.15) and (3.16).

3.3.3 Boundary Integral Matrix Blocks

The BI matrix blocks depend on the integral equation which is used. Starting with the EFIE from (2.84), a cross product by $\hat{\boldsymbol{n}}$ is first used to eliminate all occurrences of $\hat{\boldsymbol{n}}$ (the tangential nature of the equation is preserved since the basis functions $\boldsymbol{\Lambda}$ are tangential to the elements of their support). The expansions for currents in (3.19) and (3.20) are inserted and the equation is tested by the same functions as the basis functions. For test function m, the equation then becomes

$$\sum_{n=0}^{N_{\mathrm{S}}-1} \oint_{\partial\Omega} \boldsymbol{\Lambda}_m(\boldsymbol{r}) \cdot \left(\mathscr{L}\left[\boldsymbol{\Lambda}_n(\boldsymbol{r}')\bar{H}_n^{\mathrm{S}}\right] - \mathscr{K}\left[-\boldsymbol{\Lambda}_n(\boldsymbol{r})E_n^{\mathrm{S}}\right] \right) \mathrm{d}S = \oint_{\partial\Omega} \boldsymbol{\Lambda}_m(\boldsymbol{r}) \cdot \boldsymbol{E}^{\mathrm{inc}}(\boldsymbol{r}) \,\mathrm{d}S. \tag{3.27}$$

This gives a linear system on the form

$$\mathbf{P}\boldsymbol{E}^{\mathrm{S}} + \mathbf{Q}\bar{\boldsymbol{H}}^{\mathrm{S}} = \boldsymbol{b}^{\mathrm{inc}} \tag{3.28}$$

with entries given by

$$P_{mn} = P_{mn}^{\mathrm{E}} = \oint_{\partial\Omega} \boldsymbol{\Lambda}_m(\boldsymbol{r}) \cdot \mathscr{K}(\boldsymbol{\Lambda}_n(\boldsymbol{r}')) \,\mathrm{d}S \tag{3.29}$$

$$Q_{mn} = Q_{mn}^{\mathrm{E}} = \oint_{\partial\Omega} \boldsymbol{\Lambda}_m(\boldsymbol{r}) \cdot \mathscr{L}(\boldsymbol{\Lambda}_n(\boldsymbol{r}')) \,\mathrm{d}S \tag{3.30}$$

$$b_m^{\mathrm{inc}} = b_m^{\mathrm{E}} = \oint_{\partial\Omega} \boldsymbol{\Lambda}_m(\boldsymbol{r}) \cdot \boldsymbol{E}^{\mathrm{inc}}(\boldsymbol{r}) \,\mathrm{d}S. \tag{3.31}$$

As discussed in section 2.7, the $\mathscr{K}$-operator contains a singularity which gives an additional term when extracted. This term only appears for matrix entries with testing and basis functions within the same mesh triangle. Furthermore, the evaluation of matrix entries is done the same way as discussed for standard MoM in section 3.2, which means that certain entries will be singular and not possible to evaluate by numerical quadrature. Fortunately, the same methods of singularity subtraction and cancellation are also useful in the FE-BI case.

As for standard MoM, the use of the EFIE for closed surfaces like $\partial\Omega$ introduces the known issue of interior resonances. One common way to eliminate this issue is by using the CFIE instead. It is, however, important to test this equation with appropriate test functions for the interior resonance problem to fully disappear. One difficulty comes from the fact that versions of the CFIE which eliminate the interior resonance problem combine the EFIE and the MFIE with one of them having the rotating operation $\hat{\boldsymbol{n}}\times$ applied to it [130]. The suitable test functions for the rotated part of the CFIE are curl-conforming, and not simply the rotated basis functions. Instead, another type of test function, often called Buffa-Christiansen functions, can be used for that part of the CFIE to obtain an appropriately tested equation [7, 23]. These functions have been used to resolve issues with test functions for the MFIE [34], CFIE [163], and CFIE used in the FE-BI method [49].

A difficulty with the approaches using Buffa-Christiansen test functions for the CFIE is that implementations require significant amounts of additional work with such functions being defined on a different mesh. One CFIE formulation which is easy to implement with the exact same tools as for the EFIE formulation is the so called TETH formulation from [130]. This does not have any rotating operations for the EFIE or MFIE, and can use the same test functions as before. However, this formulation does not eliminate the interior resonances which was the main reason for using the CFIE. Nevertheless, it can be used to improve performance with essentially no additional effort compared to an EFIE implementation. If an iterative solver is used to solve a problem with interior resonances, the solver converges very slowly in a band around the resonance frequencies. With the TETH formulation, this band can be reduced so that solutions can be obtained with reasonable convergence at more frequencies than with the EFIE, although it is still not possible to obtain an accurate solution exactly at the resonance. The **P** and **Q** matrix blocks for the TETH formulation are obtained by linear combination of the ones for the EFIE as [130]

$$P_{mn} = \frac{1}{2}\left(P^{\mathrm{E}}_{mn} - Q^{\mathrm{E}}_{mn}\right) \tag{3.32}$$

$$Q_{mn} = \frac{1}{2}\left(P^{\mathrm{E}}_{mn} + Q^{\mathrm{E}}_{mn}\right) \tag{3.33}$$

$$b^{\mathrm{inc}}_{m} = \frac{1}{2}\left(b^{\mathrm{E}}_{m} + b^{\mathrm{M}}_{m}\right) \tag{3.34}$$

where

$$b^{\mathrm{M}}_{m} = \oint_{\partial\Omega} \boldsymbol{\Lambda}_m(\boldsymbol{r}) \cdot \bar{\boldsymbol{H}}^{\mathrm{inc}}(\boldsymbol{r})\,\mathrm{d}S. \tag{3.35}$$

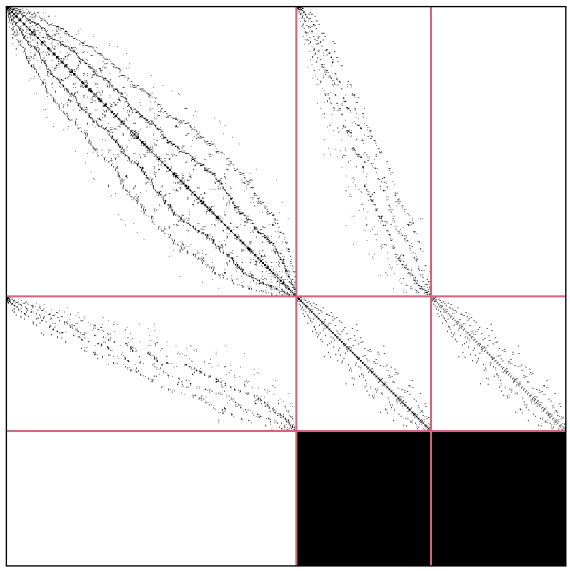

Figure 13: Illustration of the nonzero entries of the FE-BI system matrix. Purple lines are used to indicate the block structure.

These are used in the same system as (3.28).

3.3.4 Combined Linear System

When the FE and BI formulations are decided, their linear systems in (3.25) and (3.28) can be combined into the complete FE-BI system

$$\begin{bmatrix} \mathbf{K}^{\mathrm{II}} & \mathbf{K}^{\mathrm{IS}} & \mathbf{0} \\ \mathbf{K}^{\mathrm{SI}} & \mathbf{K}^{\mathrm{SS}} & \mathbf{B} \\ \mathbf{0} & \mathbf{P} & \mathbf{Q} \end{bmatrix} \begin{pmatrix} \boldsymbol{E}^{\mathrm{I}} \\ \boldsymbol{E}^{\mathrm{S}} \\ \bar{\boldsymbol{H}}^{\mathrm{S}} \end{pmatrix} = \begin{pmatrix} \boldsymbol{b}^{\mathrm{I}} \\ \boldsymbol{b}^{\mathrm{S}} \\ \boldsymbol{b}^{\mathrm{inc}} \end{pmatrix}. \tag{3.36}$$

For the FE2MS FE-BI code presented and used in papers I–III, only scattering problems are considered, which means that $\boldsymbol{b}^{\mathrm{I}}$ and $\boldsymbol{b}^{\mathrm{S}}$ become zero. The system is partly sparse, and partly dense due to the structure of the FE and BI blocks, respectively. This is illustrated in Figure 13 for a small layered dielectric sphere with 624 FE unknowns and 198 BI unknowns.

3.4 Solution Methods

All computational methods discussed in previous sections result in linear systems of equations that are to be solved. Often, such methods are classified as direct methods or iterative methods.

The oldest direct methods use a complete matrix with all entries, including zeros, directly available. Most Gaussian elimination methods and LU decomposi-

tion methods are included here. While this can be acceptable for dense matrices with few zero entries, such methods are unsuitable for sparse matrices where the majority of matrix entries are zeros. For sparse matrices, there are ways of storage that do not require all zeros to be explicitly stored, meaning large memory compression when implemented. For these types of matrices, there are other direct methods available, often through specific software packages like UMFPACK [36], SuperLU [83], MUMPS [5]. These are typically much more complex than the methods for full matrices though. Another type of direct method are fast direct methods like $\mathcal{H}$-matrix methods [17, 55]. These use underlying properties of the, typically dense, system matrix to rewrite it on a different form (the ACA method discussed in section 3.5.2 is often used as part of these methods to provide compression). This new form can then be used for a solution which can give a representation like the aforementioned LU decomposition. Similar to the methods for sparse matrices, the fast direct methods are more complex than the methods for full matrices.

Iterative methods work in very different ways compared to direct methods. While direct methods require matrices to have a certain structure, be it dense, sparse or $\mathcal{H}$-matrix, iterative methods require no knowledge of the matrix. They are instead based on matrix-vector products and can be used to solve any system for which such products can be performed. They are called iterative because they use a series of matrix-vector products with different vectors to find a solution for one right-hand side. This means that all of the matrix types described for direct methods can also be used for iterative methods without much work, as matrix-vector products are such essential building blocks for any implementation of linear algebra. It also means that combinations of different matrix types which do not easily work with direct solvers can use iterative methods. This includes the FE-BI system in (3.36) which typically is too sparse to be efficiently solved using methods for dense matrices, but too dense to be efficiently solved by methods for sparse matrices. One drawback of iterative methods compared to direct methods is that an iterative solution is only valid for one right-hand side. Direct methods like LU decomposition result in a matrix representation applicable to any right-hand side with low computational cost. In some cases, if solutions are similar, the performance of iterative methods for multiple right-hand sides can be improved by using the previous solution is as an initial guess. These considerations can be very important for electromagnetic problems with multiple excitations common in, for example, RCS computations.

One major consideration when working with iterative methods is that of convergence. The number of iterations required to solve a system can vary significantly, and depends strongly on the condition number of the matrix. Methods to reduce the condition number, or preconditioning, are highly useful to improve performance. Essentially, such methods aim to transform the system matrix to one with better convergence, and ensure that the result is still correct or can be made so with a simple transformation [121, 144]. In practice, preconditioning is typically not applied to the system matrix though, as that would be computationally expensive. Instead, the vectors in the matrix-vector products of the

iterative method are transformed by the preconditioning, achieving the same effect. Depending on which stage of the iteration the preconditioner is applied, different terms are used. In right preconditioning, the preconditioner is applied to the right of the system matrix, *i.e.*, on the vector going into the matrix-vector product. In left preconditioning, the preconditioner is instead applied to the left of the system matrix, *i.e.*, on the vector resulting from the matrix-vector product. It is also possible to combine the two [121]. There are many different preconditioning methods, some which are more general than others. Methods like Jacobian, successive over-relaxation and incomplete LU decomposition are examples of general-purpose preconditioning methods applicable to many different system matrices [121]. However, better performance is often possible if the preconditioning method is adapted to the system in question. As an example of specialized preconditioning, the FE-BI system in (3.36) based on the EFIE is considered. This system is typically very ill-conditioned and needs a good preconditioner for iterative methods to converge. The method used in the FE2MS FE-BI code described in Paper I (similar to that described in [49]) applies a sparsification procedure to the BI blocks in (3.36) to obtain a new matrix

$$\mathbf{M} = \begin{bmatrix} \mathbf{K}^{\mathrm{II}} & \mathbf{K}^{\mathrm{IS}} & \mathbf{0} \\ \mathbf{K}^{\mathrm{SI}} & \mathbf{K}^{\mathrm{SS}} & \mathbf{B} \\ \mathbf{0} & -2\mathrm{j}k_0\mathbf{P}' & -2\mathrm{j}k_0\mathbf{Q}' \end{bmatrix}. \tag{3.37}$$

The blocks $\mathbf{P}'$ and $\mathbf{Q}'$ are obtained by only considering interactions within single mesh elements, which together with the multiplication by $-\mathrm{j}k_0$ causes $\mathbf{M}$ to be both sparse and symmetric. The preconditioned vector is then obtained by solving the system

$$\mathbf{M}\boldsymbol{x} = \boldsymbol{y} \tag{3.38}$$

where $\boldsymbol{y}$ is the original vector and $\boldsymbol{x}$ the preconditioned vector. This system can be solved directly using efficient methods for sparse systems, or iteratively, though that typically requires another inner preconditioning step.

3.5 Acceleration and Compression Methods

There are many different ways to make computational codes faster, but certain methods exist that use mathematical properties of the underlying computational codes to dramatically improve performance. In this part the focus is going to be on a few methods applicable to the MoM and FE-BI computational methods, but there are many more methods that are not discussed here.

The main reason why MoM and FE-BI are discussed at the same time is that they both share the same bottleneck in performance, which is due to the use of integral equations. In the FE-BI system matrix (3.36), there are both sparse matrices coming from the FE part and dense matrices coming from the BI part. These matrix types have different complexities with regard to memory and computation times as shown in Table 1. The effect of these on the FE-BI

Table 1: Complexities for sparse and dense matrices with n unknowns. C is the number of iterations.

Resource	Sparse	Dense
Matrix storage	$O(n)$	$O(n^2)$
Matrix-vector product time	$O(n)$	$O(n^2)$
Iterative solution time	$O(Cn)$	$O(Cn^2)$

method is that the BI part dominates both in memory and time, even for small problem sizes. It is very beneficial if this complexity can be reduced.

One way of reducing the complexity is by obtaining a representation of the matrix which is significantly compressed as compared to the full matrix, and doing this in a way that is computationally efficient in its construction. Important mathematical operations like matrix-vector products also need to be possible to perform efficiently. Typically, the possibility to compress information indicates that the full representation contains redundant information [129], and this is also the case for the methods described here.

The first method described in section 3.5.1 compresses a matrix by exploiting translation invariance in the underlying operator. This means that the operator remains the same under specific translations in space, meaning that matrix entries are also unchanged for the same translations. Conceptually, it is easy to see that there is redundant information, and compression should be possible. The same properties allowing for compression as described here are also used in other methods like the conjugate gradient-FFT method [29, 104, 124] and the adaptive integral method [19]. The second method described in section 3.5.2 is the ACA which uses low-rank properties to compress a matrix, or sub-blocks of a matrix. The general property of a matrix having low rank means that it can be written using only a subset of its columns. That this allows for compression is also conceptually easy to understand. For both methods, however, the actual ways to obtain compressed representations efficiently and use them in mathematical operations take more work to understand. Of course, many other methods for compression and acceleration exist with one of the more important ones being the fast multipole method [33, 116, 117] in its multilevel implementation [135, 136]. While very important for MoM in general, it is not discussed in detail in this dissertation.

3.5.1 Acceleration of Translation Invariant Operators

This first type of acceleration is based on exploiting properties of the Green's function. Consider the free space Green's function as given by

$$G(\boldsymbol{r}, \boldsymbol{r}') = \frac{\mathrm{e}^{-\mathrm{j}k_0|\boldsymbol{r}-\boldsymbol{r}'|}}{4\pi|\boldsymbol{r}-\boldsymbol{r}'|}. \tag{3.39}$$

If the source and evaluation points $\boldsymbol{r}'$ and $\boldsymbol{r}$ are translated equally, there is no change in the function value, *i.e.*, $G(\boldsymbol{r}-\boldsymbol{r}_\mathrm{t}, \boldsymbol{r}'-\boldsymbol{r}_\mathrm{t}) = G(\boldsymbol{r}, \boldsymbol{r}')$. The Green's

function is translation invariant, which can be used to accelerate matrix-vector products for matrices based on it.

As a simple example, consider a regular rectangular grid with N_x nodes in x and N_y nodes in y such that the node coordinates are

$$\boldsymbol{r}_{m,n} = m\Delta x\hat{\boldsymbol{x}} + n\Delta y\hat{\boldsymbol{y}} \tag{3.40}$$

with grid spacing Δx and Δy. Let an identical grid, but translated in z by z_0, be defined with node coordinates

$$\boldsymbol{r}'_{m,n} = m\Delta x\hat{\boldsymbol{x}} + n\Delta y\hat{\boldsymbol{y}} + z_0\hat{\boldsymbol{z}}. \tag{3.41}$$

The Green's function for source points on one grid and observation points on the other is now expressed in a tensor form as

$$A^{m',n'}_{m\ ,n} = G(\boldsymbol{r}_{m,n}, \boldsymbol{r}'_{m',n'}) \tag{3.42}$$

and due to translation invariance in the Green's function, it holds that

$$A^{m'-m_0,n'-n_0}_{m\ -m_0,n\ -n_0} = A^{m',n'}_{m\ ,n} \tag{3.43}$$

if m_0 and n_0 are integers such that the resulting indices are not out of bounds for the grid in question. While the Green's function could have been written more traditionally as a two-dimensional matrix, the four-dimensional tensor form makes the translation invariance more explicit.

The way this translation invariance affects the tensor $A^{m',n'}_{m\ ,n}$ is similar to how a Toeplitz matrix behaves. Such a matrix with dimensions $N \times N$ is defined to have elements as [47]

$$\mathbf{T} = \begin{bmatrix} T_0 & T_{-1} & T_{-2} & \dots & T_{-(N-1)} \\ T_1 & T_0 & T_{-1} & \dots & T_{-(N-2)} \\ T_2 & T_1 & T_0 & \dots & T_{-(N-3)} \\ \vdots & \vdots & \vdots & \ddots & \vdots \\ T_{N-1} & T_{N-2} & T_{N-3} & \dots & T_0 \end{bmatrix}. \tag{3.44}$$

This type of matrix can be rewritten as a circulant matrix by embedding it in a $2N \times 2N$ matrix as

$$\widetilde{\mathbf{T}} = \left[\begin{array}{cccc|cccc} T_0 & T_{-1} & \dots & T_{-(N-1)} & 0 & T_{N-1} & \dots & T_1 \\ T_1 & T_0 & \dots & T_{-(N-2)} & T_{-(N-1)} & 0 & \dots & T_2 \\ \vdots & \vdots & \ddots & \vdots & \vdots & \vdots & \ddots & \vdots \\ T_{N-1} & T_{N-2} & \dots & T_0 & T_{-1} & T_{-2} & \dots & 0 \\ \hline 0 & T_{N-1} & \dots & T_1 & T_0 & T_{-1} & \dots & T_{-(N-1)} \\ T_{-(N-1)} & 0 & \dots & T_2 & T_1 & T_0 & \dots & T_{-(N-2)} \\ \vdots & \vdots & \ddots & \vdots & \vdots & \vdots & \ddots & \vdots \\ T_{-1} & T_{-2} & \dots & 0 & T_{N-1} & T_{N-2} & \dots & T_0 \end{array}\right] \tag{3.45}$$

where the top left block is the same as $\mathbf{T}$ and the others contain the same entries. Looking at the columns of $\widetilde{\mathbf{T}}$, it is seen that each column is the same as the previous, but shifted one entry down. This means that $\widetilde{\mathbf{T}}$ is circulant, and such a matrix is diagonalized by the discrete Fourier transform (DFT) [47]. This is important as it enables fast matrix-vector products and linear system solution using the fast Fourier transform (FFT). If $\mathbf{F}_n$ is the matrix corresponding to the DFT of dimension n, the diagonalization of $\widetilde{\mathbf{T}}$ can be written as [47, 113]

$$\widetilde{\mathbf{T}} = \mathbf{F}_n^{-1}\mathrm{diag}(\mathbf{F}_n\boldsymbol{t})\mathbf{F}_n \tag{3.46}$$

where $\boldsymbol{t}$ is the first column of $\widetilde{\mathbf{T}}$. A matrix-vector product involving $\widetilde{\mathbf{T}}$ can thus be computed as

$$\widetilde{\mathbf{T}}\boldsymbol{v} = \mathbf{F}_n^{-1}\mathrm{diag}(\mathbf{F}_n\boldsymbol{t})\mathbf{F}_n\boldsymbol{v} = \mathbf{F}_n^{-1}\left(\mathbf{F}_n\boldsymbol{t} \circ \mathbf{F}_n\boldsymbol{v}\right) \tag{3.47}$$

where $\circ$ indicates a Hadamard (elementwise) product. Operations involving $\mathbf{F}_n$ and $\mathbf{F}_n^{-1}$ are computed fast using the FFT. Since $\widetilde{\mathbf{T}}$ contains the original matrix $\mathbf{T}$ in the first N rows and columns, a matrix-vector product $\mathbf{T}\boldsymbol{w}$ is easily obtainable by appending N zeros to $\boldsymbol{w}$, applying (3.47), and extracting the first N entries of the result. Due to the performance of the FFT and the fact that only a vector with $2N$ entries is used, this can dramatically improve performance.

Going back to the original problem with the tensor $A_{m,n}^{m',n'}$, the Topelitz and circulant structures become significantly harder to write out explicitly, but similar acceleration as for matrices is possible for tensors of arbitrary order [113]. In the four-dimensional tensor case of interest here, the acceleration analogous to (3.47) changes from using a one-dimensional DFT operating on vectors to a two-dimensional DFT operating on matrices. Although the generalization is more complicated to write out explicitly and implement in a code, the underlying theory is the same as for the circulant matrices. A different situation arises if the two grids in the Green's function example are changed to only be equal in one instead of two dimensions. That could be due to a curvature preventing translation invariance in one of the two grid dimensions. In this case, translation invariance still exists in one dimension, and with an appropriate formulation of the four-dimensional tensor a circulant structure can be obtained such that a one-dimensional DFT can be used in acceleration of matrix-vector products. Of course, this is not as computationally efficient as the previous case as entries in the other dimension need to be computed fully, but it still provides acceleration.

While there are many methods using translation invariance as described here to solve MoM problems, in particular for volumetric MoM [30, 43, 169], in this dissertation it is only used for computing electric fields due to electric currents in disjoint regions. This is similar to approaches which have been used in digital holography where the typical operators act on disjoint source and observation planes [37, 52]. This implementation is simpler than would be necessary in the full solution of a problem, but still adds additional complexity compared to the Green's function example. The Green's function example is in turn more complex than the pure Toeplitz matrix for which the DFT-based acceleration was shown.

The operator needed for computing the forward problem of electric fields due to electric current is the integral operator in (2.79) with $\boldsymbol{M} = \mathbf{0}$. While the operator is still translation invariant, it is more complex than the pure Green's function as it contains more different terms and is vector-valued in input and output. Furthermore, the currents $\boldsymbol{J}$ must be represented in an appropriate way which offers the same kind of translation invariance as between points in meshed as described in the Green's function case. This could, for example, be done by using rooftop basis functions defined for each edge in the source grid. If the source and observation grids are equal in x and y, the basis functions are not aligned with the observation points and they differ in number. The algorithm is still useful, but the enumeration of source and observation quantities can become quite cumbersome in implementations. As for Green's functions, it is also possible to use translation invariance in only one direction when using the operator in (2.79). This was done in Paper IV where such an operator was used in an imaging algorithm with sources on a singly curved surface and observations in a planar grid. That work was based on similar imaging techniques for planar surfaces with full translation invariance in [60, 61].

3.5.2 The Adaptive Cross Approximation

The adaptive cross approximation (ACA) is a method for compression of matrices based on low-rank approximations. For any matrix $\mathbf{A} \in \mathbb{C}^{m\times n}$, the rank r is given by its number of linearly independent columns. If $r < m, n$ the matrix can be written on the outer product form as

$$\mathbf{A} = \mathbf{U}\mathbf{V}^{\mathrm{H}},\ \mathbf{U} \in \mathbb{C}^{m\times r},\ \mathbf{V} \in \mathbb{C}^{n\times r}. \tag{3.48}$$

It is clear that in cases where $r \ll m, n$ this form provides a more efficient way to store $\mathbf{A}$. One way to achieve this form is by using the singular value decomposition (SVD) which reads

$$\mathbf{A} = \mathbf{U}\boldsymbol{\Sigma}\mathbf{V}^{\mathrm{H}},\ \mathbf{U} \in \mathbb{C}^{m\times m},\ \mathbf{V} \in \mathbb{C}^{n\times n},\ \boldsymbol{\Sigma} \in \mathbb{C}^{m\times n} \tag{3.49}$$

and where $\boldsymbol{\Sigma}$ only has nonzero entries $\sigma_1, \ldots, \sigma_r$ on the diagonal. Any diagonal entries above r in $\boldsymbol{\Sigma}$ are zero, which directly means that the decomposition can be rewritten on the form in (3.48). However, the algorithm to compute the SVD has a memory complexity $O(n^2)$, and a computational complexity $O(n^3)$ if $m \sim n$ [144]. This offers no improvement over a direct method, so other algorithms are needed. One such algorithm is the ACA.

At its core, the ACA is an algorithm which constructs an approximate representation $\mathbf{U}\mathbf{V}^{\mathrm{H}}$ for $\mathbf{A}$ by using only a subset of its rows and columns [16, 17, 167]. Since not all of $\mathbf{A}$ is used by the algorithm, the necessary parts can be constructed as needed to greatly reduce the memory use compared to full storage of $\mathbf{A}$. An explicit description of the ACA algorithm for MoM computations can be found in [167], and readers are referred to this for details. Here, a brief overview of the algorithm, broadly based on [167], is provided. The starting point of the ACA

is before the matrix $\mathbf{A}$ is constructed. In the first step, a row is selected to be constructed, typically taken to be the first row of $\mathbf{A}$. This, normalized by its largest entry in absolute value, is saved as the first row of $\mathbf{V}^{\mathrm{H}}$. Next, a column is selected to be constructed, which is the column in $\mathbf{A}$ containing the largest entry in absolute value of the first row. This column is saved as the first column of $\mathbf{U}$. Following these two first selections, subsequent rows of $\mathbf{V}^{\mathrm{H}}$ and columns of $\mathbf{U}$ are constructed by a similar selection process, but with the entries already present subtracted. If this was the full algorithm, rows and columns would continue to be constructed until obtaining all entries, resulting in no compression. To avoid this, an estimate of the error $\left\|\mathbf{A}-\mathbf{U}\mathbf{V}^{\mathrm{H}}\right\|$ (in Frobenius norm) is computed at each iteration of the algorithm, and the iteration can be stopped when a desired error is reached. Crucially, this estimate is computed using only the information already used for the construction of $\mathbf{U}$ and $\mathbf{V}^{\mathrm{H}}$.

While the application of the ACA when constructing a matrix $\mathbf{A}$ results in a representation on outer product form, it is not optimal in the way that the SVD is, that is having $\mathbf{U}$ and $\mathbf{V}$ unitary and of minimal inner dimension. This can be remedied by using the QR decomposition and the SVD to recompress the representation from the ACA as follows [15]. The QR decompositions are written as

$$\mathbf{U}=\mathbf{Q}_{\mathrm{U}}\mathbf{R}_{\mathrm{U}},\ \mathbf{U}\in\mathbb{C}^{m\times k},\ \mathbf{Q}_{\mathrm{U}}\in\mathbb{C}^{m\times k},\ \mathbf{R}_{\mathrm{U}}\in\mathbb{C}^{k\times k} \tag{3.50}$$

$$\mathbf{V}=\mathbf{Q}_{\mathrm{V}}\mathbf{R}_{\mathrm{V}},\ \mathbf{V}\in\mathbb{C}^{n\times k},\ \mathbf{Q}_{\mathrm{V}}\in\mathbb{C}^{n\times k},\ \mathbf{R}_{\mathrm{V}}\in\mathbb{C}^{k\times k} \tag{3.51}$$

where the $\mathbf{Q}$ matrices are unitary and $\mathbf{R}$ matrices are upper triangular. The outer product form can be represented as

$$\mathbf{U}\mathbf{V}^{\mathrm{H}}=\mathbf{Q}_{\mathrm{U}}\mathbf{R}_{\mathrm{U}}\mathbf{R}_{\mathrm{V}}^{\mathrm{H}}\mathbf{Q}_{\mathrm{V}}^{\mathrm{H}}. \tag{3.52}$$

Now, the SVD can be computed for the product of the $\mathbf{R}$ matrices, which is only $k\times k$, as

$$\mathbf{R}_{\mathrm{U}}\mathbf{R}_{\mathrm{V}}^{\mathrm{H}}=\hat{\mathbf{U}}\hat{\mathbf{\Sigma}}\hat{\mathbf{V}}^{\mathrm{H}} \tag{3.53}$$

and a new outer product form is finally obtained as

$$\mathbf{U}\mathbf{V}^{\mathrm{H}}=\left(\mathbf{Q}_{\mathrm{U}}\hat{\mathbf{U}}\hat{\mathbf{\Sigma}}\right)\left(\mathbf{Q}_{\mathrm{V}}\hat{\mathbf{V}}\right)^{\mathrm{H}} \tag{3.54}$$

where both matrices are unitary and of minimal inner dimension. If $k\ll m,n$, both the QR and SVD are computed for matrices with significantly smaller dimensions than $\mathbf{A}$ and the recompression can therefore be applied without changing the complexity of the ACA algorithm [15].

An important question when it comes to the applicability of the ACA is if low rank matrices actually arise in the applications of interest. There are cases in CEM where this can happen naturally. One example is in MoM computations of large array antennas where the system matrix can be subdivided into blocks corresponding to self-interaction and coupling between array elements. In this

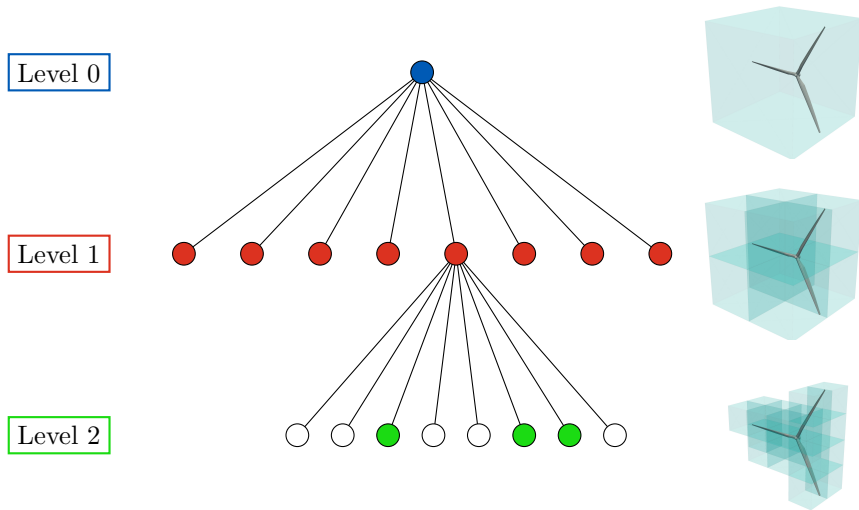

Figure 14: An octree shown as a tree data structure and geometrically at the three first levels. Note that there are several groups that are empty at level 2.

case, blocks which do not correspond to self-interaction are expected to have lower rank and can readily be compressed using the ACA [62, 63].

While the easily separable geometry in antenna arrays makes for simple ACA use, the same does not hold for general geometries. In a general mesh, it can typically not be assumed that the matrix is easily decomposed into clear blocks like array elements, but this can be achieved using an intermediate step. This step is a geometric clustering of the unknowns in the problem such that groups of unknowns are formed, which can be used similar to blocks in the array case. Typically, this is done by generating an octree, which is a hierarchical data structure originally developed for computer graphics [91]. It provides geometric clustering by creating a cubic bounding box around the geometry in question and splitting it into eight cubes. These smaller cubes are considered children to the original bounding box, and this is the start of a tree data structure of cubic groups of decreasing size as the tree deepens. The octree is refined by performing the same split into eights for each child until a stopping criterion, which could be a certain tree depth or a certain number of unknowns in a leaf node group, for example. An example of this clustering is shown in Figure 14 both as a tree and the corresponding geometrical groups.

The ACA can be applied to unknowns using the leaf groups of the octree in a similar way to that described for the array case. Typically this means that the ACA is applied to interactions between non-neighboring leaf groups. However, more improvements can be done by introducing a multilevel algorithm instead. This is similar to how the multilevel fast multipole method works, but simpler

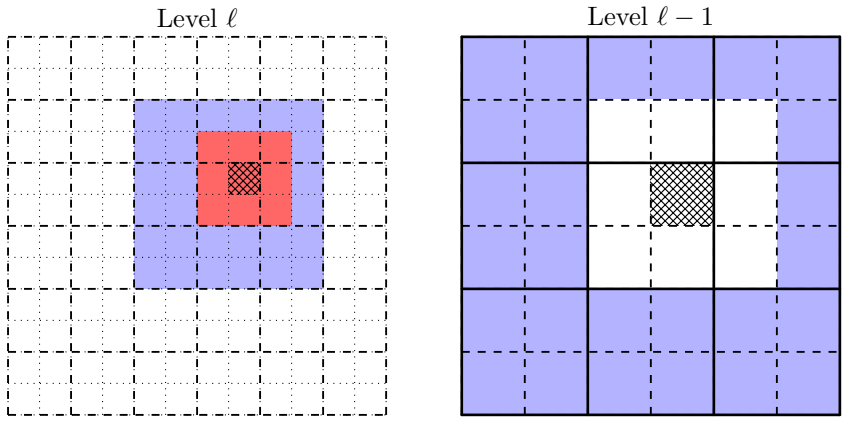

Figure 15: Near groups for full computations (red) and far interacting groups for ACA computations (blue) at two levels. The group marked with a crosshatch pattern is the source group. Boundary lines between groups are dotted for level ℓ, dashed for level $\ell - 1$ and solid for level $\ell - 2$.

to implement, which builds upon a more general concept for hierarchical computations [14, 65]. Multilevel ACA computations using an octree begin at the leaf level (level ℓ), where near interactions for sources in each group are considered first. Interactions between unknowns within the source group or this and neighboring groups are computed without the ACA as these unknowns are too close for reasonable compression. Since these interactions are few compared to the total number of system matrix entries, their entries are stored in a sparse matrix. Groups at level ℓ which are not neighbors with the source group, but whose parent groups at level $\ell-1$ are neighbors to the parent of the source group, are called "far interacting". Interactions between unknowns in these groups are computed using the ACA. After this is done for all groups at level ℓ, level $\ell - 1$ is considered. The far interacting groups at this level are identified for all groups at level $\ell - 1$, and interactions between them are computed using the ACA. In Figure 15, these group types are shown for a two-dimensional (quadtree) representation. It can be seen that the far interacting groups for the crosshatch patterned source group at level $\ell - 1$ are disjunct to those at level ℓ. As such, there is no duplication of interactions at different levels. As we travel toward the root of the octree, the group size increases as well as the separation between groups. The idea is that a larger separation results in a lower rank for a given group size, and as such the groups can contain more unknowns at higher levels.

While the ACA can be used for compression in many cases, it is optimal for use with integral operators whose kernels are smooth [17]. Unfortunately, this does not include the operators used in MoM for electrically large problems, like the scattering problems of interest to this dissertation. However, while the ACA should then be better for electrically small electromagnetic problems, the performance degradation with increasing electrical size is graceful and the ACA

can still be used with success for many problems where the kernel is not smooth, like said scattering problems [17, 71]. Typically though, it scales worse than the multilevel fast multipole method for an increasing electrical size [71]. Other methods similar to the ACA, but with better performance for kernels which are not smooth, have been developed like the butterfly decomposition [51, 93]. Nevertheless, there are certain geometries where low-rank approximations like the ACA perform particularly well like elongated and quasi-planar structures [51]. In this dissertation, the ACA was used to compress BI blocks for the FE2MS FE-BI code introduced in Paper I. One detail which can be noted is that this code is implemented using lowest order basis functions for both FE and BI parts. For the FE part in particular, the mesh tetrahedrons for these basis functions may need to be small in order to obtain sufficient accuracy, particularly if their face triangles are compared to typical sizes of BI mesh triangles. Furthermore, mesh sizes in the FE part are further reduced by scaling by the refractive index of the medium. Taken together, the BI mesh can often contain smaller mesh elements than typical sizes. These situations are well-adapted to the ACA though, as the high mesh density means that far interacting groups for lower levels in the octree are within electrically small regions where the kernel of the integral operator is comparatively smooth.

3.6 Implementing Computational Methods

While some methods for accelerating computational methods were described in section 3.5, details in how computational methods are implemented can also have dramatic consequences on performance. These are very general concepts like performance of different programming languages, optimization of code, general code architecture and the type of hardware that is used in computations.

One way to divide types of programming languages is in interpreted languages and compiled languages. In interpreted languages, each command in a program is executed directly on the machine, while in compiled languages the full program needs to be compiled into machine code that can in turn be executed on the machine. Interpreted languages are typically more flexible to use than compiled languages since commands can be executed one by one, and intermediate results are available at any point. However, compiled languages are typically much more efficient. Some examples of programming languages often used in scientific computations are the compiled languages C++ and Fortran, and the interpreted languages Python and MATLAB [18, 99]. More recently, another option called just-in-time (JIT) compilation has become more available. Languages with this feature can compile parts of a program when they are first executed, while possibly keeping features from interpreted languages for other parts. An example of a language used in scientific computations with native JIT compilation is Julia [18], but JIT compilation is also available for Python [81] and MATLAB [142].

A great aid when implementing computational methods from scratch is the availability of open-source software to use as a base. At some level, there is

always a base library of tools, regardless of what programming language is used. However, software packages with significantly higher levels of functionality may be available under open-source licenses, and what might be available depends on the programming language. One language with a large number of easily accessed open-source software packages is Python. There are many reasons for this, including, of course, Python's wide popularity and ease of use, but an important factor for the specific application of scientific computing is the common framework of efficient data structures, linear algebra functions and other utility given by the NumPy package [59].

The FE2MS FE-BI code described in Paper I is written mostly in Python, and combines many different open-source software packages for its functionality. The most important packages and some of the reasons for using them are described here, but a more in-depth discussion is available in Paper I. Before discussing packages used for computations, it is important to consider the geometry and mesh used for the code. Meshes used in the code are on the format produced by the Gmsh package [45], and since this package has a Python application programming interface (API) it is possible to handle meshing in the same Python scripts as the computations. As for the computational code itself, the FE and BI parts are considered somewhat separately, which makes sense when looking at the theory of the FE-BI method in section 3.3. The FE part is implemented using the FEniCSx package, which is a very versatile package for FEM which can handle general weak forms, many different mesh elements and basis functions, among others. FEniCSx consists of the components DOLFINx [13], FFCx [84], Basix [126,127] and UFL [3]. In addition to providing a complete implementation of the FE part, FEniCSx gives access to much of the infrastructure needed to implement the BI part. This includes data structures for mesh, basis functions and numerical quadrature. Furthermore, the connection between the two parts is facilitated by the use of FEniCSx data structures for both. Much of the BI part itself is written specifically for the FE2MS code with the lower-level computational framework from NumPy. Furthermore, JIT compilation using Numba [81] is used to dramatically improve performance of parts where standard Python performance is poor, like in assembly of system matrices. An often challenging part of integral equation methods is that of singularity handling. As described in section 3.2, singular integrals arise from typical Galerkin testing of the EFIE and MFIE, and they need to be handled appropriately. In the FE2MS code this is done using the DEMCEM package which offers efficient methods for solving singular integrals due to these equations for a triangular mesh [105–107, 109]. Since DEMCEM is implemented in C++, its use in a Python code required some additional work using the pybind11 package [69] for connecting code from the two different programming languages. To improve performance of the BI part of the FE2MS code, a multilevel ACA is used for compression of the BI blocks of the system matrix. The octrees used for geometric clustering of unknowns in this algorithm are created using the AdaptOctree package [73]. This combination of open-source software packages facilitated the development process and greatly accelerated it, especially since the development was from

scratch without an existing in-house codebase.

When working with open source, it is useful to understand some of the legal framework and licenses that are commonly used. This is especially true if publishing software based on many open-source packages which might use different licenses. Broadly, there are two types of licenses under the broader term open source: permissible licenses and copyleft licenses. Permissive licenses are, as indicated by the name, very permissive and put almost no restrictions on how the user might apply the software. A common example is the Berkeley Software Distribution (BSD) 3-clause license [100] which is, for example, used in NumPy and SciPy. Copyleft licenses, on the other hand, are more restrictive, mostly regarding distribution of derivative software. One of the most common such licenses is the general purpose license (GPL) which essentially states that software which uses GPL-licensed software can only be distributed if it is so under the same license [138]. The underlying reason is quite ideological in that it aims for open-source software to not be used in closed-source software at a later stage [138]. This license mechanism is a reason why the FE2MS FE-BI code described in Paper I is released under the GPLv3 license as opposed to, for example, BSD 3-clause.

4 Imaging Methods and Nondestructive Testing

Microwave imaging has been used in many different applications such as remote sensing, security scanners and NDT [2, 98]. Microwaves are defined as the frequencies 300 MHz–300 GHz, with a narrower region of mm-waves taken as the upper range starting at 30 GHz (corresponding to a wavelength of 1 mm). Microwave imaging has long been been performed for long-range applications such as remote sensing and radar imaging from satellites and aircraft [114, 115], but shorter-range systems have been feasible more recently [98]. These systems are lower in cost due to significant developments in hardware, and progress in signal processing means that there are more possibilities for what can be deduced from the data [2]. The decrease in cost and increase in capabilities has opened up for many new applications of microwave and mm-wave imaging [98].

In this dissertation, mm-wave imaging has been applied to NDT. NDT as a general field of study covers a vast amount of applications and physical phenomena, and as such it is difficult to give an all-encompassing introduction. The general idea behind any NDT, however, is to use some kind of physical phenomenon to learn about the properties of a device under test (DUT) without damaging its usefulness. The phenomenon used in testing should give some indication which can be connected to flaws in the DUT [131]. Depending on the property of the DUT which is to be investigated, different physical phenomena might be more or less useful. For example, mechanical properties are often evaluated using ultrasonic NDT methods since ultrasound is an acoustic wave whose propagation

properties are determined by mechanical properties of the medium [125]. A flaw, however, can have effects on many different properties. For example, hard metallic inclusions in a soft foam would result in high contrasts both for ultrasound and mm-waves.

The use of microwaves and mm-waves in NDT is relatively new compared to ultrasound, but has advantageous properties when testing many newer types of materials [74, 168]. It can be particularly interesting for applications where electromagnetic performance is one of the properties to be evaluated, in addition to mechanical flaws. One such application is radomes, where the full structure has been carefully designed for high transmission in the band of an enclosed antenna [103]. Another example may be aerospace structural elements, which can be designed for low radar cross section in some defense applications. In Paper IV, mm-wave imaging is applied to NDT of thin, low-permittivity, singly curved composite panels used in aerospace applications.

4.1 Fourier-Based Imaging

Many of the most widely used methods in microwave and mm-wave imaging are based on Fourier analysis [98]. Since Fourier analysis covers a wide range of methods focused on trigonometric functions, like time-harmonic electromagnetic waves, it is hardly surprising. The work presented in this dissertation, however, rather focuses on imaging methods based on inverse scattering as will be described in section 4.2. Nevertheless, Fourier-based imaging is always going to present itself as a natural comparison due to its prevalence. In this section, one such method is introduced as it is used as a method for comparison to the inverse scattering method in Paper IV.

The method in question is referred to as time reversal in Paper IV, but is also known as convolution-based reconstruction and migration, among others [98,139]. The main idea of the method is related to the propagation of plane waves on the form given earlier in (2.24). The measurable signal of a single plane wave propagating in z can be described as

$$s(z) = S\mathrm{e}^{-\mathrm{j}k_z z} \tag{4.1}$$

where the complex amplitude S is typically not known. This means that if the signal is measured at a z-coordinate z_0, the signal at another z-coordinate $z_1 < z_0$ can be determined as

$$s(z_1) = S\mathrm{e}^{-\mathrm{j}k_z z_1} = S\mathrm{e}^{-\mathrm{j}k_z z_0}\mathrm{e}^{\mathrm{j}k_z(z_0-z_1)} = s(z_0)\mathrm{e}^{\mathrm{j}k_z(z_0-z_1)}. \tag{4.2}$$

This is not very useful on its own as the signal measured in imaging applications is not a plane wave, but if it is combined with the concept of plane wave expansions the imaging method becomes clear. Plane waves can be used as a basis to describe any type of wave. As such, a signal s can be described as [101]

$$s(x,y,z) = \frac{1}{(2\pi)^2}\int_{-\infty}^{\infty}\int_{-\infty}^{\infty} S(k_x,k_y)\mathrm{e}^{-\mathrm{j}(k_x x+k_y y)}\mathrm{e}^{-\mathrm{j}k_z z}\,\mathrm{d}k_x\,\mathrm{d}k_y \tag{4.3}$$

where S is the signal representation in a plane-wave basis or, as commonly expressed, in the spectral domain, and the wave number in z depends on the other wave numbers as $k_z = \sqrt{k^2 - k_x^2 - k_y^2}$. Equation (4.3) is identified as a two-dimensional Fourier transform in x and y, and the representation in the spectral domain for a single pair of k_x, k_y can be treated as a single plane wave propagating in z. This means that the same approach for changing to z-coordinate that was described for a single plane wave can be applied to each spectral-domain signal component as

$$S(k_x, k_y, z_1) = S(k_x, k_y)\mathrm{e}^{-\mathrm{j}k_z z_1} = S(k_x, k_y, z_0)\mathrm{e}^{\mathrm{j}k_z(z_0 - z_1)}. \tag{4.4}$$

A measured signal $s(x, y, z_0)$ can thus be time reversed to $s(x, y, z_1)$ by a sequence of Fourier transformation, multiplication of each component by $\exp(\mathrm{j}k_z(z_0 - z_1))$ for its computed k_z and inverse Fourier transformation of the result. This enables imaging if the coordinate z_1 is selected at appropriate values. Importantly though, the model used for the signal contains no sources, and as such it is not possible to propagate the signal beyond a region containing sources (such as a transmitting antenna).

In practice, the signal measured at z_0 is only sampled at a discrete set of points (x_m, y_n, z_0), $m = 0, 1, \ldots, N_x - 1$, $n = 0, 1, \ldots, N_y - 1$. If this is done in a uniform grid, the Fourier transforms can be replaced by standard discrete Fourier transforms (DFT) efficiently computed by fast Fourier transform (FFT) algorithms. An imaging algorithm can now be written down as:

1. Obtain measured signal as a matrix with entries $s_{mn} = s(x_m, y_n, z_0)$.
2. Compute matrix in spectral domain with entries $S_{mn} = S(k_{x,m}, k_{y,n}, z_0)$ as $\mathbf{S} = \mathrm{fft2}\,(\mathbf{s})$.
3. Generate wave number matrix with entries $k_{z,mn} = \sqrt{k^2 - k_{x,m}^2 - k_{y,n}^2}$.
4. Compute image in spectral domain as $\mathbf{S^i} = \mathbf{S} \circ \mathrm{e}^{\mathbf{jk_z}(z_0 - z_1)}$ ($\circ$ denotes element-wise product, exponential taken element-wise).
5. Compute image as $\mathbf{s^i} = \mathrm{ifft2}\left(\mathbf{S^i}\right)$

where fft2 and ifft2 are used to denote the two-dimensional FFT and inverse FFT, respectively.

The time reversal algorithm as described here generates images in planes parallel to a measurement plane, but it is easy to extend to images on other surfaces. By generating images for a set of z-coordinates increasingly far from z_0, volumetric data is obtained. From such data, an image can be generated on an arbitrary surface within the data volume. This is done in Paper IV where images are generated on the surface of singly curved composite panels.

4.2 Inverse Scattering

The second type of imaging methods are based on inverse scattering. The problem of electromagnetic scattering was introduced in section 2.4 as a problem where a known object is illuminated by a known incident wave and the scattered wave should be computed. Inverse scattering is, as might be deduced from the name, an inverse of that problem. The type of inverse problem relevant here is that an unknown object is illuminated by a known incident wave and the scattered wave is measured. From the knowledge of the incident and scattered waves, the properties of the unknown object should be determined. Inverse problems like this are generally significantly more challenging than the direct scattering problem as they are ill-posed [56]. An example of why this is can be seen if the inverse problem would be to determine equivalent currents on a known object using measurements of the scattered electric field. This can be modeled using (2.79) and a discretization procedure similar to that used for MoM as described in section 3.2. However, the resulting matrix is ill-conditioned, meaning that small measurement errors lead to large errors in the reconstructed currents, and this is a typical issue in all inverse problems [56, 151]. It is necessary to use additional methods to remove this problem, called regularization methods. These enforce that the solution to the inverse problem fulfill certain properties like smoothness, often by solving some kind of optimization problem [56].

In Paper IV, an inverse equivalent source formulation is used for mm-wave imaging. This is a method based on the concept of equivalent currents in section 2.6. From a set of electric and magnetic currents, as in the case of equivalent currents, the electric field can be computed using (2.79). The inverse problem is thus a computation of the currents using a measured electric field, as in the example from the previous paragraph. Earlier work in [60] and [61] performed imaging on planar composite panels. With regards to the use of equivalent currents, purely electric currents were used with a theoretical basis that such equivalent currents on an infinite plane are easily relatable to the tangential fields, as described in section 2.6. Of course, the infinite plane was truncated to only be large enough to contain all significant sources, since this surface would correspond to unknowns in the integral operator. In paper IV though, the planar composite panels were exchanged for singly curved ones. This change brought with it a number of theoretical issues. To use the equivalence theorem on a surface, it needs to be a closed surface. In the planar case, this is simply an infinite plane, but it is not as straight-forward in the singly curved case. In addition, the move away from a planar surface meant that the simple connection between equivalent currents and tangential fields would not be the same as before.

For the problem with closing the surface, it can be noted that the original planar imaging did not use a fully closed surface either but instead relied on using a sufficiently large open reconstruction surface. This is illustrated in Figure 16 where the equivalent currents for a radiating horn antenna are shown on a planar surface. It is seen that only a subset of the full (infinite) planar surface contains significant currents, and as such it is sufficient to reconstruct the currents there.

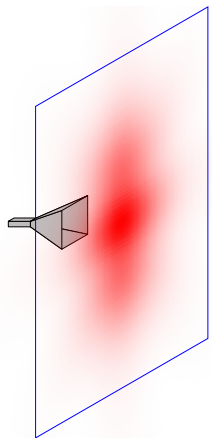

Figure 16: Horn antenna and $|\boldsymbol{M}_{\mathrm{s}}^{\mathrm{eq}}|$ on a planar surface in red. Reconstruction surface in blue covers a small region containing significant equivalent currents.

Of course, what is meant by "significant" depends on the application and how accurate the representation needs to be. The hypothesis for the singly curved surface was that the same approach could be used, even though the exact shape of the closed surface was unknown.

For the problem with the relation between equivalent currents and fields, a few solutions were already discussed in section 2.6. Of course, the use of both electric and magnetic currents with a standard zero field condition would give the usual relations in (2.74) and (2.75). This would, however, increase the number of unknowns by a factor 2, which was not desirable. Another solution would be to fill the interior with PMC/PEC and only have one type of current, but this would require custom Green's functions as opposed to the free space Green's function used previously. Finally, it is possible to simply use purely electric equivalent currents, but then the simple connection between equivalent currents and fields would be lost. However, the idea was that it would not be a critical issue for the application at hand.

One important consideration behind the choices in adapting the method for singly curved surfaces was that the intended use was primarily qualitative. In applications such as near-field-to-far-field transformations for antenna diagnostics, it is critical that equivalent currents are reconstructed correctly for the far-field computation to be correct. Our application, on the other hand, was in imaging directly on the DUT, which meant that the equivalent currents could not be used in any subsequent computation step. Furthermore, the application for the imaging was qualitative in that the goal of the NDT application is to determine whether flaws are present in a DUT or not. Reconstruction errors which might be critical in applications like antenna diagnostics can be irrelevant in such applications. However, it was necessary to test whether that actually was the case, which was one of the main points of Paper IV.

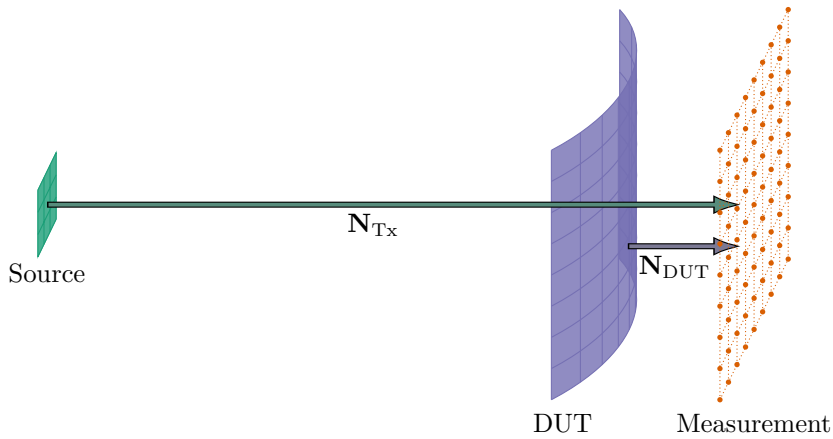

Figure 17: Geometry in transmission-based imaging. Operators $\mathbf{N}_{\mathrm{Tx}}$ and $\mathbf{N}_{\mathrm{DUT}}$ connect electric currents to electric fields.

The imaging geometry used in Paper IV is shown in Figure 17 together with operators which connect electric currents in one plane to electric fields in another. In the figure, the source and DUT surfaces are surfaces where electric currents can exist. In implementation, these are discretized as rectangular surface meshes where currents are represented using rooftop basis functions. The measurement surface does not contain any currents, but is discretized into a rectangular mesh matching the density of the DUT mesh. Electric fields due to currents on the source and DUT surfaces are computed in the node points of this measurement mesh.

4.2.1 Source Separation

To perform inverse scattering, the scattered wave is required. To obtain this, the typical procedure is to perform two measurements: one reference measurement without the DUT and one measurement with the DUT. The reference measurement is then subtracted, giving results for only the wave scattered by the DUT. However, this can be time-consuming if the measurement system is based on mechanical scanning, and it is also sensitive to changes between the measurements. Particularly in the case for mm-waves, mechanically small changes can still be significant electromagnetically due to the small wavelength. Another issue with the traditional method for the NDT application is that the scattered wave is due to the entire DUT and not just flaws.

To remove the need for two measurements, the incident electric field can be removed numerically. In Paper IV, this is done using a truncated SVD according to a method introduced in the earlier work from [60]. The method attempts to find equivalent currents for the smooth part of the measured electric field using only a single measurement of the DUT. As it is the smooth part of the electric

field that is found, it includes any such contributions from the DUT which are likely to be due to the larger structure of the DUT and not due to flaws.

The source separation algorithm attempts to perform a decomposition of the measured field $\boldsymbol{E}^{\text{meas}}$ as

$$\boldsymbol{E}^{\text{meas}} = \boldsymbol{E}^{\text{inc}} + \boldsymbol{E}^{\text{sc}} \tag{4.5}$$

where $\boldsymbol{E}^{\text{inc}}$ is the incident field from the source and the homogeneous part of the DUT and $\boldsymbol{E}^{\text{sc}}$ is the field scattered by flaws in the DUT, which is assumed to be orders of magnitude smaller than $\boldsymbol{E}^{\text{inc}}$. A plane is constructed in front of the source antenna for equivalent currents to be placed. The incident electric field is related to electric currents $\boldsymbol{J}^{\text{Tx}}$ in this source plane using a linear operator $\mathbf{N}_{\text{Tx}}$ based on (2.79) as

$$\boldsymbol{E}^{\text{inc}} = \mathbf{N}_{\text{Tx}} \boldsymbol{J}^{\text{Tx}}. \tag{4.6}$$

Insertion of this in (4.5) gives a system

$$\boldsymbol{E}^{\text{meas}} = \mathbf{N}_{\text{Tx}} \boldsymbol{J}^{\text{Tx}} + \boldsymbol{E}^{\text{sc}}. \tag{4.7}$$

Since the left-hand side is known and $\boldsymbol{E}^{\text{sc}}$ is considered to be small, it is possible to estimate $\boldsymbol{J}^{\text{Tx}}$ by considering a solution by truncated SVD regularization [56]. For this, the operator is expressed as the SVD

$$\mathbf{N}_{\text{Tx}} = \mathbf{U}\boldsymbol{\Sigma}\mathbf{V}^{\text{H}} \tag{4.8}$$

where $\mathbf{U}$ and $\mathbf{V}$ are unitary and $\boldsymbol{\Sigma}$ is diagonal with the reciprocal of singular values on the diagonal. The regularization is now performed by truncating the matrix $\boldsymbol{\Sigma}$. The elements corresponding to normalized singular values smaller than a threshold τ are set to zero. This threshold is traditionally set according to the L-curve criterion [56], but as discussed in [61] there are difficulties with this approach. Instead, the approach for selecting τ here combines analysis of the drop-off of the normalized singular values with inspection of the resulting solution $\widehat{\boldsymbol{J}}^{\text{Tx}}$. The regularized solution $\widehat{\boldsymbol{J}}^{\text{Tx}}$ is found using a Moore-Penrose pseudoinverse from the truncated SVD as [56]

$$\widehat{\boldsymbol{J}}^{\text{Tx}} = \mathbf{V}\widetilde{\boldsymbol{\Sigma}}^{-1}\mathbf{U}^{\text{H}}\boldsymbol{E}^{\text{meas}} \tag{4.9}$$

where $\widetilde{\boldsymbol{\Sigma}}$ is the truncated diagonal matrix. The solution $\widehat{\boldsymbol{J}}^{\text{Tx}}$ can now be used to compute an estimate $\widehat{\boldsymbol{E}}^{\text{inc}}$ anywhere, which for this method primarily means at the DUT and the measurement plane. At the measurement plane, it is subtracted from $\boldsymbol{E}^{\text{meas}}$ to render an estimate for the scattered field, $\widehat{\boldsymbol{E}}^{\text{sc}}$, which is used in the next step of the imaging process. An example of the source separation is shown in Figure 18 for a singly curved dielectric DUT containing four small PEC squares. This data was synthetically generated using MoM in the solver Feko [4].

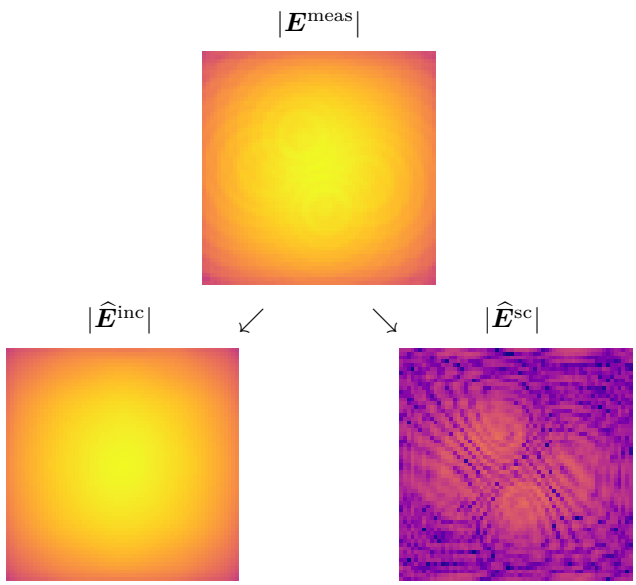

Figure 18: Images showing amplitudes of the measured field and the separation into estimated incident and scattered fields.

4.2.2 Sparse Image Reconstruction

The image reconstruction step uses the estimate for the scattered field $\widehat{\boldsymbol{E}}^{\text{sc}}$ to compute electric currents on the DUT surface. Since the inverse scattering problem is generally ill-posed, some type of regularization is necessary. We use methods based on a forward operator $\mathbf{N}_{\text{DUT}}$ from electric currents $\boldsymbol{J}^{\text{DUT}}$ on the DUT surface to scattered electric fields using (2.79) on the form

$$\boldsymbol{E}^{\text{sc}} = \mathbf{N}_{\text{DUT}} \boldsymbol{J}^{\text{DUT}}. \tag{4.10}$$

Due to uneven illumination of the DUT, though, the scattered electric field from different regions can vary in amplitude. To construct an image without this variation, the electric currents are normalized by the incident field on the DUT $\boldsymbol{E}^{\text{DUT}}$, which is computed from the source separation currents $\widehat{\boldsymbol{J}}^{\text{Tx}}$. Images are constructed from these scattering amplitudes $\boldsymbol{s}$ defined as

$$\boldsymbol{J}^{\text{DUT}} = \boldsymbol{s} \circ \boldsymbol{E}^{\text{DUT}} \tag{4.11}$$

where $\circ$ indicates a Hadamard (elementwise) product.

To construct images of $\boldsymbol{s}$ using the forward operator in (4.10), some properties specific to the NDT problem that are used, leading to a hypothesis of sparsity. Since the production methods where NDT is to be used are generally mature, it is assumed that any flaws are few and well separated such that high sparsity is achieved in a local basis. This is also dependent on the DUT being made from

low-permittivity composite materials with little scattering on its own, and further aided by the source separation removing this bulk scattering. The method for image reconstruction should therefore take sparsity into account and use only the forward operator in (4.10). As in [60,61] a method using basis pursuit denoising is used in Paper IV. This is an optimization method based on the L_1 norm which is suitable for finding sparse solutions [148]. What it amounts to is solving an optimization problem to find estimates $\hat{\boldsymbol{s}}$ of scattering amplitudes as

$$\hat{\boldsymbol{s}} = \arg\min_{\boldsymbol{s}} \|\boldsymbol{s}\|_1 \tag{4.12}$$

$$\text{s.t } \|\mathbf{N}_{\text{DUT}}(\boldsymbol{s} \circ \widehat{\boldsymbol{E}}^{\text{DUT}}) - \widehat{\boldsymbol{E}}^{\text{sc}}\|_2 \leq \kappa\sigma \tag{4.13}$$

with $\kappa \leq 1$ being a user-defined parameter and σ is given by

$$\sigma = \|\mathbf{N}_{\text{DUT}}\mathbf{N}_{\text{DUT}}^{\text{H}}\widehat{\boldsymbol{E}}^{\text{sc}} - \widehat{\boldsymbol{E}}^{\text{sc}}\|_2. \tag{4.14}$$

Here, $\mathbf{N}_{\text{DUT}}^{\text{H}}\widehat{\boldsymbol{E}}^{\text{sc}}$ is the solution from a single phase conjugation of the estimated scattered field $\widehat{\boldsymbol{E}}^{\text{sc}}$ (the measured field subtracted by the estimated incident field). The bound in (4.13) thus leads to solutions with smaller residuals in L_2 than obtained by phase conjugation, with $\kappa < 1$ enabling even tighter bounds.

Implementation-wise, the optimization problem is solved using the SPGL-1 solver in basis pursuit denoise mode [148, 149]. This solver applies the operator $\mathbf{N}_{\text{DUT}}$ and its Hermitian conjugate a large number of times before arriving at a solution. For this reason, acceleration of that particular operator can have a significant effect on the total performance. In [60, 61] the imaging method used parallel DUT and measurement planes, and as such acceleration could be achieved by exploiting translation invariance in the Green's function as described in section 3.5.1. However, in Paper IV the DUT geometry is singly curved which means that this approach is no longer fully available. Instead, such acceleration is possible along one dimension but not the other to still provide some degree of acceleration. Another important computational detail is related to the resolution in the DUT mesh. It is possible to improve this from the original spatial sampling in the measurement plane by sub-sampling, i.e. dividing the mesh elements into smaller elements. Since equal discretization is necessary for acceleration though, the grid in the measurement plane needs to be extended to match the finer sampling in the DUT mesh. These additional points in the grid are only used for computational reasons and no additional measurement data is required.

5 Measurement Techniques

While much of this introduction has focused on computations, the papers in this dissertation include electromagnetic measurements as well. As such, a brief overview of such measurements is provided with emphasis on the issues particularly related to the measurements performed for the included papers. As this

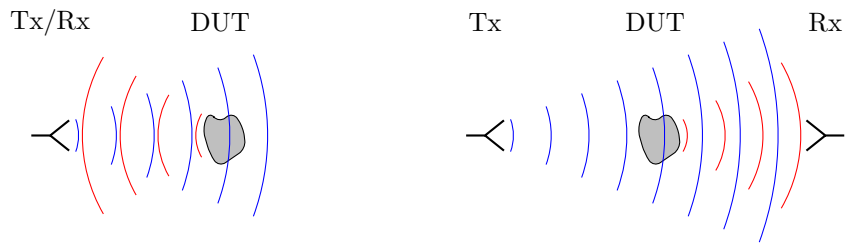

Figure 19: Monostatic (left) and bistatic (right) measurement setups. In both cases, a DUT is being measured. Note that the DUT scatters in many directions, and only the direction of interest is shown here.

dissertation focuses on electromagnetic scattering, this section focuses on scattering measurements in different forms. This typically means that there is a device under test (DUT) which is being subjected to an electromagnetic wave from a transmitting (Tx) antenna, and the waves affected by the DUT are measured using a receiving (Rx) antenna. The transmitting and receiving antennas can be in the same location, or even the same physical antenna, in which case the measurement is called monostatic. If they are in different locations, the measurement is called bistatic. This is illustrated in Figure 19.

Often the quantity of interest is the scattered electric field, but the measured quantity at the receiving end is the total electric field which is a combination of the incident and scattered waves as discussed in section 2.4. In a monostatic measurement this might not differ much from the scattered field, but in a bistatic measurement the incident field at the receiver may be significant, as seen in Figure 19. A commonly used method to obtain only the scattered field is to perform two measurements: one measurement with the DUT, and one reference measurement without the DUT. Since the situation is linear, the scattered field is obtained by subtracting the two received signals. This doubling of the number of measurements can be time-consuming though, especially if the measurement involves mechanical scanning of the receiving antenna to obtain the field in a certain region. To reduce the measurement time, the incident field can be numerically estimated using only one measurement with the DUT present. One way of doing this is by using the source separation technique described in section 4.2.1.

If a signal corresponding to the scattered wave has been measured, for example by subtracting a reference measurement, this is not sufficient for obtaining a quantity like the electric field or the RCS. The measured signal is typically a voltage which is not calibrated to the full measurement system, but is affected by the cables, the antennas, and in the case of RCS measurements, the free-space propagation. In measurements of microwave components, calibration can be done using known components to obtain accurate measurements at the ends of the cables. This type of calibration can be used in free-space measurements to remove effects of the cables, but further calibration is necessary to obtain a

calibration accurate for the electric field or the RCS. For some antennas, like open-ended waveguide probes, the effect of the antenna can be compensated for using theoretical expressions which makes them suitable for measurements in the near field [158, 159]. If measurements are done in the far field, calibration can be done by measuring a reference object with known properties and comparing measurements against that. For example, the DUT can be replaced by an object like a metallic sphere which has a well-known RCS to calibrate for [78].

5.1 Measurement Challenges and Solutions

One common problem in all measurements is the presence of random noise, which the signal of interest needs to exceed for it to be measurable. To quantify noise, the signal-to-noise ratio (SNR) which is the ratio between signal and noise power is used. This can, of course, be increased by using a larger signal power in the numerator, but there are also actions that can be performed to reduce the noise in the denominator. Noise can have many different origins, both from external sources and from within the measurement instruments, and this affects the steps which can be taken to reduce its influence. Noise sources external to the measurement instruments include other radiating devices, but also thermal radiation from surrounding objects with temperatures above 0 K [115]. One way to reduce external noise in particular is to perform measurements in a shielded chamber so that noise originating from outside the chamber is not received [78]. Significant noise also originates from within the measurement instruments, and this noise cannot be eliminated by external actions. Instead, the settings and setup of the instruments can be selected to reduce noise. Some of these settings act on noise in general, and not only instrument noise.

Due to the random nature of noise, a general action which reduces noise is averaging of the received signal over multiple samples [115]. Of course, this increases the measurement time as multiple samples are needed. Another action which is more related to the design of the receiver is to change settings for the so-called intermediate frequency (IF) filter in the receiver. How this is done in practice depends on the design of the receiver, but the result is a reduced bandwidth or increased selectivity of the filter with the bandwidth being the most important parameter. A decreased IF bandwidth increases the measurement time though, as more time is required to avoid transients of the reactive filter components [64].

Another problem in measurements is that of unwanted scattering and multipath propagation. This is a problem that needs to be considered in all measurements of freely propagating electromagnetic waves. Ideally, a measurement setup would only include the transmitting and receiving antennas as well as the device under test (DUT) suspended in free space stretching out to infinity. This way, the received signal would only be affected by the (hopefully) characterized antennas and the unknown DUT. Unfortunately, the real world does not look like that, and the received signal is also affected by all other objects which scatter electromag-

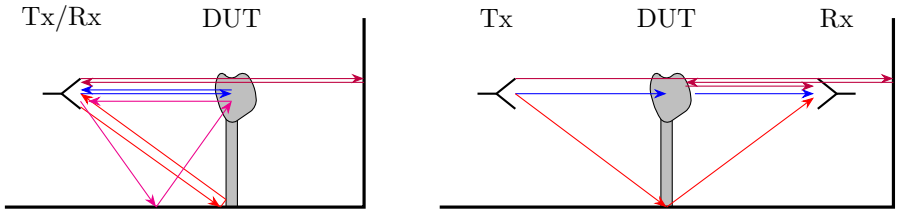

Figure 20: Examples of multipath propagation in monostatic (left) and bistatic (right) measurements.

netic waves. This is illustrated in Figure 20. If a reference measurement without the DUT is performed, much of this can be subtracted from the measurement. However, minor changes in the background between measurements can lead to significant signal components from unwanted scattering still being present after this subtraction. This is especially the case if the scattering from the DUT is weak in comparison to some of the possible scatterers.

One way to try to control this problem is by minimizing scattering from the measurement environment by using radiation-absorbent materials. These materials are engineered to absorb electromagnetic waves at certain frequencies of interest, and as such absorbers made from those materials can be used to reduce scattering by objects in the measurement setup [78]. A common use of absorbers is in anechoic chambers, where the floor, walls and ceiling are all covered by absorbers. With perfect absorbers, this environment would act as infinite free space (similar to the absorbing boundary conditions discussed in section 3.1). An example of an anechoic chamber is shown in Figure 21 where pyramidal absorbers can be seen covering most surfaces.

Other methods to reduce unwanted scattering are related to control over where waves are directed. One way to do this is by selecting transmitting and receiving antennas with narrow beamwidths such that only scattering by the DUT is captured [78]. The physical placement of the DUT is also important since a larger separation from surrounding objects means that fewer potential scatterers are visible within the beamwidth of the transmitting and receiving antennas. Objects can also be placed as to deliberately scatter waves, but in directions where they will not interfere with the measurement. This is the same idea as the concept in stealth technology where incident waves from a radar are redirected as to not return to the radar [78].

Finally, there are post-processing methods that can be used to separate the received signal into scattering by the DUT and scattering by other objects. As seen in Figure 22, the scattered waves that combine at the receiving antenna have different path lengths. These correspond to different propagation times which offers a way to remove unwanted signal components. If signals can be discriminated by the time between transmission and reception, with high enough temporal resolution, only the direct Tx-DUT-Rx signal component can be kept. This is called time gating as the unwanted components are “gated” out due to their too large

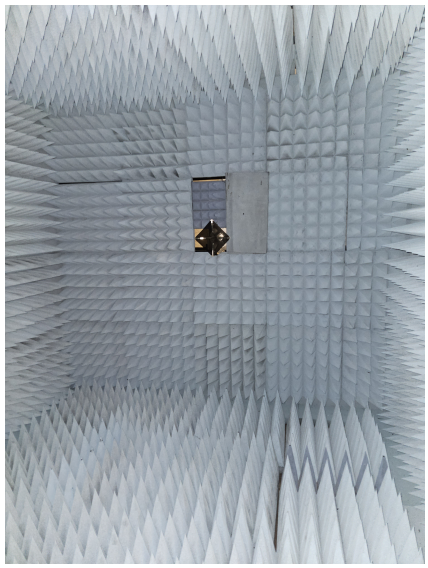

Figure 21: Anechoic chamber of the antenna laboratory at Lund University. Transmitting/receiving antenna in the center.

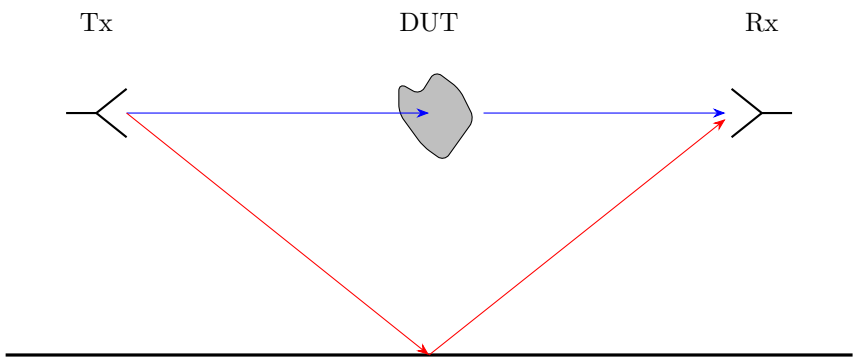

Figure 22: Two multipath components with unwanted path (red) having longer path length than the direct path (blue).

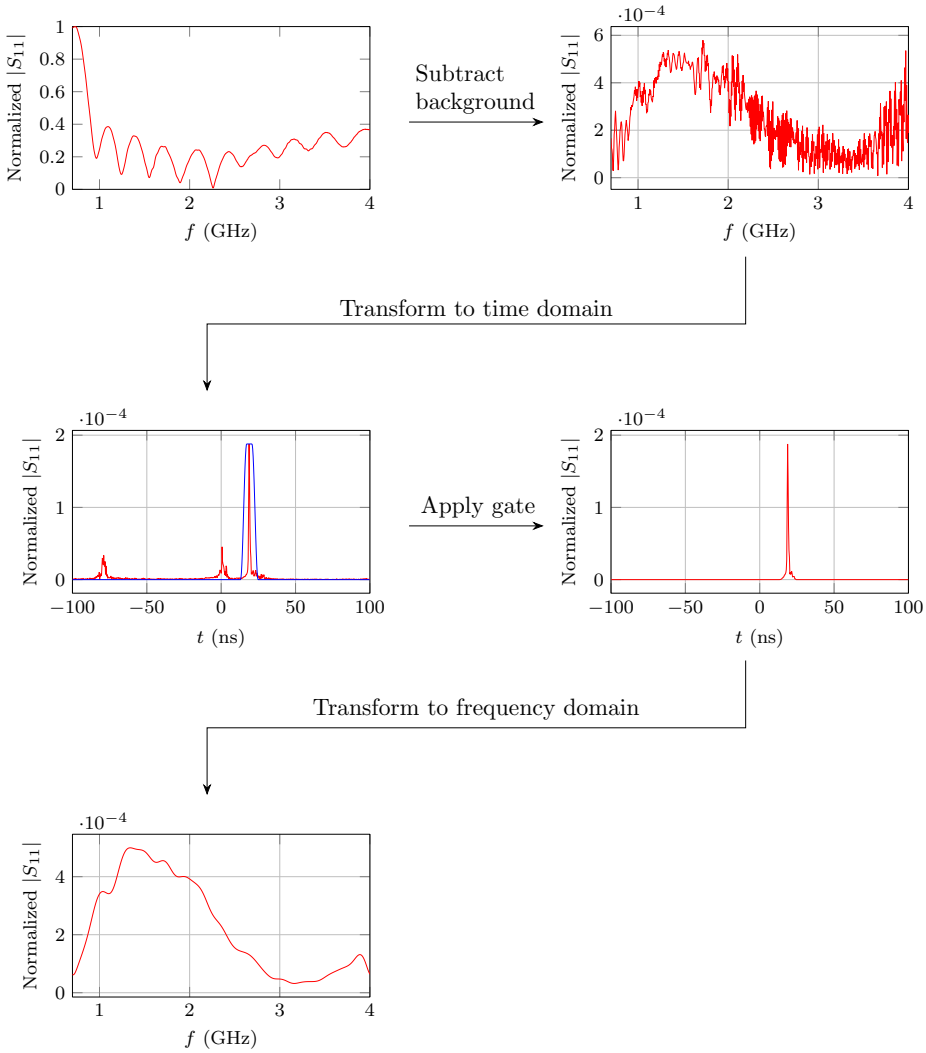

Figure 23: Example of background subtraction and time gating. The data is from a monostatic measurement of scattering by a metal sphere of radius 2.5 cm. The gate function shown in blue the third step is scaled for visualization purposes.

or too small propagation times. Typically, measurements are performed in the frequency domain so there is no direct access to the propagation times, but gating is easily done by Fourier analysis where the signal can be transformed to the time domain, processed, and transformed back to the frequency domain [78]. The application of the gate in the time domain changes the frequency content of the signal, causing sidelobes in the spectrum as the signal is transformed back to the frequency domain. There are many different window functions that can be selected as the gate to control these sidelobes [115]. An example of time gating as well as background subtraction of the raw data is shown in Figure 23 for real measurement data of monostatic scattering by a sphere. It is clear that the background subtraction is very effective, in particular due to reflections in the antenna being present in the raw data. However, the data can be improved by time gating and many unwanted scatterers are seen in the time domain plot. For time gating to be effective, the temporal resolution needs to be high enough to discriminate between different multipath components. The temporal resolution is directly related to an equivalent pulse width of the transmitter, which in turn is inversely proportional to the bandwidth. Time gating therefore puts a requirement on the bandwidth, which can be estimated if the spatial separation between scatterers in the setup is known.

5.2 Measurements in this Dissertation

Paper II, IV and V of this dissertation contain measurements with different setups, challenges and solutions. In this section, details of how the measurements were performed and why are provided. All instrument settings and details are not provided here as they are in the papers themselves. Instead, the decisions behind the measurement setups and instruments are explained.

5.2.1 Paper II: Monostatic RCS

For Paper II, the monostatic RCS of a water-based electromagnetic device was measured. This was done using a vector network analyzer (VNA) connected to a horn antenna, and in an anechoic chamber to reduce the influence of unwanted scattering. However, the chamber was set up for antenna measurements and contained a large rotation stage for the purpose of angular scanning. This was not needed for the RCS measurements, but it posed a problem as it was difficult to remove from the chamber, and was a significant scatterer compared to the DUT. The DUT was mounted on a structure made from expanded polystyrene, which typically scatters very little [78]. The measurement setup is shown in Figure 24 for measurement of a metal-coated sphere of radius 20 cm. Background subtraction using reference measurements without the DUT were necessary to remove many unwanted reflections, with reflections from the antenna being particularly important to reduce. Further reductions of unwanted reflections were necessary though, both due to the antenna and due to the rotation stage. For the rotation stage, absorbers could be placed to cover structures exhibiting particularly

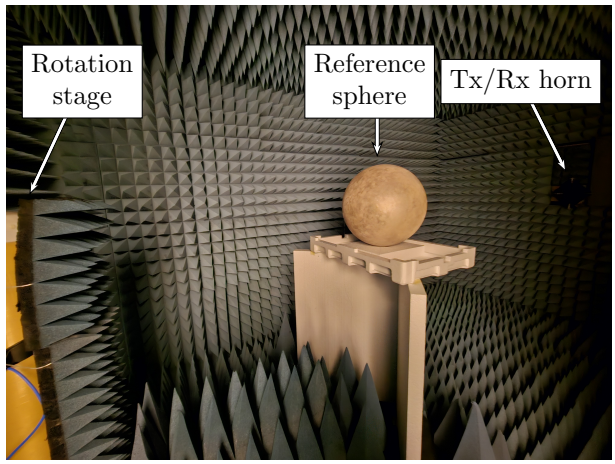

Figure 24: Measurement setup in anechoic chamber for a reference sphere. Absorbers as seen covering the rotation stage.

strong scattering like metallic corners. This had a significant effect, but did not fully eliminate the problem. Additional processing in the form of time gating was performed, which affected effects both due to the rotation stage and the antenna. This did require measurements in a larger frequency band, but since there was no mechanical scanning involved, measurement times were not large enough for this to pose any big issues.

Another issue which had to be addressed was that of noise. Measuring inside the anechoic chamber was an important part for this as it is a shielded environment, but the expected RCS was weak enough that further measures needed to be taken. One simple action was to increase the output power, which directly increases SNR. In addition to this, the bandwidth of the IF filter of the VNA was significantly reduced, and its selectivity increased, together with averaging over multiple measurements. These actions significantly increased the measurement time, but as previously discussed, this could be done to a large extent as no scanning was performed.

Finally, as RCS was the quantity to be measured it was crucial to perform an accurate calibration. Three different reference objects were used for this: one metal-coated sphere of radius 20 cm, one metallic sphere of radius 2.5 cm, and one metallic cylinder of height 8 cm and radius 2 cm. While the spheres had exact solutions for the RCS available, the RCS for the cylinder needed to be computed numerically, possibly introducing errors. However, as three different calibration objects were available, the cylinder measurements could be calibrated against a sphere to validate the numerical solution. The cylinder was eventually selected as the reference object, meaning that this intermediate step was used as indication that the final calibration could be trusted.

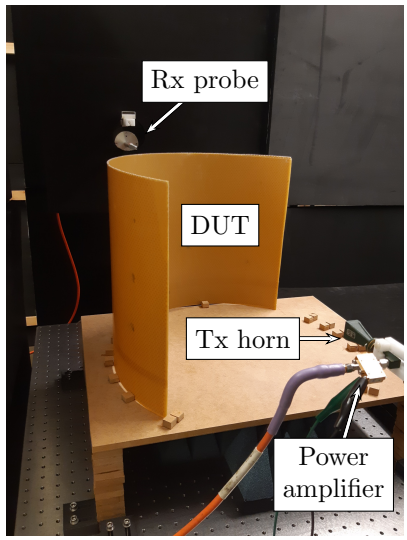

Figure 25: Setup for the mm-wave near-field scanning.

5.2.2 Paper IV: mm-Wave Near-Field Scanning

For Paper IV, near-field measurements were performed in a rectangular grid for use with the imaging algorithms described in section 4. This was done using a VNA connected to a Tx horn antenna and a mechanically scanned Rx open-ended waveguide probe. The measurement setup for a DUT mounted on a medium-density fiberboard table is shown in Figure 25. The measurements were performed on a metallic optical table, which meant that a very strong reflection in the table surface was present in the measured data, together with other unwanted scattering from holders and other surrounding objects. While absorbers could be placed in some locations, time gating was necessary to remove the effect of this reflection. Additionally, to increase the length of the reflection path and facilitate the time gating procedure, the Tx antenna, DUT and Rx probes were raised to a level significantly above the tabletop. To ensure that the time gating procedure would be effective, a large bandwidth of 10 GHz was used.

The measurements in this case were performed using mechanical scanning, and with high demands on precision in the positioning of the Rx probe. To ensure this precision, the mechanical positioning system was run with explicit stops at each measurement position, as opposed to measuring during the mechanical movement. The drawback of this is that acceleration and deceleration, as well as measurement time when the probe is stationary, makes the time for the full scan quite substantial. In the measurements, this time was roughly 7 h for 81×81 measurement points in a 300 mm $\times$ 300 mm plane. To boost the SNR without further increases to the measurement time (which would be a side-effect of changes to the IF bandwidth or averaging), an external power amplifier was used at the Tx antenna.

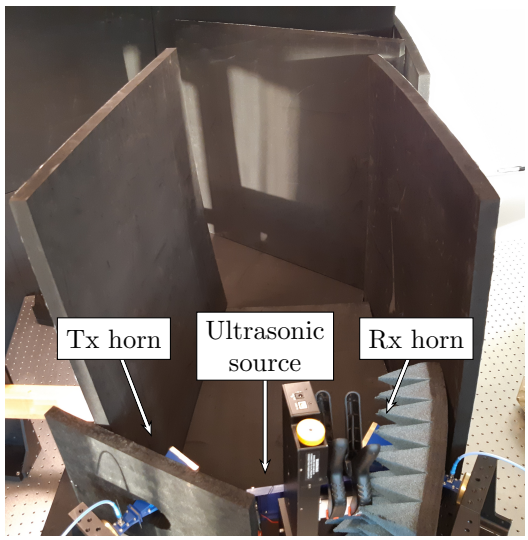

Figure 26: Setup for measurements of scattering by acoustic waves.

5.2.3 Paper V: Scattering by Acoustic Waves

For paper V, microwave scattering by an ultrasonic wave was measured. As this involved measuring a frequency shifted signal, the measurement was set up with a signal generator connected to a Tx antenna, and a separate spectrum analyzer connected to an Rx antenna. A different signal generator was needed for the ultrasonic source.

Since measurements were performed in air, the photoelastic interaction due to the ultrasonic wave was expected to be very weak. The Bragg diffraction mechanism described in section 2.5.1 had two crucial elements to enable measurements despite this difficulty. The first element was the clear scattering angle given by Bragg's law in (2.66), which could be selected by tuning the acoustic and electromagnetic wavelengths. As such, the scattering angle could be selected to place the Rx antenna outside the beam of the Tx antenna. The second, and most important element, was the frequency shift of scattered microwaves. By measuring at a frequency significantly separated from the Tx frequency, unwanted scattering would ideally not affect the measurements. This was clearly seen in the measurements as even the direct transmission between the horn gave a signal roughly 40 dB above the one scattered by ultrasound. Furthermore, this frequency shift provided a good way to verify that a measured signal was due to the ultrasonic wave as a shift in the ultrasonic frequency could immediately be seen to shift the measured microwave signal.

Despite the beneficial properties of the Bragg mechanism, unwanted scattering could still be problematic. No signal generator can provide a perfect single-frequency signal, and as the signal to be measured was very weak it was possible that the signal generator could produce significant enough levels at the frequency

shift of 40 kHz that was used. This would only be an issue if unwanted scattering was strong enough, and the main way this was reduced was by guiding the main beam away from the measurement region. Absorbers were used to enclose the measurement region, and care was taken to place them for specular reflections to guide the beam out of this region. This can be seen in Figure 26 where there is a path for waves to escape seen in the top of the figure.

Finally, due to the very low signal levels to be measured, noise reduction was crucial. The IF bandwidth of the signal generator was set to its minimum level of 10 Hz for this reason, and averaging over 10 measurements was also applied. These actions resulted in a noise floor below -130 dBm, which was sufficient to reliably measure the very weak scattering in air.

6 Contributions of Included Papers

As this dissertation is a compilation of papers, it is prudent to describe what their contributions are, and how they fit together in the bigger picture. The papers included in this dissertation can roughly be separated into two blocks: CEM software and NDT using mm-waves. However, there is still significant overlap between the two, especially with regards to integral equations which play an important role in both blocks.

6.1 Computational Electromagnetics Software

The first block is comprised of papers I–III and is about the development and use of the FE2MS software for electromagnetic scattering computations.

Paper I introduces the software which implements the FE-BI method combined with a multilevel ACA for improved performance. The paper has a particular focus on the development which was done with heavy use of open-source software, and aims to help readers who might want to work with open source by giving practical advice and insights. The FE-BI method is suitable for inhomogeneous, complex media and the software was developed to handle general bianisotropic media. The FE2MS software is itself open source, and is publicly available at https://www.github.com/nwingren/fe2ms. In the paper, there are also examples of how the software can be used, including details on accuracy and performance related to the commercial software Feko. However, all results are theoretical in the sense that they are either computed by computational software or the Mie series theoretical solution for scattering by spheres.

Paper II demonstrates that the FE2MS code can be used in realistic designs with complex geometry, and validates the results of the code against measured data. The paper presents a 3D-printed device which can be filled with water, and a siphon in the device causes given states to form as water is added. Depending on these states, the device reflects different microwave polarizations differently. While the device was primarily designed to act as a proof of concept for the use

of siphons, it is possible to imagine possible applications. By having a specific water volume trigger a sharp electromagnetic transition, it would be possible to remotely monitor water levels, or some property related to it. The design was simulated using the FE2MS software, and measurements were in good agreement with the simulated results. This demonstrates both that the software gives correct results for complicated geometries, and that it can be used in practical design work. While different materials were used in the siphon design, they were all isotropic, though the software can handle fully bianisotropic media.

Paper III uses the FE2MS software for computations involving a highly complex medium in a way that is unprecedented. The paper computes characteristic modes for structures involving nonreciprocity, which is something that has not been done previously. The application of the FE2MS software is for a rapidly rotating dielectric cylinder, which results in an effective medium which is inhomogeneous, bianisotropic and nonreciprocal. Conventional methods for computing characteristic modes are not easily adapted to this type of problem, but the FE-BI method is readily applied using a recently developed scattering formulation. The FE2MS software, in particular, is used due to its capability for bianisotropic media, which is not commonly found in commercial software.

6.2 Nondestructive Testing using mm-Waves

The second block is comprised of papers IV–V and is about using mm-waves to perform NDT of composite panels used in aerospace applications.

Paper IV uses methods from CEM to perform imaging of singly curved composite panels using mm-waves. This extends previous work on planar panels to this singly curved geometry, which finds several applications in aerodynamic structures. Significant modifications necessary to make the method work for the new geometry are presented. Additional details on theoretical concerns are considered in section 4.2 of this introduction. One point to notice is that, for the qualitative indications of discrete flaws investigated here, it was sufficient to use only electric currents instead of both electric and magnetic currents. This reduced the number of unknowns in the numerical problem by a factor of two. While mm-waves are promising for NDT, ultrasound is a commonly used method which works very well. For even better performance, one could ask if the two could be combined.

Paper V demonstrates how microwaves scattered by ultrasound in air can be clearly measured despite very low signal levels. While interaction between electromagnetic and acoustic waves is well-known, the literature is sparse when it comes to wavelengths of interest to NDT. In the paper we measure this interaction at wavelengths near those useful in NDT, but in air instead of the materials of interest. The scattering in air could be clearly measured to behave as predicted by theory, although at low signal levels. However, air is a medium with much weaker acousto-electromagnetic interaction than other media, and detection in air suggests that detection would be possible in most media. The main reason why

the detection could be made despite this difficulty was through the frequency shift of the scattered electromagnetic wave. This was done at an ultrasonic frequency of 40 kHz, which is fairly low compared to many industrial systems. An increase in the frequency shift, as well as the interaction strength itself could therefore be expected for a system used in NDT.

7 Conclusions

This dissertation has used both computational electromagnetics and measurements to investigate and evaluate electromagnetic scattering in its direct form and as an inverse problem. This is a large area to cover, and to draw any all-encompassing conclusions from my work is difficult. Nevertheless, some more general conclusions can be made where a topic has been covered by multiple papers with different approaches.

Both the FE2MS FE-BI code and the code used for imaging in Paper IV required substantial amounts of implementation work on my part. However, the starting points were quite different for the two. At the start of the development of the FE2MS code, there was no preexisting codebase to build upon. At that stage, I was very free in exploring various open-source packages which could be used to accelerate the development process. For the imaging code, on the other hand, a working code for planar imaging was already in place before I started working on extending it to singly curved imaging. In that case, there were very few opportunities where the integration of an open-source software package could have provided significant help. These two, somewhat opposed, situations tell us about the difficulty in integrating external software packages as a code matures. This can depend on the code architecture though, as it would have been fairly simple to change the optimization routine in the imaging code, but less so for the mesh handling. The reason is that the optimization was already an external open-source package, and the code around it was adapted to this. If more of the code architecture is designed for such modularity at an early stage, the challenge of integrating other code components might be smaller.

The benefits of simulation codes with direct access to the source code was also clear from the work shown in the dissertation. While commercial codes can be very capable, it is typically not possible to access all lower-level components, let alone the source code. The use of in-house codes like the FE2MS code allows for significant modifications in many cases. Before the work leading up to Paper III, the FE2MS code was only implemented with isotropic media in mind. When the interest for nonreciprocal media became clear, it was possible to change the implementation of FE forms for general bianisotropic media, and this could be done quickly with the help of FEniCSx. The algorithm computing characteristic modes could also be implemented with direct access to lower-level functions in the FE2MS code, making computations much faster than if only the high-level functions had been used. A hope is that the FE2MS code can be used in similar manners for other applications in the future, both within our research group, but

also in a wider context since the code is publicly available.

While much of the work performed for this dissertation focused on time-harmonic waves considered at single frequencies, a curious topic of frequency shifts became important in both Paper III and Paper V. In Paper III, the rotation of a cylinder affected its characteristic modes by shifting the resonance frequencies of certain modes, with the shift increasing with faster rotation. In Paper V, measurements of microwaves scattered by ultrasound was largely made possible through a frequency shift by the ultrasonic frequency. Both of these examples consider moving media in some form, and it is seen that interesting phenomena arise, which are not present in the stationary case. These phenomena are both due to fairly simple forms of movement, but illustrate why it is so interesting to pursue more complex ways of modulating media in time and space.

7.1 Future Work

There are many possible ways to further improve the FE2MS code presented in Paper I. One extension with much promise, which has been hinted towards in this introduction, would be the implementation of a fast direct solution method. A good reason for this is that the FE-BI system is typically ill-conditioned and needs an expensive preconditioner for iterative solvers to converge. This is computationally expensive, both in time and memory, and this issue is avoided if direct methods are used. Furthermore, such methods would be highly useful for problems with many right-hand sides as they only need to be solved once, in contrast to once per right-hand side for iterative solvers. Fast direct methods are well established for fully dense systems such as those in MoM, but less work has been done for the partly sparse, partly dense FE-BI system. Another improvement to the code which would increase its applicability would be to adapt it to distributed computing on clusters. While the code has some elements of parallel execution, the main drawback of the current approach is that there is no implementation for distributed memory. To be able to handle truly large problems, this would be necessary. Looking at the scaling of different parts of the FE-BI system, the BI part would likely be the part where this is necessary first, even with compression of the BI blocks. Some of the support in FEniCSx for distributed memory might be useful since some of its functionality, like mesh handling, are used in the BI part.

The water-based scatterer shown in Paper II was presented mainly as a proof of concept for the use of siphons for reconfigurability in water-based devices. It would be interesting if siphons, like the self-priming siphon used in our design, could be used in other devices with other applications. While our device would possibly enable some types of polarization-based remote measurements of whether a specific amount of water had been collected, there are likely other applications that could benefit from using siphons. Compared to other ways of controlling water for use in electromagnetic devices like pumps, siphons are mechanically simple, robust, and require no moving parts or external power. This

could make them interesting in, for example, environments where use of pumps would be difficult.

For the use of characteristic modes in problems exhibiting nonreciprocity shown in Paper III, the work presented here is in a very early stage. To our knowledge, this has not been attempted before, and as such there could be many ways in which to proceed. In the paper, the examples are mostly presented to demonstrate that it is in fact possible to compute modes for these problems, but less so to demonstrate particularly practical problems where characteristic modes might help. It would be good to identify such problems in future work. Since there is a large interest in devices with modulation in space and time, possibly with nonreciprocal behavior, the use of characteristic modes could be of interest. Especially the identification of modes which exhibit nonreciprocal behavior and modes which do not, as seen in Paper III, could be of interest when designing devices which should be explicitly nonreciprocal.

The mm-wave imaging algorithm for NDT presented in Paper IV could be improved upon in some different ways. One interesting development would be to use multi-frequency data in the reconstruction. The current algorithm uses only single-frequency data for that step, although multi-frequency data is collected in measurements for use in the time gating procedure. A hope would be that by using data for multiple frequencies, the number of spatial data points could be reduced. Experiments with multi-frequency data in the current algorithm have not produced good results, indicating that the problem formulation may need to change in that case. Another idea, which would follow the planar imaging algorithm, is to extend the algorithm from transmission- to reflection-based measurements. This was done for planar imaging using a ground plane and the theory of image currents, but the same method was not immediately applicable to imaging of singly curved surfaces. A more recent development which could be interesting to explore is that of large array-based measurement systems. With the arrival of 5G and more mm-wave systems to the market, such measurement systems have become more common. The largest bottleneck of the NDT method in Paper IV is the mechanical near-field scanning which took roughly 7 h for the measurements in the paper. With a one-dimensional array this time would be drastically reduced, and with a two-dimensional array it would, for all practical purposes, be eliminated.

With regards to Paper V and interaction between acoustic and electromagnetic waves, an interesting path for future work would be to investigate the interaction in some other medium than air, where the NDT application might be explored. For sufficiently high resolution in such an application, the wavelengths of both electromagnetic and acoustic waves may need to be smaller. Due to a likely higher propagation speed for acoustic waves in the medium, the ultrasonic frequency would then have to be significantly higher, requiring another type of transducer. There could also be some challenges for how to insert the waves into the medium, particularly for the ultrasonic waves. In many applications, they are guided into denser samples using water or gels at the interface, but the question is how that affects the microwave scattering.

Appendix A Derivations

A.1 Weak Form for Media without Magnetoelectric Coupling

This derivation begins with the vector wave equation as written in (3.3). A weak form can be derived for this by multiplying (3.3) by a test function $\boldsymbol{W}_m$ and an integrating over Ω, giving

$$\int_\Omega \boldsymbol{W}_m \cdot \left[\nabla \times \left(\overline{\overline{\mu_\mathrm{r}}}^{-1} \cdot \nabla \times \boldsymbol{E}\right) - k_0^2 \overline{\overline{\varepsilon_\mathrm{r}}} \cdot \boldsymbol{E}\right] \mathrm{d}V = -\mathrm{j}k_0\eta_0 \int_\Omega \boldsymbol{W}_m \cdot \boldsymbol{J}\,\mathrm{d}V. \quad \text{(A.1)}$$

The curl can be transferred to the test function by using the identity

$$\nabla \cdot (\boldsymbol{A} \times \boldsymbol{B}) = (\nabla \times \boldsymbol{A}) \cdot \boldsymbol{B} - (\nabla \times \boldsymbol{B}) \cdot \boldsymbol{A} \quad \text{(A.2)}$$

giving

$$\begin{aligned}\int_\Omega \left[(\nabla \times \boldsymbol{W}_m) \cdot \left(\overline{\overline{\mu_\mathrm{r}}}^{-1} \cdot \nabla \times \boldsymbol{E}\right) - k_0^2 \boldsymbol{W}_m \cdot \overline{\overline{\varepsilon_\mathrm{r}}} \cdot \boldsymbol{E}\right] \mathrm{d}V \\ - \int_\Omega \nabla \cdot \left[\boldsymbol{W}_m \times \left(\overline{\overline{\mu_\mathrm{r}}}^{-1} \cdot \nabla \times \boldsymbol{E}\right)\right] \mathrm{d}V = -\mathrm{j}k_0\eta_0 \int_\Omega \boldsymbol{W}_m \cdot \boldsymbol{J}\,\mathrm{d}V. \quad \text{(A.3)}\end{aligned}$$

The second integral is now rewritten using the divergence theorem, giving the weak form as

$$\begin{aligned}\int_\Omega \left[(\nabla \times \boldsymbol{W}_m) \cdot \left(\overline{\overline{\mu_\mathrm{r}}}^{-1} \cdot \nabla \times \boldsymbol{E}\right) - k_0^2 \boldsymbol{W}_m \cdot \overline{\overline{\varepsilon_\mathrm{r}}} \cdot \boldsymbol{E}\right] \mathrm{d}V \\ + \oint_{\partial\Omega} \boldsymbol{W}_m \cdot \left[\hat{\boldsymbol{n}} \times \left(\overline{\overline{\mu_\mathrm{r}}}^{-1} \cdot \nabla \times \boldsymbol{E}\right)\right] \mathrm{d}S = -\mathrm{j}k_0\eta_0 \int_\Omega \boldsymbol{W}_m \cdot \boldsymbol{J}\,\mathrm{d}V. \quad \text{(A.4)}\end{aligned}$$

If the boundary condition from (2.16) is used on the external boundary, i.e.

$$\hat{\boldsymbol{n}} \times \left(\overline{\overline{\mu_\mathrm{r}}}^{-1} \cdot \nabla \times \boldsymbol{E}\right) = -\mathrm{j}k_0 \hat{\boldsymbol{n}} \times \bar{\boldsymbol{H}},\ \boldsymbol{r} \in \partial\Omega \quad \text{(A.5)}$$

the surface integral in the weak form can be replaced. This gives a weak form for the interior FE problem for the FE-BI formulation as

$$\begin{aligned}\int_\Omega \left[(\nabla \times \boldsymbol{W}_m) \cdot \left(\overline{\overline{\mu_\mathrm{r}}}^{-1} \cdot \nabla \times \boldsymbol{E}\right) - k_0^2 \boldsymbol{W}_m \cdot \overline{\overline{\varepsilon_\mathrm{r}}} \cdot \boldsymbol{E}\right] \mathrm{d}V \\ + \mathrm{j}k_0 \oint_{\partial\Omega} \hat{\boldsymbol{n}} \cdot (\boldsymbol{W}_m \times \bar{\boldsymbol{H}})\,\mathrm{d}S = -\mathrm{j}k_0 \int_\Omega \boldsymbol{W}_m \cdot \bar{\boldsymbol{J}}\,\mathrm{d}V. \quad \text{(A.6)}\end{aligned}$$

A.2 Weak Form for Media with Magnetoelectric Coupling

This derivation begins with Maxwell's equations on the form in (3.5)–(3.6). These are combined in a similar way as for the case without magnetoelectric interaction, giving

$$\nabla \times \left(\overline{\overline{\mu_\mathrm{r}}}^{-1} \cdot \nabla \times \boldsymbol{E}\right) = -\mathrm{j}\omega\mu_0 \left[\frac{1}{\eta_0}\nabla \times \left(\overline{\overline{\mu_\mathrm{r}}}^{-1} \cdot \overline{\overline{\zeta}} \cdot \boldsymbol{E}\right) + \boldsymbol{J} + \mathrm{j}\omega\varepsilon_0 \overline{\overline{\varepsilon_\mathrm{r}}} \cdot \boldsymbol{E} - \varepsilon_0\eta_0 \overline{\overline{\xi}} \cdot \left(\frac{1}{\mu_0}\overline{\overline{\mu_\mathrm{r}}} \cdot \nabla \times \boldsymbol{E} + \mathrm{j}\omega\frac{1}{\eta_0}\overline{\overline{\mu_\mathrm{r}}}^{-1} \cdot \overline{\overline{\zeta}} \cdot \boldsymbol{E}\right)\right]. \quad \text{(A.7)}$$

Rearranging and rewriting gives the equation corresponding to the previous vector wave equation as.

$$\nabla \times \left(\overline{\overline{\mu_\mathrm{r}}}^{-1} \cdot \nabla \times \boldsymbol{E}\right) - k_0^2 \left(\overline{\overline{\varepsilon_\mathrm{r}}} - \overline{\overline{\xi}} \cdot \overline{\overline{\mu_\mathrm{r}}}^{-1} \cdot \overline{\overline{\zeta}}\right) \cdot \boldsymbol{E} + \mathrm{j}k_0 \left[\nabla \times \left(\overline{\overline{\mu_\mathrm{r}}}^{-1} \cdot \overline{\overline{\zeta}} \cdot \boldsymbol{E}\right) - \overline{\overline{\xi}} \cdot \overline{\overline{\mu_\mathrm{r}}}^{-1} \cdot \nabla \times \boldsymbol{E}\right] = -\mathrm{j}k_0\eta_0 \boldsymbol{J}. \quad \text{(A.8)}$$

Using the same steps as for media without magnetoelectric coupling, the weak form can also be derived. Multiplication by a test function $\boldsymbol{W}_m$ and integration over Ω gives

$$\begin{aligned}&\int_\Omega \boldsymbol{W}_m \cdot \left[\nabla \times \left(\overline{\overline{\mu_\mathrm{r}}}^{-1} \cdot \nabla \times \boldsymbol{E}\right)\right] \mathrm{d}V + \mathrm{j}k_0 \int_\Omega \boldsymbol{W}_m \cdot \left[\nabla \times \left(\overline{\overline{\mu_\mathrm{r}}}^{-1} \cdot \overline{\overline{\zeta}} \cdot \boldsymbol{E}\right)\right] \mathrm{d}V \\ &- \mathrm{j}k_0 \int_\Omega \boldsymbol{W}_m \cdot \left(\overline{\overline{\xi}} \cdot \overline{\overline{\mu_\mathrm{r}}}^{-1} \cdot \nabla \times \boldsymbol{E}\right) \mathrm{d}V - k_0^2 \int_\Omega \boldsymbol{W}_m \cdot \left(\overline{\overline{\varepsilon_\mathrm{r}}} - \overline{\overline{\xi}} \cdot \overline{\overline{\mu_\mathrm{r}}}^{-1} \cdot \overline{\overline{\zeta}}\right) \cdot \boldsymbol{E} \, \mathrm{d}V \\ &= -\mathrm{j}k_0\eta_0 \int_\Omega \boldsymbol{W}_m \cdot \boldsymbol{J} \, \mathrm{d}V. \quad \text{(A.9)}\end{aligned}$$

The first integral is the same as for the problem without magnetoelectric coupling, and is rewritten in the same way as

$$\begin{aligned}&\int_\Omega \boldsymbol{W}_m \cdot \left[\nabla \times \left(\overline{\overline{\mu_\mathrm{r}}}^{-1} \cdot \nabla \times \boldsymbol{E}\right)\right] \mathrm{d}V \\ &= \int_\Omega (\nabla \times \boldsymbol{W}_m) \cdot \left(\overline{\overline{\mu_\mathrm{r}}}^{-1} \cdot \nabla \times \boldsymbol{E}\right) \mathrm{d}V + \oint_{\partial\Omega} \boldsymbol{W}_m \cdot \left[\hat{\boldsymbol{n}} \times \left(\overline{\overline{\mu_\mathrm{r}}}^{-1} \cdot \nabla \times \boldsymbol{E}\right)\right] \mathrm{d}S. \quad \text{(A.10)}\end{aligned}$$

The second integral is treated similarly as

$$\begin{aligned}&\int_\Omega \boldsymbol{W}_m \cdot \left[\nabla \times \left(\overline{\overline{\mu_\mathrm{r}}}^{-1} \cdot \overline{\overline{\zeta}} \cdot \boldsymbol{E}\right)\right] \mathrm{d}V \\ &\quad = \int_\Omega (\nabla \times \boldsymbol{W}_m) \cdot \overline{\overline{\mu_\mathrm{r}}}^{-1} \cdot \overline{\overline{\zeta}} \cdot \boldsymbol{E} \, \mathrm{d}V - \int_\Omega \nabla \cdot \left[\boldsymbol{W}_m \times \left(\overline{\overline{\mu_\mathrm{r}}}^{-1} \cdot \overline{\overline{\zeta}} \cdot \boldsymbol{E}\right)\right] \mathrm{d}V \\ &= \int_\Omega (\nabla \times \boldsymbol{W}_m) \cdot \overline{\overline{\mu_\mathrm{r}}}^{-1} \cdot \overline{\overline{\zeta}} \cdot \boldsymbol{E} \, \mathrm{d}V - \oint_{\partial\Omega} \hat{\boldsymbol{n}} \cdot \left[\boldsymbol{W}_m \times \left(\overline{\overline{\mu_\mathrm{r}}}^{-1} \cdot \overline{\overline{\zeta}} \cdot \boldsymbol{E}\right)\right] \mathrm{d}S \quad \text{(A.11)}\end{aligned}$$

where (A.2) and the divergence theorem were used. A weak form can be written as

$$\begin{aligned}\int_\Omega (\nabla \times \boldsymbol{W}_m) \cdot \left(\overline{\overline{\mu_\mathrm{r}}}^{-1} \cdot \nabla \times \boldsymbol{E}\right) \mathrm{d}V - k_0^2 \int_\Omega \boldsymbol{W}_m \cdot \left(\overline{\overline{\varepsilon_\mathrm{r}}} - \overline{\overline{\xi}} \cdot \overline{\overline{\mu_\mathrm{r}}}^{-1} \cdot \overline{\overline{\zeta}}\right) \cdot \boldsymbol{E} \, \mathrm{d}V \\ + \mathrm{j}k_0 \int_\Omega (\nabla \times \boldsymbol{W}_m) \cdot \overline{\overline{\mu_\mathrm{r}}}^{-1} \cdot \overline{\overline{\zeta}} \cdot \boldsymbol{E} \, \mathrm{d}V - \mathrm{j}k_0 \int_\Omega \boldsymbol{W}_m \cdot \left(\overline{\overline{\xi}} \cdot \overline{\overline{\mu_\mathrm{r}}}^{-1} \cdot \nabla \times \boldsymbol{E}\right) \mathrm{d}V \\ + \oint_{\partial\Omega} \boldsymbol{W}_m \cdot \left[\hat{\boldsymbol{n}} \times \left(\overline{\overline{\mu_\mathrm{r}}}^{-1} \cdot \nabla \times \boldsymbol{E}\right)\right] \mathrm{d}S - \mathrm{j}k_0 \oint_{\partial\Omega} \hat{\boldsymbol{n}} \cdot \left[\boldsymbol{W}_m \times \left(\overline{\overline{\mu_\mathrm{r}}}^{-1} \cdot \overline{\overline{\zeta}} \cdot \boldsymbol{E}\right)\right] \mathrm{d}S \\ = -\mathrm{j}k_0 \eta_0 \int_\Omega \boldsymbol{W}_m \cdot \boldsymbol{J} \, \mathrm{d}V. \quad \text{(A.12)}\end{aligned}$$

As for the simpler case in A.1, the boundary condition from (2.16) is used on the external boundary to give a new weak form. In this case, the boundary condition appears explicitly only in one surface integral, but some more effort is required to include it in the second one. This second surface integral can be written as

$$-\mathrm{j}k_0 \oint_{\partial\Omega} \boldsymbol{W}_m \cdot \left[\hat{\boldsymbol{n}} \times \left(\overline{\overline{\mu_\mathrm{r}}}^{-1} \cdot \overline{\overline{\zeta}} \cdot \boldsymbol{E}\right)\right] \mathrm{d}S. \quad \text{(A.13)}$$

This can be rewritten using (3.5) written as

$$-\mathrm{j}k_0 \overline{\overline{\mu_\mathrm{r}}}^{-1} \cdot \overline{\overline{\zeta}} \cdot \boldsymbol{E} = \overline{\overline{\mu_\mathrm{r}}}^{-1} \cdot \nabla \times \boldsymbol{E} + \mathrm{j}k_0 \bar{\boldsymbol{H}} \quad \text{(A.14)}$$

giving the surface integral as

$$\oint_{\partial\Omega} \boldsymbol{W}_m \cdot \left[\hat{\boldsymbol{n}} \times \left(\overline{\overline{\mu_\mathrm{r}}}^{-1} \cdot \nabla \times \boldsymbol{E}\right) + \mathrm{j}k_0 \hat{\boldsymbol{n}} \times \bar{\boldsymbol{H}}\right] \mathrm{d}S. \quad \text{(A.15)}$$

This can be identified in the boundary condition, showing that the second surface integral is identically zero. Now the final weak form can be written as

$$\begin{aligned}\int_\Omega (\nabla \times \boldsymbol{W}_m) \cdot \left(\overline{\overline{\mu_\mathrm{r}}}^{-1} \cdot \nabla \times \boldsymbol{E}\right) \mathrm{d}V - k_0^2 \int_\Omega \boldsymbol{W}_m \cdot \left(\overline{\overline{\varepsilon_\mathrm{r}}} - \overline{\overline{\xi}} \cdot \overline{\overline{\mu_\mathrm{r}}}^{-1} \cdot \overline{\overline{\zeta}}\right) \cdot \boldsymbol{E} \, \mathrm{d}V \\ + \mathrm{j}k_0 \int_\Omega (\nabla \times \boldsymbol{W}_m) \cdot \overline{\overline{\mu_\mathrm{r}}}^{-1} \cdot \overline{\overline{\zeta}} \cdot \boldsymbol{E} \, \mathrm{d}V - \mathrm{j}k_0 \int_\Omega \boldsymbol{W}_m \cdot \left(\overline{\overline{\xi}} \cdot \overline{\overline{\mu_\mathrm{r}}}^{-1} \cdot \nabla \times \boldsymbol{E}\right) \mathrm{d}V \\ + \mathrm{j}k_0 \oint_{\partial\Omega} \hat{\boldsymbol{n}} \cdot \left(\boldsymbol{W}_m \times \bar{\boldsymbol{H}}\right) \mathrm{d}S = -\mathrm{j}k_0 \int_\Omega \boldsymbol{W}_m \cdot \bar{\boldsymbol{J}} \, \mathrm{d}V. \quad \text{(A.16)}\end{aligned}$$

References

[1] Acconeer. Applications. https://www.acconeer.com/applications/. Accessed 7 Feb. 2024.

[2] S. S. Ahmed, A. Schiessl, F. Gumbmann, M. Tiebout, S. Methfessel, and L. Schmidt. Advanced microwave imaging. *IEEE Microwave Magazine*, **13**(6), pp. 26–43, 2012.

[3] M. S. Alnæs, A. Logg, K. B. Ølgaard, M. E. Rognes, and G. N. Wells. Unified form language: A domain-specific language for weak formulations of partial differential equations. *ACM Transactions on Mathematical Software*, **40**(2), 2014.

[4] Altair Engineering Inc. Electromagnetic Simulation for Connectivity, Compatibility, and Radar | Altair Feko. https://altair.com/feko. Accessed 2 Feb. 2024.

[5] P. R. Amestoy, I. S. Duff, J.-Y. L'Excellent, and J. Koster. A fully asynchronous multifrontal solver using distributed dynamic scheduling. *SIAM Journal on Matrix Analysis and Applications*, **23**(1), pp. 15–41, 2001.

[6] J. B. Andersen. History of communications/radio wave propagation from Marconi to MIMO. *IEEE Communications Magazine*, **55**(2), pp. 6–10, 2017.

[7] F. P. Andriulli, K. Cools, H. Bagci, F. Olyslager, A. Buffa, S. Christiansen, and E. Michielssen. A multiplicative calderon preconditioner for the electric field integral equation. *IEEE Transactions on Antennas and Propagation*, **56**(8), pp. 2398–2412, 2008.

[8] P. Arcioni, M. Bressan, and L. Perregrini. On the evaluation of the double surface integrals arising in the application of the boundary integral method to 3-D problems. *IEEE Transactions on Microwave Theory and Techniques*, **45**(3), pp. 436–439, 1997.

[9] Axis Communications. Radar in surveillance. White Paper, 2023. https://www.axis.com/dam/public/ae/b8/7d/radar-in-surveillance-en-US-407095.pdf. Accessed 7 Feb. 2024.

[10] I. Badia, B. Caudron, X. Antoine, and C. Geuzaine. A well-conditioned weak coupling of boundary element and high-order finite element methods for time-harmonic electromagnetic scattering by inhomogeneous objects. *SIAM Journal on Scientific Computing*, **44**(3), pp. B640–B667, 2022.

[11] C. A. Balanis. *Antenna Theory: analysis and design.* John Wiley & Sons, Inc., 2nd edition, 1997.

[12] L. Baldini and V. Chandrasekar. *100 Years of the International Union of Radio Science*, chapter 24: Commission F Contribution: Radio Wave Remote Sensing of the Earth, pp. 499–518. URSI Press, Gent, Belgium, 2021.

[13] I. A. Baratta, J. P. Dean, J. S. Dokken, M. Habera, J. S. Hale, C. N. Richardson, M. E. Rognes, M. W. Scroggs, N. Sime, and G. N. Wells. DOLFINx: The next generation FEniCS problem solving environment, 2023.

[14] J. Barnes and P. Hut. A hierarchical O(N log N) force-calculation algorithm. *Nature*, **324**(6096), pp. 446–449, 1986.

[15] M. Bebendorf and S. Kunis. Recompression techniques for adaptive cross approximation. *The Journal of Integral Equations and Applications*, **21**(3), pp. 331–357, 2009.

[16] M. Bebendorf. Approximation of boundary element matrices. *Numerische Mathematik*, **86**(4), pp. 565–589, 2000.

[17] M. Bebendorf. *Hierarchical Matrices*. Springer-Verlag, Berlin, Heidelberg, Germany, 2008.

[18] J. Bezanson, A. Edelman, S. Karpinski, and V. B. Shah. Julia: A fresh approach to numerical computing. *SIAM Review*, **59**(1), pp. 65–98, 2017.

[19] E. Bleszynski, M. Bleszynski, and T. Jaroszewicz. AIM: Adaptive integral method for solving large-scale electromagnetic scattering and radiation problems. *Radio Science*, **31**(5), pp. 1225–1251, 1996.

[20] W. H. Bragg and W. L. Bragg. The reflection of X-rays by crystals. *Proceedings of the Royal Society of London. Series A, Containing Papers of a Mathematical and Physical Character*, **88**(605), pp. 428–438, 1913.

[21] S. C. Brenner and L. R. Scott. *The Mathematical Theory of Finite Element Methods*. Springer Science+Business Media, New York, NY, USA, 3rd edition, 2008.

[22] L. Brillouin. Diffusion de la lumière et des rayons X par un corps transparent homogène - influence de l'agitation thermique. *Annales de Physique*, **9**(17), pp. 88–122, 1922.

[23] A. Buffa and S. Christiansen. A dual finite element complex on the barycentric refinement. *Mathematics of computation*, **76**(260), pp. 1743–1769, 2007.

[24] G. J. Burke and A. J. Poggio. Numerical electromagnetic code (NEC)-method of moments. NOSC Technical Document 116, Naval Ocean Systems Center, San Diego, CA, 1977.

[25] G. Burke, E. Miller, and A. Poggio. The numerical electromagnetics code (NEC) - a brief history. In *IEEE Antennas and Propagation Society Symposium, 2004.*, volume 3, pp. 2871–2874, 2004.

[26] M. Cabedo-Fabres, E. Antonino-Daviu, A. Valero-Nogueira, and M. F. Bataller. The theory of characteristic modes revisited: A contribution to the design of antennas for modern applications. *IEEE Antennas and Propagation Magazine*, **49**(5), pp. 52–68, 2007.

[27] C. Caloz and Z.-L. Deck-Léger. Spacetime metamaterials—part I: General concepts. *IEEE Transactions on Antennas and Propagation*, **68**(3), pp. 1569–1582, 2020.

[28] M. Capek, J. Lundgren, M. Gustafsson, K. Schab, and L. Jelinek. Characteristic mode decomposition using the scattering dyadic in arbitrary full-wave solvers. *IEEE Transactions on Antennas and Propagation*, **71**(1), pp. 830–839, 2023.

[29] M. Catedra, J. Cuevas, and L. Nuno. A scheme to analyze conducting plates of resonant size using the conjugate-gradient method and the fast Fourier transform. *IEEE Transactions on Antennas and Propagation*, **36**(12), pp. 1744–1752, 1988.

[30] M. Catedra, E. Gago, and L. Nuno. A numerical scheme to obtain the RCS of three-dimensional bodies of resonant size using the conjugate gradient method and the fast Fourier transform. *IEEE Transactions on Antennas and Propagation*, **37**(5), pp. 528–537, 1989.

[31] V. C. Chen, F. Li, S. . Ho, and H. Wechsler. Micro-doppler effect in radar: phenomenon, model, and simulation study. *IEEE Transactions on Aerospace and Electronic Systems*, **42**(1), pp. 2–21, 2006.

[32] W. C. Chew, M. S. Tong, and B. Hu. *Integral Equation Methods for Electromagnetic and Elastic Waves*, volume 12 of *Synthesis Lectures on Computational Electromagnetics*. Morgan & Claypool, 2008.

[33] R. Coifman, V. Rokhlin, and S. Wandzura. The fast multipole method for the wave equation: a pedestrian prescription. *IEEE Antennas and Propagation Magazine*, **35**(3), pp. 7–12, 1993.

[34] K. Cools, F. P. Andriulli, D. De Zutter, and E. Michielssen. Accurate and conforming mixed discretization of the MFIE. *IEEE Antennas and Wireless Propagation Letters*, **10**, pp. 528–531, 2011.

[35] D. B. Davidson. *Computational Electromagnetics for RF and Microwave Engineering*. Cambridge University Press, Cambridge, UK, 2 edition, 2011.

[36] T. A. Davis. Algorithm 832: UMFPACK V4.3—an unsymmetric-pattern multifrontal method. *ACM Transactions on Mathematical Software*, **30**(2), pp. 196–199, 2004.

[37] T. H. Demetrakopoulos and R. Mittra. Digital and optical reconstruction of images from suboptical diffraction patterns. *Applied Optics*, **13**(3), pp. 665–670, 1974.

[38] L. F. Demkowicz. *Mathematical Theory of Finite Elements*. Society for Industrial and Applied Mathematics, Philadelphia, PA, USA, 2024.

[39] M. G. Duffy. Quadrature over a pyramid or cube of integrands with a singularity at a vertex. *SIAM journal on Numerical Analysis*, **19**(6), pp. 1260–1262, 1982.

[40] T. Eibert and V. Hansen. On the calculation of potential integrals for linear source distributions on triangular domains. *IEEE Transactions on Antennas and Propagation*, **43**(12), pp. 1499–1502, 1995.

[41] A. Ericsson, D. Sjöberg, C. Larsson, and T. Martin. Scattering from a multilayered sphere - applications to electromagnetic absorbers on double curved surfaces. Technical Report LUTEDX/(TEAT-7249)/1-32/(2017), Electromagnetic Theory Department of Electrical and Information Technology Lund University Sweden, 2017.

[42] M. Fink. Multiwave imaging and super resolution. *Physics Today*, **63**(2), pp. 28, 2010.

[43] H. Gan and W. Chew. A discrete BCG-FFT algorithm for solving 3D inhomogeneous scatterer problems. *Journal of Electromagnetic Waves and Applications*, **9**(10), pp. 1339–1357, 1995.

[44] R. J. Garbacz. *A Generalized Expansion for Radiated and Scattered Fields*. PhD thesis, The Ohio State Univ., 1968.

[45] C. Geuzaine and J.-F. Remacle. Gmsh: A 3-D finite element mesh generator with built-in pre-and post-processing facilities. *International journal for numerical methods in engineering*, **79**(11), pp. 1309–1331, 2009.

[46] V. Girault and P.-A. Raviart. *Finite Element Methods for Navier-Stokes Equations*. Springer-Verlag, Berlin, Heidelberg, Germany, 1986.

[47] G. H. Golub and C. F. V. Loan. *Matrix Computations*. Johns Hopkins University Press, Baltimore, MD, USA, 3rd edition, 1996.

[48] R. Graglia. On the numerical integration of the linear shape functions times the 3-D Green's function or its gradient on a plane triangle. *IEEE Transactions on Antennas and Propagation*, **41**(10), pp. 1448–1455, 1993.

[49] J. Guan, S. Yan, and J. Jin. An accurate and efficient finite element-boundary integral method with GPU acceleration for 3-D electromagnetic analysis. *IEEE Transactions on Antennas and Propagation*, **62**(12), pp. 6325–6336, 2014.

[50] J. Guan, S. Yan, and J. Jin. A multi-solver scheme based on combined field integral equations for electromagnetic modeling of highly complex objects. *IEEE Transactions on Antennas and Propagation*, **65**(3), pp. 1236–1247, 2017.

[51] H. Guo, Y. Liu, J. Hu, and E. Michielssen. A butterfly-based direct integral-equation solver using hierarchical LU factorization for analyzing scattering from electrically large conducting objects. *IEEE Transactions on Antennas and Propagation*, **65**(9), pp. 4742–4750, 2017.

[52] M. Gustafsson, M. Sebesta, B. Bengtsson, S. Pettersson, P. Egelberg, and T. Lenart. High-resolution digital transmission microscopy—a Fourier holography approach. *Optics and Lasers in Engineering*, **41**(3), pp. 553–563, 2004.

[53] M. Gustafsson, L. Jelinek, K. Schab, and M. Capek. Unified theory of characteristic modes: Part I – Fundamentals. *IEEE Transactions on Antennas and Propagation*, **70**(12), pp. 11814–11824, 2022.

[54] M. Gustafsson, L. Jelinek, K. Schab, and M. Capek. Unified theory of characteristic modes: Part II – Tracking, losses, and FEM evaluation. *IEEE Transactions on Antennas and Propagation*, **70**(12), pp. 11814–11824, 2022.

[55] W. Hackbusch. *Hierarchical Matrices: Algorithms and Analysis*. Springer-Verlag, Berlin, Heidelberg, Germany, 2015.

[56] P. C. Hansen. *Discrete Inverse Problems : Insight and Algorithms*. Society for Industrial and Applied Mathematics, Philadelphia, PA, USA, 2010.

[57] R. F. Harrington and J. R. Mautz. Theory of characteristic modes for conducting bodies. *IEEE Transactions on Antennas and Propagation*, **19**(5), pp. 622–628, 1971.

[58] R. F. Harrington. *Time-Harmonic Electromagnetic Fields*. Wiley – IEEE Press, 2001.

[59] C. R. Harris, K. J. Millman, S. J. van der Walt, R. Gommers, P. Virtanen, D. Cournapeau, E. Wieser, J. Taylor, S. Berg, N. J. Smith, R. Kern, M. Picus, S. Hoyer, M. H. van Kerkwijk, M. Brett, A. Haldane, J. F. del Río, M. Wiebe, P. Peterson, P. Gérard-Marchant, K. Sheppard, T. Reddy, W. Weckesser, H. Abbasi, C. Gohlke, and T. E. Oliphant. Array programming with NumPy. *Nature*, **585**(7825), pp. 357–362, 2020.

[60] J. Helander, A. Ericsson, M. Gustafsson, T. Martin, D. Sjöberg, and C. Larsson. Compressive sensing techniques for mm-wave nondestructive testing of composite panels. *IEEE Transactions on Antennas and Propagation*, **65**(10), pp. 5523–5531, 2017.

[61] J. Helander, J. Lundgren, D. Sjöberg, C. Larsson, T. Martin, and M. Gustafsson. Reflection-based source inversion for sparse imaging of low-loss composite panels. *IEEE Transactions on Antennas and Propagation*, **68**(6), pp. 4860–4870, 2020.

[62] J. Helander. *Millimeter Wave Imaging and Phased Array Antennas for 5G and Aerospace Applications*. Doctoral thesis (compilation), Department of Electrical and Information Technology, Lund University, 2019.

[63] J. Helander, D. Tayli, and D. Sjöberg. Synthesis of large endfire antenna arrays using convex optimization. *IEEE Transactions on Antennas and Propagation*, **66**(2), pp. 712–720, 2018.

[64] A. D. Helfrick. *Electrical spectrum and network analyzers: a practical approach*. Academic Press, Inc., San Diego, CA, USA, 1991.

[65] L. Hernquist. Hierarchical N-body methods. *Computer Physics Communications*, **48**(1), pp. 107–115, 1988.

[66] L. Hörmander. *The Analysis of Linear Partial Differential Operators I: Distribution theory and Fourier analysis*. Springer-Verlag, Berlin, Heidelberg, Germany, 2nd edition, 1990.

[67] Infineon Technologies. Radar sensors for IoT. https://www.infineon.com/cms/en/product/sensor/radar-sensors/radar-sensors-for-iot/. Accessed 7 Feb. 2024.

[68] J. D. Jackson. *Classical Electrodynamics*. John Wiley & Sons, Inc., Hoboken, NJ, USA, 1999.

[69] W. Jakob, J. Rhinelander, and D. Moldovan. pybind11 – seamless operability between C++11 and Python, 2017. https://github.com/pybind/pybind11. Accessed 4 Mar. 2024.

[70] J.-M. Jin and V. Liepa. Application of hybrid finite element method to electromagnetic scattering from coated cylinders. *IEEE Transactions on Antennas and Propagation*, **36**(1), pp. 50–54, 1988.

[71] J.-M. Jin. *Theory and Computation of Electromagnetic Fields*. John Wiley & Sons, Ltd, Hoboken, NJ, USA, 2010.

[72] J.-M. Jin. *The finite element method in electromagnetics*. John Wiley & Sons, 2015.

[73] S. Kailasa and T. Betcke. AdaptOctree: Adaptive linear octrees in Python, 2021. https://github.com/Excalibur-SLE/AdaptOctree. Accessed 4 Mar. 2024.

[74] S. Kharkovsky and R. Zoughi. Microwave and millimeter wave nondestructive testing and evaluation - overview and recent advances. *IEEE Instrumentation Measurement Magazine*, **10**(2), pp. 26–38, 2007.

[75] M. A. Khayat, D. R. Wilton, and P. W. Fink. An improved transformation and optimized sampling scheme for the numerical evaluation of singular and near-singular potentials. *IEEE Antennas and Wireless Propagation Letters*, **7**, pp. 377–380, 2008.

[76] P.-S. Kildal and A. Kishk. EM modeling of surfaces with stop or go characteristics – artificial magnetic conductors and soft and hard surfaces. *Applied Computational Electromagnetics Society Journal*, **18**(1), pp. 32–40, 2003.

[77] W. R. Klein and B. D. Cook. Unified approach to ultrasonic light diffraction. *IEEE Transactions on Sonics and Ultrasonics*, **14**(3), pp. 123–134, 1967.

[78] E. F. Knott, J. F. Shaeffer, and M. T. Tuley. *Radar Cross Section*. SciTech Publishing, Inc., Raleigh, NC, USA, 2nd edition, 2004.

[79] A. Korpel. *Acousto-optics*. Optical engineering, 16. Marcel Dekker Inc, New York, NY, USA, 1st edition, 1988.

[80] G. Kristensson. *Scattering of electromagnetic waves by obstacles*. SciTech, Edison, NJ, USA, 2016.

[81] S. K. Lam, A. Pitrou, and S. Seibert. Numba: A LLVM-based Python JIT compiler. In *Proceedings of the Second Workshop on the LLVM Compiler Infrastructure in HPC*, LLVM '15, New York, NY, USA, 2015. Association for Computing Machinery.

[82] B. Lau, M. Capek, and A. M. Hassan. Characteristic modes: Progress, overview, and emerging topics. *IEEE Antennas and Propagation Magazine*, **64**(2), pp. 14–22, 2022.

[83] X. S. Li. An overview of SuperLU: Algorithms, implementation, and user interface. *ACM Transactions on Mathematical Software*, **31**(3), pp. 302–325, 2005.

[84] A. Logg, K. B. Ølgaard, M. Rognes, G. N. Wells, and M. S. Alnæs. FFCx: Next generation FEniCS form compiler, 2023. https://github.com/FEniCS/ffcx. Accessed 4 Mar. 2024.

[85] J. Lundgren, K. Schab, M. Capek, M. Gustafsson, and L. Jelinek. Iterative calculation of characteristic modes using arbitrary full-wave solvers. *IEEE Antennas and Wireless Propagation Letters*, **22**(4), pp. 799–803, 2023.

[86] S. N. Makarov. *Antenna and EM Modeling with MATLAB*. John Wiley and Sons, Inc., New York, NY, USA, 2002.

[87] Y. Mao, Y. Zhong, Q. Zhan, D. Wang, and Q. H. Liu. A simple way of applying the Calderón preconditioner to a finite-element boundary-integral method. *IEEE Transactions on Antennas and Propagation*, **71**(6), pp. 5510–5515, 2023.

[88] J. M. Marshall, A. M. Peterson, and A. A. Barnes. Combined radar-acoustic sounding system. *Applied Optics*, **11**(1), pp. 108–112, 1972.

[89] P. T. May, R. G. Strauch, K. P. Moran, and W. L. Ecklund. Temperature sounding by RASS with wind profiler radars: a preliminary study. *IEEE Transactions on Geoscience and Remote Sensing*, **28**(1), pp. 19–28, 1990.

[90] B. McDonald and A. Wexler. Finite-element solution of unbounded field problems. *IEEE Transactions on Microwave Theory and Techniques*, **20**(12), pp. 841–847, 1972.

[91] D. Meagher. Geometric modeling using octree encoding. *Computer Graphics and Image Processing*, **19**(2), pp. 129–147, 1982.

[92] K. Mei. Unimoment method of solving antenna and scattering problems. *IEEE Transactions on Antennas and Propagation*, **22**(6), pp. 760–766, 1974.

[93] E. Michielssen and A. Boag. A multilevel matrix decomposition algorithm for analyzing scattering from large structures. *IEEE Transactions on Antennas and Propagation*, **44**(8), pp. 1086–1093, 1996.

[94] G. Mie. Beiträge zur optik trüber medien, speziell kolloidaler metallösungen. *Annalen der Physik*, **330**(3), pp. 377–445, 1908.

[95] C. G. Montgomery, R. H. Dicke, and E. M. Purcell. *Principles of Microwave Circuits*. McGraw-Hill, New York, United States, 1948.

[96] M. Morgan and K. Mei. Finite-element computation of scattering by inhomogeneous penetrable bodies of revolution. *IEEE Transactions on Antennas and Propagation*, **27**(2), pp. 202–214, 1979.

[97] M. Morgan, C. Chen, S. Hill, and P. Barber. Finite element-boundary integral formulation for electromagnetic scattering. *Wave Motion*, **6**(1), pp. 91–103, 1984.

[98] N. K. Nikolova. *Introduction to Microwave Imaging*. EuMA High Frequency Technologies Series. Cambridge University Press, 2017.

[99] T. E. Oliphant. Python for scientific computing. *Computing in Science & Engineering*, **9**(3), pp. 10–20, 2007.

[100] Open Source Initiative. The 3-clause BSD license. https://opensource.org/license/bsd-3-clause/. Accessed 1 Feb. 2024.

[101] S. J. Orfanidis. *Diffraction – Plane-Wave Spectrum*, chapter 19, pp. 844 – 922. Electromagnetic Waves and Antennas. Rutgers University, 2016.

[102] K. Paulsen, D. Lynch, and J. Strahbehn. Three-dimensional finite, boundary, and hybrid element solutions of the maxwell equations for lossy dielectric media. *IEEE Transactions on Microwave Theory and Techniques*, **36**(4), pp. 682–693, 1988.

[103] K. Persson, M. Gustafsson, G. Kristensson, and B. Widenberg. Radome diagnostics—source reconstruction of phase objects with an equivalent currents approach. *IEEE Transactions on Antennas and Propagation*, **62**(4), pp. 2041–2051, 2014.

[104] T. Peters and J. Volakis. Application of a conjugate gradient FFT method to scattering from thin planar material plates. *IEEE Transactions on Antennas and Propagation*, **36**(4), pp. 518–526, 1988.

[105] A. G. Polimeridis and J. R. Mosig. Complete semi-analytical treatment of weakly singular integrals on planar triangles via the direct evaluation method. *International Journal for Numerical Methods in Engineering*, **83**(12), pp. 1625–1650, 2010.

[106] A. G. Polimeridis and J. R. Mosig. On the direct evaluation of surface integral equation impedance matrix elements involving point singularities. *IEEE Antennas and Wireless Propagation Letters*, **10**, pp. 599–602, 2011.

[107] A. G. Polimeridis, J. M. Tamayo, J. M. Rius, and J. R. Mosig. Fast and accurate computation of hypersingular integrals in Galerkin surface integral equation formulations via the direct evaluation method. *IEEE Transactions on Antennas and Propagation*, **59**(6), pp. 2329–2340, 2011.

[108] A. G. Polimeridis, F. Vipiana, J. R. Mosig, and D. R. Wilton. DIRECTFN: Fully numerical algorithms for high precision computation of singular integrals in Galerkin SIE methods. *IEEE Transactions on Antennas and Propagation*, **61**(6), pp. 3112–3122, 2013.

[109] A. G. Polimeridis and T. V. Yioultsis. On the direct evaluation of weakly singular integrals in Galerkin mixed potential integral equation formulations. *IEEE Transactions on Antennas and Propagation*, **56**(9), pp. 3011–3019, 2008.

[110] D. M. Pozar. *Microwave Engineering*. John Wiley & Sons, Inc., 3rd edition, 2005.

[111] J. L. A. Quijano and G. Vecchi. Field and source equivalence in source reconstruction on 3D surfaces. *Progress In Electromagnetics Research*, **103**, pp. 67–100, 2010.

[112] S. Rao, D. Wilton, and A. Glisson. Electromagnetic scattering by surfaces of arbitrary shape. *IEEE Transactions on Antennas and Propagation*, **30**(3), pp. 409–418, 1982.

[113] M. Rezghi and L. Eldén. Diagonalization of tensors with circulant structure. *Linear Algebra and its Applications*, **435**(3), pp. 422–447, 2011.

[114] J. A. Richards. *Remote Sensing with Imaging Radar*. Springer-Verlag, Berlin, Heidelberg, Germany, 2009.

[115] M. A. Richards, J. A. Scheer, and W. A. Holm, editors. *Principles Of Modern Radar*, volume 1: Basic Principles. SciTech Publishing, Inc., Raleigh, NC, USA, 2010.

[116] V. Rokhlin. Rapid solution of integral equations of scattering theory in two dimensions. *Journal of Computational Physics*, **86**(2), pp. 414–439, 1990.

[117] V. Rokhlin. Diagonal forms of translation operators for the helmholtz equation in three dimensions. *Applied and Computational Harmonic Analysis*, **1**(1), pp. 82–93, 1993.

[118] T. Rossing, editor. *Springer Handbook of Acoustics*. Springer-Verlag, 2nd edition, 2014.

[119] W. L. Rubin. Radar–acoustic detection of aircraft wake vortices. *Journal of Atmospheric and Oceanic Technology*, **17**(8), pp. 1058–1065, 2000.

[120] T. Rylander, P. Ingelström, and A. Bondesson. *Computational Electromagnetics*. Springer Science+Business Media, New York, NY, USA, 2nd edition, 2013.

[121] Y. Saad. *Iterative Methods for Sparse Linear Systems*. Society for Industrial and Applied Mathematics, Philadelphia, USA, 2nd edition, 2003.

[122] Y. G. Sahin and T. Ince. Early forest fire detection using radio-acoustic sounding system. *Sensors*, **9**(3), pp. 1485–1498, 2009.

[123] B. E. A. Saleh and M. C. Teich. *Acousto-Optics*, chapter 19, pp. 804–833. Fundamentals of Photonics. John Wiley & Sons, Inc., Hoboken, New Jersey, 2nd edition, 2007.

[124] T. Sarkar, E. Arvas, and S. Rao. Application of FFT and the conjugate gradient method for the solution of electromagnetic radiation from electrically large and small conducting bodies. *IEEE Transactions on Antennas and Propagation*, **34**(5), pp. 635–640, 1986.

[125] L. W. Schmerr. *Fundamentals of Ultrasonic Nondestructive Evaluation*. Springer Series in Measurement Science and Technology. Springer International Publishing, 2nd edition, 2016.

[126] M. W. Scroggs, I. A. Baratta, C. N. Richardson, and G. N. Wells. Basix: a runtime finite element basis evaluation library. *Journal of Open Source Software*, **7**(73), pp. 3982, 2022.

[127] M. W. Scroggs, J. S. Dokken, C. N. Richardson, and G. N. Wells. Construction of arbitrary order finite element degree-of-freedom maps on polygonal and polyhedral cell meshes. *ACM Transactions on Mathematical Software*, **48**(2), 2022.

[128] M. W. Scroggs et al. DefElement: an encyclopedia of finite element definitions, 2024. https://defelement.com. Accessed 5 Jan. 2024.

[129] C. E. Shannon. A mathematical theory of communication. *The Bell System Technical Journal*, **27**(3), pp. 379–423, 1948.

[130] X.-Q. Sheng, J.-M. Jin, J. Song, C.-C. Lu, and W. C. Chew. On the formulation of hybrid finite-element and boundary-integral methods for 3-D scattering. *IEEE Transactions on Antennas and Propagation*, **46**(3), pp. 303–311, 1998.

[131] P. J. Shull. *Nondestructive evaluation: theory, techniques, and applications*. CRC press, Boca Raton, FL, USA, 2002.

[132] D. Sievenpiper, L. Zhang, R. Broas, N. Alexopolous, and E. Yablonovitch. High-impedance electromagnetic surfaces with a forbidden frequency band. *IEEE Transactions on Microwave Theory and Techniques*, **47**(11), pp. 2059–2074, 1999.

[133] P. Silvester and M.-S. Hsieh. Finite-element solution of 2-dimensional exterior-field problems. *Proceedings of the Institution of Electrical Engineers*, **118**(12), pp. 1743–1747, 1971.

[134] A. Sommerfeld. *Partial Differential Equations in Physics*. Academic Press, New York, NY, USA, 1949.

[135] J. Song, C.-C. Lu, and W. C. Chew. Multilevel fast multipole algorithm for electromagnetic scattering by large complex objects. *IEEE Transactions on Antennas and Propagation*, **45**(10), pp. 1488–1493, 1997.

[136] J. M. Song and W. C. Chew. Multilevel fast-multipole algorithm for solving combined field integral equations of electromagnetic scattering. *Microwave and Optical Technology Letters*, **10**(1), pp. 14–19, 1995.

[137] D. L. Sounas and A. Alù. Non-reciprocal photonics based on time modulation. *Nature Photonics*, **11**(12), pp. 774–783, 2017.

[138] R. Stallman. The GNU general public license v3.0, 2007. https://www.gnu.org/licenses/gpl-3.0.html. Accessed 1 Feb. 2024.

[139] R. H. Stolt. Migration by Fourier transform. *Geophysics*, **43**(1), pp. 23–48, 1978.

[140] Texas Instruments. mmWave radar sensors. https://www.ti.com/sensors/mmwave-radar/overview.html. Accessed 7 Feb. 2024.

[141] The Institute of Electrical and Electronics Engineers, Inc. IEEE standard for radar definitions. *IEEE Std 686-2017 (Revision of IEEE Std 686-2008)*, p. 33, 2017.

[142] The MathWorks, Inc. MATLAB performance - MATLAB & Simulink. https://www.mathworks.com/products/matlab/performance.html. Accessed 7 Feb. 2024.

[143] E. Tiesinga, P. J. Mohr, D. B. Newell, and B. N. Taylor. CODATA recommended values of the fundamental physical constants: 2018. *Journal of Physical and Chemical Reference Data*, **50**(3), pp. 033105, 09 2021.

[144] L. N. Trefethen and D. Bau. *Numerical Linear Algebra*. Society for Industrial and Applied Mathematics, Philadelphia, PA, 1997.

[145] J. Van Bladel. Electromagnetic fields in the presence of rotating bodies. *Proceedings of the IEEE*, **64**(3), pp. 301–318, 1976.

[146] J. Van Bladel. *Singular electromagnetic fields and sources*. Clarendon Press, Oxford, UK, 1991.

[147] J. G. Van Bladel. *Electromagnetic Fields*. John Wiley & Sons, Hoboken, NJ, USA, 2007.

[148] E. van den Berg and M. P. Friedlander. Probing the Pareto frontier for basis pursuit solutions. *SIAM Journal on Scientific Computing*, **31**(2), pp. 890–912, 2008.

[149] E. van den Berg and M. P. Friedlander. SPGL1: A solver for large-scale sparse reconstruction, 2019. https://friedlander.io/spgl1. Accessed 3 Mar. 2024.

[150] F. Vipiana, D. R. Wilton, and W. A. Johnson. Advanced numerical schemes for the accurate evaluation of 4-D reaction integrals in the method of moments. *IEEE Transactions on Antennas and Propagation*, **61**(11), pp. 5559–5566, 2013.

[151] C. R. Vogel. *Computational Methods for Inverse Problems*. Society for Industrial and Applied Mathematics, Philadelphia, PA, USA, 2002.

[152] J. L. Volakis and K. Sertel. *Integral equation methods for electromagnetics*. SciTech Publishing, Raleigh, NC, USA., 2012.

[153] J. L. Volakis, M. Shields, G. Manara, S. R. Rengarajan, and Y. Hao. *100 Years of the International Union of Radio Science*, chapter 28: URSI Commission B Centennial History Contribution, pp. 411–436. URSI Press, Gent, Belgium, 2021.

[154] M. N. Vouvakis, Seung-Cheol Lee, Kezhong Zhao, and Jin-Fa Lee. A symmetric FEM-IE formulation with a single-level IE-QR algorithm for solving electromagnetic radiation and scattering problems. *IEEE Transactions on Antennas and Propagation*, **52**(11), pp. 3060–3070, 2004.

[155] C. Waldschmidt, J. Hasch, and W. Menzel. Automotive radar — from first efforts to future systems. *IEEE Journal of Microwaves*, **1**(1), pp. 135–148, 2021.

[156] T. Wan, M. Z. Li, and L. F. Li. Direct solution of finite element-boundary integral system for electromagnetic analysis in half-space. *IEEE Transactions on Antennas and Propagation*, **68**(8), pp. 6461–6466, 2020.

[157] N. Wingren. Acousto-electromagnetic interaction in materials for aerospace composites. M.s. thesis, Dept. of Elect. and Inform. Technol., Lund Univ., Lund, Sweden, 2019.

[158] A. Yaghjian. Approximate formulas for the far field and gain of open-ended rectangular waveguide. *IEEE Transactions on Antennas and Propagation*, **32**(4), pp. 378–384, 1984.

[159] A. Yaghjian. An overview of near-field antenna measurements. *IEEE Transactions on Antennas and Propagation*, **34**(1), pp. 30–45, 1986.

[160] M. Yang, B. Wu, H. Gao, and X. Sheng. An effective $\mathcal{H}$-LU-based preconditioner for the FE-BI-MLFMA for 3-D scattering problems. *IEEE Antennas and Wireless Propagation Letters*, **18**(12), pp. 2766–2770, 2019.

[161] X. Yang, M. Jiang, L. Shen, P.-H. Jia, Z. Rong, Y. Chen, L. Lei, and J. Hu. A flexible FEM-BEM-DDM for EM scattering by multiscale anisotropic objects. *IEEE Transactions on Antennas and Propagation*, **69**(12), pp. 8562–8573, 2021.

[162] Z. Yang, X.-W. Yuan, X.-W. Huang, M.-L. Yang, and X.-Q. Sheng. Resistive sheet boundary condition-based nonconformal domain decomposition FE-BI-MLFMA for electromagnetic scattering from inhomogeneous objects with honeycomb structures. *IEEE Transactions on Antennas and Propagation*, **70**(10), pp. 9483–9496, 2022.

[163] P. Ylä-Oijala, S. P. Kiminki, K. Cools, F. P. Andriulli, and S. Järvenpää. Mixed discretization schemes for electromagnetic surface integral equations. *International Journal of Numerical Modelling: Electronic Networks, Devices and Fields*, **25**(5-6), pp. 525–540, 2012.

[164] S. Yrjölä, M. Matinmikko-Blue, and P. Ahokangas. *The Changing World of Mobile Communications*, chapter 2: The Evolution of Mobile Communications, pp. 13–44. Palgrave Macmillan, Cham, Switzerland, 2024.

[165] X. Yuan. Three-dimensional electromagnetic scattering from inhomogeneous objects by the hybrid moment and finite element method. *IEEE Transactions on Microwave Theory and Techniques*, **38**(8), pp. 1053–1058, 1990.

[166] X. Yuan, D. Lynch, and J. Strohbehn. Coupling of finite element and moment methods for electromagnetic scattering from inhomogeneous objects. *IEEE Transactions on Antennas and Propagation*, **38**(3), pp. 386–393, 1990.

[167] K. Zhao, M. Vouvakis, and J.-F. Lee. The adaptive cross approximation algorithm for accelerated method of moments computations of EMC problems. *IEEE Transactions on Electromagnetic Compatibility*, **47**(4), pp. 763–773, 2005.

[168] R. Zoughi. *Microwave Non-Destructive Testing and Evaluation*. Kluwer academic publishers, Dordrecht, The Netherlands, 2000.

[169] P. Zwamborn and P. M. van den Berg. Computation of electromagnetic fields inside strongly inhomogeneous objects by the weak-conjugate-gradient fast-Fourier-transform method. *Journal of the Optical Society of America A*, **11**(4), pp. 1414–1421, 1994.

Part II: Included Papers

Using Open Source to Accelerate Development of a Finite Element-Boundary Integral Code

Paper I

N. Wingren and D. Sjöberg

Published as: N. Wingren and D. Sjöberg, "Using Open Source to Accelerate Development of a Finite Element-Boundary Integral Code," *IEEE Open Journal of Antennas and Propagation*, vol. 5, no. 3, pp. 587–600, 2024.

Abstract

Open-source software has been highly influential on software development in many fields, and also has a history within computational electromagnetics. With large amounts of open-source code available, both from within computational electromagnetics and from other fields, new combinations can be made by using already existing code packages. This can be especially beneficial to developers who do not otherwise have access to a substantial codebase. In this article we describe how a finite element-boundary integral code using the adaptive cross approximation was developed by combining different existing open-source software packages with new code in Python. We provide a brief overview of the numerical methods used, but our focus is on the implementation and insights that might be useful to others who could benefit from using open-source software in their work. Three numerical examples are also presented to demonstrate accuracy, performance and use of complex materials. Our code is provided at github.com/nwingren/fe2ms both to demonstrate how the open-source packages were combined in practice, but also for those who wish to test the code themselves.

1 Introduction

Open source is a term used in software development for making the source code of a program freely available for inspection, modification and redistribution. In computational electromagnetics, this has been used at least since early versions of the numerical electromagnetics code (NEC) developed in the 1970s, which was particularly important for development related to the method of moments (MoM) [1,2]. Today there are many other open-source codes suitable for electromagnetics such as the finite-difference time-domain (FDTD) codes Meep [3] and gprMax [4] or the finite element method (FEM) codes Elmer [5] and FEniCSx [6–10]. Much more code development happens outside of CEM though, and utilizing these resources can be a great help when working with open-source software. Although some parts of a code are specific to CEM, there are more generic parts which can benefit from combining code from other fields.

Combining code from different sources can prove challenging at times, especially if the codes are written in different programming languages. Traditionally in computational applications, fast compiled languages like Fortran or C++ have been used, however, they suffer from low flexibility and time consuming development compared to languages like Python or Julia [11, 12]. While Julia is in many regards superior to Python [12], it still lacks the sheer number of native packages that Python has available. This can be exemplified by comparing the Python Package Index with about 500 000 packages [13] to the much fewer number of about 10 000 registered packages for Julia [14] (as of December 2023). Many highly developed computational packages also have native Python interfaces, like the aforementioned Meep, gprMax and FEniCSx. While the nominal performance of Python is quite poor compared to many other languages, it can

be improved by using packages like NumPy [15] and SciPy [16] with fast underlying code. More recently, performance gain has also become possible through just-in-time (JIT) compilation using tools like Numba [17].

One use case which can benefit from a combination of different computational codes is the development of a hybrid code, as there might then exist good implementations of the different constituent parts that are not yet combined. The finite element-boundary integral (FE-BI) method is a hybrid method combining FEM and MoM. Its origins are from outside electromagnetics [18–20], but there is a long history within the field as well [21–23]. From an FEM point of view, it can be seen as an exact boundary condition for open boundaries, playing a similar role as absorbing boundary conditions like perfectly matched layers (PML) [24]. In certain situations, the hybrid method can outperform other open boundary methods in FEM. An example could be multiple reflecting geometries or widely separated scatterers, where, for example, enclosing the computational region with a PML would require discretization of large regions of free space.

Pure MoM is widely used, and its surface formulations perform particularly well for problems involving perfect electric conductors (PEC) or homogeneous dielectric structures [25–27]. However, more expensive volumetric formulations are typically required for problems containing inhomogeneous dielectrics [28], or more complex media containing anisotropy [29, 30] or magnetoelectric interaction [31, 32]. With the FE-BI method, all these cases can be handled with ease [33]. One more notable detail about MoM is the need for methods that reduce the required memory and accelerate the solution process as the problem size grows. Many different methods exist such as the multilevel fast multipole algorithm (MLFMA) [34,35], the adaptive cross approximation (ACA) [36,37] and the adaptive integral method (AIM) [38]. The same need for such acceleration methods is present for the FE-BI hybrid method as the BI part dominates with regards to memory and computational complexity, and many different schemes have been applied [39–41]. This is a natural consequence of dense matrices arising from integral equations in MoM, as opposed to sparse matrices arising from differential equations in FEM. Recent work related to the FE-BI method has focused on, among others, domain decomposition [42–44], $\mathcal{H}$-matrix methods for fast direct solution [41] and preconditioning [45, 46].

The purpose of this article is to describe our implementation of the FE-BI method done by combining many different open-source packages in a way that can help readers who might be interested in using the same approach in their own work. We describe the method briefly, but the focus is primarily on the development process and what we have learned from it. Some results showing the capability of the code are also included to demonstrate that reasonable performance is achieved by using a multilevel ACA, and that the code can be used for general problems involving linear bianisotropic media. The code is written primarily in Python and is publicly available at github.com/nwingren/fe2ms under the GNU general purpose license, version 3. The code is mainly based on the FEniCSx package for FEM computations, but the article also describes how many other packages, as well as new code, are combined into the presented FE-BI

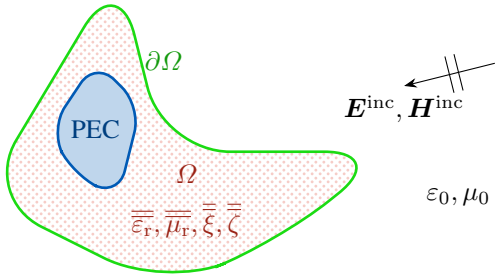

Figure 1: General scattering problem geometry. The volume Ω can contain inhomogeneous linear media and internal PEC regions defined by their boundaries. Excitation is due to an incident plane wave or combinations of plane waves from the exterior.

code. The article is structured as follows. Firstly, in section 2 the FE-BI method is introduced briefly, as well as the multilevel ACA. In section 3 the development of the code is described, with emphasis on how it was done and insights others might benefit from. In section 4 the different components of the code are described. In section 5 three different scattering problems are presented, and the results demonstrate the capabilities and accuracy of the code. Finally, the article is concluded in section 6.

2 Method Description

2.1 Formulations

To introduce the mathematical formulation of the FE-BI method, a general scattering problem geometry is shown in Fig. 1. A volume Ω with boundary $\partial\Omega$ is considered. Within Ω, the problem is described by the finite element method. On $\partial\Omega$ the boundary integral method is used as a boundary condition which describes the physics of the open boundary without approximation.

The FE formulation depends on the constitutive relations of the problem media. In this work, we distinguish between general linear magnetoelectric media as

$$\boldsymbol{D} = \varepsilon_0 \left(\overline{\overline{\varepsilon_\mathrm{r}}} \cdot \boldsymbol{E} + \eta_0 \overline{\overline{\xi}} \cdot \boldsymbol{H} \right) \tag{2.1}$$

$$\boldsymbol{B} = \mu_0 \left(\frac{1}{\eta_0} \overline{\overline{\zeta}} \cdot \boldsymbol{E} + \overline{\overline{\mu_\mathrm{r}}} \cdot \boldsymbol{H} \right) \tag{2.2}$$

and more simple linear media as

$$\boldsymbol{D} = \varepsilon_0 \overline{\overline{\varepsilon_\mathrm{r}}} \cdot \boldsymbol{E} \tag{2.3}$$

$$\boldsymbol{B} = \mu_0 \overline{\overline{\mu_\mathrm{r}}} \cdot \boldsymbol{H} \tag{2.4}$$

where ε_0, μ_0 and η_0 are the free space permittivity, permeability and wave impedance, respectively, whereas $\overline{\overline{\varepsilon_\mathrm{r}}}$, $\overline{\overline{\mu_\mathrm{r}}}$, $\overline{\overline{\xi}}$ and $\overline{\overline{\zeta}}$ are unitless tensor quantities describing the medium. The distinction follows into the governing equations used in the FE formulation. These are

$$\begin{aligned}\nabla \times \left(\overline{\overline{\mu_\mathrm{r}}}^{-1} \cdot \nabla \times \boldsymbol{E}\right) - k_0^2 \left(\overline{\overline{\varepsilon_\mathrm{r}}} - \overline{\overline{\xi}} \cdot \overline{\overline{\mu_\mathrm{r}}}^{-1} \cdot \overline{\overline{\zeta}}\right) \cdot \boldsymbol{E} \\ + \mathrm{j}k_0 \left[\nabla \times \left(\overline{\overline{\mu_\mathrm{r}}}^{-1} \cdot \overline{\overline{\zeta}} \cdot \boldsymbol{E}\right) - \overline{\overline{\xi}} \cdot \overline{\overline{\mu_\mathrm{r}}}^{-1} \cdot \nabla \times \boldsymbol{E}\right] = \boldsymbol{0}\end{aligned} \tag{2.5}$$

for general linear magnetoelectric media [33] and

$$\nabla \times \left(\overline{\overline{\mu_\mathrm{r}}}^{-1} \cdot \nabla \times \boldsymbol{E}\right) - k_0^2 \overline{\overline{\varepsilon_\mathrm{r}}} \cdot \boldsymbol{E} = \boldsymbol{0} \tag{2.6}$$

for more simple linear media [24]. By enforcing a boundary condition

$$\hat{\boldsymbol{n}} \times \left(\overline{\overline{\mu_\mathrm{r}}}^{-1} \cdot \nabla \times \boldsymbol{E}\right) = -\mathrm{j}k_0 \eta_0 \hat{\boldsymbol{n}} \times \boldsymbol{H} \tag{2.7}$$

on $\partial\Omega$, the FE system matrix entries can be derived as

$$\begin{aligned}K_{mn}^{\mathrm{XY}} = &\int_\Omega (\nabla \times \boldsymbol{N}_m^{\mathrm{X}}) \cdot \left(\overline{\overline{\mu_\mathrm{r}}}^{-1} \cdot \nabla \times \boldsymbol{N}_n^{\mathrm{Y}}\right) \mathrm{d}V \\ &- k_0^2 \int_\Omega \boldsymbol{N}_m^{\mathrm{X}} \cdot \left(\overline{\overline{\varepsilon_\mathrm{r}}} - \overline{\overline{\xi}} \cdot \overline{\overline{\mu_\mathrm{r}}}^{-1} \cdot \overline{\overline{\zeta}}\right) \cdot \boldsymbol{N}_n^{\mathrm{Y}} \,\mathrm{d}V \\ &+ \mathrm{j}k_0 \int_\Omega (\nabla \times \boldsymbol{N}_m^{\mathrm{X}}) \cdot \overline{\overline{\mu_\mathrm{r}}}^{-1} \cdot \overline{\overline{\zeta}} \cdot \boldsymbol{N}_n^{\mathrm{Y}} \,\mathrm{d}V \\ &- \mathrm{j}k_0 \int_\Omega \boldsymbol{N}_m^{\mathrm{X}} \cdot \left(\overline{\overline{\xi}} \cdot \overline{\overline{\mu_\mathrm{r}}}^{-1} \cdot \nabla \times \boldsymbol{N}_n^{\mathrm{Y}}\right) \mathrm{d}V\end{aligned} \tag{2.8}$$

for general linear magnetoelectric meda [33] and

$$K_{mn}^{\mathrm{XY}} = \int_\Omega \left(\nabla \times \boldsymbol{N}_m^{\mathrm{X}}\right) \cdot \left(\overline{\overline{\mu_\mathrm{r}}}^{-1} \cdot \nabla \times \boldsymbol{N}_n^{\mathrm{Y}}\right) \mathrm{d}V - k_0^2 \int_\Omega \boldsymbol{N}_m^{\mathrm{X}} \cdot \overline{\overline{\varepsilon_\mathrm{r}}} \cdot \boldsymbol{N}_n^{\mathrm{Y}} \,\mathrm{d}V \tag{2.9}$$

for more simple linear media [24], as well as

$$B_{mn} = \mathrm{j}k_0 \oint_{\partial\Omega} \hat{\boldsymbol{n}} \cdot (\boldsymbol{N}_m^{\mathrm{S}} \times \boldsymbol{N}_n^{\mathrm{S}}) \,\mathrm{d}S \tag{2.10}$$

in both cases [24]. $\boldsymbol{N}$ are curl conforming basis functions and $\mathrm{X}, \mathrm{Y} \in \{\mathrm{I}, \mathrm{S}\}$. I and S indicate that the quantity is connected to mesh edges on the interior of Ω and on the boundary $\partial\Omega$, respectively. The full FE-BI system is written as [24]

$$\begin{bmatrix} K^{\mathrm{II}} & K^{\mathrm{IS}} & 0 \\ K^{\mathrm{SI}} & K^{\mathrm{SS}} & B \\ 0 & P & Q \end{bmatrix} \begin{Bmatrix} E^{\mathrm{I}} \\ E^{\mathrm{S}} \\ \bar{H}^{\mathrm{S}} \end{Bmatrix} = \begin{Bmatrix} 0 \\ 0 \\ b^{\mathrm{E}} \end{Bmatrix}. \tag{2.11}$$

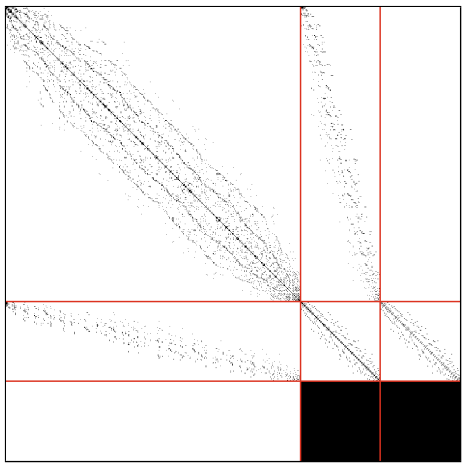

Figure 2: Nonzero entries of a FE-BI system matrix with red lines showing limits of the blocks in (2.11). The system corresponds to a small PEC sphere coated by a thin dielectric layer.

where P, Q and b^{E} are determined by connecting $\boldsymbol{E}$ and $\boldsymbol{H}$ on $\partial\Omega$ using an integral equation. This is a partly sparse, partly dense system due to the inherent characteristics of the FE and BI parts respectively, as is illustrated in Fig. 2. With this system, it is assumed that the problem is a pure scattering problem, as the right-hand side would otherwise have additional non-zero entries. Interior sources can be added to model, for instance, a transmitting antenna.

Different integral formulations can be used to obtain P, Q and b^{E}, and they have different benefits and drawbacks. An easily implementable formulation is the electric field integral equation (EFIE) using the TE formulation from [39], giving the different blocks as

$$P_{mn} = \oint_{\partial\Omega} \boldsymbol{\Lambda}_m(\boldsymbol{r}) \cdot \left(\tilde{\mathscr{K}}(\boldsymbol{\Lambda}_n)(\boldsymbol{r}) - \frac{1}{2}\hat{\boldsymbol{n}} \times \boldsymbol{\Lambda}_n(\boldsymbol{r}) \right) \mathrm{d}S \tag{2.12}$$

$$Q_{mn} = \oint_{\partial\Omega} \boldsymbol{\Lambda}_m(\boldsymbol{r}) \cdot \mathscr{L}(\boldsymbol{\Lambda}_n)(\boldsymbol{r}) \, \mathrm{d}S \tag{2.13}$$

$$b^{\mathrm{E}}_m = \oint_{\partial\Omega} \boldsymbol{\Lambda}_m(\boldsymbol{r}) \cdot \boldsymbol{E}^{\mathrm{inc}}(\boldsymbol{r}) \, \mathrm{d}S. \tag{2.14}$$

where $\boldsymbol{\Lambda}$ are divergence conforming basis functions, $\tilde{\mathscr{K}}$ and $\mathscr{L}$ are integral operators connecting magnetic currents to electric fields, and electric currents to electric fields, respectively, and $\boldsymbol{E}^{\mathrm{inc}}$ is the incident electric field. The tilde on the $\tilde{\mathscr{K}}$ operator indicates that the integral operator is computed in a principal value sense due to a singularity extraction. One drawback of EFIE-based systems is that they are susceptible to interior resonances which can result in inaccurate solutions at certain frequencies, as well as poor performance for iterative solvers in a band around those frequencies [39]. This can be remedied using

other formulations based on the combined field integral equation (CFIE), though they typically require different test functions than shown in (2.12)–(2.13) to be fully effective. There is a possibility to reduce some effects of interior resonances through the TETH (meaning tangential testing of $\boldsymbol{E}$ and $\boldsymbol{H}$) CFIE formulation from [39] which only uses linear combinations of (2.12) and (2.13). This does not eliminate interior resonances though, but it typically improves the performance for iterative solvers at frequencies near a resonance. Another way to eliminate the interior resonance problem is to use one of the stationary FE-BI formulations described in [47], which also results in a symmetric system matrix.

2.2 The Multilevel Adaptive Cross Approximation

To improve performance of the method, the dense matrices P and Q from the BI part are assembled on an $\mathcal{H}$-matrix form using a multilevel adaptive cross approximation (ACA). The direct effect of this is that representations of the matrices can be stored using much less memory than by storing them fully. Furthermore, if the compression achieved using this representation is significant, matrix-vector multiplications can be computed with fewer operations than would be needed using a full matrix. The result of using the multilevel ACA is thus reduced memory usage as well as accelerated iterative methods, which are based on matrix-vector multiplications. The ACA is only one such acceleration method among many, but one advantage it has is that the algorithm itself is purely algebraic. This means that the same implementation of the ACA can be used for many different kernels without modification, and experimentation with different formulations in the BI part of the method is therefore easy. With that said, it is good to keep in mind that the performance of the method depends on the problem it is applied to, and the type of clustering that is used.

The ACA has been thoroughly described in the literature [36, 37, 48] and will only be briefly presented here. The main point of the algorithm is compression of rank-deficient matrices. In general, an $m \times n$ matrix A of rank k can be written on the form

$$A = UV^{\mathrm{H}} \tag{2.15}$$

where U is $m \times k$ and V is $n \times k$. The ACA generates an approximation of matrices on this form by performing assembly only of some rows and columns of the matrix A. In addition, there is a stopping criterion based only on a desired error tolerance, requiring no prior knowledge of k.

For efficient compression using the ACA, the matrix A needs to have a numerical rank $k \ll m, n$ (for some error tolerance). This is typically not the case for an entire BI system matrix, but rank-deficient and compressible sub-blocks can be found. This subdivision into blocks is typically done by geometric clustering of unknowns using an octree, which creates groups at different levels as illustrated in Fig. 3. Assembly is then performed fully for interactions within groups and between directly adjacent groups at the leaf level of the octree. For

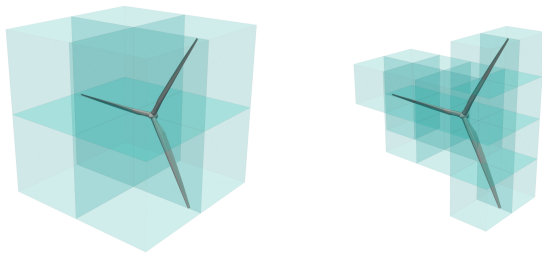

Figure 3: Two consecutive octree levels for a wind turbine rotor geometry. The left level has no non-adjacent groups while the right level has several. Empty groups are not shown.

non-adjacent groups, assembly is performed using the ACA, and this can be done in a multilevel way. The structure of a BI matrix A after this procedure is

$$A \approx A_{\text{near}} + \sum_i U_{A,i} V_{A,i}^{\text{H}} \tag{2.16}$$

where A_{near} is a sparse matrix representing the near interactions (including singular terms), and the sum is over all group interactions assembled using the ACA. The blocks assembled using the ACA can be further compressed using a recompression technique based on the QR and singular value decompositions (SVD) [49].

3 Implementation using Open-Source Software

3.1 Background

The code described in this paper has its origin in a project named Fast and Efficient ElectroMagnetic Solvers (hence the abbreviation FE2MS for the code presented here) where a FE-BI hybrid code was needed, and at an early stage it was decided that it would use existing open-source software. There were many considerations leading to this decision, but a crucial factor was that we did not have access to an existing in-house code to build upon. The options at the outset were to either implement a complete code from scratch, or investigate whether there was existing open-source software which could be used. The latter offered a possibility of much faster development, which was appealing, especially since the active code development was performed by the first author of the paper as a single developer. As will be discussed in the following sections, this open-source approach can range from using fairly mature open-source packages with only

Table 1: Python code snippets for assembly-related tasks in FeniCSx and Bempp-cl.

FEniCSx

```
ufl_form = (
    ufl.inner(
        inv_mur * ufl.curl(u), ufl.curl(v)
    )
    - k0**2 * ufl.inner(epsr * u, v)
) * ufl.dx
K = dolfinx.fem.assemble_matrix(
    dolfinx.fem.form(ufl_form)
)
```

Bempp-cl

```
ops = bempp.api.operators.boundary.maxwell
Q = ops.electric_field(
    trace_space, range_space, dual_space, k0
).weak_form()
```

small additions, to more substantial development with open-source code used for specific functions.

3.2 Initial Implementation

A first implementation of a FE-BI hybrid code was based on the two open-source packages FEniCSx and Bempp-cl. FEniCSx is a highly versatile FEM package consisting of the components DOLFINx [6], FFCx [7], Basix [8, 9] and UFL [10]. Bempp-cl is a package for boundary element methods with support for a number of operators including some based on Maxwell's equations [50]. Particularly interesting was that Bempp-cl was designed to be compatible to FEniCSx, with demos available to show how to connect them. To use these packages would mean that there could be more focus on testing various formulations and solution methods and less on developing low-level functionality.

Both FeniCSx and Bempp-cl have interfaces in Python, using the rich framework for scientific computing available through NumPy and SciPy. While FeniCSx has its core written in C++ for performance, Bempp-cl is written almost purely in Python with performance obtained using Numba and OpenCL. For an end user, these distinctions are not necessary to keep in mind though as both packages have simple public interfaces. Python was selected as the main programming language primarily due to these two packages, and this facilitated further connections between different packages. One main reason for this is the wide use of NumPy ndarray data structures in Python packages for scientific computing. Since so many packages use this data structure, as well as other functionality from NumPy, it becomes easy to combine software packages that were not designed to be compatible.

The public interface to FEniCSx is simple to use, but still very powerful and versatile. As an example, the essential parts related to defining a weak form and assembling its matrix are considered. Creating the K matrix in (2.9) using FEniCSx is done in Python as shown in the top row of Table 1. In this, `inv_mur`

and `epsr` correspond to μ_{r}^{-1} and ε_{r}, respectively, `k0` corresponds to k_0 and `u` and `v` are test and trial functions corresponding to $\boldsymbol{N}_n^{\mathrm{X}}$ and $\boldsymbol{N}_m^{\mathrm{X}}$, respectively. This code snippet illustrates how implementing a weak form in FEniCSx is very similar to writing the mathematics explicitly. The way it is written is using the FEniCSx component UFL (Unified Form Language) and is very versatile in what equations can be used. This is then automatically compiled by the component FFCx (FEniCS Form Compiler) into a format that can be assembled by the component DOLFINx. To the user, most of this is hidden by default, making it very easy to define weak forms freely. This can be exemplified by the fact that the much more complicated (2.8) would only require a trivial amount of additional work to implement in FEniCSx compared to (2.9) (essentially, two additional lines corresponding to additional integrals are added to `form`).

Bempp-cl also has a simple public interface, but it is not as versatile as FEniCSx. Instead of freely defining equations to solve, it is based on a number of pre-defined operators that can be used. Creating the matrix Q in (2.13) can be done in Python as shown in the bottom row of Table 1. This contains three variables for function spaces which are defined with appropriate basis functions using other functions from Bempp-cl.

Both FEniCSx and Bempp-cl can generate simple simulation meshes, but they are limited to simple shapes and not suitable for much more than testing purposes. For general geometries, both packages are compatible with the Gmsh mesh format. Gmsh is an open-source meshing software with many other functions, for example related to creating geometries [51]. While Gmsh can be run as a standalone program using a graphical user interface or script files, it is also possible to use it through its application programming interface (API). This API is available for Python, and this gives the convenience of writing geometry/meshing code and FEniCSx/Bempp-cl code in the same simulation script, which makes it easy to parametrize the geometry and mesh. For more complicated geometries, this generation method can be difficult to use and in those cases STEP files can be imported to Gmsh. Geometries can then be created in more sophisticated computer-aided design (CAD) software, and exported as STEP files where different files can correspond to different media. The different media as well as boundaries of interest can be tagged in Gmsh so that the information is transferred to the msh file after meshing. This process is illustrated in Fig. 4.

3.3 Implementation using Custom BI Code

The implementation based on FEniCSx and Bempp-cl worked well as a starting point, but it was difficult to modify for more in-depth numerical experiments as the boundary integral formulations that could be used were determined by the operators pre-defined in Bempp-cl. Working with, for example, the ACA would require significant modification to the internal code of Bempp-cl, which was estimated to be more difficult than implementing the BI part ourselves. One major reason behind this decision was that much of the infrastructure related to mesh

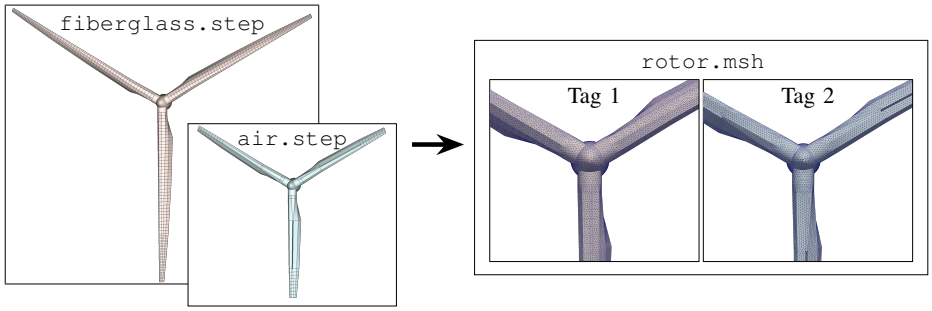

Figure 4: Combination of STEP files into a common mesh with elements tagged accordingly. STEP files correspond to different materials in a (simplified) wind turbine rotor: a fiberglass shell and the air in its interior.

and basis functions could be taken from FEniCSx without much modification. In addition to this, a code for singularity handling in the BI part was available as the open-source package DEMCEM [52–55]. While DEMCEM is a C++ package, it could be used in Python by using the package pybind11 [63]. This package makes it possible to use C++ code in Python if additional pieces of code (bindings) are written for this connection. In the case of DEMCEM, this did not require very much effort as the communication needed between Python and C++ was quite limited.

Initial versions of the custom BI code were written in a very basic way which did not lead to high performance, especially due to the typically poor performance of native Python. This was particularly clear from the assembly time for non-singular matrix entries which dominated the total solution time at every problem size. During further development, two main approaches were used to improve performance: NumPy vectorization and Numba JIT compilation.

The NumPy vectorization approach is based on reformulating code as operations on NumPy arrays. These data structures can be manipulated using highly optimized lower level code in NumPy. By reformulating operations in Python (like loops) into operations on NumPy arrays it can be possible to achieve significant performance improvements. However, this approach can be difficult to generalize to very large procedures such as the assembly of a full matrix block, and the resulting code is often difficult to read and debug.

The Numba JIT compilation approach is based on rewriting the code in a format which can be compiled using the package Numba. This is a package based on the LLVM compiler language, which can compile a subset of the Python language and NumPy into fast machine code, and has support for parallelization [17]. If a function is declared to be JIT compiled using Numba, it will be compiled when it is first called and the resulting machine code is stored in a cache for subsequent calls. To achieve optimal performance in Numba, typically the code is structured in a different way compared to typical Python code. For example, iterating over entries in multiple lists is typically done in Python without explicitly defining

Table 2: Python functions for the same simple matrix assembly using three different approaches.

Python loops

```
def assemble_loops(points, matrix, k0):
    for m, r_m in enumerate(points):
        for n, r_n in enumerate(points):
            if m != n:
                dist = numpy.linalg.norm(r_m - r_n)
                matrix[m, n] = numpy.exp(-1j * k0 * dist) / 4 / numpy.pi / dist
```

NumPy vectorization

```
def assemble_vectorize(points, matrix, k0):
    r_m = numpy.repeat(points[None, :, :], points.shape[0], axis=0)
    r_n = numpy.repeat(points[:, None, :], points.shape[0], axis=1)
    non_diag = ~numpy.eye(points.shape[0], dtype=numpy.bool8)
    dist = numpy.linalg.norm(r_m - r_n, axis=2)[non_diag]
    matrix[non_diag] = numpy.exp(-1j * k0 * dist) / 4 / numpy.pi / dist
```

Numba JIT compilation

```
@numba.jit(nopython=True, fastmath=True, error_model='numpy', parallel=True)
def assemble_numba(points, matrix, k0):
    for m in numba.prange(points.shape[0]):
        for n in range(points.shape[0]):
            if m != n:
                dist = 0.
                for coord in range(3):
                    dist += (points[m, coord] - points[n, coord])**2
                dist = numpy.sqrt(dist)
                matrix[m, n] = numpy.exp(-1j * k0 * dist) / 4 / numpy.pi / dist
```

iteration variables (using the `zip` command). In Numba, on the other hand, it is preferred to iterate over an indexation variable, making the code seem less "Pythonic" and more similar to what it might look like in lower-level languages. The language is still Python though, and interoperability between Numba functions and regular Python code is mostly seamless.

As a comparison between the different approaches, consider the assembly of an $N \times N$ matrix with entries corresponding to the free space Green's function as

$$A_{mn} = \frac{\mathrm{e}^{-\mathrm{j}k_0\,|\boldsymbol{r}_m - \boldsymbol{r}_n|}}{4\pi|\boldsymbol{r}_m - \boldsymbol{r}_n|} \tag{3.1}$$

where $\boldsymbol{r}_i$ is point i on a mesh. The entries for $m = n$ are ignored to only consider the non-singular entries in this example. This computation has similarities to non-singular assembly of BI operators, but is much more simple to make the code easier to follow. The computation can be implemented using standard Python loops, using NumPy vectorization and using Numba JIT compilation as shown in Table 2. For the Numba computation, the outer loop was run in parallel on 6 cores using the `prange` command. Computations were performed for $k_0 = 1\ \mathrm{m}^{-1}$ with points equally spaced on a square surface with side length 1 m. The run times for an increasing number of points are shown in Fig. 5 for the three approaches. It is seen that NumPy vectorization is significantly faster than the standard Python approach, and Numba is even faster. In more

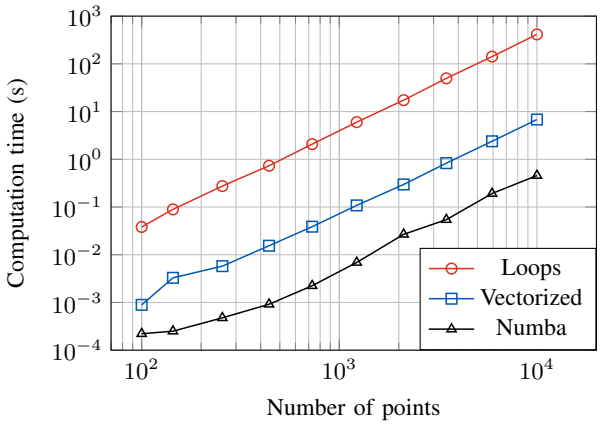

Figure 5: Computation times for an increasing number of mesh points using the functions displayed in Table 2.

complicated computations, like those found in our actual BI assembly code, the difference between vectorization and Numba can grow even more. With more variables to access and use in computations, it becomes increasingly difficult to write good vectorized code. Loops will almost inevitably have to be introduced at some point for the code to be readable and maintainable. With Numba, on the other hand, loops are fast due to the JIT compilation and it is easy to write readable, fast code for more complicated computations. In our work, this made the performance boost when switching to Numba very dramatic, with an improvement in assembly time of around two orders of magnitude compared to an earlier partly vectorized implementation.

3.4 Work with the ACA

One of the main reasons for implementing our own custom BI code was that it would make it easier to experiment with compression methods like the ACA. The core ACA algorithm as described in [36, 37] is not very difficult to implement, and for this reason our work related to fast methods started with our own implementation. In the first steps, a single level algorithm was implemented as this was also a step on the way to a multilevel algorithm. The implementation of a multilevel algorithm did not require much more effort, mainly due to the use of the AdaptOctree package [56] for subdivision of the geometry. Similar to the already existing BI code, the AdaptOctree package uses Numba to improve performance.

As demonstrated in section 5, our ACA implementation provides significant compression of system matrices. There are, however, multiple packages available which provide not only implementations of the ACA or similar compression methods, but also a more complete $\mathcal{H}$-matrix algebra [57, 58]. These could be highly

Table 3: Source lines of code and estimated effort of some packages. Estimated effort uses the default COCOMO model of SLOCCount and should be interpreted with caution.

Package	SLOC (Python)	SLOC (C++)	Estimated effort (person-years)
FE2MS	2 706	277	0.63
DEMCEM	0	14 626	3.4
FEniCSx	23 004	49 663	18
AdaptOctree	1 094	0	0.22

interesting in extensions to the code as such packages could provide functionality for better preconditioning or fast direct methods. The coupling to the current code would be nontrivial though, as these packages are typically not written in Python and $\mathcal{H}$-matrix assembly requires stronger coupling between different languages than, for example, was required for DEMCEM. Nevertheless, such extensions constitute a natural way forward, and the work required to couple the code with external packages is likely less than what is required to implement the equivalent functionality from scratch.

3.5 Effort Saved by using Open Source

To give an idea of how much effort might have been saved by using open-source software as described in this section, data generated using David A. Wheeler's 'SLOCCount' is presented. This includes source lines of code (SLOC), as well as very simple estimated efforts using the Constructive Cost Model (COCOMO) [59]. While these metrics should be interpreted with caution, it still gives an idea of the benefit in using existing open-source software in this way. A comparison between our code (FE2MS) and some of the used packages is shown in Table 3. The counted lines are for the source code, excluding demos and tests, of the versions used in our code as of writing this paper.

The 0.63 person-years estimated development effort for FE2MS can be compared to a calendar-based estimate of 0.7 years, which is reasonably close. This second estimate is based on timestamps from git commits, with some known times of other major activities like teaching, courses and conferences subtracted. This is, of course, also a crude estimate. On one hand, the estimate does not include time for code that was reused from the earlier version based on Bempp-cl, but on the other hand, it includes activities that are unrelated to the direct code development. Regardless, both estimates give an order of magnitude idea of the development times. It is difficult to gauge how close the estimates are for other packages though, and looking at SLOC for the two languages might be more fair, though still not a perfect metric.

A comparison to DEMCEM is interesting as most functionality of this package is used. It is also an example of code in another programming language that is connected to Python through our own pybind11 code. In fact, that connection

code exactly represents the 277 C++ SLOC for FE2MS in Table 3, which is fairly simple code as it only interfaces directly to C++ functions in DEMCEM. This can be contrasted to the much larger SLOC number in DEMCEM which also represents significantly more complex code.

While DEMCEM is fairly limited in its scope, FEniCSx is very general and versatile as indicated by its large SLOC numbers in Table 3. Here, all components DOLFINx, FFCx, Basix and UFL are included. Much of this is not used directly in the FE2MS code, and if a bare-bones version would be written it could have been done with significantly fewer SLOC. However, the size and scope of FEniCSx should by no means be seen as unnecessary, as it is precisely this that made it very easy to extend the code from simple dielectrics to general bianisotropic media.

As a final example, AdaptOctree is included in Table 3. This is a small package used only to generate octree data structures from points in the mesh, and this is reflected in the metrics. It would not have been an unreasonable effort to implement this functionality ourselves, but the use of open-source software for that purpose still meant that other things could be prioritized instead.

While all metrics discussed above are uncertain, it is very clear that a substantial amount of development effort has been saved by the use of existing open-source software. Had we opted for developing a similar code completely from scratch, it would probably have taken much longer and with a less versatile and less capable end result. We believe that these insights hold for a wider context than just our work with FE-BI codes as combinations of different functionality is a much more general principle, and there are likely many in the CEM community who could benefit from using more open-source software.

4 Overview of Code Components

In the following, an overview of the components in the code is given, with more attention to how the open-source packages discussed in section 3 were combined. For those with a particular interest in the actual code and details on the use of different packages, we refer to the GitHub repository at github.com/nwingren/fe2ms. This repository also includes installation instructions and demos showing how the code can be used, as well as a link to documentation of the code. In the demo script for the coated PEC sphere on GitHub the steps described in this overview can be seen and are commented upon, although not to the same level of detail as here. The most important open-source packages used by the code were introduced in section 3, and an overview of how they work together is shown in Fig. 6. More detailed descriptions of different steps follow.

4.1 Geometry and Meshing

The code uses Gmsh to generate geometry and mesh using its Python API. An example of how this is done can be found in the demos on our GitHub repository,

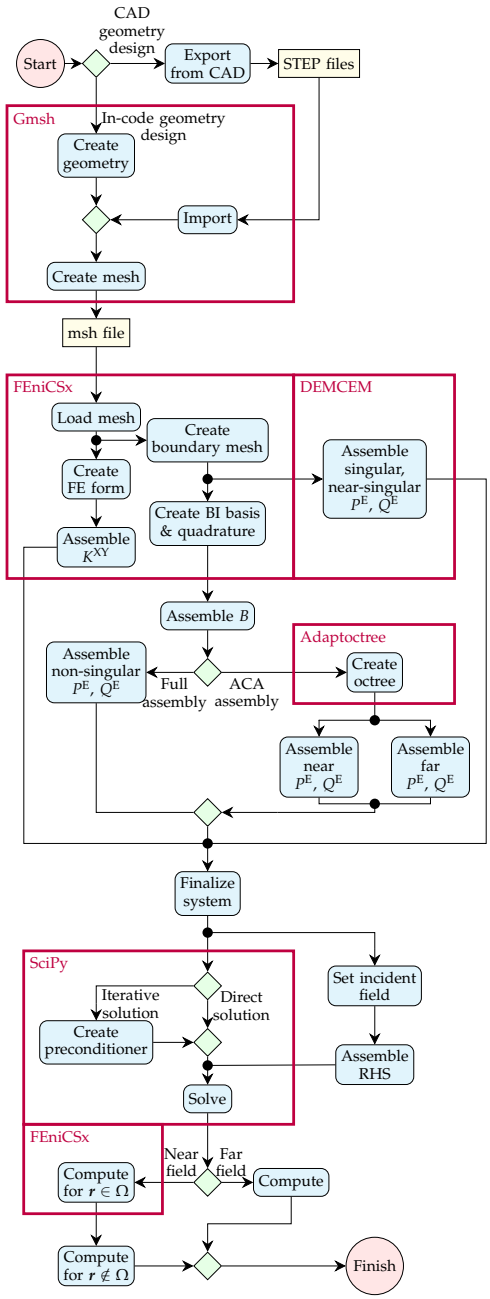

Figure 6: Flowchart showing how different packages work together. Note that this is a simplification which does not reflect the exact structure of the code.

but tutorials are also available at the Gmsh website gmsh.info. Mesh generation using STEP files, as described in section 3, can also be used (with tutorials available on the Gmsh website).

4.2 Computational Volume and System

The parameters for Ω (mesh, boundary conditions and material parameters) are combined as a "computational volume" data structure in the code. This is created by loading a mesh from a msh file into DOLFINx, listing the material properties for different parts of the mesh and defining boundaries. The tags defined in Gmsh are used here to appropriately link properties to mesh elements. From this linking, DOLFINx data structures are generated from the different material properties $\overline{\overline{\varepsilon_\mathrm{r}}}$, $\overline{\overline{\mu_\mathrm{r}}}$, $\overline{\overline{\xi}}$, $\overline{\overline{\zeta}}$, as well as boundaries corresponding to $\partial\Omega$ and PEC. When a computational volume has been generated, a system for a specific frequency is defined either with fully assembled matrix blocks, or with BI blocks assembled using the ACA. The FE formulation (conventional or magnetoelectric) is automatically inferred from the material parameters in the computational volume.

4.3 Assembly

The assembly is performed differently for the FE and BI parts. For the FE part, FEniCSx is used to efficiently assemble the matrix blocks K^{XY} as sparse matrices. The UFL package in FEniCSx is used to easily generate any necessary FE form, of which there are two different types in this work, depending on whether to include bianisotropy or not as described earlier. The DOLFINx data structures for material and boundary data from the computational volume are used here. Assembled FE blocks are converted to SciPy sparse arrays for use together with BI blocks.

The BI part uses a mesh on $\partial\Omega$ generated from DOLFINx using the previously defined data structures for this boundary. If assembly is to be performed using the ACA, an octree is generated using AdaptOctree for edges in this mesh. The octree is generated with a setting for maximum number of edges per leaf group, and this can be used to iteratively find a tree with a desired mean number of edges per non-empty leaf group.

For both full assembly and ACA assembly, all singular and near-singular entries of BI matrices need to be fully computed. This is done using DEMCEM where entries are computed for basis and testing functions on the same facet, on facets sharing a common edge and on facets sharing a common vertex. For non-singular assembly, basis functions and quadrature rules are defined on the mesh using Basix. If full assembly is used, assembly is done for all edge pairs not included in the previous step. If ACA assembly is used, non-singular assembly is performed in two steps. The first is full assembly of terms corresponding to near interactions, i.e. leaf groups in the octree which are neighbors. Together with the previously computed singular and near-singular terms, the results are stored as

SciPy sparse matrices. Next, assembly using the ACA is done for far interactions on each level of the octree. Regardless of the assembly type, JIT compilation with Numba is used in the BI part to improve the Python performance.

4.4 Solution

If the system is assembled fully, it is possible to use classical direct methods from SciPy such as Gaussian elimination or LU decomposition to solve the problem. In addition to the classical direct methods designed for dense matrices, there are also similar methods designed for sparse matrices. The system matrix for this problem has both sparse and dense blocks though, meaning that neither of those approaches is optimal. Methods designed for dense matrices would require all zeros in the system matrix to be explicitly stored, greatly increasing memory use, while methods designed for sparse matrices would suffer from fill-in due to the large dense regions, both increasing memory use and computation times. Iterative solvers based on matrix-vector multiplication are typically more memory efficient, and many such solvers are available in SciPy. The ACA, as it is implemented at the time of writing, also only supports iterative solvers and is not well suited toward classical direct methods. It is, however, very well suited toward fast direct methods based on $\mathcal{H}$-matrix algebra, but this has not been implemented at the moment of writing as discussed in section 3.

For iterative solvers it is typically crucial to use a good preconditioner for the convergence. This is especially important for the FE-BI method as it is based on a system that is ill-conditioned [39]. In this code we use a preconditioner similar to that in [64] which is based on creating a sparse, symmetric system based on the blocks in (2.11). This system can be written as

$$M = \begin{bmatrix} K^{\mathrm{II}} & K^{\mathrm{IS}} & 0 \\ K^{\mathrm{SI}} & K^{\mathrm{SS}} & B \\ 0 & -2\mathrm{j}k_0 P' & -2\mathrm{j}k_0 Q' \end{bmatrix} \tag{4.1}$$

where P' and Q' are made sparse by only considering interactions within single mesh elements. By careful inspection of (2.10) and (2.12), it can be seen that $B^{\mathrm{T}} = -2\mathrm{j}k_0 P'$ since the operator $\tilde{\mathscr{K}}$ vanishes for interactions within a single planar mesh element. The blocks P' and Q' are generated using singular and near-singular entries already computed earlier. A SciPy sparse array corresponding to (4.1) is created using these and the FE blocks. For a vector y, the preconditioned vector x is given by solving the system $Mx = y$. This can be solved directly by computing a sparse LU decomposition using UMFPACK through a SciPy interface. This has the advantage of only being required once for all right-hand sides, but on the other hand it can be memory demanding. For a lower memory usage, $Mx = y$ can instead be solved iteratively each time a preconditioned vector is required. This in turn requires an inner preconditioning step for most problem sizes. PETSc [60–62] is used for this inner iteration through the Python interface petsc4py [65]. In either case, right preconditioning is used in iterative solvers.

Right-hand sides for the problem can be generated for one or a combination of incident plane waves with given amplitude, polarization and direction. The system can then be solved for this right-hand side using a desired solver and preconditioner. After the solution has been computed, the far field, radar cross section (RCS) and near field can be computed. If multiple right-hand sides are required, for example when computing monostatic RCS, the procedure has to be repeated multiple times, but without needing to recompute the preconditioner.

5 Numerical Examples

To demonstrate the capabilities and accuracy of the code, three numerical examples are presented. The first example is a coated PEC sphere, which is used to illustrate convergence of the method. The second example is a wind turbine rotor, chosen to illustrate a CAD geometry. The third example shows that bianisotropic material properties can be handled by the code. If not stated otherwise, the ACA with recompression was used with a mean number of non-empty leaf groups set to the square root of the number of BI unknowns and an ACA/SVD tolerance set to 10^{-3}. Furthermore, the iterative solver LGMRES [66] was used with a relative tolerance 10^{-5}. All simulations were run on a desktop computer with an Intel(R) Core(TM) i5-9600K CPU @ 3.70GHz and 96 GB RAM.

5.1 Coated PEC Sphere

The first numerical example is scattering by a PEC sphere coated by two isotropic dielectric layers, as shown in the inset of Fig. 7. The PEC sphere radius was $0.15\lambda_0$ and the coatings were $0.05\lambda_0$ thick with $\lambda_0 = 1$ m being the free-space wavelength at the simulation frequency 300 MHz.

The geometry was both created and meshed in Gmsh, with element sizes varying between simulations to study the h-convergence. Direct preconditioning was used, except for the one with the most unknowns where iterative preconditioning with LGMRES and Gauss-Seidel inner preconditioning was used. The bistatic RCS was computed in the E- and H-planes, as well as the absorption cross section from the near fields at $\partial\Omega$. These were compared to the same values from an exact Mie solution [67].

The bistatic RCS is shown in Fig. 7 for 414 000 FE unknowns and 10 857 BI unknowns computed both using full BI matrices and BI matrices compressed by the ACA. Exact reference values computed using a Mie solution are also shown. Good agreement between the exact Mie solution and the FE-BI solution is seen, both for the solution using full BI matrices and the solution using ACA compression. The errors were computed for all simulations with varying mesh element sizes, and these are shown in Fig. 8 with errors for the solution in Fig. 7 encircled. Convergence is seen for increasing mesh density, both in the near field (absorption) and far field (RCS).

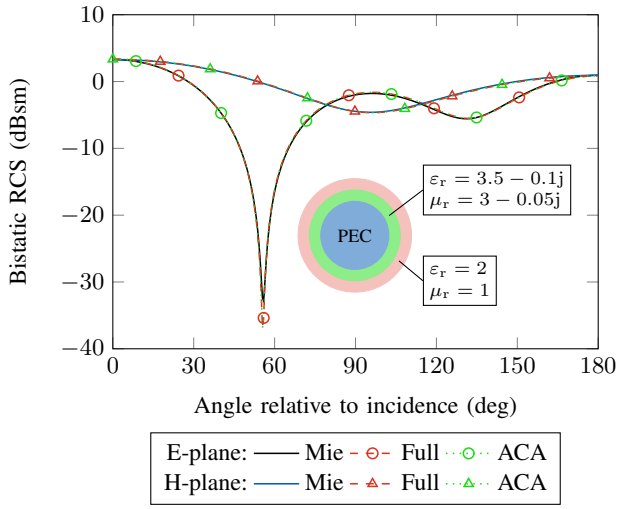

Figure 7: Bistatic RCS in E- and H-planes. Inset shows a schematic figure of the sphere with material parameters of the layers.

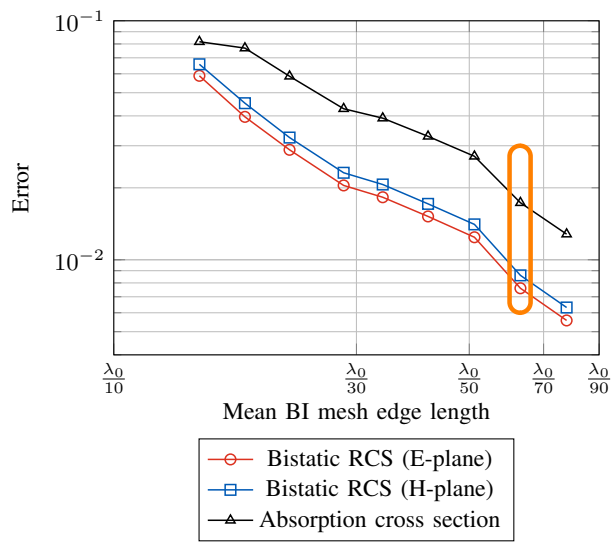

Figure 8: Errors between FE-BI solution using the ACA and Mie solution. The RCS errors are quantified as root mean square errors normalized to the maximum RCS value. The absorption cross section error is quantified as the relative error. Encircled values are for the solution with RCS shown in Fig. 7.

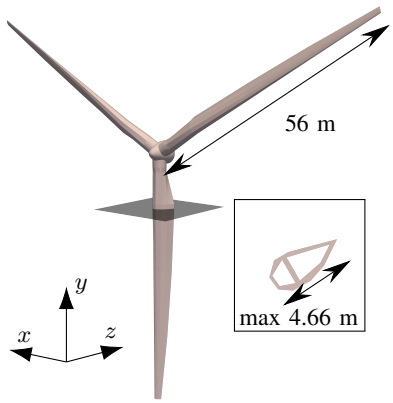

Figure 9: CAD model of wind turbine rotor. Inset shows internal structure along cut plane.

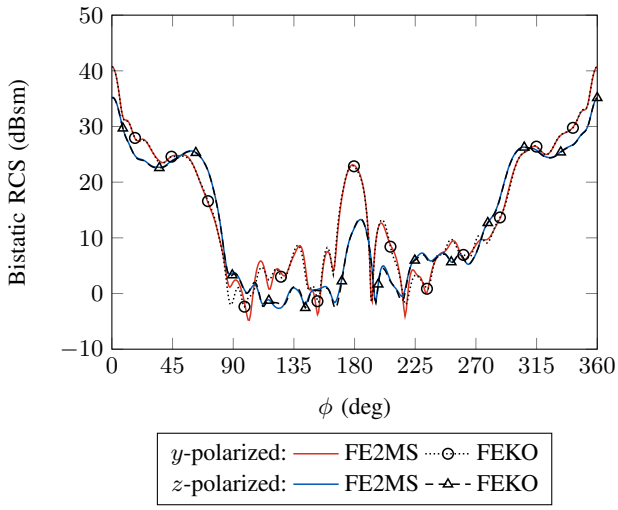

Figure 10: Bistatic RCS for two different polarizations of the incident field.

5.2 Wind Turbine Rotor

For a more geometrically complex and larger problem, scattering by a wind turbine rotor (as shown in Fig. 9) was considered. A simplified model was used where the rotor was constructed as a fiberglass shell with shear webs on the interior of the blades. The frequency was set to 30 MHz. FR-4 was used to model the fiberglass walls due to it being a well-characterized fiberglass material with some similarities to that used in wind turbine blades. Its properties were set to $\varepsilon_r = 4.9 - 0.086\text{j}$, $\mu_r = 1$, corresponding to FR-4 at 1 MHz with a volume fraction of 55 % resin [68].

Table 4: Performance metrics for simulation of wind turbine rotor.

Metric	FE2MS	Feko
BI memory	17 GB	9.2 GB
Preconditioner memory	1.7 GB	56 GB + 2.7 GB on hard drive
Total time	1484 s	644 s
Assembly time	729 s	135 s
Preconditioning time	5.4 s	451 s
Solver time	613 s	50 s

The geometry was created in FreeCAD and transferred to Gmsh using STEP files. It was then meshed with a total number of 224 484 FE unknowns and 72 000 BI unknowns. For comparison, the same mesh was imported in Feko (using both Gmsh and COMSOL Multiphysics to convert the mesh format) where a FE-BI simulation using the MLFMA was performed. The simulation used the EFIE, linear basis functions and double precision to more closely match similar settings used in our code. The bistatic RCS was computed in the xy-plane for plane waves incident along x and polarized along y and z using both our code and Feko. The results are shown in Fig. 10. The agreement is good where RCS values are high, but discrepancies are seen at lower levels. These discrepancies can be due to the different fast methods used in our code (ACA) and Feko (MLFMA). Both these methods are based on approximations, but not the same ones and as such some differences should be expected. Better agreement could be seen if instead second order basis functions were used in Feko for the same mesh. However, since our method is based on first order basis functions, the same was kept in Feko to keep the performance metrics more comparable.

Due to the large separations between different geometrical regions and the large elongated structures, it could be expected that a compression method based on low rank approximations like the ACA performs well. The theoretical memory required to store the BI matrices P and Q fully for this problem is 166 GB (based on storing two $72\,000 \times 72\,000$ matrices using 128 bit complex floats). This is significantly more than the available memory on the used machine. Table 4 shows memory use and times for some parts of the simulations. It is clear that the use of the ACA results in significant compression, although not as significant as the MLFMA in Feko. This should not come as a surprise as the ACA is theoretically less efficient than the MLFMA for non-static problems [24]. Looking at preconditioning in Table 4, Feko required much more memory than our code. There could be a multitude of reasons for this, but it is not fully clear to the authors as such details are not typically disclosed for commercial codes. It might be that the preconditioning used in Feko leads to faster convergence than in our code, but the memory use is still very high and this sets a hard limit on what can be computed. In terms of peak memory use, both codes used more than the sum of the two listed components, with Feko still using more than our code.

If the times in Table 4 are compared, our code is slower than Feko for all listed metrics except preconditioning. There are some cases where it could be

due to the algorithms themselves, like the time for the solver. Although the iterative solvers were not identical, it could be observed that Feko required fewer iterations than our code. This obviously has a direct impact on the solver time, and also strengthens the hypothesis that the preconditioning in Feko leads to faster convergence than our preconditioning. In cases with many more right-hand sides than this example, such decisions can matter significantly. It should be noted that the code used in our solver, particularly for ACA matrix-vector multiplication, could likely be optimized for a significant performance boost. Similarly, other slow run times in our code can be explained by differences in programming languages and, maybe most importantly, optimization of the code. With Feko being a commercial code developed by a large company, it is to be expected that it is optimized for fast run times. As a single developer, it is difficult to match this. Still, while the total run time for our code is more than twice that of Feko, it is not an extreme run time in the sense that it makes the code unusable.

5.3 Bianisotropic Medium

To demonstrate the ability of computations involving more complex media, an example from [32] with inhomogeneous complex media was considered. The geometry was a stacked structure with five layers of different media, each with the dimensions $0.5\lambda_0 \times 0.5\lambda_0 \times 0.05\lambda_0$, as shown in the inset of Fig.11. The properties were

$$\overline{\overline{\varepsilon_\mathrm{r}}} = \overline{\overline{\mu_\mathrm{r}}} = \begin{bmatrix} 1.5 & 0 & 0 \\ 0 & 1.5 & 0 \\ 0 & 0 & 2 \end{bmatrix} \tag{5.1}$$

for the anisotropic layer,

$$\overline{\overline{\varepsilon_\mathrm{r}}} = \overline{\overline{\mu_\mathrm{r}}} = (2 - \mathrm{j})\overline{\overline{I}} \tag{5.2}$$

for the isotropic layer and

$$\overline{\overline{\varepsilon_\mathrm{r}}} = \overline{\overline{\mu_\mathrm{r}}} = \begin{bmatrix} 2 & \mathrm{j} & 0 \\ -\mathrm{j} & 2 & 0 \\ 0 & 0 & 1.5 \end{bmatrix}, \ \overline{\overline{\xi}} = \overline{\overline{\zeta}}^{\,*} = (0.5 - 0.5\mathrm{j})\overline{\overline{I}} \tag{5.3}$$

for the bianisotropic layer [32]. To be able to incorporate the PEC layers in the FE-BI geometry, the structure was coated by a $0.03\lambda_0$ thick layer of air which was not present in [32]. The excitation was a plane wave incident along $-z$ polarized along x. A mesh was generated with 26 747 FE unknowns and 5 406 BI unknowns. Due to the small number of unknowns, full BI matrices without use of ACA were used in the simulations.

The bistatic RCS was computed in two cut planes corresponding to the xz ($\phi = 0°$) and yz ($\phi = 90°$) planes, and the resulting RCS normalized to λ_0^2 is shown in Fig. 11, together with results from [32] using a volume integral equation (VIE) based on the CFIE. Good agreement between the two methods is seen in both cut planes.

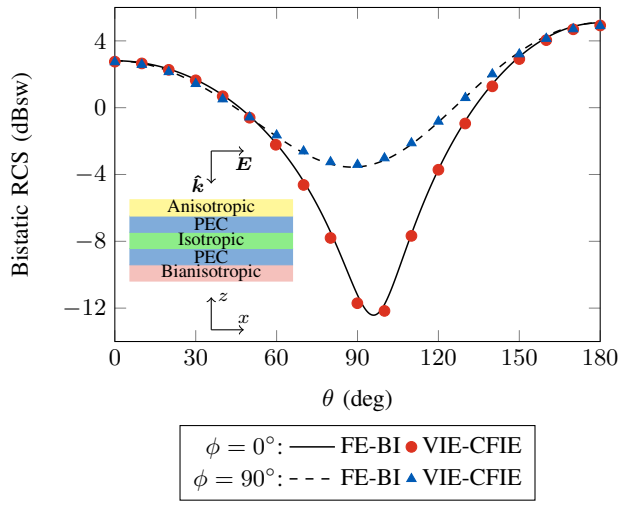

Figure 11: Bistatic RCS in two cut planes computed using FE-BI code from this work and VIE-CFIE code from [32]. Data from [32] extracted using WebPlotDigitizer [69]. Inset shows a schematic figure of the structure and the incident field.

6 Discussion and Conclusion

In all three numerical examples presented, there is clear agreement between the results from our FE-BI code and the reference results, which acts as a non-exhaustive verification of the code. The ACA compression has been shown to be effective, particularly in the wind turbine example. The three examples together demonstrate that a wide range of scattering problems can be solved by the code, and it is not limited to only small problems.

While the code can clearly perform computations for problems of a significant size, it is not yet able to handle the very large problems where computer clusters are required. In its current form, the code supports parallel execution on multiple cores on a single computer using Numba's automatic parallelization and parallel functionality included in other packages. More development would be needed for cluster computing with distributed memory. Much of FeniCSx is already prepared for this though, which could make that work easier. Another improvement to the code performance would be to use fast direct methods, as discussed briefly in section 3. These types of algorithms would be very suitable for problems with many right-hand sides and would also reduce the influence of the ill-conditioned FE-BI system.

In this article we have described how different open-source packages have been combined in the hope that this will be useful to others in the field. It can be difficult and time-consuming to experiment with different algorithms if they have to be implemented from scratch, and as we have described in this paper, much

development effort was saved by opting for this approach. We hope that others active in the field might be inspired to work more with open-source software as a wider use of this type of development could benefit the field greatly. With more software openly available for well-understood algorithms, possibilities open up for more contributors to work on the parts not yet understood.

References

[1] G. Burke, E. Miller, and A. Poggio, "The numerical electromagnetics code (NEC) - a brief history," in *IEEE Antennas and Propagation Society Symposium, 2004.*, vol. 3, 2004, pp. 2871–2874.

[2] G. J. Burke and A. J. Poggio, "Numerical electromagnetic code (NEC)-method of moments," Naval Ocean Systems Center, San Diego, CA, NOSC Technical Document 116, 1977.

[3] A. F. Oskooi, D. Roundy, M. Ibanescu, P. Bermel, J. Joannopoulos, and S. G. Johnson, "Meep: A flexible free-software package for electromagnetic simulations by the FDTD method," *Computer Physics Communications*, vol. 181, no. 3, pp. 687–702, 2010.

[4] C. Warren, A. Giannopoulos, and I. Giannakis, "gprMax: Open source software to simulate electromagnetic wave propagation for ground penetrating radar," *Computer Physics Communications*, vol. 209, pp. 163–170, 2016.

[5] M. Malinen and P. Råback, "Elmer finite element solver for multiphysics and multiscale problems," *Multiscale Model. Methods Appl. Mater. Sci.*, vol. 19, pp. 101–113, 2013.

[6] M. S. Alnæs, A. Bergersen, J. Blechta, R. E. Bredesen, J. Brown, S. Bruvoll, P. Farrell, G. Foufas, T. Gustafsson, J. B. Haga, J. Hake, J. S. Hale, J. Hoffman, A. E. Johansen, J. Jansson, N. Jansson, A. Jarosch, K. Kaasbjerg, B. Kehlet, A. Knudsen, E. Lezar, T. Li, M. Liertzer, D. Lindbo, G. T. Lines, A. Logg, N. Lopes, K.-A. Mardal, A. Massing, L. Mitchell, M. Morandini, M. Mortensen, C. Maurini, H. Narayanan, C. Richardson, J. Ring, M. E. Rognes, B. Sawicki, N. Schlömer, K. Selim, A. Simone, O. Skavhaug, E. Svensson, A. Terrel, J. Tilander, F. Valdmanis, M. Vikstrøm, S. Walker, G. N. Wells, I. Wilbers, C. Wilson, I. Yashchuk, M. Zaffalon, Åsmund Ødegård, and K. Ølgaard. (2023) DOLFINx: Next generation FEniCS problem solving environment. [Online]. Available: https://github.com/FEniCS/dolfinx

[7] A. Logg, K. B. Ølgaard, M. Rognes, G. N. Wells, and M. S. Alnæs. (2023) FFCx: Next generation FEniCS form compiler. [Online]. Available: https://github.com/FEniCS/ffcx

[8] M. W. Scroggs, J. S. Dokken, C. N. Richardson, and G. N. Wells, "Construction of arbitrary order finite element degree-of-freedom maps on polygonal and polyhedral cell meshes," *ACM Trans. Math. Softw.*, vol. 48, no. 2, may 2022.

[9] M. W. Scroggs, I. A. Baratta, C. N. Richardson, and G. N. Wells, "Basix: a runtime finite element basis evaluation library," *Journal of Open Source Software*, vol. 7, no. 73, p. 3982, 2022.

[10] M. S. Alnæs, A. Logg, K. B. Ølgaard, M. E. Rognes, and G. N. Wells, "Unified form language: A domain-specific language for weak formulations of partial differential equations," *ACM Trans. Math. Softw.*, vol. 40, no. 2, mar 2014.

[11] T. E. Oliphant, "Python for scientific computing," *Computing in Science & Engineering*, vol. 9, no. 3, pp. 10–20, 2007.

[12] J. Bezanson, A. Edelman, S. Karpinski, and V. B. Shah, "Julia: A fresh approach to numerical computing," *SIAM Review*, vol. 59, no. 1, pp. 65–98, 2017.

[13] PyPI · the Python package index. Accessed Dec. 13, 2023. [Online]. Available: https://pypi.org/

[14] Packages · JuliaHub. Accessed Dec. 13, 2023. [Online]. Available: https://juliahub.com/ui/Packages

[15] C. R. Harris, K. J. Millman, S. J. van der Walt, R. Gommers, P. Virtanen, D. Cournapeau, E. Wieser, J. Taylor, S. Berg, N. J. Smith, R. Kern, M. Picus, S. Hoyer, M. H. van Kerkwijk, M. Brett, A. Haldane, J. F. del Río, M. Wiebe, P. Peterson, P. Gérard-Marchant, K. Sheppard, T. Reddy, W. Weckesser, H. Abbasi, C. Gohlke, and T. E. Oliphant, "Array programming with NumPy," *Nature*, vol. 585, no. 7825, pp. 357–362, Sep. 2020.

[16] P. Virtanen, R. Gommers, T. E. Oliphant, M. Haberland, T. Reddy, D. Cournapeau, E. Burovski, P. Peterson, W. Weckesser, J. Bright, S. J. van der Walt, M. Brett, J. Wilson, K. J. Millman, N. Mayorov, A. R. J. Nelson, E. Jones, R. Kern, E. Larson, C. J. Carey, İ. Polat, Y. Feng, E. W. Moore, J. VanderPlas, D. Laxalde, J. Perktold, R. Cimrman, I. Henriksen, E. A. Quintero, C. R. Harris, A. M. Archibald, A. H. Ribeiro, F. Pedregosa, P. van Mulbregt, and SciPy 1.0 Contributors, "SciPy 1.0: Fundamental Algorithms for Scientific Computing in Python," *Nature Methods*, vol. 17, pp. 261–272, 2020.

[17] S. K. Lam, A. Pitrou, and S. Seibert, "Numba: A LLVM-based Python JIT compiler," in *Proceedings of the Second Workshop on the LLVM Compiler Infrastructure in HPC*, ser. LLVM '15. New York, NY, USA: Association for Computing Machinery, 2015.

[18] P. Silvester and M.-S. Hsieh, "Finite-element solution of 2-dimensional exterior-field problems," *Proceedings of the Institution of Electrical Engineers*, vol. 118, no. 12, pp. 1743–1747, 1971.

[19] B. McDonald and A. Wexler, "Finite-element solution of unbounded field problems," *IEEE Transactions on Microwave Theory and Techniques*, vol. 20, no. 12, pp. 841–847, 1972.

[20] O. C. Zienkiewicz, D. W. Kelly, and P. Bettess, "The coupling of the finite element method and boundary solution procedures," *International Journal for Numerical Methods in Engineering*, vol. 11, no. 2, pp. 355–375, 1977.

[21] K. Paulsen, D. Lynch, and J. Strahbehn, "Three-dimensional finite, boundary, and hybrid element solutions of the maxwell equations for lossy dielectric media," *IEEE Transactions on Microwave Theory and Techniques*, vol. 36, no. 4, pp. 682–693, 1988.

[22] J.-M. Jin and V. Liepa, "Application of hybrid finite element method to electromagnetic scattering from coated cylinders," *IEEE Transactions on Antennas and Propagation*, vol. 36, no. 1, pp. 50–54, 1988.

[23] X. Yuan, "Three-dimensional electromagnetic scattering from inhomogeneous objects by the hybrid moment and finite element method," *IEEE Transactions on Microwave Theory and Techniques*, vol. 38, no. 8, pp. 1053–1058, 1990.

[24] J. Jin, *Theory and Computation of Electromagnetic Fields.* Hoboken, NJ, USA: John Wiley & Sons, Ltd, 2010.

[25] R. F. Harrington, *Field Computation by Moment Methods.* New York: Macmillan, 1968.

[26] A. J. Poggio and E. K. Miller, "Integral equation solutions of three-dimensional scattering problems," in *Computer Techniques for Electromagnetics*, R. Mittra, Ed. Elmsford: Pergamon Press, 1973, pp. 159–264.

[27] S. Rao, D. Wilton, and A. Glisson, "Electromagnetic scattering by surfaces of arbitrary shape," *IEEE Transactions on Antennas and Propagation*, vol. 30, no. 3, pp. 409–418, 1982.

[28] D. Schaubert, D. Wilton, and A. Glisson, "A tetrahedral modeling method for electromagnetic scattering by arbitrarily shaped inhomogeneous dielectric bodies," *IEEE Transactions on Antennas and Propagation*, vol. 32, no. 1, pp. 77–85, 1984.

[29] R. Graglia, P. Uslenghi, and R. Zich, "Moment method with isoparametric elements for three-dimensional anisotropic scatterers," *Proceedings of the IEEE*, vol. 77, no. 5, pp. 750–760, 1989.

[30] G. Kobidze and B. Shanker, "Integral equation based analysis of scattering from 3-D inhomogeneous anisotropic bodies," *IEEE Transactions on Antennas and Propagation*, vol. 52, no. 10, pp. 2650–2658, 2004.

[31] P. Ylä-Oijala, J. Markkanen, and S. Järvenpää, "Current-based volume integral equation formulation for bianisotropic materials," *IEEE Transactions on Antennas and Propagation*, vol. 64, no. 8, pp. 3470–3477, 2016.

[32] J. Liu, J. Yuan, Z. Li, and J. Song, "A well-conditioned integral equation for electromagnetic scattering from composite inhomogeneous bi-anisotropic material and closed perfect electric conductor objects," *IET Microwaves, Antennas & Propagation*, vol. 15, no. 4, pp. 404–414, 2021.

[33] Y. Zhang, X. Wei, and E. Li, "Electromagnetic scattering from three-dimensional bianisotropic objects using hybrid finite element-boundary integral method," *Journal of Electromagnetic Waves and Applications*, vol. 18, no. 11, pp. 1549–1563, 2004.

[34] R. Coifman, V. Rokhlin, and S. Wandzura, "The fast multipole method for the wave equation: a pedestrian prescription," *IEEE Antennas and Propagation Magazine*, vol. 35, no. 3, pp. 7–12, 1993.

[35] J. Song, C.-C. Lu, and W. C. Chew, "Multilevel fast multipole algorithm for electromagnetic scattering by large complex objects," *IEEE Transactions on Antennas and Propagation*, vol. 45, no. 10, pp. 1488–1493, 1997.

[36] M. Bebendorf, "Approximation of boundary element matrices," *Numerische Mathematik*, vol. 86, no. 4, pp. 565–589, 2000.

[37] K. Zhao, M. Vouvakis, and J.-F. Lee, "The adaptive cross approximation algorithm for accelerated method of moments computations of EMC problems," *IEEE Transactions on Electromagnetic Compatibility*, vol. 47, no. 4, pp. 763–773, 2005.

[38] E. Bleszynski, M. Bleszynski, and T. Jaroszewicz, "AIM: Adaptive integral method for solving large-scale electromagnetic scattering and radiation problems," *Radio Science*, vol. 31, no. 5, pp. 1225–1251, 1996.

[39] X.-Q. Sheng, J.-M. Jin, J. Song, C.-C. Lu, and W. C. Chew, "On the formulation of hybrid finite-element and boundary-integral methods for 3-D scattering," *IEEE Transactions on Antennas and Propagation*, vol. 46, no. 3, pp. 303–311, 1998.

[40] M. N. Vouvakis, Seung-Cheol Lee, Kezhong Zhao, and Jin-Fa Lee, "A symmetric FEM-IE formulation with a single-level IE-QR algorithm for solving electromagnetic radiation and scattering problems," *IEEE Transactions on Antennas and Propagation*, vol. 52, no. 11, pp. 3060–3070, 2004.

[41] T. Wan, M. Z. Li, and L. F. Li, "Direct solution of finite element-boundary integral system for electromagnetic analysis in half-space," *IEEE Transactions on Antennas and Propagation*, vol. 68, no. 8, pp. 6461–6466, 2020.

[42] X. Yang, M. Jiang, L. Shen, P.-H. Jia, Z. Rong, Y. Chen, L. Lei, and J. Hu, "A flexible FEM-BEM-DDM for EM scattering by multiscale anisotropic objects," *IEEE Transactions on Antennas and Propagation*, vol. 69, no. 12, pp. 8562–8573, 2021.

[43] I. Badia, B. Caudron, X. Antoine, and C. Geuzaine, "A well-conditioned weak coupling of boundary element and high-order finite element methods for time-harmonic electromagnetic scattering by inhomogeneous objects," *SIAM Journal on Scientific Computing*, vol. 44, no. 3, pp. B640–B667, 2022.

[44] Z. Yang, X.-W. Yuan, X.-W. Huang, M.-L. Yang, and X.-Q. Sheng, "Resistive sheet boundary condition-based nonconformal domain decomposition FE-BI-MLFMA for electromagnetic scattering from inhomogeneous objects with honeycomb structures," *IEEE Transactions on Antennas and Propagation*, vol. 70, no. 10, pp. 9483–9496, 2022.

[45] M. Yang, B. Wu, H. Gao, and X. Sheng, "An effective $\mathcal{H}$-LU-based preconditioner for the FE-BI-MLFMA for 3-D scattering problems," *IEEE Antennas and Wireless Propagation Letters*, vol. 18, no. 12, pp. 2766–2770, 2019.

[46] Y. Mao, Y. Zhong, Q. Zhan, D. Wang, and Q. H. Liu, "A simple way of applying the Calderón preconditioner to a finite-element boundary-integral method," *IEEE Transactions on Antennas and Propagation*, vol. 71, no. 6, pp. 5510–5515, 2023.

[47] M. M. Botha and J.-M. Jin, "On the variational formulation of hybrid finite element-boundary integral techniques for electromagnetic analysis," *IEEE Transactions on Antennas and Propagation*, vol. 52, no. 11, pp. 3037–3047, 2004.

[48] M. Bebendorf, *Hierarchical Matrices*. Springer-Verlag Berlin Heidelberg, 2008.

[49] M. Bebendorf and S. Kunis, "Recompression techniques for adaptive cross approximation," *The Journal of Integral Equations and Applications*, vol. 21, no. 3, pp. 331–357, 2009.

[50] T. Betcke and M. W. Scroggs, "Bempp-cl: A fast python based just-in-time compiling boundary element library." *Journal of Open Source Software*, vol. 6, no. 59, p. 2879, 2021.

[51] C. Geuzaine and J.-F. Remacle, "Gmsh: A 3-D finite element mesh generator with built-in pre-and post-processing facilities," *International journal for numerical methods in engineering*, vol. 79, no. 11, pp. 1309–1331, 2009.

[52] A. G. Polimeridis and T. V. Yioultsis, "On the direct evaluation of weakly singular integrals in galerkin mixed potential integral equation formulations," *IEEE Transactions on Antennas and Propagation*, vol. 56, no. 9, pp. 3011–3019, 2008.

[53] A. G. Polimeridis and J. R. Mosig, "Complete semi-analytical treatment of weakly singular integrals on planar triangles via the direct evaluation method," *International Journal for Numerical Methods in Engineering*, vol. 83, no. 12, pp. 1625–1650, 2010.

[54] A. G. Polimeridis, J. M. Tamayo, J. M. Rius, and J. R. Mosig, "Fast and accurate computation of hypersingular integrals in galerkin surface integral equation formulations via the direct evaluation method," *IEEE Transactions on Antennas and Propagation*, vol. 59, no. 6, pp. 2329–2340, 2011.

[55] A. G. Polimeridis and J. R. Mosig, "On the direct evaluation of surface integral equation impedance matrix elements involving point singularities," *IEEE Antennas and Wireless Propagation Letters*, vol. 10, pp. 599–602, 2011.

[56] S. Kailasa and T. Betcke. (2022) AdaptOctree: Adaptive linear octrees in Python. [Online]. Available: https://github.com/Excalibur-SLE/AdaptOctree

[57] S. Börm and L. Grasedyck. Hierarchical matrices: HLib package. Accessed: 20 Nov 2023. [Online]. Available: http://www.hlib.org/

[58] Y. Liu. ButterflyPACK: Fast PDE solvers and transforms. Accessed: 20 Nov 2023. [Online]. Available: https://portal.nersc.gov/project/sparse/butterflypack/

[59] D. A. Wheeler. Accessed: 21 Nov. 2023. [Online]. Available: https://dwheeler.com/sloccount/

[60] S. Balay, S. Abhyankar, M. F. Adams, S. Benson, J. Brown, P. Brune, K. Buschelman, E. M. Constantinescu, L. Dalcin, A. Dener, V. Eijkhout, J. Faibussowitsch, W. D. Gropp, V. Hapla, T. Isaac, P. Jolivet, D. Karpeev, D. Kaushik, M. G. Knepley, F. Kong, S. Kruger, D. A. May, L. C. McInnes, R. T. Mills, L. Mitchell, T. Munson, J. E. Roman, K. Rupp, P. Sanan, J. Sarich, B. F. Smith, S. Zampini, H. Zhang, H. Zhang, and J. Zhang, "PETSc Web page," https://petsc.org/, 2023. [Online]. Available: https://petsc.org/

[61] S. Balay, S. Abhyankar, M. F. Adams, S. Benson, J. Brown, P. Brune, K. Buschelman, E. Constantinescu, L. Dalcin, A. Dener, V. Eijkhout, J. Faibussowitsch, W. D. Gropp, V. Hapla, T. Isaac, P. Jolivet, D. Karpeev, D. Kaushik, M. G. Knepley, F. Kong, S. Kruger, D. A. May, L. C. McInnes, R. T. Mills, L. Mitchell, T. Munson, J. E. Roman, K. Rupp, P. Sanan,

J. Sarich, B. F. Smith, S. Zampini, H. Zhang, H. Zhang, and J. Zhang, "PETSc/TAO users manual," Tech. Rep. ANL-21/39 - Revision 3.19, 2023.

[62] S. Balay, W. D. Gropp, L. C. McInnes, and B. F. Smith, "Efficient management of parallelism in object oriented numerical software libraries," in *Modern Software Tools in Scientific Computing*, E. Arge, A. M. Bruaset, and H. P. Langtangen, Eds. Birkhäuser Press, 1997, pp. 163–202.

[63] W. Jakob, J. Rhinelander, and D. Moldovan, "pybind11 – seamless operability between C++11 and Python," 2017, https://github.com/pybind/pybind11.

[64] J. Guan, S. Yan, and J. Jin, "An accurate and efficient finite element-boundary integral method with GPU acceleration for 3-D electromagnetic analysis," *IEEE Transactions on Antennas and Propagation*, vol. 62, no. 12, pp. 6325–6336, 2014.

[65] L. D. Dalcin, R. R. Paz, P. A. Kler, and A. Cosimo, "Parallel distributed computing using Python," *Advances in Water Resources*, vol. 34, no. 9, pp. 1124 – 1139, 2011, new Computational Methods and Software Tools.

[66] A. H. Baker, E. R. Jessup, and T. Manteuffel, "A technique for accelerating the convergence of restarted GMRES," *SIAM Journal on Matrix Analysis and Applications*, vol. 26, no. 4, pp. 962–984, 2005.

[67] A. Ericsson, D. Sjöberg, C. Larsson, and T. Martin, "Scattering from a multilayered sphere - applications to electromagnetic absorbers on double curved surfaces," Electromagnetic Theory Department of Electrical and Information Technology Lund University Sweden, Tech. Rep. LUTEDX/(TEAT-7249)/1-32/(2017), 2017.

[68] S. J. Mumby and J. Yuan, "Dielectric properties of FR-4 laminates as a function of thickness and the electrical frequency of the measurement," *Journal of Electronic Materials*, vol. 18, no. 2, pp. 287–292, 1989.

[69] A. Rohatgi, "Webplotdigitizer: Version 4.6," 2022. [Online]. Available: https://automeris.io/WebPlotDigitizer

Demonstrating Reconfigurability in Water-based Electromagnetic Devices using a 3D-printed Siphon

Paper II

N. Wingren and D. Sjöberg

Published as: N. Wingren and D. Sjöberg, "Demonstrating Reconfigurability in Water-based Electromagnetic Devices using a 3D-printed Siphon," *Microwave and Optical Technology Letters*, Vol. 66, No. 7, 2024.

Abstract

The rise of water-based electromagnetic devices opens up new possibilities for controlling electromagnetic performance due to the liquid state of crucial parts of the device. This letter proposes the siphon mechanism as a novel way to achieve reconfigurability in these types of electromagnetic devices. To demonstrate this, a simple polarization-reconfigurable device based on a siphon is introduced. The device is designed to scatter horizontal and vertical polarizations differently depending on the amount of water added to it. The siphon mechanism offers a sharp transition between two states after water is added above a threshold. The device is simulated, manufactured using 3D printing, and measured in different states filled with both distilled and tap water. The results demonstrate that polarization reconfigurability is achieved with the different states scattering the two polarizations as expected. Siphons similar to this could be used to offer new types of control in other electromagnetic devices based on liquids.

1 Introduction

Electromagnetic devices based on water or other liquids have been proposed for many different applications such as antennas, metasurfaces or microwave devices [1–7]. These devices can be designed with reconfigurability in mind, and hydraulic mechanisms and properties of liquids can be used to enable this. Some examples of mechanisms are the use of pumps [8,9] and liquid in a container staying level as the container changes shape [10, 11]. Another mechanism which can be used for liquids is the siphon, which is used to empty a vessel. Siphons which automatically empty a vessel after filling it up to a certain level have been known since ancient times, with several types described by Hero of Alexandria [12]. Today, similar siphons can be found in applications such as toilets, washing machines and various drainage systems. For water-based electromagnetic devices, siphons offer a novel type of reconfigurability by transporting water from one vessel to another.

In this letter, we describe a device which uses a siphon to obtain polarization reconfigurability of scattered waves. It is a simple device presented to introduce the mechanism which, to the authors' knowledge, has not been used explicitly for electromagnetic applications. The device has four states which depend on the added amount of water, and scatter horizontally and vertically polarized waves differently. Water was selected, as opposed to other liquids, due to the fact that it is ubiquitous (even in distilled form), nontoxic, and easy to work with. While one common issue with water in electromagnetics is its temperature-sensitive properties [2], the proposed device does not depend on resonances where this issue would be critical. Additionally, water is well established for use in siphons and different mechanical properties, like surface tension, of other liquids may affect the siphon effect [13]. We present the device performance using the monostatic radar cross section (RCS) for different polarizations, and for each of the four states. Polarization reconfigurability is shown both in numerical

simulations using the finite element-boundary integral (FE-BI) method, as well as in measurements of a 3D printed device.

2 Siphon Design

We envision that a siphon in water-based electromagnetic devices can be used to provide reconfigurability with a sharp transition when water reaches a specific level. In this work, a device is shown as a proof of concept where the monostatic RCS of different polarizations is reconfigurable. The device has two elongated sections: one horizontal and one vertical, as seen in the geometry of Fig. 1 where some dimensions of the device are shown to give an idea of the size and amount of water in different states. The idea behind the two sections is that the siphonic action can transfer water from the vertical to the horizontal section, thereby affecting its response to vertical and horizontal polarization. The sections are designed such that the water columns would be a significant fraction of the wavelength in one dimension, and much smaller in the other. This provides the desired polarization selectivity. The operation of the device is shown in Fig. 1 with four different states achieved in the following sequence. State 0 is the initial state without any water filling. State 1 is achieved by filling the vertical section to its maximum level. State 2 is achieved by filling the vertical section more, causing the siphon to activate and move the water to the horizontal section. Some of this water is drained out at the bottom as the horizontal section has lower volume than the vertical. State 3 is achieved by once again filling the vertical section to its maximum level. Subsequent fills of the vertical section lead to cycling between state 2 and state 3. A video showing the siphon as it is filled with water is available as supplementary material to this letter for easier visualization of its function and the different states.

The actual design of the siphon was performed with the aim of operations in the lower GHz frequency range. This was due to a variety of reasons: water provides a high contrast with $\varepsilon_{\mathrm{r}} \approx 80$ at these frequencies, a design could be manufactured using 3D printing as a single print (no gluing), and measurements could be performed using existing equipment. The design work had to be done both from a hydraulically and electromagnetic standpoint. The hydraulic design was to ensure that siphonic action could transfer most of the water from the vertical to the horizontal section. As the principle is quite simple, this was achieved by a few design cycles using the open source computer aided design (CAD) software FreeCAD to generate stereolithography (STL) files which were 3D printed using a Prusa i3 MK3 printer and tested. A filament of polyethylene terephthalate glycol (PETG) (a copolymer of polyethylene terephthalate (PET)) and 100 % infill to ensure good resistance to water. There were limitations when designing for 3D printing, one of which was related to the overhangs in enclosed pipes. These overhangs needed to have sufficiently steep slopes to be able to print without additional support, and for this reason equilateral triangles were used as seen in Fig. 1. When a design with a functioning siphonic action had

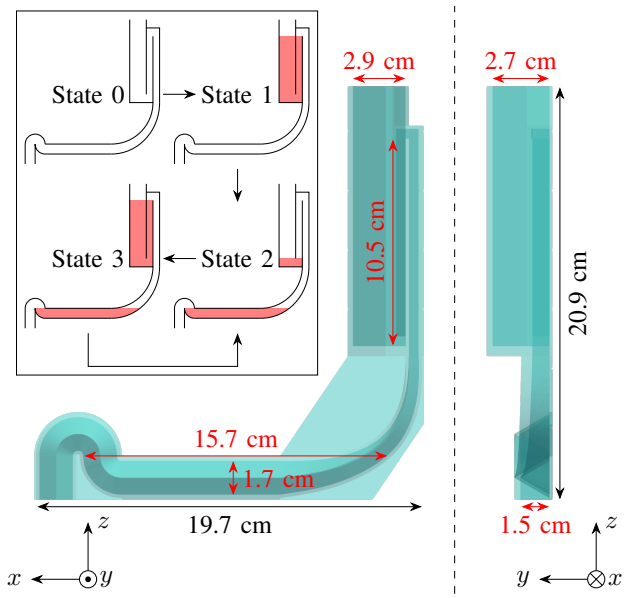

Figure 1: Siphon geometry viewed from the front and side. Red dimensions are some of the interior dimensions of sections which can hold water. Partially transparent for visibility of the interior structure. Inset shows a schematic view of the siphon operation.

been found, the electromagnetic design was done. In this part of the design process, the focus was on adapting the dimensions of the water-filled vertical and horizontal sections for the desired polarization selectivity. We aimed for an isolation on the order of a few 10s of dB between the co-polarized monostatic RCS σ_{HH} (horizontal-horizontal) and σ_{VV} (vertical-vertical) in states 1 and 2, but it should be noted that this was a somewhat arbitrary requirement. Initial guesses were based mostly on rough ideas for suitable length and cross sections, under the constraint that the device should not be larger than the 3D print surface. Designs were simulated numerically in all states, and improved iteratively until acceptable performance was achieved.

3 Numerical Simulations

Numerical simulations were performed to ensure that the design would provide the desired polarization reconfigurability. A simulation mesh was generated from the geometry designed for 3D printing. The geometry was split into sections corresponding to different media, including interior regions containing water and air selected to match all states shown in the inset of Fig. 1. The sections were exported to STEP files and loaded in gmsh [14] where the simulation mesh was

generated. The structure, including all interior regions, was discretized using tetrahedral elements. Simulations were performed using the open source Python FE-BI code FE2MS [15–17] which is based on, among others, FEniCSx [18–22], DEMCEM [23–26] and AdaptOctree [27]. The code is accelerated by a multilevel adaptive cross approximation (ACA) [28, 29] with recompression [30].

All numerical simulations were performed in the frequency range 1 GHz – 2 GHz. The monostatic scattering was simulated for incident plane waves propagating along $-y$ in Fig. 1, with polarization along either x (horizontal) or z (vertical). Each of the states shown in the inset of Fig. 1 was simulated separately with the 3D printed shell taken to have $\varepsilon_{\mathrm{r}} = 2.9 - 0.045j$, corresponding to PET at 1 GHz [31], water according to the model for pure water in [32] at 20°C and air equal to free space. The co-polarized monostatic RCS σ_{HH} and σ_{VV} were computed for these states.

4 Measurements

4.1 Setup

Measurements were conducted in the anechoic chamber of the antenna laboratory at Lund University, Sweden. The chamber was set up with a rotational stage for antenna measurements, and additional absorbers were placed around this to reduce unwanted scattering. A Rohde & Schwarz ZNB8 vector network analyzer (VNA) was connected with port 1 and 2 to the vertical and horizontal ports, respectively, of an ETS-Lindgren 3164-04 diagonal dual polarized horn antenna. This horn antenna was fixed at one end of the anechoic chamber. An initial calibration of the VNA was performed for a reference plane at the interface between the cables and the horn. The VNA was set to sweep 661 frequency points from 700 MHz to 4 GHz at a power of 10 dBm using an intermediate frequency (IF) filter with 100 Hz bandwidth and selectivity setting “High”. Averaging was performed across 5 sweeps to further reduce noise. All S-parameters were measured to be able to inspect both co-polarized and cross-polarized scattering.

Objects to be measured were placed on a structure made from expanded polystyrene (EPS) as shown in Fig. 2. The distance between the end of the horn and the center of the object was roughly 2.7 m. Depending on the size of the object to be measured, additional EPS layers were stacked to put the center of the object at the same height as the horn. The siphon device under test (DUT) was fixed to the EPS using wooden sticks as shown in Fig. 3, while reference spheres were placed directly on EPS sheets with grooves to keep them in place.

To obtain a reference measurement for RCS calibration, a metal circular cylinder of diameter 4 cm and height 8 cm was measured with a polarization co-polarized to the axis of symmetry. This reference object was selected for its simple shape, as well as its RCS being close to the expected RCS of the DUT in states 1–3. A sphere of diameter 4 cm was also measured to validate the use of the reference cylinder for RCS calibration. The DUT was measured filled with either

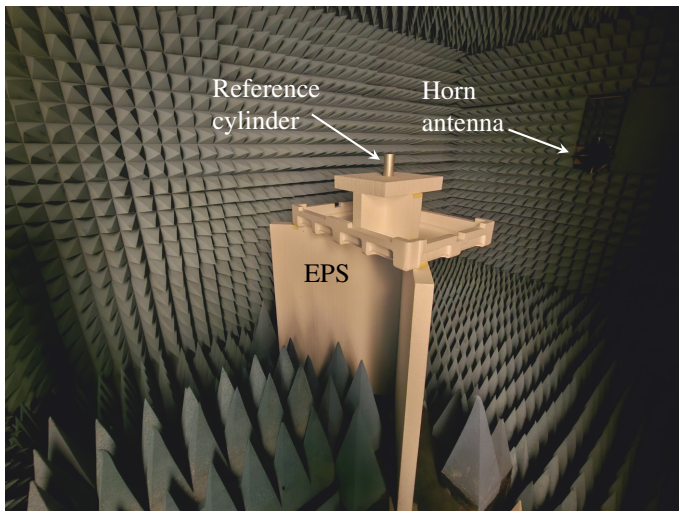

Figure 2: Measurement setup for the metallic reference cylinder.

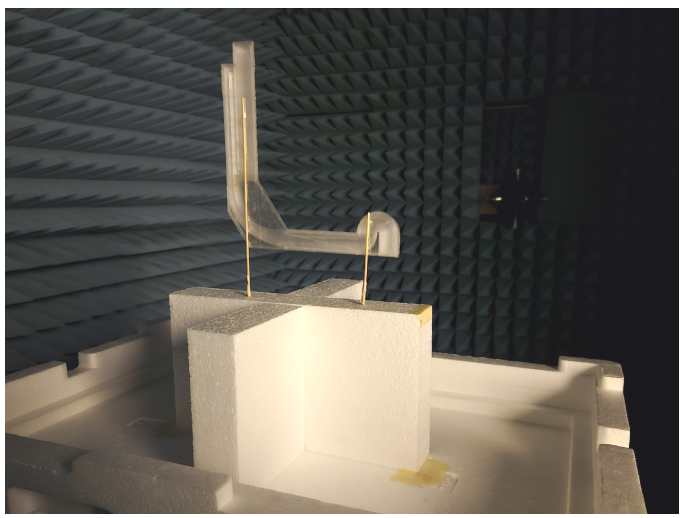

Figure 3: Close-up of the measurement setup for the DUT.

distilled water or tap water. It was filled to obtain, in sequence, state 0 through 3, and measurements were performed for each state. Before each measurement, reference object as well as siphon, a background measurement was performed for the chamber without the object to be measured. For measurements of the DUT, the wooden sticks were not part of the background measurement as they were fixed to the structure.

4.2 Data Processing and Calibration

The measurement data corresponding to co-polarized reflections, S_{11} and S_{22}, was processed using background subtraction, time gating and RCS calibration against known reference objects [33]. Background subtraction and time gating were performed identically for reference objects and the DUT. Background subtraction was performed first by subtracting the S-parameter data by the corresponding background S-parameter data. Time gating was performed on this background subtracted data by transforming the frequency domain data to the time domain and applying a Tukey (tapered cosine) window with a tapering fraction 0.7 centered at a bin corresponding to the range 2.86 m. Transformation back to the frequency domain significantly reduced unwanted reflections. The full window width was selected to be equivalent to a difference in range of 1.8 m to avoid other peaks, and this was determined using manual inspection for the measurement data with the DUT in state 1. The same window settings were used for all measurements.

RCS calibration was performed using this data to obtain the RCS of the DUT, σ_{DUT}, from that of the reference object, σ_{ref}. The full data processing and calibration can be expressed as

$$\sigma_{\mathrm{DUT}} = \frac{\sigma_{\mathrm{ref}}}{|\mathcal{T}(V_{\mathrm{ref}} - V^0_{\mathrm{ref}})|^2} |\mathcal{T}(V_{\mathrm{DUT}} - V^0_{\mathrm{DUT}})|^2 \tag{4.1}$$

where V denote S_{11} or S_{22} for a measurement with an object, V^0 denote S_{11} or S_{22} for a background measurement and $\mathcal{T}$ denotes the time gating procedure. Note that different backgrounds were used for reference and DUT. The reference values σ_{ref} was computed by numerical simulation using only the MoM part of the FE2MS code for the cylinder. To validate this simulation, the RCS for the cylinder was found by calibrating against the sphere with σ_{ref} from a Mie solution. Good agreement was seen between this measurement and the simulation, indicating that the simulated reference data for the cylinder would be accurate to use for calibrating the DUT. While a large bandwidth was used in measurements, not all of it was practically useful when considering the RCS as too high frequencies would put the measured object in the near field. For this reason, only the range 1 GHz – 2 GHz was used for the calibrated results.

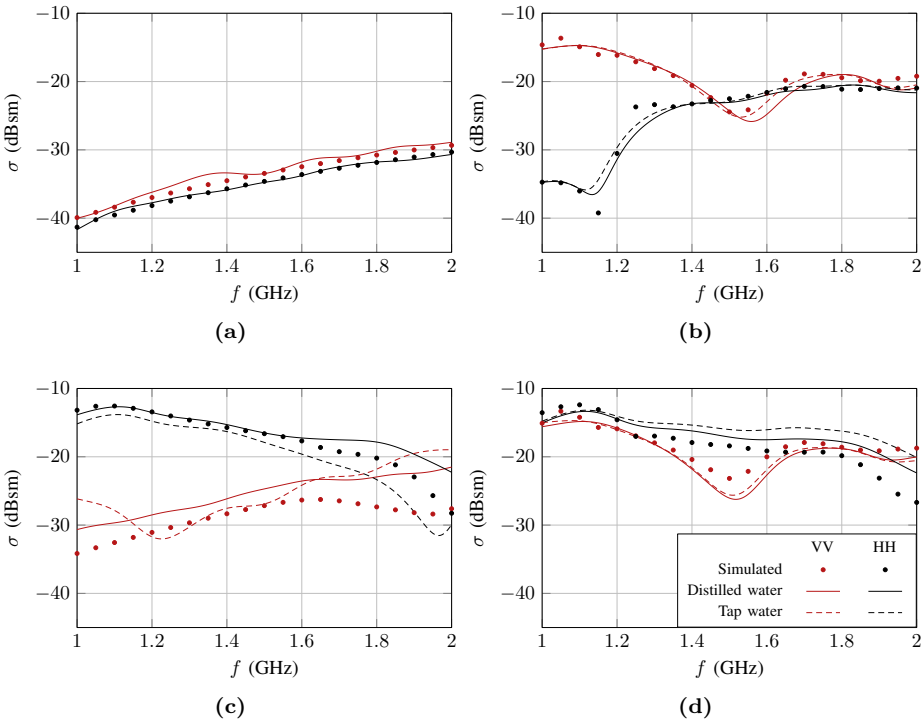

Figure 4: Simulated and measured monostatic RCS for the DUT in state 0 (a), state 1 (b), state 2 (c) and state 3 (d). Calibrated using the metallic cylinder with incident wave co-polarized with cylinder axis. The legend holds for all subfigures.

5 Results and Discussion

The monostatic RCS for numerical simulations and measurements are shown for the four different states of the DUT in Fig. 4. Both measurements with distilled water and tap water are shown. It is seen that the DUT achieves polarization reconfigurability at the lower frequencies, When the vertical section is filled in Fig. 4(b), the RCS is roughly 20 dB higher for VV polarization than for HH polarization. When the horizontal section is filled in Fig. 4(c), the opposite holds but with less separation between polarizations and more variation between the curves. It is also clear by comparison with Fig. 4(a) that there is a significant difference between an empty DUT and a DUT with any section filled with water. As the frequency increases, the polarization selectivity in states 1 and 2 is lost, which is an effect of the thicknesses of the horizontal and vertical sections. The polarization selectivity of state 2 (Fig.4(c)) seems to hold at higher frequencies than that of state 1 (Fig.4(b)), further showing that the reason is the thickness as the horizontal section is thinner than the vertical section.

If a comparison is made between simulations and measurements (with distilled water), it is clear that some states of the DUT show better agreement between simulations and measurements than others. The agreement is best in Fig.4(a) where no water is present in the DUT. This is the state with the lowest uncertainty, as adding water introduced a water level which could vary. This is particularly clear for the states with water in the horizontal sections (state 2 and 3) in Fig. 4(c)-(d). Both of these states are achieved after water is siphoned from the vertical to the horizontal section of the DUT, and it was observed during measurements that the water in the lower section could vary, both in volume and distribution along the x-axis (see Fig. 1). Later testing indicated that these factors might stabilize with further cycling of the states 2 and 3, but no measurements were performed for this process.

When comparing results for distilled water to those for tap water, differences are once again most clear for state 2 (Fig. 4(c)). As two different measurements were performed, the uncertainty in water level as discussed previously should be present. If instead state 1 (Fig. 4(b)) is considered, the water level was much closer between different measurements. The difference in RCS between the two types of water is also much smaller here than for state 2. One of the major differences between distilled and tap water is their ion content, which primarily affects the imaginary part of ε_{r} [1]. The small differences between the water types in Fig. 4(b) then indicate that the scattering response is mainly due to the high contrast between the different media.

While the device presented here differs from many water- and liquid-based electromagnetic devices in the literature, it can still be interesting to compare some properties. First, it can be noted that the frequency of operation for this device is at 1 GHz with a range of a few 100 MHz, as seen in Fig. 4. This was selected both due to the high contrast of water at those frequencies, as well as practical considerations for measurements. Many water-based electromagnetic devices have operating frequencies within an order of magnitude of this [2], which is reasonable as the permittivity of water changes drastically at higher frequencies [1, 32]. Other liquids than water can provide better frequency stability [2]. Another property of interest is that of reconfigurability. This device, along with many other reconfigurable liquid-based electromagnetic devices, relies upon mechanical processes for reconfigurability. This, of course, affects the reconfiguration speeds which can be obtained, and this particular device had a reconfiguration time of roughly 10 s (from state 1 to state 2). In particular, such speeds are orders of magnitude slower than those of electrical reconfiguration mechanisms, and this should be kept in mind when imagining possible applications.

6 Conclusion

In this paper, a simple siphon structure was designed and measured to demonstrate the possibility for electromagnetic reconfigurability. It could be observed

that by adding water to the siphon, the polarization response of the structure could be changed. Some uncertainties, primarily with regard to water levels in the siphon, were present. This suggests that designs based on this mechanism would benefit from a more rigorous hydraulic design process and more characterization than shown in this work. Nevertheless, the example presented here clearly demonstrates that reconfigurability can be achieved through the use of a siphon.

The device presented in this work was primarily used as a demonstration of how a siphon can enable different polarization states of a device with sharp transitions based on the water level. However, possible applications as a type of sensor for critical levels of water could be envisioned. The change in polarization response would make it possible to remotely monitor whether water has reached the critical level without electrical equipment at the measurement site. Perhaps more interestingly, the upper and lower sections of the device presented here could be redesigned for a more interesting application. In this work, the electrical design of those sections was simple in that they mainly provided dipole-like interactions for two orthogonal polarizations. An example of a more intricate electrical design could be to replace the straight pipe sections by interconnected pipes arranged in a grating structure. By using different spacing between pipes in the upper and lower sections, the activation of the siphon would result in an altered frequency response. Of course, such a device would require more complex design work both electrically and mechanically, and is beyond the scope of the simple proof-of-concept for siphons presented here. Another way to use the siphon mechanism, but not the exact design would be as a volume regulating step for other water-based electromagnetic devices. The sharp transition obtained using a siphon would ensure that a minimum volume of water is transferred to the outlet of the siphon, which can be connected to other components. This could be of interest if, for example, a water-based metasurface should be reconfigured by an intermittent supply of water coming from a source external to the electromagnetic system.

Acknowledgments

This work was supported in part by the Swedish Armed Forces, in part by the Swedish Defence Materiel Administration, in part by the National Aeronautics Research Program and in part by the Swedish Governmental Agency for Innovation Systems.

References

[1] Jacobsen RE, Arslanagić S, Lavrinenko AV. Water-based devices for advanced control of electromagnetic waves. *Applied Physics Reviews.* 2021;8(4):041304.

[2] Huang Y, Xing L, Song C, Wang S, Elhouni F. Liquid Antennas: Past,

Present and Future. *IEEE Open Journal of Antennas and Propagation.* 2021;2:473-487.

[3] Kingsley SP, O'Keefe SG. Beam steering and monopulse processing of probe-fed dielectric resonator antennas. *IEE Proceedings - Radar, Sonar and Navigation.* 1999;146(3):121-125.

[4] Chen CH, Peroulis D. Liquid RF MEMS Wideband Reflective and Absorptive Switches. *IEEE Transactions on Microwave Theory and Techniques.* 2007;55(12):2919-2929.

[5] Yoo YJ, Ju S, Park SY, et al. Metamaterial Absorber for Electromagnetic Waves in Periodic Water Droplets. *Scientific Reports.* 2015;5(1):14018.

[6] Jacobsen RE, Nielsen JØ, Lavrinenko AV, Arslanagić S. Tunable water-based metasurface for anomalous wave reflection. *Journal of Physics D: Applied Physics.* 2020;53(50):505104.

[7] Jacobsen RE, Lavrinenko AV, Arslanagić S. Reconfigurable dielectric resonators with imbedded impedance surfaces—From enhanced and directional to suppressed scattering. *Applied Physics Letters.* 2023;122(8):081701.

[8] Tam DWS, inventor; US Department of Navy, assignee . Electrolytic fluid antenna with signal enhancer. US Patent 8,368,605 B1. February 5 2013.; .

[9] Xing L, Xu Q, Zhu J, et al. A High-Efficiency Wideband Frequency-Reconfigurable Water Antenna With a Liquid Control System: Usage for VHF and UHF Applications. *IEEE Antennas and Propagation Magazine.* 2021;63(1):61-70.

[10] Andryieuski A, Kuznetsova SM, Zhukovsky SV, Kivshar YS, Lavrinenko AV. Water: Promising Opportunities For Tunable All-dielectric Electromagnetic Metamaterials. *Scientific Reports.* 2015;5(1):13535.

[11] Song C, Bennett EL, Xiao J, et al. Passive Beam-Steering Gravitational Liquid Antennas. *IEEE Transactions on Antennas and Propagation.* 2020;68(4):3207-3212.

[12] Hero of Alexandria . *The pneumatics of Hero of Alexandria: From the original Greek.* London, UK: Taylor, Walton and Maberly, 1851.

[13] Boatwright A, Hughes S, Barry J. The height limit of a siphon. *Scientific Reports.* 2015;5(1):16790.

[14] Geuzaine C, Remacle JF. Gmsh: A 3-D finite element mesh generator with built-in pre-and post-processing facilities. *International journal for numerical methods in engineering.* 2009;79(11):1309–1331.

[15] Wingren N, Sjöberg D. Investigating Low-Rank Approximations for the Finite Element-Boundary Integral Method. In: 2023 17th European Conference on Antennas and Propagation (EuCAP). 26-31 March 2023; Florence, Italy.

[16] Wingren N, Sjöberg D. Simulating Magnetized Plasma using an Accelerated Finite Element-Boundary Integral Code. In: 2023 XXXVth General Assembly and Scientific Symposium of the International Union of Radio Science (URSI GASS). 19-26 August 2023; Sapporo, Japan.

[17] Wingren N. FE2MS: A finite element-boundary integral code for solving electromagnetic scattering problems. https://github.com/nwingren/fe2ms. Accessed February 9, 2024.

[18] Baratta IA, Dean JP, Dokken JS, et al. DOLFINx: The next generation FEniCS problem solving environment. preprint; 2023. https://doi.org/10.5281/zenodo.10447666. Accessed February 9, 2024.

[19] Logg A, Ølgaard KB, Rognes M, Wells GN, Alnæs MS. FFCx: Next generation FEniCS form compiler. https://github.com/FEniCS/ffcx. Accessed February 9, 2024.

[20] Scroggs MW, Dokken JS, Richardson CN, Wells GN. Construction of Arbitrary Order Finite Element Degree-of-Freedom Maps on Polygonal and Polyhedral Cell Meshes. *ACM Trans. Math. Softw.*. 2022;48(2).

[21] Scroggs MW, Baratta IA, Richardson CN, Wells GN. Basix: a runtime finite element basis evaluation library. *Journal of Open Source Software.* 2022;7(73):3982.

[22] Alnæs MS, Logg A, Ølgaard KB, Rognes ME, Wells GN. Unified Form Language: A Domain-Specific Language for Weak Formulations of Partial Differential Equations. *ACM Trans. Math. Softw.*. 2014;40(2).

[23] Polimeridis AG, Yioultsis TV. On the Direct Evaluation of Weakly Singular Integrals in Galerkin Mixed Potential Integral Equation Formulations. *IEEE Transactions on Antennas and Propagation.* 2008;56(9):3011-3019.

[24] Polimeridis AG, Mosig JR. Complete semi-analytical treatment of weakly singular integrals on planar triangles via the direct evaluation method. *International Journal for Numerical Methods in Engineering.* 2010;83(12):1625-1650.

[25] Polimeridis AG, Tamayo JM, Rius JM, Mosig JR. Fast and Accurate Computation of Hypersingular Integrals in Galerkin Surface Integral Equation Formulations via the Direct Evaluation Method. *IEEE Transactions on Antennas and Propagation.* 2011;59(6):2329-2340.

[26] Polimeridis AG, Mosig JR. On the Direct Evaluation of Surface Integral Equation Impedance Matrix Elements Involving Point Singularities. *IEEE Antennas and Wireless Propagation Letters.* 2011;10:599-602.

[27] Kailasa S, Betcke T. AdaptOctree: Adaptive Linear Octrees in Python. https://github.com/Excalibur-SLE/AdaptOctree. Accessed February 9, 2024.

[28] Bebendorf M. Approximation of boundary element matrices. *Numerische Mathematik.* 2000;86(4):565–589.

[29] Zhao K, Vouvakis M, Lee JF. The adaptive cross approximation algorithm for accelerated method of moments computations of EMC problems. *IEEE Transactions on Electromagnetic Compatibility.* 2005;47(4):763-773.

[30] Bebendorf M, Kunis S. Recompression techniques for adaptive cross approximation. *The Journal of Integral Equations and Applications.* 2009;21(3):331–357.

[31] Zechmeister J, Lacik J. Complex Relative Permittivity Measurement of Selected 3D-Printed Materials up to 10 GHz. In: 2019 Conference on Microwave Techniques (COMITE). 16-18 April 2019; Pardubice, Czech Republic.

[32] Ellison WJ. Permittivity of Pure Water, at Standard Atmospheric Pressure, over the Frequency Range –25THz and the Temperature Range –100°C. *Journal of Physical and Chemical Reference Data.* 2007;36(1):1-18.

[33] Knott EF, Shaeffer JF, Tuley MT. *Radar Cross Section.* Raleigh, NC, USA: SciTech Publishing, Inc. 2nd ed., 2004.

Characteristic Modes of Nonreciprocal Systems

Paper III

N. Wingren, D. Sjöberg, M. Gustafsson, J. Lundgren,
M. Capec, L. Jelinek, and K. Schab

Published as: N. Wingren, D. Sjöberg, M. Gustafsson, J. Lundgren, M. Capec, L. Jelinek, and K. Schab, "Characteristic Modes of Nonreciprocal Systems," *IEEE Antennas and Wireless Propagation Letters*, vol. 23, no. 12, pp. 4483–4487, 2024.

Abstract

The scattering formulation of characteristic mode decomposition is utilized to extend modal analysis to lossless scatterers breaking time-reversal symmetry. This enables characteristic modes analysis on devices containing gyrotropic or moving media. The resulting nonreciprocity introduces features not observed in reciprocal scenarios, such as asymmetric phase progression in characteristic far fields. These new phenomena are carefully discussed using examples of varying complexity. Indicators of nonreciprocity based on modal data are also introduced.

1 Introduction

Characteristic modes are an intensively studied branch of classical electrodynamics with applications in antenna and scattering theory [1]. Commonly, characteristic mode analysis is associated with the method of moments and the study of perfectly conducting bodies [2, 3], but its original scattering formulation [4, 5], recently expanded and formalized in [6–8], significantly broadens the application of characteristic modes to scatterers comprised of arbitrary materials. This immediately raises questions about the properties of characteristic modes in the presence of exotic materials, such as those with bianisotropic response and/or those in which nonreciprocity stems from breaking time-reversal symmetry [9]. These scenarios emerge when studying antennas on gyrotropic substrates (*e.g.*, , ferrite materials) [10–12] or material bodies in motion [13], and give characteristic modes additional parameterization in quantities such as the intensity of a biasing field or velocity. This letter initiates a discussion on the characteristic modes of linearized, lossless, nonreciprocal scatterers by showing their fundamental properties and examining indicators of modal nonreciprocity.

2 Scattering-Based Characteristic Modes

This paper uses a formulation of characteristic modes based on an object's scattering matrix [4] recently formalized in [6–8]. In contrast to impedance formulations [2,14], the scattering approach avoids problems reported in [6] in cases where the radiation matrix is not equal to the real (Hermitian) part of the impedance matrix, see [2, Eqs. (10)–(11)].

Using the scattering matrix $\mathbf{S}$ of a linear[1] material object or circuit network [4, 16], characteristic modes are computed by the eigenvalue problem [6, 17, 18]

$$\mathbf{S}\mathbf{a}_n = s_n \mathbf{a}_n, \tag{2.1}$$

[1] While realistic nonreciprocal materials exhibit nonlinear characteristics, here we approximate all materials using a standard, linear, bianisotropic constitutive relation [15].

where the complex eigenvalue $s_n = 1 + 2t_n$ is commonly parametrized by a real characteristic number λ_n via relation $s_n = -(1 - \mathrm{j}\lambda_n)/(1 + \mathrm{j}\lambda_n)$ and where eigenvectors $\mathbf{a}_n$ collect the expansion coefficients of the fields in the selected basis, such as spherical vector waves commonly used in the case of finite scatterers in free space [19]. The modal significance of an eigenvector is denoted as $|t_n| = |1 + \mathrm{j}\lambda_n|^{-1} = |s_n - 1|/2$. Other characteristic quantities, such as the characteristic currents, can be computed by exciting the system with the vector $\mathbf{a}_n$ and evaluating the desired quantity [6].

For lossless scatterers, the scattering matrix is unitary, $\mathbf{S}^{\mathrm{H}}\mathbf{S} = \mathbf{1}$, and pairs of characteristic excitations can be made orthonormal, *i.e.*, , $\mathbf{a}_m^{\mathrm{H}}\mathbf{a}_n = \delta_{mn}$, where δ_{mn} is the Kronecker delta and $^{\mathrm{H}}$ denotes Hermitian transpose.

3 Characterizing Reciprocity and Nonreciprocity

Characteristic modes of a lossless scatterer satisfy [6, App. B]

$$\mathbf{S}^{\mathrm{T}}\mathbf{a}_n^* = s_n\mathbf{a}_n^* \tag{3.1}$$

due to the unitarity of $\mathbf{S}$. The scattering matrix is symmetric $\mathbf{S}^{\mathrm{T}} = \mathbf{S}$ for reciprocal scatterers, in which case both $\mathbf{a}_n$ and $\mathbf{a}_n^*$ are eigenvectors of $\mathbf{S}$ with the same eigenvalue. Hence, the eigenvectors can always be made real-valued[2], akin to the treatment of characteristic currents [2]. Due to symmetries of vector spherical waves [19, Sec. 7.8], the real-valued characteristic vectors $\mathbf{a}_n$ imply conjugate inversion symmetry [20, Eqs. (29)–(30)] of the characteristic far fields

$$\boldsymbol{F}_n(-\hat{\boldsymbol{r}}) = -\boldsymbol{F}_n^*(\hat{\boldsymbol{r}}), \tag{3.2}$$

where $\hat{\boldsymbol{r}}$ is an observation direction $\hat{\boldsymbol{r}} = \boldsymbol{r}/r$ and the far field $\boldsymbol{F}$ is defined by the scattered field $\boldsymbol{E}_{\mathrm{s}}$ as $\boldsymbol{F}(\hat{\boldsymbol{r}}) = r\exp\{\mathrm{j}kr\}\,\boldsymbol{E}_{\mathrm{s}}(\boldsymbol{r})$ for $r \to \infty$. This property also follows from selecting real-valued currents in reciprocal EFIE formulations of characteristic modes[3].

The above-mentioned properties of reciprocal systems (real-valued eigenvectors, far-field inversion symmetry) are lost in nonreciprocal systems where $\mathbf{S} \neq \mathbf{S}^{\mathrm{T}}$, and their absence can be utilized as distinguishing features to characterize nonreciprocity. To detect nonreciprocity of characteristic modes, the scattering matrix $\mathbf{S}$ is decomposed into its symmetric and antisymmetric parts as $\mathbf{S} = (\mathbf{S}+\mathbf{S}^{\mathrm{T}})/2+(\mathbf{S}-\mathbf{S}^{\mathrm{T}})/2$. This implies that the cycle-mean outgoing power P_{o} can be written

$$P_{\mathrm{o}} = \frac{1}{2}|\mathbf{S}\mathbf{a}|^2 = \frac{1}{8}\left|(\mathbf{S}+\mathbf{S}^{\mathrm{T}})\mathbf{a}\right|^2 + \frac{1}{8}\left|(\mathbf{S}-\mathbf{S}^{\mathrm{T}})\mathbf{a}\right|^2 + \frac{1}{4}\left(|\mathbf{S}\mathbf{a}|^2 - \left|\mathbf{S}^{\mathrm{T}}\mathbf{a}\right|^2\right). \tag{3.3}$$

[2]Eigenvectors for non-degenerate cases are generally equiphase (with orthonormal $\mathbf{a}_n$ satisfying $|\mathbf{a}_n^{\mathrm{T}}\mathbf{a}_n| = 1$). For a degenerate case, the modes can exhibit phase progression, but linear combinations of vectors $\mathbf{a}_n$ and $\mathbf{a}_n^*$ can be used to produce real-valued eigenvectors [6, App. B]

[3]The integral relationship between a real-valued current distribution and its radiated far-field [21, §3.5-3.6] illustrates this property.

We denote the first term on the right-hand side as the reciprocal outgoing power P_o^r, while the second row corresponds to the nonreciprocal outgoing power P_o^nr. Note that the final term vanishes for lossless scatterers. We then propose the ratio

$$\nu = P_\mathrm{o}^\mathrm{nr}/P_\mathrm{o} \in [0,1] \tag{3.4}$$

to characterize the presence of nonreciprocity for a given excitation at a particular frequency. Furthermore, modal far fields $\boldsymbol{F}_n$ violating (3.2), such as those with asymmetric phase progression, are an indicator of nonreciprocal behavior. Together, the study of the quantity ν and modal phase progression serve to classify individual characteristic modes as either reciprocal or nonreciprocal. Another classification of nonreciprocity based on extinction cross section has recently been proposed in [22], but is not readily applicable to characteristic modes.

4 Examples

4.1 Ideal Circulator

The definition of characteristic modes in (1) can be applied to any system described by a scattering matrix, including general circuit networks [16], such as N-port (nonreciprocal) circulators [23, §7.1] with the scattering matrix

$$\mathbf{S} = \begin{bmatrix} 0 & 1 & 0 & \cdots & 0 \\ 0 & 0 & 1 & \cdots & 0 \\ \vdots & \vdots & \vdots & \ddots & \vdots \\ 0 & 0 & 0 & \cdots & 1 \\ 1 & 0 & 0 & \cdots & 0 \end{bmatrix}. \tag{4.1}$$

This operator exhibits N-fold rotational C_N symmetry and the characteristic modes (in this case, eigenmodes of the matrix $\mathbf{S}$ [6]) associated with this system [24] can be classified as progressive phase modes

$$\mathbf{a}_{\pm p} = N^{-1/2}\left[1, \mathrm{e}^{\pm \mathrm{j}2p\pi/N}, \cdots, \mathrm{e}^{\pm \mathrm{j}2p\pi(N-1)/N}\right]^\mathrm{T}, \tag{4.2}$$

and $s_{\pm p} = \mathrm{e}^{\pm \mathrm{j}2p\pi/N}$ for $1 \leq p \leq (N-1)/2$ with $|\mathbf{a}_{\pm p}^\mathrm{T}\mathbf{a}_{\pm p}| = 0$, an equiphase even mode

$$\mathbf{a}_\mathrm{e} = N^{-1/2}\left[1, 1, \cdots, 1\right]^\mathrm{T}, \quad s_\mathrm{e} = 1, \tag{4.3}$$

with $|\mathbf{a}_\mathrm{e}^\mathrm{T}\mathbf{a}_\mathrm{e}| = 1$, and an equiphase odd mode (even N only)

$$\mathbf{a}_\mathrm{o} = N^{-1/2}\left[1, -1, \cdots, 1, -1\right]^\mathrm{T}, \quad s_\mathrm{o} = -1 \tag{4.4}$$

with $|\mathbf{a}_\mathrm{o}^\mathrm{T}\mathbf{a}_\mathrm{o}| = 1$. Application of the definition in (3.4) to each class of characteristic modes gives

$$\nu_{\pm p} = \sin^2(2p\pi/N), \quad \nu_\mathrm{e} = 0, \quad \nu_\mathrm{o} = 0. \tag{4.5}$$

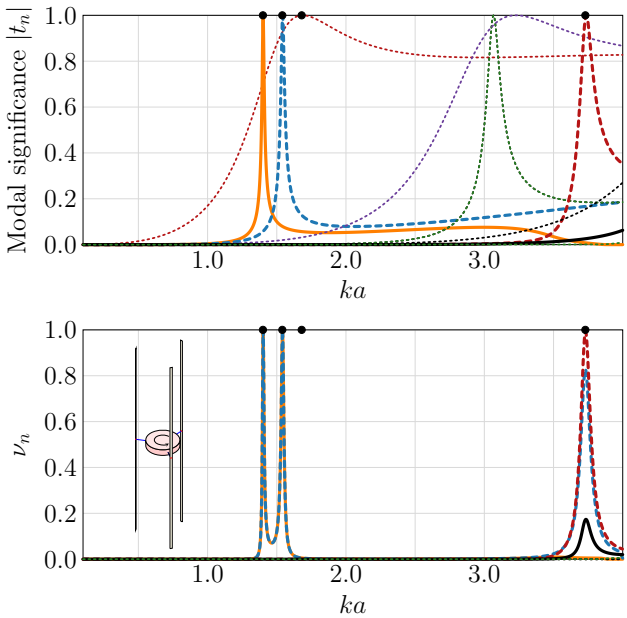

Figure 1: (Top) Modal significances of three parallel dipoles connected to an ideal circulator. (Bottom) Nonreciprocity ratio ν corresponding to modes depicted in the top panel.

Similarly, the modal significance of the modes reads

$$|t_{\pm p}| = |\sin(p\pi/N)|\,, \quad |t_{\mathrm{e}}| = 0, \quad |t_{\mathrm{o}}| = 1. \tag{4.6}$$

These results show that characteristic modes of nonreciprocal devices (such as this ideal circulator) can exhibit a range of values of the parameter ν, including particular excitations which, to the outside observer, cause the system to behave in a completely reciprocal manner with $\nu = 0$, *cf.*, the equiphase even / odd modes in (4.5). In contrast, the progressive phase modes $\mathbf{a}_{\pm p}$ cannot be normalized to be real-valued and exhibit non-zero values ν, both indicators of non-reciprocal behavior.

Scattering or transition matrices analogous to (4.1) can be used to describe hypothetical objects exhibiting nonreciprocal coupling between the incident and scattered spherical waves, and a scattering dyadic can be constructed to describe non-reciprocal scattering on a direction-by-direction basis [8].

4.2 Nonreciprocal Subcircuit

The second example deals with a free-space scatterer in which nonreciprocity is induced by the presence of an ideal lumped circulator. Specifically, the circulator is connected to delta-gap ports of three thin-strip dipoles of length L and

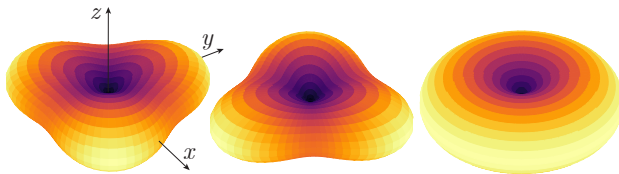

Figure 2: Directivity patterns corresponding to solid orange peak at $ka \approx 1.40$, dashed blue peak at $ka \approx 1.54$, and dotted red peak at $ka \approx 1.68$ in Fig. 1, see black circle markers at the top of the plot.

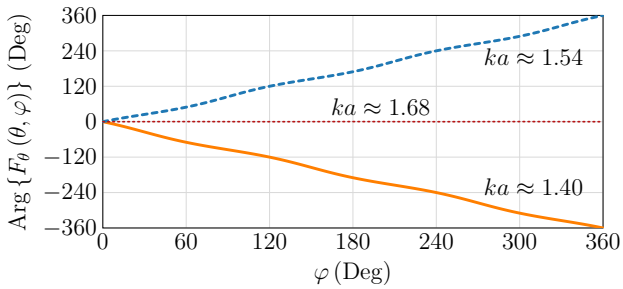

Figure 3: Phase of electric far-field corresponding to Fig. 2. Only θ-component in the xy plane is shown.

width $L/50$, see the inset in Fig. 1. The dipoles are made of a perfect electric conductor, are parallel to the z-axis, and are positioned so that their centers lie on the circle with radius $L/8$. The dipoles are distributed uniformly along this circle. The circulator is placed at the origin and is connected with the dipole ports via radial transmission lines of length $L/8$ and characteristic impedance $Z_0 = 50\,\Omega$ matching the system impedance of the ideal circulator. The scattering scenario is modeled using a combination of the method-of-moments [25] and the scattering matrix of a three-port circuit [23].

Modal significances of this system are depicted in the top panel of Fig. 1, while the nonreciprocity ratio ν is shown in the bottom panel of Fig. 1. The color coding of both figures is identical. Most of the modal spectrum shows negligible values of the ratio ν. Exceptions are peaks at $ka \approx \{1.40, 1.54, 3.73\}$, see black circle markers at the top of the plots, also exhibiting high modal significance in the same modes. The other modes with high modal significance, such as those belonging to the red dotted line in Fig. 1, show reciprocal behavior with $\nu = 0$ and symmetric equiphase radiation patterns satisfying (3.2).

The nonreciprocal effects associated with the two peaks at $ka \approx 1.40$ and $ka \approx 1.54$ are best observed in the modal far fields, which are depicted in Fig. 2 as a directivity pattern and in Fig. 3 as a phase of the θ component of the electric far field in the xy-plane ($\theta = \pi/2$). As a reference, the right panel in Fig. 2 shows the radiation pattern of an omnidirectional (inversely symmetric) significant reciprocal mode at $ka \approx 1.68$. The dashed red trace in Fig. 3 also shows

that this radiation pattern is equiphase. It can be seen that both nonreciprocal examples share features which contrast with the reciprocal mode. Notably, their radiation diagrams lack inversion symmetry (3.2) and exhibit 120° rotational symmetry and phase progression along angular direction φ, features that are not present around reciprocal scatterers. Because this system contains the C_3 symmetry subgroup, its low-order progressive phase characteristic modes bear a strong resemblance to the $p = \pm 1$ modes of the ideal circulator discussed in (4.2) for $N = 3$, with lobes separated by 120° in phase and angle in the xy plane, while the equiphase mode corresponds to the even circulator mode in (4.3).

4.3 General Nonreciprocal Media

The last example presents characteristic modes of a penetrable body made of a nonreciprocal medium, showing the generality of the scattering-based formulation of characteristic modes for systems not readily analyzed using impedance-based methods. Consider a cylinder of radius ρ and height h, centered at the origin with its axis lying along axis z, filled with a homogeneous, real-valued permittivity $\varepsilon_\mathrm{r}\varepsilon_0$ and permeability $\mu_\mathrm{r}\mu_0$. Let the cylinder rotate around its axis with angular frequency ω such that the velocity of a point of the cylinder reads $\boldsymbol{v} = \omega\,(x\hat{\boldsymbol{y}} - y\hat{\boldsymbol{x}})$. The maximum speed is assumed to be much smaller than the speed of light $c_0 = 1/\sqrt{\mu_0\varepsilon_0}$, *i.e.*, $\beta_\rho = \omega\rho/c_0 \ll 1$.

The unidirectional movement of the cylinder breaks time-reversal symmetry and introduces nonreciprocity analogous to the motion of fluid studied in [9, 26]. To study the electromagnetic scattering from such an object and to evaluate its characteristic modes, the rotating cylinder can be replaced by a stationary cylinder with constitutive relations [13, 27]

$$\begin{aligned} \boldsymbol{D} &= \boldsymbol{\varepsilon}\cdot\boldsymbol{E} + c_0^{-1}\boldsymbol{\xi}\cdot\boldsymbol{H} \\ \boldsymbol{B} &= c_0^{-1}\boldsymbol{\varsigma}\cdot\boldsymbol{E} + \boldsymbol{\mu}\cdot\boldsymbol{H} \end{aligned} \tag{4.7}$$

where $\boldsymbol{\varepsilon} = \varepsilon_\mathrm{r}\varepsilon_0\mathbf{1}$ and $\boldsymbol{\mu} = \mu_\mathrm{r}\mu_0\mathbf{1}$ with $\mathbf{1}$ denoting the identity tensor and (using the Cartesian coordinate system)

$$\boldsymbol{\xi} = \omega\frac{\varepsilon_\mathrm{r}\mu_\mathrm{r} - 1}{c_0}\begin{pmatrix} 0 & 0 & x \\ 0 & 0 & y \\ -x & -y & 0 \end{pmatrix}, \quad \boldsymbol{\varsigma} = -\boldsymbol{\xi}. \tag{4.8}$$

The constitutive relations above describe a lossless ($\boldsymbol{\varepsilon} = \boldsymbol{\varepsilon}^\mathrm{H}$, $\boldsymbol{\mu} = \boldsymbol{\mu}^\mathrm{H}$, $\boldsymbol{\varsigma} = \boldsymbol{\xi}^\mathrm{H}$), but inhomogeneous and nonreciprocal ($\boldsymbol{\varsigma} \neq -\boldsymbol{\xi}^\mathrm{T}$) stationary medium replacing the rotating medium [19]. This example is representative of constitutive relations encountered when modeling biased ferrites or other practical nonreciprocal media.

A common benchmarking example for characteristic modes is a dielectric cylinder of radius $\rho = 5.25\,\mathrm{mm}$ and height $h = 4.6\,\mathrm{mm}$ with $\varepsilon_\mathrm{r} = 38$, and $\mu_\mathrm{r} = 1$ [7]. Applying the transformation in (4.7)–(4.8), the characteristic modes of this system are computed for various relative speeds $\beta_\rho \leq 0.01$ using the iterative

Table 1: Resonant frequencies in GHz of modes in Fig. 4 at different β_ρ.

β_ρ	TE_{01}	HEM_{11}		HEM_{12}		TM_{10}
0	4.86	6.35	6.35	6.63	6.63	7.53
0.005	4.86	6.30	6.39	6.59	6.68	7.53
0.01	4.86	6.27	6.44	6.55	6.73	7.54

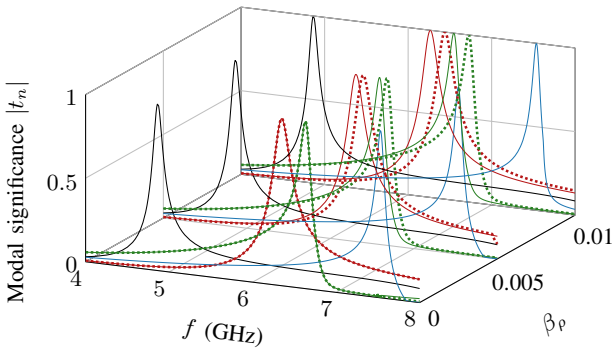

Figure 4: Modal significances of a rotating cylinder for different β_ρ. The first 6 modes are displayed, corresponding to TE_{01} (black), HEM_{11} (red), HEM_{12} (green) and TM_{01} (blue). Both HEM modes are degenerated at $\beta_\rho = 0$.

method [28], which employs a finite element-boundary integral hybrid solver capable of computations involving general bianisotropic media [29]. Speeds of this order have been shown to significantly impact the scattering characteristics compared to the stationary case [27].

Modal significances of the cylinder at three different β_ρ are shown in Fig. 4. The resonant frequencies of the modes at different β_ρ are shown in Table 1 for clarity. For the stationary case ($\beta_\rho = 0$), the results match those in [7]. There are six modes displayed, two of which are rotationally symmetric (TE_{01} and TM_{01}) and four of which are degenerate pairs (HEM_{11} and HEM_{12}). All modes have $\nu = 0$ and exhibit symmetric far fields satisfying (3.2). As rotation increases ($\beta_\rho = 0.005$ and $\beta_\rho = 0.01$), the symmetric TE_{01} and TM_{01} modes are relatively unaffected and preserve their symmetry properties, as their symmetry axis matches the axis of rotation. In contrast, the mode pairs which are degenerate at $\beta_\rho = 0$ show level splitting with their frequency separation increasing for higher β_ρ, similarly to the case studied in [9].

For $\beta_\rho = 0.01$, modal significances and ν are shown in Fig. 5 for the 10 first modes. It is seen that non-zero ν is present in all modes which exhibit level splitting. It is, however, also seen that the mode drawn as a blue line has significant ν at $f > 7.62\,\text{GHz}$. The modal significance of this mode matches the TM_{01} at $f < 7.62\,\text{GHz}$, but is swapped with the solid purple line at $f > 7.62\,\text{GHz}$ due to crossing avoidance, which occurs in nonsymmetric meshes [30]. This forces the far field of the blue line to abruptly change from rotationally symmetric to non-symmetric, which is accompanied by a similarly abrupt change in ν. The

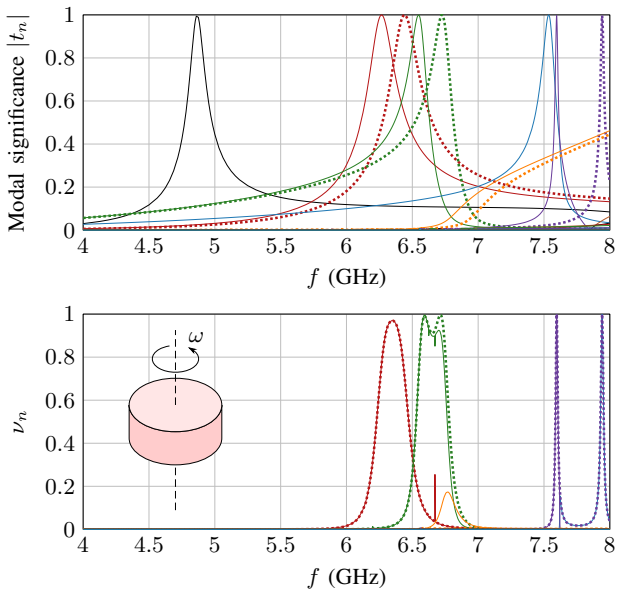

Figure 5: (Top) Modal significance of a rotating cylinder with $\beta_\rho = 0.01$. (Bottom) Nonreciprocity ratio ν corresponding to modes depicted in the top panel. Solid/dashed lines of the same color are degenerate modes at $\beta_\rho = 0$.

spikes in ν for the solid green and red lines at $f = 6.67\,\text{GHz}$ are also related to the tracking as they correspond to a point where crossing avoidance does not happen due to coarse frequency resolution. Together, these observations show how the characterization of nonreciprocity in characteristic modes is sensitive to tracking.

The far field corresponding to one of the nonreciprocal modes is illustrated in Fig. 6 for the cylinder stationary and rotating with $\beta_\rho = 0.01$. It is seen that the far field can be selected to be purely real with inversion symmetry (3.2) in the stationary case, but not in the rotating case. In the stationary case, the HEM mode is degenerated with the far field of the other degenerate mode being shifted 90° in the φ coordinate. While the two far fields in Fig. 6 look very different, it is noted that a far field very similar to that at $\beta_\rho = 0.01$ can be obtained by linearly combining the two degenerate modes at $\beta_\rho = 0$ with one mode phase shifted $\pi/2$.

5 Conclusion

This letter describes how characteristic mode analysis can be applied to nonreciprocal devices, thereby extending the established theoretical and computational state-of-the-art. This advance enables the analysis of problems involving

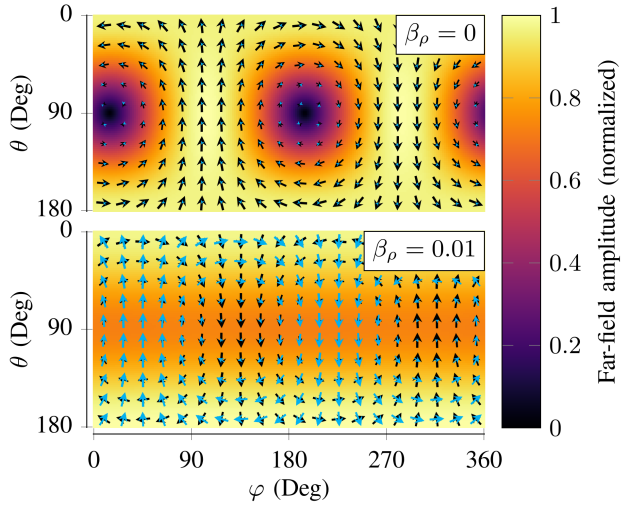

Figure 6: Far field for the HEM_{11} mode corresponding to the solid red line in Fig. 4 at two different β_ρ. Color images show the amplitude of the far field normalized to its peak value, while arrows indicate the directions of real (black) and imaginary (blue) parts.

gyrotropic materials, moving media, and lumped non-reciprocal devices. The decomposition employs scattering matrices, which can be computed numerically in arbitrary full-wave solvers. Certain cases, such as a spherical shell filled with bianisotropic material, even retain the potential for analytical solutions [19].

Examples discussed throughout the letter illustrate how specific modal properties are lost when a system exhibits nonreciprocal behavior. Modal nonreciprocity varies with frequency, hindering straightforward single-frequency classification of a mode as being (non)reciprocal. Open challenges include defining a measure that effectively quantifies modal nonreciprocity and incorporating losses and nonlinear effects commonly associated with realistic nonreciprocal materials.

References

[1] B. Lau, M. Capek, and A. M. Hassan, "Characteristic modes: Progress, overview, and emerging topics," *IEEE Antennas Propagat. Mag.*, vol. 64, pp. 14–22, Apr. 2022.

[2] R. F. Harrington and J. R. Mautz, "Theory of characteristic modes for conducting bodies," *IEEE Trans. Antennas Propag.*, vol. 19, pp. 622–628, Sept. 1971.

[3] M. Capek and K. Schab, "Computational aspects of characteristic mode decomposition: An overview," *IEEE Antennas Propagat. Mag.*, vol. 64, no. 2,

pp. 23–31, 2022.

[4] C. G. Montgomery, R. H. Dicke, and E. M. Purcell, *Principles of Microwave Circuits*. New York, United States: McGraw-Hill, 1948.

[5] R. J. Garbacz, *A Generalized Expansion for Radiated and Scattered Fields*. PhD thesis, The Ohio State Univ., 1968.

[6] M. Gustafsson, L. Jelinek, K. Schab, and M. Capek, "Unified theory of characteristic modes: Part I – Fundamentals," *IEEE Trans. Antennas Propag.*, vol. 70, pp. 11814–11824, Dec. 2022.

[7] M. Gustafsson, L. Jelinek, K. Schab, and M. Capek, "Unified theory of characteristic modes: Part II – Tracking, losses, and FEM evaluation," *IEEE Trans. Antennas Propag.*, vol. 70, pp. 11814–11824, Dec. 2022.

[8] M. Capek, J. Lundgren, M. Gustafsson, K. Schab, and L. Jelinek, "Characteristic mode decomposition using the scattering dyadic in arbitrary full-wave solvers," *IEEE Trans. Antennas Propag.*, vol. 71, no. 1, pp. 830–839, 2023.

[9] R. Fleury, D. L. Sounas, C. F. Sieck, M. R. Haberman, and A. Alù, "Sound isolation and giant linear nonreciprocity in a compact acoustic circulator," *Science*, vol. 343, no. 6170, pp. 516–519, 2014.

[10] D. M. Pozar, "Radiation and scattering characteristics of microstrip antennas on normally biased ferrite substrates," *IEEE Trans. Antennas Propag.*, vol. 40, no. 9, pp. 1084–1092, 1992.

[11] U. Ozgur, Y. Alivov, and H. Morkoc, "Microwave ferrites, Part 1: fundamental properties," *J. Mater. Sci.: Mater. Electron.*, vol. 20, pp. 789–834, Jun. 2009.

[12] U. Ozgur, Y. Alivov, and H. Morkoc, "Microwave ferrites, Part 2: passive components and electrical tuning," *J. Mater. Sci.: Mater. Electron.*, vol. 20, pp. 911–952, Jun. 2009.

[13] J. Van Bladel, *Relativity and engineering*, vol. 15. Springer Science & Business Media, 2012.

[14] R. F. Harrington and J. R. Mautz, "Computation of characteristic modes for conducting bodies," *IEEE Trans. Antennas Propag.*, vol. 19, pp. 629–639, Sep. 1971.

[15] J. A. Kong, *Electromagnetic wave theory*. Nashville, TN: John Wiley & Sons, 2 ed., 1990.

[16] J. Mautz and R. Harrington, "Modal analysis of loaded n-port scatterers," *IEEE Trans. Antennas Propag.*, vol. 21, no. 2, pp. 188–199, 1973.

[17] R. Garbacz, "Modal expansions for resonance scattering phenomena," *Proc. IEEE*, vol. 53, pp. 856–864, Aug. 1965.

[18] K. Schab, F. W. Chen, L. Jelinek, M. Capek, J. Lundgren, and M. Gustafsson, "Characteristic modes of frequency-selective surfaces and metasurfaces from S-parameter data," *IEEE Trans. Antennas Propag.*, vol. 71, no. 12, pp. 9696–9706, 2023.

[19] G. Kristensson, *Scattering of Electromagnetic Waves by Obstacles*. Edison, NJ: SciTech Publishing, an imprint of the IET, 2016.

[20] W. Kahn and H. Kurss, "Minimum-scattering antennas," *IEEE Trans. Antennas Propag.*, vol. 13, no. 5, pp. 671–675, 1965.

[21] C. A. Balanis, *Antenna Theory Analysis and Design*. Wiley, 3 ed., 2005.

[22] N. Nefedkin, M. Cotrufo, and A. Alù, "Nonreciprocal total cross section of quantum metasurfaces," *Nanophotonics*, vol. 12, no. 3, pp. 589–606, 2023.

[23] D. M. Pozar, *Microwave Enginnering*. Wiley, 4th ed., 2011.

[24] B. A. Auld, "The synthesis of symmetrical waveguide circulators," *IRE Trans. Microwave Theory Tech.*, vol. 7, no. 2, pp. 238–246, 1959.

[25] "Antenna Toolbox for MATLAB (AToM)," 2023. www.antennatoolbox.com.

[26] Y. Wang, H. Goh, S. A. Mann, and A. Alù, "Strong nonreciprocal acoustic extinction and asymmetric audibility from spinning fluid scatterers," *Phys. Rev. B*, vol. 108, no. 16, p. 165129, 2023.

[27] J. Van Bladel, "Electromagnetic fields in the presence of rotating bodies," *Proc. IEEE*, vol. 64, no. 3, pp. 301–318, 1976.

[28] J. Lundgren, K. Schab, M. Capek, M. Gustafsson, and L. Jelinek, "Iterative calculation of characteristic modes using arbitrary full-wave solvers," *IEEE Antennas Wireless Propag. Lett.*, vol. 22, no. 4, pp. 799–803, 2023.

[29] N. Wingren, "FE2MS: A finite element-boundary integral code for solving electromagnetic scattering problems," 2023. Accessed: 16 Nov. 2023. [Online]. Available: https://github.com/nwingren/fe2ms.

[30] K. R. Schab and J. T. Bernhard, "A group theory rule for predicting eigenvalue crossings in characteristic mode analyses," *IEEE Antennas Wireless Propag. Lett.*, no. 16, pp. 944–947, 2017.

Nondestructive Testing Using mm-Wave Sparse Imaging Verified for Singly Curved Composite Panels

N. Wingren and D. Sjöberg

Paper IV

Published as: N. Wingren and D. Sjöberg, "Nondestructive Testing Using mm-Wave Sparse Imaging Verified for Singly Curved Composite Panels," *IEEE Transactions on Antennas and Propagation*, Vol. 71, No. 1, pp. 1185–1189, 2022.

Abstract

Nondestructive testing of composite materials is important in aerospace applications, and mm-wave imaging has been increasingly used for this purpose. Imaging is traditionally performed using Fourier methods, with inverse methods being an alternative. This communication presents a mm-wave imaging method with an inverse approach intended for nondestructive testing of singly curved composite panels with sparsely distributed flaws. It builds on previous work which was limited to imaging on planar panels. The move from planar to singly curved panels increases the applicability of the method for aerospace applications. The imaging method is reference-free due to a numerical source separation algorithm and exploits sparsity in reconstruction of scatterers. It is demonstrated using near-field measurements at 60 GHz of an industrially manufactured composite panel with deliberate flaws. Compared to a more traditional Fourier imaging method, our method generates images with higher resolution and higher dynamic range. Flaw detection is also easier using our method as it generates images with less background clutter.

1 Introduction

Composite materials are increasingly used for a wide range of applications such as automotive parts, sports equipment and aerospace structures [1]. Specifically in aerospace, reasons for using composite materials can be their high strength-to-weight ratio and electromagnetic (EM) performance [2]. The latter is especially important for radomes, but also for aircraft structural components in some cases. Doubly curved and singly curved structures are used for aerodynamic surfaces, with singly curved structures being less costly and easier to manufacture [3]. During production and maintenance of such structures, nondestructive testing (NDT) is typically performed to detect flaws without detrimental effects on performance [4]. An interesting method for NDT in general, and for evaluation of EM properties of composites in particular is millimeter wave (mm-wave) (30-300 GHz) imaging [5, 6]. One of its main advantages is an inherently high resolution, but there are many others such as contactless operation, compact systems and a relatively low cost [5, 7]. A typical mm-wave imaging system consists of a transmitting (Tx) antenna illuminating the DUT, and a receiving (Rx) antenna sampling the signal scattered by the DUT at a set of spatial points. This sampling can be done in a simple way by mechanically scanning a single Rx antenna between the desired spatial points [8].

A traditional way of performing microwave and mm-wave imaging is through Fourier methods. One common example is synthetic aperture radar (SAR), which has proven useful in a wide range of NDT applications [9–12]. SAR is traditionally performed by sampling the scattered signal over one spatial dimension and using a large bandwidth to obtain a two dimensional image [13]. A Fourier method with close similarities to SAR is time reversal imaging (commonly known as migration in geophysics) [14, 15]. In contrast to traditional SAR, this method

can be performed using a single frequency but with sampling of the scattered signal over two spatial dimensions. If sampling is performed in a plane, the signal can be translated to other parallel planes, which allows for simple imaging on a planar DUT.

Imaging can also be approached as an inverse problem, often using methods from computational electromagnetics where the fundamental EM equations are solved numerically [16–20]. As with time reversal imaging, inverse methods can be performed with spatial sampling in a plane using a single frequency. However, while time reversal imaging results in images in parallel planes, the inverse approach allows for images conformal to an arbitrary DUT surface [21]. One way of setting up the imaging problem from fundamental EM equations is with an inverse equivalent source formulation, where the known signal is related to unknown currents using an integral equation. This integral equation is then discretized to obtain a linear system of equations which can be solved to obtain the currents [20–22]. The system is often not solved directly, but through the use of appropriate optimization methods. Methods utilizing L_1-minimization have shown promise for the solution of underdetermined systems where the solution is known beforehand to be sparse in the selected basis [23, 24].

This communication builds upon the previous work in [25] and [26] where an inverse equivalent source technique was developed to generate high resolution and high dynamic range mm-wave images of planar DUTs. A source separation technique was used to estimate the scattered signal without the need for a reference measurement, and an L_1-minimization technique was used for sparse scatterer reconstruction on the DUT. The sparsity in the reconstruction stemmed from the intended application of industrially manufactured low-loss, low-permittivity aerospace composite panels, as flaws were then assumed to be few and physically small.

The purpose of this communication is to demonstrate transmission-based imaging on a singly curved surface enclosing a DUT. If the DUT is itself singly curved, the image can be conformal to its surface. This makes the method more suited towards the intended application of NDT of aerospace structures as it extends the possible geometries of DUTs. As singly curved structures are less difficult and costly to manufacture than doubly curved structures, the extension of the DUT geometry made in this work is expected to be relevant for many realistic structures. The images presented in this communication use data from near-field measurements at 60 GHz of an industrially manufactured singly curved composite panel. For comparison, images are generated both using the inverse approach and more conventional time reversal imaging. As in previous work, the images produced using the sparse imaging approach have high resolution and high dynamic range, especially when compared to those produced using time reversal.

The communication is organized as follows. Section 2 briefly describes the imaging algorithms of interest. Section 3 describes the experimental setup used to retrieve data. Section 4 presents and discusses imaging results, which is followed by conclusions in Section 5.

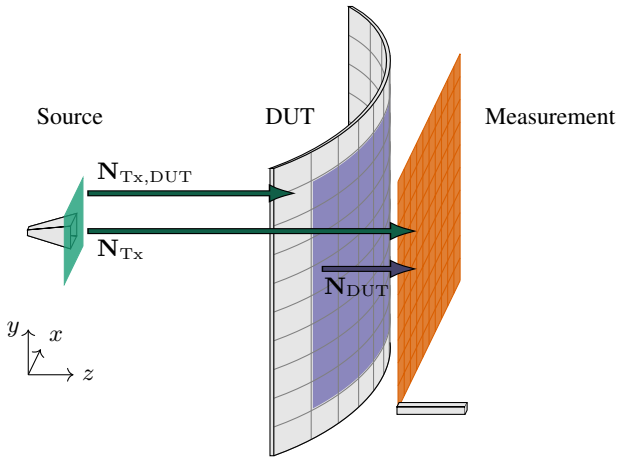

Figure 1: Illustration of the measurement setup with surfaces of interest (source, DUT, measurement) highlighted and operators between surfaces as arrows.

2 Imaging Algorithms

The problem of interest is visualized in Fig. 1 where a source (the Tx antenna) illuminates a singly curved DUT and the transmitted signal is measured in a planar grid by the Rx antenna. The objective of an imaging algorithm is to use the data from the measurement plane to reconstruct an image of the DUT showing EM flaws. An inverse equivalent source approach is used to reconstruct equivalent electric currents on a planar surface in front of the source and a singly curved surface on the DUT (the surfaces highlighted in Fig. 1). For this purpose, operators mapping electrical currents to electric fields are used, with operators of interest drawn in Fig. 1. The details of this approach are found in [25, 26] for planar surfaces, and in this work we primarily highlight the differences required for imaging on singly curved surfaces.

The sparse imaging used in this work specifically uses two steps detailed in [25, 26]: source separation and L_1-minimization. The source separation step uses a truncated singular value decomposition (SVD) regularization to numerically estimate the field due to the source and the background medium of the DUT. This is then subtracted from the measured data, resulting in a field due to flaws in the DUT without use of a reference measurement. The general methodology is independent of DUT geometry, and as such it is the same as used in earlier work.

The L_1-minimization step is used to reconstruct flaws using the data from the source separation step. The nominal manufacturing quality is deemed to be good enough that flaws are few and far apart, which corresponds to a sparsity condition for scatterers in a pixel basis. Due to this, the imaging problem is

formulated as a basis pursuit denoising problem [24], which reads

$$\hat{\boldsymbol{s}} = \arg\min_{\boldsymbol{s}} \ \|\boldsymbol{s}\|_1 \tag{2.1}$$

$$\text{s.t } \|\mathbf{N}_{\text{DUT}}(\boldsymbol{s} \circ \widehat{\boldsymbol{E}}_{\text{DUT}}) - \widehat{\boldsymbol{E}}_{\text{sc}}\|_2 \leq \kappa\sigma. \tag{2.2}$$

In the above, $\boldsymbol{s}$ are scattering amplitudes, $\widehat{\boldsymbol{E}}_{\text{DUT}}$ is an estimate of the field incident on the DUT (computed from the source separation), $\widehat{\boldsymbol{E}}_{\text{sc}}$ is the scattered field obtained from the source separation step, $\kappa \leq 1$ is a user-defined parameter and σ is the L_2-norm of the residual given by a phase-conjugation solution. The bound in (2.2) thus produces solutions with smaller residuals in L_2 than obtained by phase conjugation, with $\kappa < 1$ enabling even tighter bounds. The implementation uses the SPGL1 solver for MATLAB [24, 27]. While the general method is the same as presented in earlier work, the singly curved shape of the DUT required changes in certain parts. Since the previous work used planar geometries, care was taken to adapt the DUT mesh to be conformal to an arbitrary singly curved surface. Due to the large electrical size of the imaging problem, the operator $\mathbf{N}_{\text{DUT}}$ in Fig. 1 is accelerated by exploiting translational invariance in the Green's function. For a planar DUT, translational invariance can be obtained in both x and y, making the operator similar to a Toeplitz matrix. Matrix-vector multiplications for this matrix type can be computed by fast Fourier transforms (FFT) [28], enabling the operator to be applied using a two-dimensional FFT. For the DUT geometry used in this work, translational invariance can only be obtained in y, changing the structure of the operator. The acceleration method was modified to reflect this, with the operator being applied using a combination of FFT's and summation instead.

As an alternative to the sparse imaging method, data is also processed using a Fourier method. A time reversal approach [14, 15] is used since this allows for imaging using single frequency data in two spatial dimensions. Since the method translates the signal from the measurement plane to other parallel planes, multiple translations are required for imaging on a singly curved surface. For each x-coordinate in the measured data, the signal is translated in $-z$ such that the resulting image plane intersects with the DUT surface at that x-coordinate. The image data along that intersection is then extracted, generating an image conformal to the DUT surface when this is done for every x. Finally, the image is normalized to that obtained from a reference measurement with the DUT absent.

3 Measurement Setup

Measurements were performed in the microwave laboratory at Lund University, Sweden. A photograph of the measurement setup is shown in Fig. 2, which can be compared to the schematic view in Fig. 1. The setup was mounted on a Newport RS 2000 optical table. The Tx antenna was a Flann 25240-20 standard gain horn and the Rx antenna was an MVG OEW5000 open-ended waveguide.

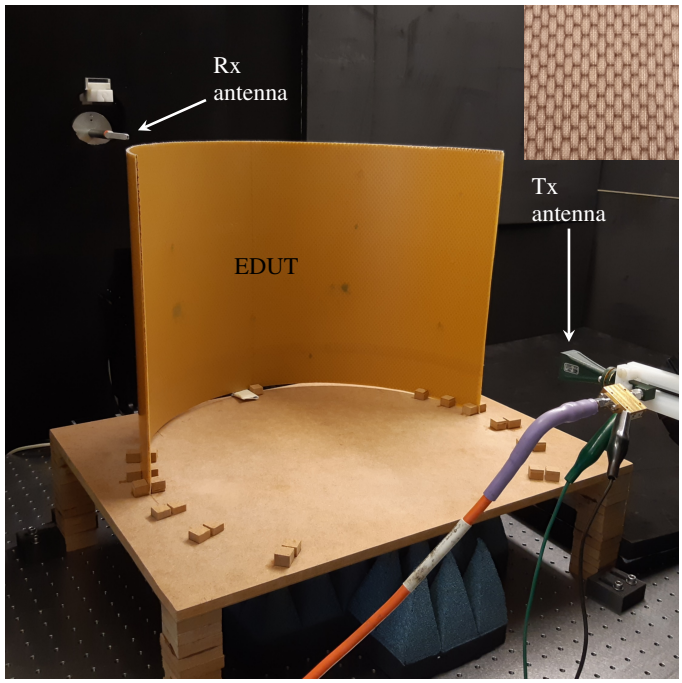

Figure 2: Experimental setup with the example DUT (EDUT) mounted for imaging of its center. Top right inset shows close-up view of EDUT structure.

An SHF 827 RF amplifier was used at the Tx end of the system to boost the signal level. The Rx antenna was scanned along the measurement surface using two THORLABS LTS300/M positioners. The Tx and Rx ends of the system were connected to a Rhode & Schwarz ZVA 67 GHz vector network analyzer (VNA) where S21 was measured. Measurements were performed for 201 linearly spaced frequency points in the band 55-65 GHz to allow for reduction of multipath propagation by time gating. The frequency of interest to image reconstruction was centered in this band at 60 GHz. A laptop was used to control measurements using a GPIB connection to the VNA and USB connections to the positioners. Data was then retrieved for all frequency points in 81×81 regularly spaced points over a 300 mm $\times$ 300 mm measurement plane, a scan which took roughly 7 h to complete. The sampling distance was thus 3.75 mm, which corresponds to $3\lambda/4$ at 60 GHz. This is in violation of the Nyquist criterion, which is of interest to Fourier based steps in the post-processing. However, the wavenumber spectrum at the Rx antenna is restricted by the beamwidth of the Tx antenna and the system geometry. This allows for a larger sampling distance before aliasing occurs than that given by the standard Nyquist criterion [29]. The DUT, referred to as the example DUT (EDUT) in the following, was an industrially manufactured composite panel provided by SAAB Aeronautics. The panel was shaped as a semi-circular cylindrical shell with a radius of 24 cm and a height of

35 cm. It was constructed as a sandwich-structured composite with a 2 mm low-permittivity overexpanded Nomex honeycomb core between two 0.5 mm sheets of Toray EX-1515, a cyanate ester quartz fabric pre-preg [30]. The adhesive Toray EX-1516, developed for bonding solid, honeycomb, or foam core structures used in aircraft and space applications [30], was used to assemble the panel and it was covered with a fluoropolymer film. A close-up of the EDUT showing the honeycomb structure is shown in the inset of Fig. 2.

A medium-density fiberboard platform was used to elevate the EDUT to a height appropriate for scanning of the Rx antenna. Blocks mounted on the top of the platform allowed for consistent rotation of the EDUT so that different parts could be imaged. The boresight distance between the Tx antenna and the EDUT was 570 mm, while the Rx antenna was scanned in a measurement plane 60 mm further away. These distances were selected to place the EDUT in the far-field of the Tx antenna, enable enough illumination of the EDUT and capture most of the scattered field in the measurement plane.

Two types of scans were performed: reference measurements and EDUT measurements. For the reference measurement, the setup was identical to that described above but with the EDUT removed. While one of the stated advantages of the sparse imaging approach was reference-free imaging, time reversal imaging required a reference measurement for normalization. EDUT measurements were performed with the EDUT rotated between scans, assisted by blocks mounted on the top of the platform. There was no overlap between imaged parts of the EDUT. The labels *right* and *left* used in following parts of this work refer to the directions when the EDUT is viewed from the Rx antenna towards the Tx antenna.

After capturing the data and before performing imaging, two post-processing steps were conducted: time gating and probe correction. As described earlier, a wideband measured signal was used for the purpose of reducing multipath components using time gating. More specifically, the frequency domain data for each spatial sample was zero-padded and transformed to the time domain where a Tukey window centered on the first peak in the signal was applied. A window length of 0.9 ns, corresponding to a 27 cm propagation distance in free space, was selected after inspection of the signal characteristics in the time domain. Transformation back to the frequency domain then resulted in a reduction of the multipath components of the signal. A single-frequency dataset at 60 GHz was extracted and probe correction was applied to it. This standard technique for open-ended waveguides, which is described in [8, 31], aims to remove the influence of the probe from measurement data. After these two post-processing steps, electric field data without multipath components could be obtained.

4 Imaging Results and Discussion

Images were generated from the time-gated and probe corrected measurement data using sparse imaging and time reversal imaging. To improve the resolution

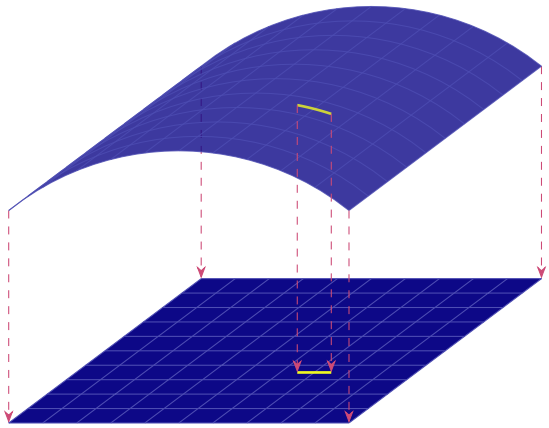

Figure 3: Image on the singly curved EDUT surface together with the same image projected to an xy-plane.

of the sparse images, a sub-sampling of 4 was used, replacing each mesh element on the EDUT by 4×4 smaller elements. The resolution of the time reversal images was equal to the measurement resolution as this was limited by the method itself. All processing was performed on a desktop computer with 32 GB RAM. While there were no processing parameters to set for time-reversal imaging, the sparse scatterer reconstruction step required selection of the parameters τ_{SVD} (truncation threshold in the SVD used in the source separation) and κ (from (2.2)) as discussed in [26]. For the images shown in this work, the parameters $\tau_{\mathrm{SVD}} = 0.01$ and $\kappa = 0.85$ were used.

In all images, reconstruction was done on the singly curved surface of the EDUT, but for visualization clarity they are shown here as planar images. These are projections from the original image on the singly curved surface to an xy-plane as illustrated in Fig. 3. The final images of the EDUT generated using time reversal imaging and sparse imaging are shown in Figs. 4 and 5 together with photos of the imaged parts of the EDUT. The color scale is equal for all images, although the quantities represented by that scale are different. This is done to illustrate differences in dynamic range between images rather than details in individual images.

Starting with the right part of the EDUT shown in Fig. 4, the sparse image in (b) shows six clearly visible indications which correspond to visual indications of flaws in (a). Most of the background is zero due to suppression of nonzero pixels by the L_1-minimization routine. For time reversal imaging in Fig. 4(c), it is seen that the indications are not as clearly distinguishable from the background as for sparse imaging. The resolution is also visibly lower as no sub-sampling could be performed. Of the visible indications, only the one near $(x, y) = (-30, 20)$ mm is similar to Fig. 4(b) in separation from the background. For other indications, the separation is only a few dB, which is not very far from the variation in the background. Those near $x = 100$ mm are especially difficult to distinguish due to

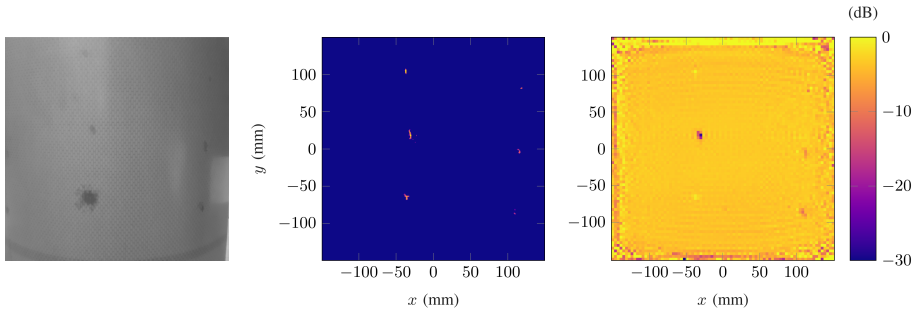

Figure 4: Images for the right part of the EDUT retrieved using different methods. (a) Photo of the measurement area. (b) Absolute values of the scattering amplitudes from sparse imaging. (c) Amplitude of the time reversed field normalized to reference field.

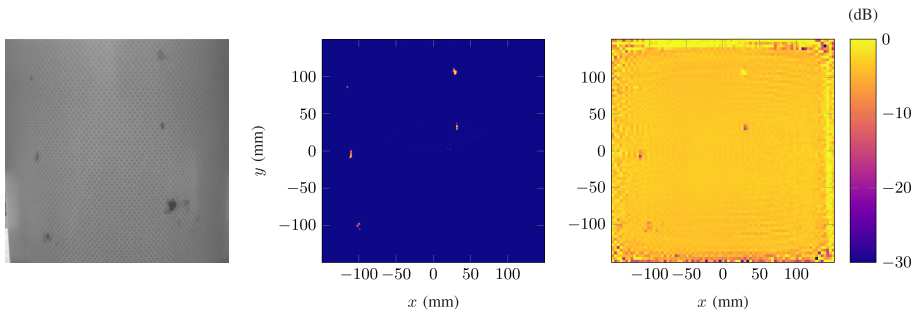

Figure 5: Images for the left part of the EDUT retrieved using different methods. (a) Photo of the measurement area. (b) Absolute values of the scattering amplitudes from sparse imaging. (c) Amplitude of the time reversed field normalized to reference field.

the spurious background near the edges. The spurious background near the edges can be related to the normalization. Both the measured and reference fields have smaller main lobes after the time reversal translation, resulting in very low and noisy values near the edges. Normalization increases the low amplitudes, but the noise remains. Even away from the spurious values near the edges of the image, the background is not as homogeneous as in the sparse imaging case.

The left part of the EDUT is shown in Fig. 5. In this case, the sparse image in Fig. 5(b) shows four clear indications which correspond to visual indications in (a), and one weak indication near $(x, y) = (-100, 100)$ mm. In the background some clutter at low levels is visible. This can be attributed to the selected κ

since a higher value would reduce clutter, but at the expense of the number of visible indications. For time reversal imaging in Fig. 5(c), the indications which were clear in (b) are seen but with the expected lower resolution and a smaller separation to the background. In the top left, it is difficult to identify a flaw due to the spurious background. There is one strong visual indication in the lower right of Fig. 5(a) which is not present in either (b) or (c). An additional transmission measurement was set up to investigate this discrepancy. This measurement was simpler than that used for the main results and consisted of the same Tx antenna in line with a fixed Rx probe connected to a ZVA67 VNA measuring S21 at 60 GHz. Different parts of the EDUT were moved between the antenna and the probe while S21 was monitored. All flaws affected S21 except for the one not seen in Figs. 5(b) and (c). Since three different methods using two separate measurements failed to detect that flaw, it is concluded that its electromagnetic properties are similar to the EDUT background medium. This apparent absence of electromagnetic contrast makes the detection failure less concerning as the purpose of our method is primarily to evaluate electromagnetic performance.

For both time reversal imaging and sparse imaging, it can be observed that some flaws near the edges of the measurement plane give weaker indications on images than those in the center, e.g. near $x = 100$ mm in Fig. 4(b). For time reversal imaging, this can be partly attributed to the spurious background near the edges. However, scattering amplitudes from sparse imaging are also weaker near the edges without any spurious background. One explanation for this effect lies in the collection of the scattered field. If the location of a scatterer is near the center of the measurement plane, a large part of the scattered field is captured by the measurement. For scatterers further away from the center, less of the scattered field is captured which gives less data for image reconstruction. A system implication of this is that the measurement plane should be larger than the section of interest on the DUT.

5 Conclusion

The aim of this work was to demonstrate a mm-wave imaging method developed for NDT of singly curved composite panels. A comparison has been made between our sparse imaging method and a more traditional time reversal imaging method. The sparse imaging method has been demonstrated to provide images with multiple benefits over the time reversal imaging method such as higher resolution, higher dynamic range and more homogeneous background. While the method used in this work is an extension of one developed for planar DUTs, the imaging on singly curved DUTs presented in this work is likely to be more relevant to NDT on structures found in aerospace applications.

While the method presented in this work can be used for NDT of industrially manufactured panels as demonstrated, it can be improved upon to streamline usage in an industrial setting. One easily identified limitation is the measurement time, which was 7 h in this work. It could be reduced greatly by replacing the

single Rx antenna used in this work with an antenna array. This comes at a cost and complexity deemed unnecessary at this stage, but would likely not impact the presented algorithms. Another limitation is the need to accurately know the DUT shape and position beforehand. In this work, a simple semi-circular cylindrical shell was used and it was carefully positioned. While more complicated DUTs can still have known geometries, the method could be made more versatile by the use of some other technology like 3D laser scanning for geometry characterization. This could also increase accuracy since small changes in DUT geometry and position can be accounted for. An interesting extension of this work would be to move from transmission-based to reflection-based imaging since NDT could then be performed with access to only one side of the DUT. While this extension was done for planar DUTs in our previous work, a more considerable effort would be needed to do the same for singly curved DUTs.

Acknowledgment

The authors would like to thank P. Hallander and M. Petersson at SAAB Aeronautics, Linköping, Sweden for manufacturing the composite panel. They would also like to thank C. Cederberg at the Department of Electrical and Information Technology, Lund University, for manufacturing mechanical components used in the measurements.

References

[1] K. K. Chawla, *Composite Materials: Science and Engineering*, 4th ed. Cham, Switzerland: Springer International Publishing, 2019.

[2] P. Irving and C. Soutis, Eds., *Polymer Composites in the Aerospace Industry*, 2nd ed. Duxford, United Kingdom: Woodhead Publishing, 2020.

[3] M. Hagnell and M. Åkermo, "A composite cost model for the aeronautical industry: Methodology and case study," *Composites Part B: Engineering*, vol. 79, pp. 254 – 261, 2015.

[4] P. J. Shull, *Nondestructive evaluation: theory, techniques, and applications*. Boca Raton, FL, USA: CRC press, 2002.

[5] S. Kharkovsky and R. Zoughi, "Microwave and millimeter wave nondestructive testing and evaluation - overview and recent advances," *IEEE Instrumentation Measurement Magazine*, vol. 10, no. 2, pp. 26–38, April 2007.

[6] M. A. Abou–Khousa, A. Ryley, S. Kharkovsky, R. Zoughi, D. Daniels, N. Kreitinger, and G. Steffes, "Comparison of x-ray, millimeter wave, shearography and through-transmission ultrasonic methods for inspection of honeycomb composites," *AIP Conference Proceedings*, vol. 894, no. 1, pp. 999–1006, 2007.

[7] S. S. Ahmed, A. Schiessl, F. Gumbmann, M. Tiebout, S. Methfessel, and L. Schmidt, "Advanced microwave imaging," *IEEE Microwave Magazine*, vol. 13, no. 6, pp. 26–43, Sep. 2012.

[8] A. Yaghjian, "An overview of near-field antenna measurements," *IEEE Transactions on Antennas and Propagation*, vol. 34, no. 1, pp. 30–45, 1986.

[9] J. T. Case, M. T. Ghasr, and R. Zoughi, "Optimum two-dimensional uniform spatial sampling for microwave SAR-based NDE imaging systems," *IEEE Transactions on Instrumentation and Measurement*, vol. 60, no. 12, pp. 3806–3815, Dec 2011.

[10] M. J. Horst, M. T. Ghasr, and R. Zoughi, "A compact microwave camera based on chaotic excitation synthetic-aperture radar," *IEEE Transactions on Antennas and Propagation*, vol. 67, no. 6, pp. 4148–4161, June 2019.

[11] H. C. Rhim and O. Büyüköztürk, "Wideband microwave imaging of concrete for nondestructive testing," *Journal of Structural Engineering*, vol. 126, no. 12, pp. 1451–1457, 2000.

[12] T. Truong, A. Dinh, and K. Wahid, "An ultra-wideband frequency system for non-destructive root imaging," *Sensors*, vol. 18, no. 8, p. 2438, Jul 2018.

[13] M. A. Richards, J. A. Scheer, and W. A. Holm, Eds., *Principles Of Modern Radar*. Raleigh, NC, USA: SciTech Publishing, Inc., 2010, vol. 1: Basic Principles.

[14] R. H. Stolt, "Migration by Fourier transform," *Geophysics*, vol. 43, no. 1, pp. 23–48, 1978.

[15] C. Gilmore, I. Jeffrey, and J. LoVetri, "Derivation and comparison of SAR and frequency-wavenumber migration within a common inverse scalar wave problem formulation," *IEEE Transactions on Geoscience and Remote Sensing*, vol. 44, no. 6, pp. 1454–1461, 2006.

[16] D. Colton and R. Kress, *Inverse Acoustic and Electromagnetic Scattering Theory*, 3rd ed. Cham, Switzerland: Springer Nature Switzerland AG, 2019.

[17] P. C. Hansen, *Discrete Inverse Problems : Insight and Algorithms*. Philadelphia, PA, USA: Society for Industrial and Applied Mathematics, 2010.

[18] N. Joachimowicz, C. Pichot, and J. P. Hugonin, "Inverse scattering: an iterative numerical method for electromagnetic imaging," *IEEE Transactions on Antennas and Propagation*, vol. 39, no. 12, pp. 1742–1753, 1991.

[19] S. Caorsi, A. Massa, M. Pastorino, and M. Donelli, "Improved microwave imaging procedure for nondestructive evaluations of two-dimensional structures," *IEEE Transactions on Antennas and Propagation*, vol. 52, no. 6, pp. 1386–1397, 2004.

[20] K. Persson, M. Gustafsson, G. Kristensson, and B. Widenberg, "Radome diagnostics—source reconstruction of phase objects with an equivalent currents approach," *IEEE Transactions on Antennas and Propagation*, vol. 62, no. 4, pp. 2041–2051, 2014.

[21] T. F. Eibert and C. H. Schmidt, "Multilevel fast multipole accelerated inverse equivalent current method employing Rao–Wilton–Glisson discretization of electric and magnetic surface currents," *IEEE Transactions on Antennas and Propagation*, vol. 57, no. 4, pp. 1178–1185, April 2009.

[22] J. L. A. Quijano and G. Vecchi, "Field and source equivalence in source reconstruction on 3D surfaces," *Progress In Electromagnetics Research*, vol. 103, pp. 67–100, 2010.

[23] M. Zibulevsky and M. Elad, "L1-L2 optimization in signal and image processing," *IEEE Signal Processing Magazine*, vol. 27, no. 3, pp. 76–88, 2010.

[24] E. van den Berg and M. P. Friedlander, "Probing the Pareto frontier for basis pursuit solutions," *SIAM Journal on Scientific Computing*, vol. 31, no. 2, pp. 890–912, 2008.

[25] J. Helander, A. Ericsson, M. Gustafsson, T. Martin, D. Sjöberg, and C. Larsson, "Compressive sensing techniques for mm-wave nondestructive testing of composite panels," *IEEE Transactions on Antennas and Propagation*, vol. 65, no. 10, pp. 5523–5531, Oct. 2017.

[26] J. Helander, J. Lundgren, D. Sjöberg, C. Larsson, T. Martin, and M. Gustafsson, "Reflection-based source inversion for sparse imaging of low-loss composite panels," *IEEE Transactions on Antennas and Propagation*, vol. 68, no. 6, pp. 4860–4870, 2020.

[27] E. van den Berg and M. P. Friedlander, "SPGL1: A solver for large-scale sparse reconstruction," December 2019. [Online]. Available: https://friedlander.io/spgl1

[28] G. H. Golub and C. F. V. Loan, *Matrix Computations*, 3rd ed. Baltimore, MD, USA: Johns Hopkins University Press, 1996.

[29] A. C. Newell, "Error analysis techniques for planar near-field measurements," *IEEE Transactions on Antennas and Propagation*, vol. 36, no. 6, pp. 754–768, 1988.

[30] Toray Advanced Composites. Accessed Sept. 24, 2021. [Online]. Available: https://www.toraytac.com/

[31] A. Yaghjian, "Approximate formulas for the far field and gain of open-ended rectangular waveguide," *IEEE Transactions on Antennas and Propagation*, vol. 32, no. 4, pp. 378–384, 1984.

Measurements of microwave scattering by ultrasound in air at oblique incidence

N. Wingren and D. Sjöberg

Paper V

Published as: N. Wingren and D. Sjöberg, "Measurements of microwave scattering by ultrasound in air at oblique incidence," *Europhysics Letters*, Vol. 131, No. 5, 2020. Accepted manuscript, published version available at DOI 10.1209/0295-5075/131/54003.

Abstract

Scattering of electromagnetic waves against acoustic waves has been studied in acousto-optics and radio acoustic sounding of the atmosphere, among others. Strong interaction requires phase matching, which occurs at two angles between waves. These depend on the wavelength ratio. The scattered electromagnetic wave is frequency shifted by the acoustic frequency, either up or down depending on the angle between waves. This work presents experimental verification of this scattering for 27.3 GHz microwaves and 40 kHz ultrasound in air. Both up- and down-shifting of the scattered wave is shown. Previous work has mostly focused on either nearly perpendicular or parallel incidence. In contrast, this work considers oblique incidence with frequencies differing from those used in acousto-optics and radio acoustic sounding.

1 Introduction

Electromagnetic scattering by acoustic waves has been widely studied in the field of acousto-optics [1]. This started in the early 20th century with a prediction by Brillouin [2], resulting in experimental verification and deepening of the theory [1]. With the invention of the laser, acousto-optics grew and many devices were developed for manipulating laser beams [1]. As the name indicates, the electromagnetic frequencies in acousto-optics are in the optical range [3]. Ultrasound in the MHz range is often used in practical devices [4].

The interaction has also found use in meteorology through the Radio Acoustic Sounding System (RASS) [5]. This is a system measuring temperature and water vapor profiles in the atmosphere [6], and has been proposed for detecting aircraft wake vortices [7] as well as forest fires [8]. The system is often an addition to atmospheric radars for observation of clear air, with frequencies ranging from 10s of MHz to 1 GHz [6]. RASS requires an acoustic wavelength half that of the electromagnetic wavelength [5]. The relevant radar frequencies thus places acoustic frequencies in the audible range.

Though the frequency range for RASS differs from that in acousto-optics, the interaction mechanism is very similar. The basis of the interaction is the acoustic wave affecting dielectric properties of the medium [9]. It is commonly explained as the acoustic pressure modulating the density of the medium, which in turn modulates the refractive index [6]. This description is sufficient for fluid media, but a more complicated model is required for solid media [3].

In both acousto-optics and RASS, phase matching between the acoustic and electromagnetic waves is a crucial part of obtaining stronger scattering [3, 5]. This can only happen under very specific circumstances. For RASS and much of acousto-optics it is described by the Bragg condition, which relates the angle of incidence to the acoustic and electromagnetic wavelengths [9]. The condition is affected by parameters of the medium, which is how changing atmospheric conditions are detected in RASS [10]. In acousto-optics, devices such as modulators,

scanners and filters utilize the Bragg condition to manipulate laser beams [3]. Another important detail is a frequency shift of scattered electromagnetic waves. For Bragg interaction, the shift is by a single acoustic frequency up or down [3,9]. The frequency shift is not always used in acousto-optics, but it is crucial for RASS [9].

This work focuses on the Bragg mechanism, but other interaction mechanisms exist. Vibrations caused by acoustic excitation can be detected with radar as a Doppler-shifted echo, with possible applications in land mine detection [11] and non-destructive testing [12]. A similar mechanism uses amplitude modulated acoustic waves to cause vibration inside objects, which has been proposed for use in medical imaging [13]. Both of these interaction mechanisms can be explained using the micro-Doppler effect [14]. In the emerging field of ultrasound-mediated optical tomography, a frequency shift is instead caused in light from ultrasound modulation of optical path length and refractive index [15].

This work presents experimental verification on Bragg diffraction of electromagnetic waves by acoustic waves for a novel frequency range and incidence of the waves. The frequency of the electromagnetic waves was 27.3 GHz, placing them near the mm-wave range. The acoustic waves were 40 kHz ultrasound. For these frequencies in air, the angle between the wave vectors was determined (from the Bragg condition) to be 50°. This is between acousto-optics which has nearly perpendicular incidence and RASS which has parallel incidence. The emphasis of the measurements was to detect scattered power at the expected angle and frequency shift.

2 Interaction Mechanism

The interaction mechanism of interest to this work has its basis in photoelasticity. In general, photoelasticity relates the displacement gradient in a medium to the inverse of the relative permittivity tensor [16]. The full formulation uses a fourth-rank photoelastic tensor with no symmetry, which is necessary for many solids [16]. In this work though, a much simpler scalar relation is assumed as is often done in acousto-optics [1, 3]. For small perturbations in a mechanically and electrically isotropic medium where the photoelastic tensor has equal components, the following can be derived from a more complete tensor relation [17]

$$\varepsilon_1 = \frac{\varepsilon_r^2 \mathfrak{p}}{K} p. \tag{2.1}$$

Here, ε_1 is the perturbation in relative permittivity, ε_r is the unperturbed relative permittivity, $\mathfrak{p}$ is the scalar photoelastic constant, K is the bulk modulus and p is the pressure. The total permittivity is $\varepsilon = \varepsilon_0(\varepsilon_r + \varepsilon_1)$. Since an acoustic wave is a pressure variation, (2.1) shows that a permittivity variation can be expected to follow.

An electromagnetic wave incident on the acoustic wave is scattered against the dielectric perturbation, where stronger scattering can occur due to phase

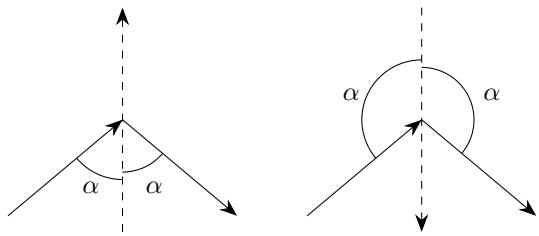

Figure 1: Propagation directions for acoustic (dashed) and electromagnetic waves where (2.3) holds. (−) case to the left and (+) case to the right.

matching between the acoustic and electromagnetic waves [1, 3]. In acousto-optics, two types of scattering are commonly considered: Raman-Nath diffraction and Bragg diffraction [1]. What type is relevant depends on what is commonly called the Klein-Cook parameter [1, 18]

$$Q = \frac{2\pi\lambda L}{\Lambda^2} \tag{2.2}$$

where λ is the electromagnetic wavelength, L is the length for which the electromagnetic wave overlaps with the acoustic wave and Λ is the acoustic wavelength. Raman-Nath diffraction occurs for $Q \ll 1$ and Bragg diffraction for $Q \gg 1$ [18]. This work considers the case when $\lambda \sim \Lambda$ and the interaction length L is a number of wavelengths. Thus, Raman-Nath diffraction is not valid. For large L this work is clearly in the Bragg regime, but for L closer to Λ the interaction is still similar to Bragg diffraction [18].

In the Bragg regime, phase matching for given wavelengths λ and Λ can only occur for two orientations of the beams. This is described by the Bragg condition, which in acousto-optics is commonly defined using the angle of incidence [3]. However, in this work it is expressed equivalently as [17]

$$\cos\alpha = \mp\frac{\lambda}{2\Lambda} \tag{2.3}$$

where α is the angle between the acoustic and electromagnetic beams, λ is the electromagnetic wavelength and Λ is the acoustic wavelength. The scattered field has the same angle towards the acoustic wave as the incident field [3]. This is shown in fig. 1 for the two cases in (2.3).

One important property of the scattered field is that its frequency is shifted when compared with the incident field. This shift is $\pm F$ where F is the acoustic frequency [3]. The $\pm$ sign follows the same convention as the $\mp$ sign in (2.3). Thus, the frequency shift is positive if $\alpha > 90°$ and negative if $\alpha < 90°$. Further in this work (+) and (−) are used to denote scattering resulting in positive and negative frequency shifts.

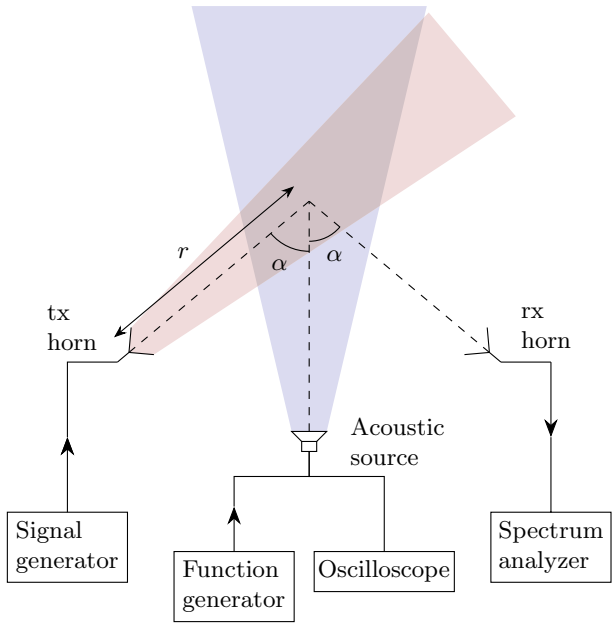

Figure 2: Setup and geometry for measurements.

3 Measurement Setup

Measurements were performed in the microwave laboratory at Lund University, Sweden. A schematic view of the setup is shown in fig. 2. Two sets of measurements were performed: one where the ultrasound frequency was varied and one where the ultrasound wave was reflected.

Both the transmitting and receiving antennas were 26.5-50 GHz standard gain horns. The polarization of the antennas was perpendicular to the plane of interaction shown in fig. 2. The ultrasound source consisted of two 40 kHz transducers with their centers spaced roughly 1 cm and fed with the same signal. The geometry was set up for the $(-)$ case of (2.3) such that $\alpha = 50°$ and $r = 22.5$ cm (see fig. 2). The antennas and ultrasound source are shown in fig. 3. Microwave absorbers where placed such that most of the direct microwave power would be either absorbed or reflected away from the receiving antenna.

The transmitted microwave signal was a 27.3 GHz continuous wave signal at a power of 20 dBm generated by an Agilent E8257D signal generator. The ultrasound signal was a 40 kHz modified square wave with a peak voltage around 15 V generated by a Tektronix FG504 function generator. The ultrasound signal was measured using a Rohde & Schwarz RTB2004 oscilloscope for inspection of the signal characteristics. The received microwave signal was measured using a Rohde & Schwarz FSU50 spectrum analyzer. For all measurements it had a resolution bandwidth set to 10 Hz and a video bandwidth set to 1 Hz. Logarithmic

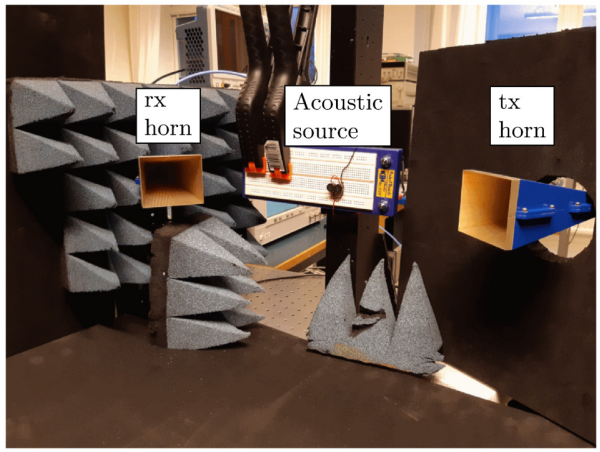

Figure 3: Antennas and ultrasound source.

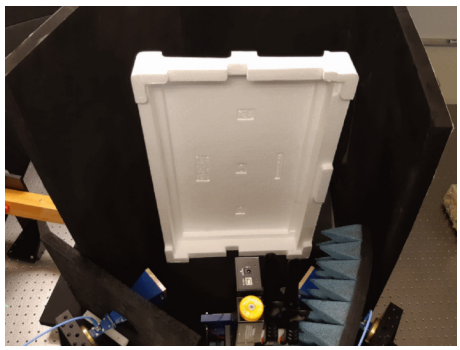

Figure 4: Setup with polystyrene sheet as ultrasound reflector.

averaging was applied over 10 sweeps.

Equation (2.3) would suggest a microwave frequency of 27.43 GHz for maximum scattering, given $\alpha = 50°$ and an ultrasound frequency of 40 kHz. However, due to uncertainties in the angle the actual maximum would not necessarily be at that frequency. In addition, the system response varied with the microwave frequency. After varying the microwave frequency, 27.3 GHz was found to maximize the scattered microwave signal.

In the first set of measurements, the ultrasound frequency was varied to investigate the effect on the frequency shifted microwave signal. Due to instrument limitations such as phase noise, it was difficult to achieve good precision for the ultrasound frequency. Three different ultrasound frequencies on the order of 10 Hz away from 40 kHz were used. Measurements were taken in spans of 200 Hz around the transmitted microwave frequency and 40 kHz below.

In the second set of measurements, the ultrasound beam was reflected to

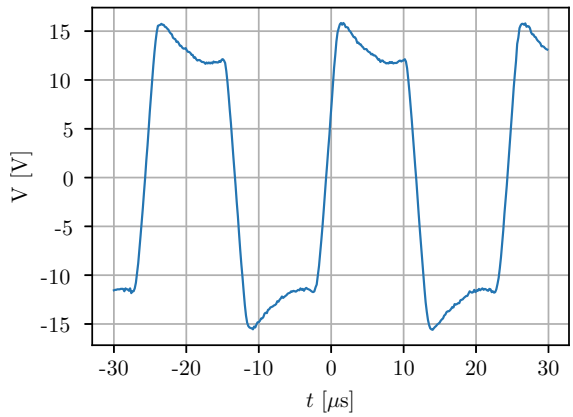

Figure 5: Ultrasound waveform used in measurements.

investigate the (+) case of (2.3). For a beam reflected 180°, the new angle α results in (2.3) holding for the (+) case. To achieve a good ultrasound reflection without excessively affecting the microwave beam, a sheet of polystyrene was placed in front of the ultrasound source as shown in fig. 4. The sheet was placed such that it would not block the overlap of the ultrasound and microwave beams. The result of this should involve a standing ultrasound wave, but in this work it is more practical to view it as two beams with opposite propagation directions. Measurements were taken in spans of 200 Hz around the transmitted microwave frequency, 40 kHz above and 40 kHz below.

4 Results

The waveform used for the ultrasound signal is shown in fig. 5. Variation of instrument parameters for maximum amplitude in combination with distortion from the ultrasonic transducers caused the unconventional waveform. The frequency was varied between measurements, which caused slight variation in the waveform. In general, no frequency shifted microwave signal was observed if the ultrasound source was turned off. With the ultrasound source turned on, a frequency shifted microwave signal could be observed. The frequency of this new microwave signal depended, as expected, on the microwave and ultrasound frequencies. When the microwave frequency was increased and approached 30 GHz, the power of the frequency shifted microwave signal decreased.

The results from the first set of measurements are shown in figs. 6 and 7. Figure 6 shows the leaked microwave signal directly transmitted between the two horns. The peak power level of -74 dBm gives an isolation of 94 dB between the transmitter and receiver without acoustic power. This leaked signal was used to determine characteristics for the transmitted microwave signal. It can be seen that there are peaks at frequencies other than the center frequency. These were

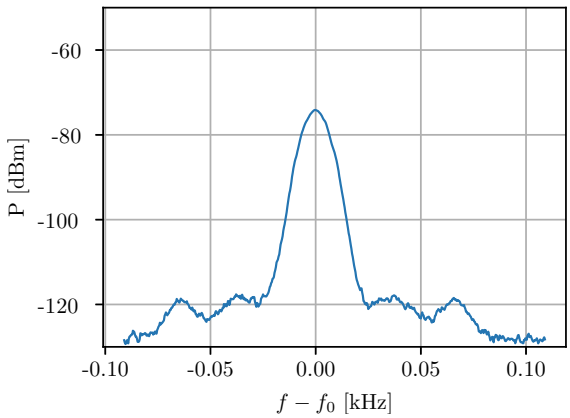

Figure 6: Microwave signal for direct transmission between horns. $f_0 = 27.300000275$ GHz.

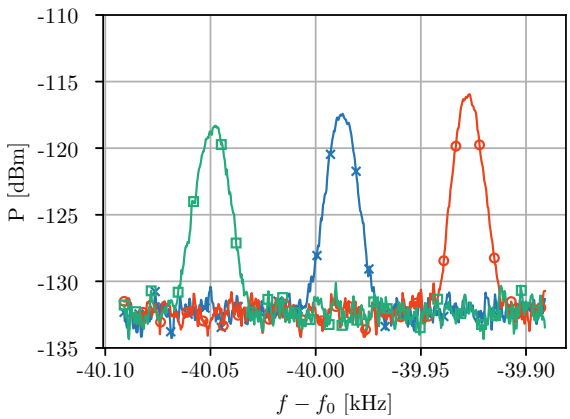

Figure 7: Frequency shifted microwave signals for different ultrasound frequencies. Frequency scale relative to $f_0 = 27.300000275$ GHz.

present regardless of the state of the ultrasound source, and are therefore assumed to be due to sidelobes in the signal generator. The center frequency in fig. 6 was measured to be 275 Hz above 27.3 GHz. This actual center frequency f_0 is also used when comparing the scattered microwave signals. The 3 dB linewidth in fig. 6 is 10 Hz and the 10 dB linewidth is 18 Hz. The frequency shifted microwave signals from the three ultrasound frequencies are shown in fig. 7. It can be seen that they are all within 100 Hz of $f_0 - 40$ kHz. Their frequency shifts are clearly different, which is to be expected since the ultrasound frequencies were different. The 3 dB linewidths of the peaks are (from left to right in fig. 7) 12 Hz, 11 Hz and 10 Hz while the 10 dB linewidths are 26 Hz, 21 Hz and 23 Hz. The linewidths of the frequency shifted microwave signals were thus on the same order of magnitude as that of the signal generator. The acoustic linewidth can also be expected to

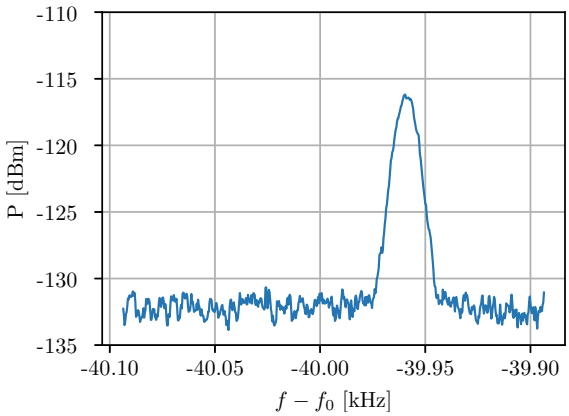

Figure 8: Microwave signal for negative frequency shift. Frequency scale relative to $f_0 = 27.300000162$ GHz.

affect the linewidths in fig. 7, but this linewidth was not recorded.

The results from the second set of measurements are shown in figs. 8 and 9. The direct transmission microwave signal was similar to that in fig. 6 but with a level of the peak roughly 15 dB higher. This can be explained by reflection of the transmitted beam by the polystyrene sheet. The actual center frequency f_0 in this case was 162 Hz above 27.3 GHz. Figure 8 shows the microwave signal with a negative frequency shift. It is very similar in shape and power level compared with the signals in fig. 7, which is to be expected since the involved beams are mostly unaffected by the polystyrene reflector. Figure 9 shows the microwave signal with a positive frequency shift. This is roughly 10 dB weaker than previous scattered microwave signals, but it is still possible to distinguish it from the noise. For clarification, no such signal was present before the addition of the polystyrene sheet. The weakening when compared with previous signals is due to the ultrasound beam being reflected by the polystyrene sheet. As such it traveled a longer distance than the original beam, leading to a lower acoustic pressure and a lower scattered power. The peaks in fig. 8 and fig. 9 are both located at frequencies near 40 kHz from the transmitted frequency. However, the negative shift is 39.96 kHz while the positive shift is 39.93 kHz. The difference of 30 Hz can probably be attributed to oscillator drift, especially since the two measurements were not taken simultaneously.

5 Discussion

Measurements verified that the scattering as predicted by (2.3) occurred with the expected frequency shifts and with the expected angle α. A significant change in the wavelength ratio with α fixed resulted in a decrease in received power. This showed that if (2.3) does not hold, the scattered power is affected. The results

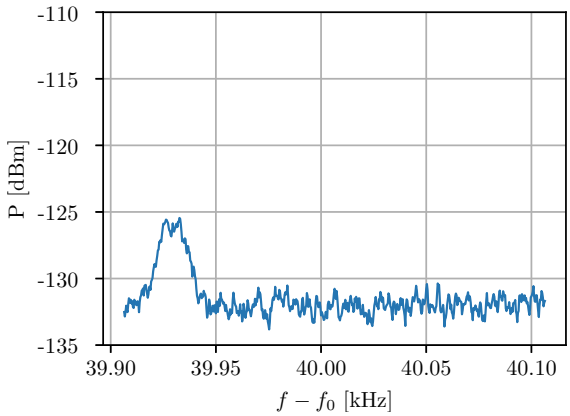

Figure 9: Microwave signal for positive frequency shift. Frequency scale relative to $f_0 = 27.300000162$ GHz.

are in accordance with established research fields and technologies relying on this type of scattering.

However, most measurements known to the authors have used other ratios between λ and Λ. The most established field investigating this kind of interaction is acousto-optics where commonly $\lambda \ll \Lambda$ [3]. The incidence of beams in acousto-optics is close to perpendicular, both in the Raman-Nath and Bragg regimes [3]. In RASS, the system is set up with collocated transmitters and receivers such that the scattered wave is focused back at the receiver [5]. The incidence is then parallel, necessitating $\lambda = 2\Lambda$. The current work has a ratio λ/Λ which is closer to that of RASS than that of acousto-optics.

Nevertheless, there are some significant differences between parallel and oblique incidence. The aforementioned focusing back towards the receiver should provide a possibility of increased scattered power [5]. Furthermore, with parallel incidence the overlap between the acoustic and electromagnetic beams is theoretically infinite, although in practice it depends on the length of pulsed signals [9]. For oblique incidence, the overlap is determined by the beamwidths and the angle α.

To increase the scattered electromagnetic power, a fairly obvious action would be to increase the power emitted by the acoustic source. This would result in a higher acoustic pressure and subsequently, as can be seen from (2.1), a higher dielectric perturbation. Another improvement would be to use larger arrays for both the acoustic and electromagnetic sources. This can be understood from the plane-wave spectrum of the sources. An arbitrary single-frequency wave can be seen as a spectrum of plane waves with different wave vectors, where power is divided among the modes [19]. In this work, α is the angle between the acoustic and electromagnetic wave vectors $\boldsymbol{q}$ and $\boldsymbol{k}$. For a given α, phase matching is only obtained for $\boldsymbol{q}$ and $\boldsymbol{k}$ fulfilling the Bragg condition. Due to tolerance in the Bragg condition, wave vectors close to these also contribute to the received

power [3]. Parts of the plane-wave spectra far from the optimal $\boldsymbol{q}$ and $\boldsymbol{k}$ contribute less. Using larger arrays, power can be concentrated to parts of the plane-wave spectra near the optimal $\boldsymbol{q}$ and $\boldsymbol{k}$ which should increase the received power.

The interaction between ultrasound and microwaves presented in this work has a potential application in non-destructive testing with a length scale of interest near 1 cm. A contrast in effective material properties, as caused by a defect, affects the Bragg condition and in turn the amplitude of the frequency shifted signal. This is similar to how RASS works [10]. Microwaves and ultrasound are used individually in non-destructive testing, but a combined system would be sensitive to contrasts in both electromagnetic and acoustic properties of a sample. This could lead to better detection of low-contrast defects, which has been stated as an advantage for combining ultrasound and microwaves in medical imaging [13]. Some examples where microwave and ultrasonic testing are used individually at length scales near 1 cm are timber [20, 21], concrete structures [22, 23] and thick composites [24]. Another possible application is detection of uneven ultrasonic propagation. Effects such as reflections and wave guiding can cause ultrasonic propagation in undesired directions when performing ultrasonic non-destructive testing. The interaction with an incident microwave would be altered by these effects, possibly allowing for detection using the frequency shifted microwave signal. The weak interaction strength observed during measurements might be an issue for practical applications. However, measurements in this work were performed in air where interaction is expected to be very weak due to its photoelastic constant $\mathfrak{p} = 0.00059$ [25]. Other media can have $\mathfrak{p}$ several orders of magnitude higher than this [26, 27].

6 Conclusions

The scattering of microwaves against ultrasound in air was measured. The effects of Bragg diffraction could be observed. An electromagnetic wave incident on an acoustic wave at the Bragg angle was scattered with a negative frequency shift corresponding to the ultrasound frequency. A slight change of the acoustic frequency resulted in a corresponding change in the frequency shift. A large change in the microwave frequency reduced scattered power at the original angle.

Reflection of the acoustic wave gave rise to a new scattering component with a positive frequency shift corresponding to the acoustic frequency. Thus, for given acoustic and electromagnetic frequencies both up- and down-shifting Bragg diffraction was observed.

* * *

The authors would like to thank J. Nilsson from the Department of Biomedical Engineering, Lund University for valuable discussions and for providing the ultrasonic transducers used in the measurements. This work was supported in

part by the Swedish Armed Forces, in part by the Swedish Defence Materiel Administration, in part by the National Aeronautics Research Program and in part by the Swedish Governmental Agency for Innovation Systems.

References

[1] Korpel A., *Acousto-optics* 1st Edition Optical engineering, 16 (Marcel Dekker Inc, New York) 1988.

[2] Brillouin L., *Ann. Phys.,* **9** (1922) 88.

[3] Saleh B. E. A. and Teich M. C., *Acousto-Optics* 2nd Edition Fundamentals of Photonics (John Wiley & Sons, Inc., Hoboken, New Jersey) 2007 Ch. 19 pp. 804–833.

[4] Savage N., *Nat. photonics,* **4** (2010) 728.

[5] Marshall J. M., Peterson A. M. and Barnes A. A., *Appl. Opt.,* **11** (1972) 108.

[6] Fukao S. and Hamazu K., *Radar for Meteorological and Atmospheric Observations* (Springer Japan) 2014.

[7] Rubin W. L., *J. atmos. ocean. technol.,* **17** (2000) 1058.

[8] Sahin Y. G. and Ince T., *Sensors (Basel),* **9** (2009) 1485.

[9] Gurvich A. S., Kon A. I. and Tatarskii V. I., *Radiophys. quantum electron.,* **30** (1987) 347.

[10] May P. T., Strauch R. G., Moran K. P. and Ecklund W. L., *IEEE trans. geosci. remote sens.,* **28** (1990) 19.

[11] Scott W. R. and Martin J. S., *Proc. SPIE,* **3710** (1999) 204.

[12] Buerkle A. and Sarabandi K., *IEEE trans. antennas propag.,* **57** (2009) 3628.

[13] Tafreshi A. K., Top C. B. and Gençer N. G., *Phys. med. biol.,* **62** (2017) 4852.

[14] Chen V. C., Li F., Ho S. and Wechsler H., *IEEE trans. aerosp. electron. syst.,* **42** (2006) 2.

[15] Elson D. S., Li R., Dunsby C., Eckersley R. and Tang M.-X., *Interface Focus,* **1** (2011) 632.

[16] Nelson D. F. and Lax M., *Phys. rev. B,* **3** (1971) 2778.

[17] Wingren N. *Acousto-electromagnetic interaction in materials for aerospace composites*, M.s. thesis Dept. of Elect. and Inform. Technol., Lund Univ., Lund, Sweden (2019).

[18] Klein W. R. and Cook B. D., *IEEE trans. sonics ultrason.,* **14** (1967) 123.

[19] Orfanidis S. J., *Diffraction – Plane-Wave Spectrum* Electromagnetic Waves and Antennas (Rutgers University) 2016 Ch. 19 pp. 844 – 922.

[20] Riggio M., Sandak J. and Franke S., *Constr. build. mater.,* **101** (2015) 1241.

[21] Vössing K. J. and Niederleithinger E., *Holzforschung,* **72** (2018) 467.

[22] McCann D. and Forde M., *NDT & E International,* **34** (2001) 71.

[23] Rehman S. K. U., Ibrahim Z., Memon S. A. and Jameel M., *Construction and Building Materials,* **107** (2016) 58.

[24] Ibrahim M., *Compos., Part A Appl. sci. manuf.,* **64** (2014) 36.

[25] Wingren N. and Sjöberg D., *Analytical modeling and multiphysics simulation of acousto-electromagnetic interaction* in proc. of *2020 14th European Conference on Antennas and Propagation (EuCAP)* 2020 pp. 1–5.

[26] Dixon R. W., *J. appl. physi.,* **38** (1967) 5149.

[27] Uchida N., *Japanese Journal of Applied Physics,* **7** (1968) 1259.